Accurate Dosimetry for Ocular Brachytherapy:
Measurement, Delivery Uncertainty, and Dose Calculation Studies

by

Hali Morrison

A thesis submitted in partial fulfillment of the requirements for the degree of

Doctor of Philosophy

in

Medical Physics

Department of Oncology
University of Alberta

Abstract

Ocular brachytherapy has been found to be an excellent alternative for the treatment of ocular melanomas compared to the predominantly used treatment prior to the 1980s of enucleation. Tumour control rates are generally >90%, overall survival rates are equivalent to enucleation, and ocular brachytherapy offers the major benefit of globe preservation and for many patients, vision retention. There are however relatively high rates of long-term toxicity and radiation side-effects which can affect the visual outcomes for patients receiving this treatment. Current clinical guidelines for ocular brachytherapy given by the American Association of Physicists in Medicine (AAPM) Task Group (TG)-129 and American Brachytherapy Society Ophthalmic Oncology Task Force (ABS-OOTF) reports include recommendations for treatment dose rate, dose prescription, irradiation duration, plaque size selection, radionuclide selection, and treatment planning/dose calculation methods. There are however a number of limitations in the current dosimetry formalism.

This work makes improvements to three areas of ocular brachytherapy dosimetry including experimental measurement methodology, treatment delivery, and dose calculation, all in a concerted effort to improve the accuracy and quality of clinical ocular brachytherapy. This in turn is expected to improve the comparison of different treatment protocols, provide more accurate experimental treatment verification, and lead to a better understanding of the current limitations and sources of uncertainty associated with this treatment.

Experimental dosimetry methods using EBT3 Gafchromic film were developed and specifically optimized for low-dose-rate and low-energy brachytherapy sources, which reduced the uncertainty in low-energy brachytherapy dose measurements by more than a factor of two. This enabled high accuracy measurements to be performed with two different styles of eye

plaques loaded with I-125 sources (16 mm COMS and Super9 Eye Physics plaques). Comparisons were made with the Plaque Simulator treatment planning system (TPS), which performs water-based dose calculations with corrections for the heterogeneous plaque materials, and with the Monte Carlo (MC) package MCNP6. The results of this work provided additional computational and experimental validation of Plaque Simulator within the central region of the plaque where agreements were very good. However, larger differences at off-axis positions and in some of the EBT3 film measurements indicated areas of uncertainty present in the treatment planning calculations and also in treatment delivery.

These uncertainties as well as others present in the full treatment process were comprehensively analyzed to determine the total treatment uncertainty at the prescription point (tumour apex) for the two plaques studied. Total uncertainty at the tumour apex is on the order of 15% (k=2), indicating that the tumour could potentially be under-dosed by a corresponding amount. Some centres apply an apex margin to account for tumour height uncertainty, but the size of an appropriate dosimetric margin has not been previously determined. Our analysis provides an uncertainty-based rational approach to determining the margin size required to ensure adequate dose coverage of the tumour apex, which ranged from 1.2 to 1.8 mm. The application of this dosimetric margin can potentially reduce the risk of local failure due to insufficient radiation dose.

The current dose calculation formalism for brachytherapy assumes an infinite homogeneous water medium, which has been shown to be inaccurate for many types of treatments, including ocular brachytherapy. With the goal of performing fully patient specific dose calculations accounting for both heterogeneous plaque and patient tissues, I-125 source data and COMS eye plaques were for the first time adapted for implementation in a newly available

TPS utilizing a collapsed-cone superposition dose calculation algorithm. The accuracy of the algorithm (trade named Advanced Collapsed cone Engine [ACE]) was evaluated for single I-125 seeds, for differently sized COMS plaques in water, and for two scenarios incorporating heterogeneous patient tissues: a voxelized eye phantom, and a patient CT dataset. Overall, ACE was found to agree well with MC simulations within the tumour and along the plaque central axis, however larger differences were found near the edge of the plaque lip and at tissue interfaces. Doses calculated with ACE were consistently closer to MC doses than those determined by Plaque Simulator, which ignores the effect of heterogeneous patient tissues. This work establishes a foundation to perform model based dose calculations for ocular brachytherapy in clinical practice.

Preface

The entirety of this thesis represents original research motivated by the objectives of my Ph.D. project. This research was supervised by Dr. R.S. Sloboda (primary supervisor), and Dr. G. Menon (co-supervisor). The work presented in this thesis was made possible with the assistance of and input from several collaborators; a summary of these contributions are provided following.

The portion of Chapter 3 pertaining to radiochromic film calibration has been published as: H. Morrison, G. Menon, and R.S. Sloboda, "Radiochromic film calibration for low-energy seed brachytherapy dose measurement," *Med. Phys.* **41**, 072101 (2014). This part of the chapter was initially conceptualized by R.S. Sloboda. I was responsible for all data collection and analysis and manuscript composition. G. Menon assisted with portions of the data collection, and provided guidance with data interpretation and contributed to manuscript edits. R.S. Sloboda was the supervising author, and was also involved in manuscript edits and project oversight. I initiated and led the remaining portion of Chapter 3 pertaining to triple-channel film heterogeneity correction methods. G. Menon created the EDW plans in Eclipse used to irradiate the films, and provided general guidance and editorial comments. R.S. Sloboda also provided guidance for this work and editorial comments.

The experimental verification of eye plaque dosimetry presented in Chapter 4 represents work that I initiated and led. I was responsible for all experimental film measurements and Monte Carlo simulations. G. Menon assisted with seed procurement for the film irradiations, as well as data interpretation, and provided editorial comments. R.S. Sloboda assisted with data interpretation and project oversight as well as providing editorial comments.

A slightly altered version of the work presented in Chapter 5 was published as: H. Morrison, G. Menon, M.P. Larocque, H.-S. Jans, E. Weis, and R.S. Sloboda, "Delivered dose uncertainty analysis at the tumor apex for ocular brachytherapy," *Med. Phys.* **43**, 2891-4902 (2016). The work described in this chapter was performed, initiated and led by me. I was responsible for all measurements, analysis of data, and manuscript composition. M.P. Larocque and E. Weis assisted with the clinical aspects and implications of the project as well as providing manuscript edits. H.-S. Jans assisted with all microCT image acquisition as well as manuscript

edits. G. Menon and R.S. Sloboda were both involved in project conceptualization, methodology development, manuscript edits, and project oversight.

The work presented in Chapter 6 is work that I initiated, performed, led, and helped conceptualize. G. Menon assisted with the use of OcB and provided general guidance as well as assistance with data interpretation and provided editorial feedback. R.S. Sloboda provided the initial conceptualization of this work, established the initial collaboration with Elekta, and provided editorial feedback. He also assisted with interpretation of the results and provided project oversight and guidance. G. Menon and R.S. Sloboda were responsible for the patient CT acquisition with significant assistance from B. Long. Y. Niatsetski and B. van Veelen with Elekta created the applicator models and I-125 sources in OcB based on the CAD drawings and PSS data I provided to them. M.P. Larocque assisted with creating the Plaque Simulator plans and E. Weis assisted with data interpretation.

The literature review, general description of ocular brachytherapy treatment methodology and outcomes and theoretical background material in Chapters 1 and 2, as well as the concluding comments in Chapter 7 were conceived and written independently, with editorial suggestions from my supervisors.

The patient melanoma images in Chapter 1 and the CT dataset of the ocular brachytherapy patient in Chapter 6 were used with ethics approval by the Health Research Ethics Board of Alberta (HREBA) Cancer Committee, Project name: "Preclinical evaluation of heterogeneous corrections in brachytherapy treatment planning," Project Number: HREBA.CC-16-0657, August 30, 2016.

Acknowledgements

There are many people I would like to acknowledge and thank for their help and support throughout this project. First and foremost, I would like to acknowledge and sincerely thank my primary supervisor, Dr. Ron Sloboda, and co-supervisor, Dr. Geetha Menon, for their significant contribution to my research project as well as my overall graduate experience. Their supervision, insight, guidance, and encouragement were above and beyond what I expected and I am extremely grateful for the opportunity to work with and learn from both of them.

I also want to thank Dr. Matthew Larocque for his contributions to my project, for good discussions and brainstorming, for encouragement and advice, and for being available to help answer all of my (many) ocular brachytherapy related questions. I am very grateful for the help and support from Dr. Ezekiel Weis, our ophthalmologist extraordinaire. Dr. Weis provided clinical input to my project, invited me into the OR and taught me the ins and outs of the surgical procedure and was always very encouraging and excited about all aspects of my project, for which I am very grateful.

I am also very thankful to my supervisory committee, Dr. Brad Warkentin and Dr. Gino Fallone, for their guidance and input to my project over the years. I also want to thank those who participated in my candidacy exam, Dr. Don Robinson, Dr. Richard Marchand, and my supervisory committee. As well, a sincere thank you to those who participated in my thesis defense including the chair, Dr. Satyapal Rathee, and examiners Dr. Don Robinson, Dr. Rowan Thomson, and my supervisory committee, for reading my thesis and giving me very helpful questions, comments, and corrections.

I also want to thank others who helped with components of my project. Dr. Hans Jans for helping with all of my microCT imaging, Mr. Brent Long for help with the patient CT imaging, and a big thank you to the machinists for building my phantoms and helping me with the "arts and crafts" portion of my project. I also want to sincerely thank all of the other medical physicists at the Cross Cancer Institute for their instruction during courses and labs, good discussions over the years, and contributing to an overall excellent graduate student experience.

I also want to acknowledge the financial support I received while at the University of Alberta, including the Vanier Canada Graduate Scholarship, the Alberta Innovates Health Solutions Graduate Studentship, the University of Alberta, as well as the Alberta Cancer

Table of Contents

List of Figures

List of Tables

List of Abbreviations

AAPM	American Association of Physicists in Medicine
ABS	American Brachytherapy Society
ACE	Advanced Collapsed cone Engine
AJCC	American Joint Committee on Cancer
CAD	Computer-aided drafting
CAX	Central AXis
CC	Collapsed-cone
CCD	Charged-coupled device
CCI	Cross Cancer Institute
CDF	Cumulative distribution function
CLRP	Carleton Laboratory for Radiation Physics
COMS	Collaborative Ocular Melanoma Study
CPE	Charged particle equilibrium
CSDA	Continuous slowing down approximation
CT	Computed tomography
DE	Dose energy
DF	Dose function
EBRT	External beam radiotherapy
EDW	Enhanced dynamic wedge
ENDF	Evaluated Nuclear Data File
EPDL	Evaluated Photon Data Library
ESTRO	European SocieTy for Radiotherapy and Oncology
FL-COMS	Fully loaded – COMS
GBBS	Grid-based Boltzmann solver
GEC	Groupe Européen de Curiethérapie
GTV	Gross tumour volume
GUM	Guide to the expression of Uncertainty in Measurement
hACE	High accuracy mode ACE
HDR	High dose rate
HU	Hounsfield unit
HVL	Half value layer
ICRP	International Commission on Radiological Protection
ICRU	International Commission on Radiation Units and Measurements
KERMA	Kinetic Energy Released per MAss
LBTE	Linear Boltzmann transport equation
LDR	Low dose rate
MBDCA	Model-based dose calculation algorithm
MC	Monte Carlo
MCNP	Monte Carlo N-Particle

MOSFET	Metal-oxide-semiconductor field effect transistor
netOD	Net optical density
NIST	National Institute of Standards and Technology
NNDC	National Nuclear Data Centre
OAR	Organ at risk
OcB	Oncentra® Brachy
OD	Optical density
OOTF	Ophthalmic Oncology Task Force
PDR	Pulsed dose rate
PMMA	Polymethyl methalcrylate
POI	Point of interest
PSS	Primary scatter separated
PTV	Planning target volume
PV	Pixel value
RNG	Random number generator
ROI	Region of interest
ROPES	Radiation Oncology Physics and Engineering Services
SAD	Source-to-axis distance
SCERMA	Scattered Energy Released per Mass
SS-COMS	Single seed – COMS
SSR	Source surface read
SSW	Source surface write
TG	Task group
TIFF	Tagged image file format
TLD	Thermoluminescent dosimeter
TPS	Treatment planning system
TTT	Transpupillary thermotherapy
TVL	Tenth value layer
WAFAC	Wide-angle free air chamber

Chapter 1 Introduction

1.1 Radiation therapy

In Canada, it is estimated that 2 in 5 people will develop cancer in their lifetimes and 1 in 4 will die of the disease. As such, it is the leading cause of death in Canada.[1] The primary treatment methods for cancer are surgery, chemotherapy, and radiation therapy, the latter being used for about 60% of cancer patients at some time during their treatment.[2] Radiation therapy uses ionizing radiation (such as photons, electrons, protons etc.) to kill the cancer cells by causing ionizations either directly in the DNA contained in the cell nucleus or in the surrounding materials, which in turn create highly reactive chemical species that damage the DNA. The goal of this DNA damage is to disrupt the cell's ability to function properly and replicate, and thereby induce cell death.[3,4] The intention then is to deliver an adequate amount of radiation to the tumour to either kill all cancer cells or to obtain a high probability of tumour control, while sparing as much normal tissue as possible to avoid radiation complications.

There are two main types of radiation therapy: external beam radiation therapy (EBRT) and brachytherapy. As the name suggests, EBRT delivers radiation from a source located outside of the patient, with energies in the kilovoltage (kV) to megavoltage (MV) range. The lower energy beams (75-300 kV), delivered by orthovoltage machines, are typically used to treat skin or superficial tumours, while the higher energy MV beams (such as from Co-60 or a high energy linear accelerator (linac)), are used to treat more deep-seated tumours.[5]

Conversely, brachytherapy (from the ancient Greek word 'brachy' meaning short distance) involves the use of a sealed source of radioactive material placed in close proximity or in contact with the tumour. The source can be applied by interstitial (within the tissue), intracavitary (within a cavity of the body), intraluminal (within the lumen of a vessel, such as a blood vessel, bronchus, esophagus, or bile duct), or by surface contact methods.[3,5,6]

1.1.1 Brachytherapy

The use of brachytherapy to treat cancer has a long history starting shortly after the discovery of radium in 1896 by Marie Curie. The first documented treatments with radium were performed by Dr. Margaret Cleaves in September 1903 in which she used a glass vial containing 1 g of radium

bromide to treat a patient with a sarcoma on the inner cheek, and a patient with advanced cervical squamous cell carcinoma.[7,8]

Prior to the advent of nuclear reactors and particle accelerators to produce non-naturally occurring or rare isotopes, brachytherapy was performed with naturally occurring radionuclides, predominantly radium and radon. However, these are seldom used today in favour of the artificially produced radionuclides, mainly due to the hazards and radioactive toxicity of radium and its by-products and the high energy emissions which require greater radiation safety precautions.[9] The factors that make a radionuclide appropriate for brachytherapy treatments are numerous, including: cost of production; high specific activity (activity per unit mass) such that sources with an adequately high activity are reasonably small; ease of filtering unwanted radiation emissions (charged particles or low energy x-rays); absence of toxic gases produced in the radionuclide decay; suitability of the energies of emitted photons or particles and half-life for the intended application of the source; as well as fulfillment of other safety precautions during fabrication and use.[10] The main radionuclides used in brachytherapy today are Ir-192, Co-60, Cs-137 (high-energy sources with emission >300 keV); I-125, Pd-103, Cs-131 (low-energy sources with emissions <50 keV); Sr-90, P-32, Y-90 (beta-emitting sources); and Cf-252 (neutron-emitting source).[9]

A couple of different classifications are used for brachytherapy sources and treatments, including the dose rate and duration of treatment. The dose rate of a treatment is generally categorized as either low (LDR) or high (HDR). The International Commission for Radiation Units and Measurements (ICRU) Report No. 89 defines the dose rate of LDR treatments to be 0.4 to 1.0 Gy/h, and of HDR treatments to be more than 12 Gy/h (0.2 Gy/min).[11] Ocular brachytherapy falls in the LDR category with a recommended dose rate of $\geq$ 0.6 Gy/h.

The duration of an implant treatment is classified as either permanent or temporary. In permanent implants, the brachytherapy sources remain in place indefinitely and the treatment is delivered over a prolonged period of time. Permanent implants are usually performed with a relatively short-lived radionuclide such that the radiation decays to a safe level within a few weeks or months, with a fairly low-activity source to maintain a low dose rate, and with moderate or low-energy emissions to reduce radiation safety risks. The most common permanent LDR implant uses I-125 seeds to treat prostate cancer. For temporary implants, the source is introduced into or in close proximity to the tumour and removed when the desired radiation dose

has been delivered. Brachytherapy treatments can be delivered in one session or in multiple sessions (fractions). Temporary implants typically make use of high dose rates delivered with high-energy sources like Ir-192, as for treatment of gynecological cancers, but can also involve low dose rates delivered with low-energy sources like I-125, as for ocular plaque therapy.[6] In the following sections the use of brachytherapy to treat ocular melanomas is discussed in detail.

1.2 Uveal melanoma

1.2.1 Anatomy of the eye

The eye is composed of three main parts: the globe, the orbit, and the adnexal structures. The globe is composed of three main layers (or tunics): the sclera, the uvea, and the retina. The sclera is the tough white outer layer (fibrous layer) of the eye, and is continuous with the cornea where it is clear to let light into the eye. The uvea is the middle layer of the globe (the vascular layer) and is composed of three main parts: the iris, the choroid, and the ciliary body. The iris is the coloured muscle with a small opening that forms the pupil, which lets light pass into the eye. The choroid is a thin, pigmented layer which lines the eye and contains capillaries which supply the retina and the front of the eye with blood. The ciliary body contains the ciliary muscles that change the shape of the lens to adjust the focus of the eye, and the ciliary epithelium that creates the aqueous humor contained in the anterior chamber of the eye, between the cornea and iris. The third and inner layer of the globe (sensory layer) is the retina, composed of specialized light sensitive nerve cells which are connected to the optic nerve. Within the retina and located at the posterior pole is the fovea, which is characterized by an absence of blood vessels and a predominance of cones in the photoreceptor layer, and is responsible for high acuity vision. Located on the nasal side of the fovea is the optic disc where the axons of ganglion cells exit through the sclera and join the optic nerve. The remainder of the eye is filled with fluid and is called the vitreous body.[12] The orbit of the eye consists of tissues surrounding the globe, and includes the muscles and optic nerve attached to the eye. The adnexal structures are accessory structures around the eye and include the eyelids and tear glands. These anatomical features are all shown in Figure 1.1.
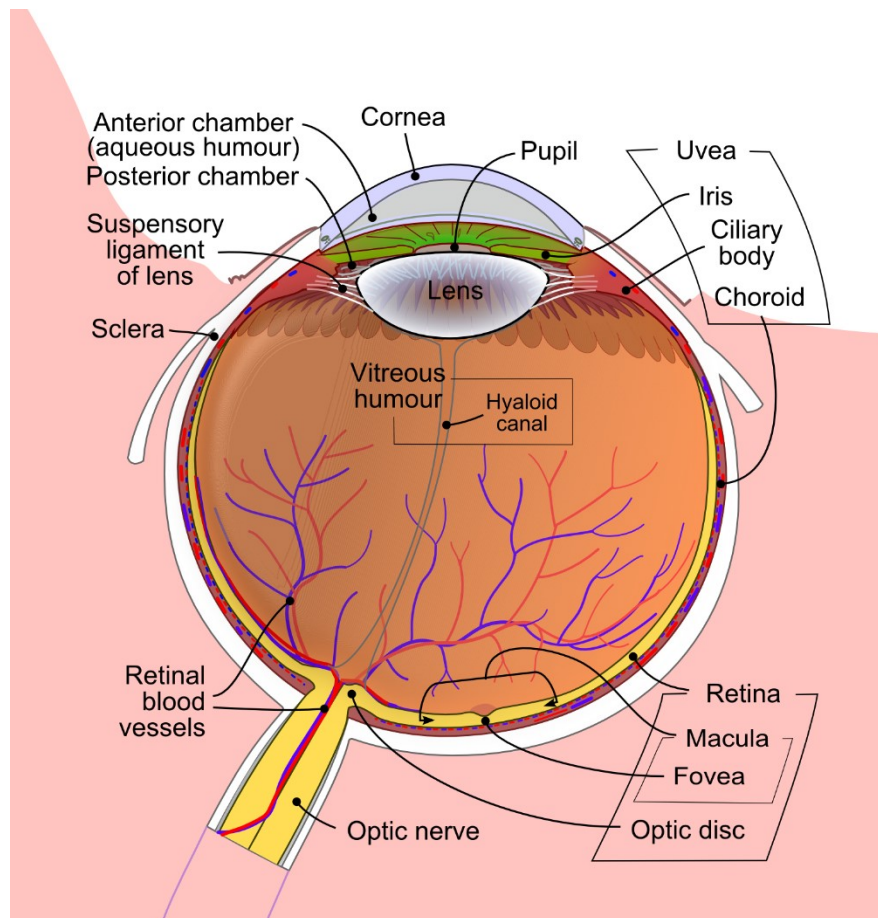
Figure 1.1 Anatomy of the right eye, viewed from above (transverse view through the eye). (Image from https://en.wikipedia.org/wiki/Human_eye.)

1.2.2 Intraocular tumours: types, location, staging, and prognosis

Ocular melanomas can arise from four different tissues in the eye including the uvea, conjunctiva, eyelid, and orbit, the most common of these being the uvea.[12] Uveal melanomas (arising in the choroid, ciliary body, or the iris) are also the most common form of intraocular cancer, with an incidence rate of approximately 5 cases per million person years worldwide,[13] and approximately 2500-3000 cases annually in North America.[14,15] Other types of intraocular cancers (which are not melanocytic) include intraocular lymphoma and retinoblastomas. All of these are considered primary intraocular cancers. Secondary intraocular cancers are those that originate elsewhere in the body and spread to the eye, but these are not considered true "eye cancers".

Uveal melanomas form from the pigment-making cells in the eye called melanocytes (thus classified as melanomas); the majority of these (80%) form in the choroid (choroidal melanomas), while the remainder form in the ciliary body (12%), or the iris (8%). Of these three possible sites, melanomas forming in the iris have the best prognosis, while those forming in the ciliary body have the poorest prognosis.[15,16] Histopathological classification reveals different types of uveal melanomas with different prognoses dependent on the cell types present in the tumour. Ranging from best to worst prognosis they are: spindle cell melanoma, mixed-cell type melanoma, and epithelioid cell type melanoma.[17]

Choroidal melanomas appear in one of three shapes including dome, mushroom, or diffuse. Most melanomas are dome shaped for which the growth pattern is towards the inner part of the globe, and frequently spreads along the choroid or inner sclera (basal edge). A mushroom-shaped tumour occurs when the cancer breaks through the Bruch's membrane, a thin layer covering the choroid. The tumour then herniates into the sub-retinal space. Due to the membrane's elasticity, it compresses around the base of the tumour and creates the mushroom shape, for which the head of the tumour is typically larger in diameter than the base.[14,17] Infrequently (4% of cases), the tumour appears flat with minimal thickness/height and grows laterally along its base rather than towards the centre of the eye.[14,18] Nearly all choroidal melanomas lead to some type of retinal damage due to impaired blood supply or retinal detachment in the direct vicinity of the tumour or at the inferior side following gravity. Extrascleral extension or infiltration into the optic nerve is very rarely observed, even in juxta- or peri-papillary tumours (those adjacent to/touching or surrounding the optic disc).[17] Examples of uveal melanomas are shown in Figure 1.2.
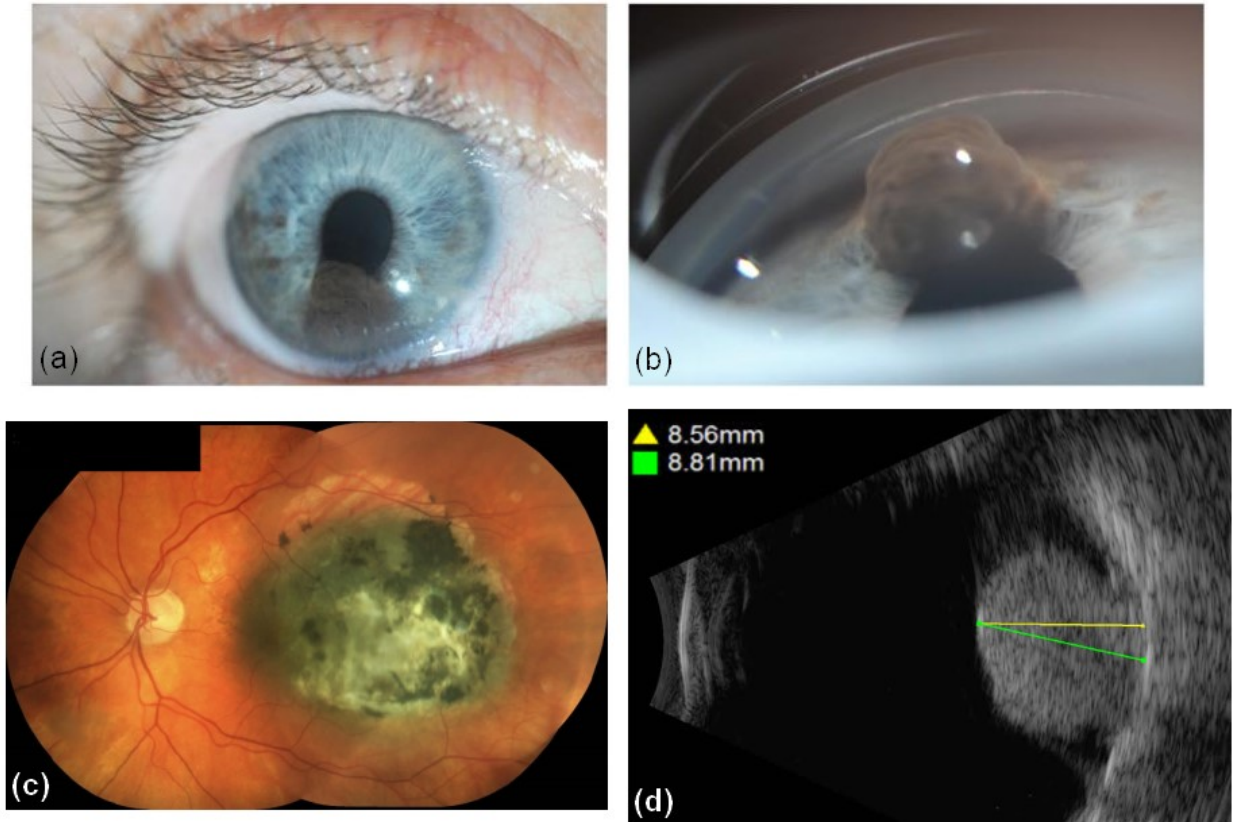
Figure 1.2 Uveal melanomas: front view of an iris melanoma (a), side-view of the same iris melanoma showing the growth of the tumour into the anterior chamber (b), a fundus photographic image of a posterior choroidal melanoma (c), and an ultrasound image of a mushroom shaped tumour (d). (Images courtesy of the Alberta Ocular Brachytherapy Program.)

The size of the tumour is generally described by the tumour height (or apex/apical height) which is measured from the base of the tumour to the furthest intraocular extent, and the basal dimensions (radial and circumferential, or the largest basal diameter) which are measured across the tumour from the inner scleral edges of the tumour. The position of the tumour is measured using its clock hour position and chord length distance back from the limbus, which can then be used to map the tumour onto a fundus diagram (Figure 1.3). The fundus diagram separates the eye into three regions demarcated by the equator, the ora serrata, and the limbus. The innermost region, bounded by the equatorial circumference in the coronal plane, represents the interior surface of the eye from the equator to the posterior pole. This region contains the optic disc and macula, and though it is the smallest circle in the fundus diagram, it represents the largest surface

area of the eye; the scale for the distance from the limbus on a fundus diagram is therefore non-linear. The ora serrata is the serrated junction in the eye between the retina and the ciliary body, and the limbus is the border at which the sclera meets the cornea.[19]
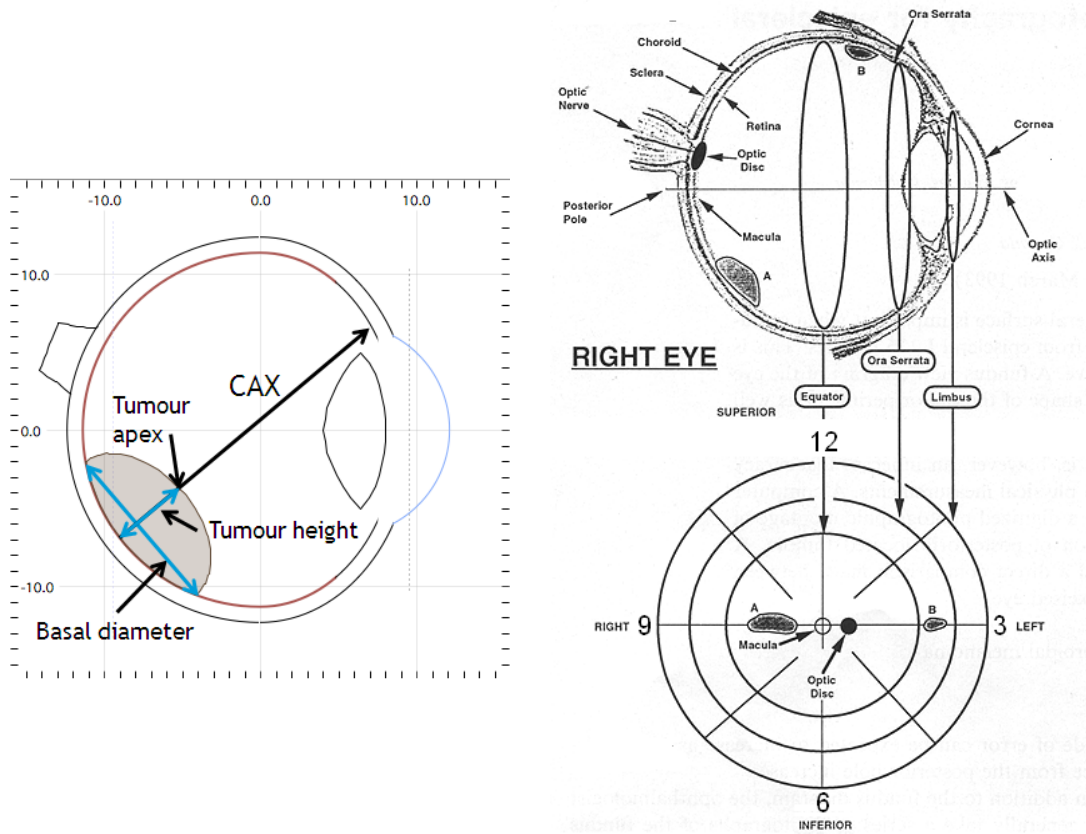
Figure 1.3 Diagram of a choroidal melanoma in the eye indicating the tumour apex, tumour height, basal diameter, and central axis (CAX) of the tumour (left), and diagram of the eye with corresponding fundus diagram detailing the position of the equator, ora serrata, limbus, optic disc, and macula/posterior pole, and clock hour positions (right; figure adapted from Evans *et al.* "Tumor localization using fundus view photography for episcleral plaque therapy," Med. Phys. **20**, 769–775 (1993)[19] with permission from John Wiley and Sons).

The main tumour staging classification systems used are those of the Collaborative Ocular Melanoma Study (COMS) and the American Joint Committee on Cancer (AJCC), the latter being now more widely used and accepted. The COMS staging system classifies tumours as small, medium, or large.[20–22] The AJCC system follows a TNM classification in which 'T'

describes the size of the primary tumour and whether or not it has invaded nearby structures, 'N' describes whether the cancer has spread to nearby lymph nodes, and 'M' indicates whether or not the cancer has metastasized to other parts of the body. Numbers after each letter indicate the severity, ranging from 0-4 (0 being negative, and 4 being very severe) or assigned as 'X' indicating it cannot be assessed, and letters following the numbers further subdivide the categories.[16] A summary of the staging of the primary tumour for both classification systems is given in Table 1.1. Treatment can be safely deferred for patients with small T1 melanomas that are observed for growth before treatment,[23–26] while patients with T2-T4 melanomas who are otherwise healthy [without metastatic disease (N0, M0; no nodal involvement and no metastatic spread), or those with risk factors for future growth (risk factors include tumour thickness > 2 mm, presence of subretinal fluid, visual symptoms, orange pigmentation, close proximity to the optic nerve, absence of drusen, acoustic hollowness on ultrasound, and absence of a halo pigmentation pattern)], should receive treatment immediately.[23,25–30]

Table 1.1 Tumour staging classification systems for choroidal melanomas.

COMS[20–22]		AJCC[16]	
Small	1-2.4 mm in height, and 5-16 mm in diameter	T1	$\leq$ 3 mm deep and $\leq$ 12 mm across, OR 3.1-6 mm deep and $\leq$ 9 mm across
Medium	2.5-10 mm in height,* and $\leq$ 16 mm in diameter	T2	$\leq$ 3 mm deep and 12.1 - 18 mm across, OR 3.1 - 6 mm deep and 9.1 - 15 mm across, OR 6.1 - 9 mm deep and $\leq$ 12 mm across
Large	> 10 mm in height, or > 16 mm across	T3	3.1 - 6 mm deep and 15.1 - 18 mm across, OR 6.1 - 9 mm deep and 12.1 - 18 mm across, OR 9.1 - 12 mm deep and $\leq$ 18 mm across, OR 12.1 - 15 mm deep and $\leq$ 15 mm or less across
		T4	> 15 mm deep and any width, OR > 18 mm across and any depth, OR 12.1 - 15 mm deep and 15.1 - 18 mm across

*Changed in November 1990 from 3.1-8 mm

The overall 5-year survival rate for uveal melanoma is 62%, but varies based on prognostic factors (tumour size, cell type, location of the anterior margin, degree of ciliary body involvement, extraocular extension, mitotic rate, and lymphocytic infiltration), and decreases to

47% at 10 years, and 25% at 20 years.[15,31] Uveal melanoma is often fatal, most commonly due to distant metastatic spread of the disease, accounting for approximately 83% of deaths at 5 years, even though local tumour control rates with treatment are quite high.[31] As well, failure to achieve local control following treatment of choroidal melanoma has been associated with a nearly 4-fold increase in melanoma-related death rates.[32] Following the incidence of metastatic disease, patient survival is very poor, with an average survival of 2–7 months.[33] Due to the lack of lymphogenous routes from the eye, metastatic spread is almost exclusively by hematogenous routes (through the blood),[12,33] most commonly to the liver (91% of the time), though it can occasionally spread to the lung (28%), bones (18%), and more rarely to other sites (skin, lymph nodes, brain, and spinal cord).[34,35] Occasionally the uveal melanoma will grow through the posterior transcleral emissary channels and spread locally to the orbit or conjunctiva.[36] To date, no systemic or locoregional therapies have been found to be effective in treating metastatic uveal melanoma.[33,37–39]

1.2.3 Types of treatments

Primary management of uveal melanoma includes observation, surgical resection, radiotherapy, and transpupillary thermotherapy (TTT; typically not a primary treatment, but given in conjunction with other forms of treatment). Each will be briefly discussed here. Prior to the 1980s, the most common treatment was enucleation, with only a limited number of cases managed using some form of eye sparing treatment. As previously mentioned, observation is typically only employed with small or indeterminate lesions, and not with lesions having risk factors for future growth.

Surgical resection includes both local resection of the tumour, and enucleation, which is the complete removal of the eye. Local resection is best suited for iris melanomas, select ciliary body melanomas, or small anterior choroidal melanomas.[40] Enucleation is most suitable for patients with a blind and painful eye, those with large tumours > 10 mm thick and/or >18 mm in basal diameter, for tumours that surround or invade the optic nerve, or for eyes with neovascular glaucoma.[39,41,42]

Radiation therapies for uveal melanoma have the goal of delivering an adequate amount of radiation dose to the tumour while sparing nearby structures in the eye or organs at risk (OAR). Therefore, compared to enucleation, radiotherapy offers the potential for tumour control, while at

the same time sparing of vision and preservation of the globe.[41] Radiation therapy treatments for uveal melanoma are delivered by two methods: external-beam irradiation and episcleral plaque brachytherapy (described in Section 1.3). External-beam treatments make use of protons or other heavy charged particles, or high energy photons produced by either a linear accelerator or Gamma Knife® Co-60 irradiator. Treatments with protons have been found to result in high local tumour control rates of 89%–98%, 5-year survival rates of ~80%,[43,44] and a 5-year eye preservation rate of 90%.[45] Comparative studies between protons or helium ion beams and I-125 or Ru-106/Rh-106 plaque therapy have shown both treatment options to result in good local tumour control and visual outcomes; however, secondary enucleation rates were higher for proton and helium ion therapy than for plaque therapy.[46,47] External beam photon treatments (using a linear accelerator or the Gamma Knife) also have good 5-year tumour control rates >90%.[48,49] However, all external beam therapies (ion and photon beams) require anterior or adnexal structure entry to the eye resulting in higher doses to these structures and more anterior segment complications, including eyelash loss, dry eye, neovascular glaucoma, and cataracts,[50–53] though for ion beam therapies, there is generally more posterior and lateral tissue sparing.[42] Patient immobilization also poses a significant challenge for external beam treatments.[42,48,49,54]

TTT delivers heat to the tumour using a modified diode laser, which induces tumour cell necrosis by hyperthermia. Long term results of TTT as a primary therapy have been poor, therefore it is mainly used in conjunction with radiotherapy for radio-resistant tumours or tumours with a high risk of local failure when treated with radiotherapy alone.[38,55]

1.3 Ocular brachytherapy

The first documented treatment of a uveal melanoma with brachytherapy was in 1930 by Dr. R. Moore, who surgically placed a 1 mCi radon seed directly into the tumour, and removed it 14 days later.[56] Modern ocular brachytherapy techniques involve the use of a metal disc called a plaque that serves as a backing to hold the radioactive material, which is then placed adjacent to the tumour. Co-60 plaques were introduced in the 1960s,[57] but it was not until the 1980s that plaque brachytherapy was routinely used instead of enucleation. Numerous different radionuclides in combination with varying prescription doses, varying dose rates, and a multitude of plaque designs made outcome comparisons of tumour control rates, long-term survival rates, and visual acuity between the different treatment methods difficult.

The COMS Group provided the first standardized methods for administering ocular brachytherapy treatments for uveal melanoma in 1985, and conducted two randomized trials, the second of which compared enucleation against I-125 plaque radiation therapy for medium-sized choroidal melanomas using the COMS style plaques.[58] Equivalent survival rates were found between the two treatment methods, indicating that ocular brachytherapy is as effective as enucleation, with the added benefit of eye preservation, and for some patients, functional vision retention.[22,27] The following sections briefly outline the treatment method for ocular brachytherapy, the different types of plaques and radionuclides available for treatment, and the clinical outcomes.

1.3.1 Treatment method

Tumours appropriate for ocular brachytherapy treatment include stage T1, T2, T3, and T4a-d uveal melanomas (using the AJCC staging system). Patients with peri-papillary or subfoveal tumours and those with exudative retinal detachments usually have poorer visual prognosis, but can still receive ocular brachytherapy treatment. Tumours inappropriate for ocular brachytherapy treatment include T4e tumours with extraocular extension, tumours with basal diameters exceeding the limits of brachytherapy (larger than available plaque sizes), blind painful eyes, and eyes with no light perception.[42]

Following the decision to treat with ocular brachytherapy and if not already employed during patient diagnosis and work-up, a number of imaging modalities are commonly used to determine the tumour dimensions and position, which are then used for treatment planning. Ultrasound imaging utilizing both A-scans and B-scans is employed to determine the tumour apex height and basal dimensions, the tumour shape, and the presence of any extrascleral or extra-ocular extension. Fundus imaging (photography of the interior surface of the back of the eye including the retina, macula/fovea, optic disc, and posterior pole) using a low-powered microscope is used to create a fundus diagram of the eye including the tumour clock hour orientation, radial and circumferential diameters, largest basal diameter, and the distances from the tumour to the fovea, posterior pole, and optic nerve. This information is derived in conjunction with the ultrasound measurements, ophthalmic examinations including slit-lamp or indirect ophthalmoscopy, and CT or MRI imaging to assist in determining orbit dimensions including the positions of and distances between the optic nerve, lens, and posterior pole.[59]

Treatment planning is performed to deliver a desired minimum prescription dose to the entirety of the uveal melanoma lesion. This can be done either by prescribing a dose to the tumour base or to the tumour apex. The American Brachytherapy Society – Ophthalmic Oncology Task Force (ABS-OOTF) guidelines recommend that the tumour apex or point of maximal thickness be used as the prescription point, that the prescription isodose line should encompass the entire tumour, and that a minimum dose rate of 0.60 Gy/h (in the case of treatment with I-125) be used.[42] More details on treatment planning methods and dose calculations are given in Section 2.2. After the plaque is assembled in accordance with the treatment plan, it is sterilized prior to insertion. Ocular muscles (rectus and oblique muscles) may need to be resected (cut and stitched for re-attachment at plaque removal), in order to position the plaque as well as to rotate the eye as needed. Suture coordinates are mapped onto the eye surface using a caliper and toric axis marker, and a dummy plaque is sutured in place (a dummy plaque has a clear backing/window, and contains no radioactive material). The alignment of the dummy plaque is verified with transpupillary or transocular illumination. Transillumination can also be used to mark the margins of the tumour on the sclera for further verification of the placement of the dummy plaque. Other localization methods such as intraoperative ophthalmic ultrasound and posterior point source illumination can also be used. Once the dummy plaque and sutures are in the correct position, the sutures are un-tied and the dummy plaque is replaced with the actual plaque and secured in position using the same sutures. The plaque is left in place typically for 4-7 days, after which time it is surgically removed and any resected ocular muscles are reattached.[12,42]

1.3.2 Radionuclides and types of plaques

Due to the high energy of the photon emissions from Co-60 (average energy of 1.25 MeV), very little shielding is possible for critical structures in the eye and other parts of the head behind the plaque. This resulted in radionuclides with lower energy emissions gaining favour over Co-60.[59,60] Photon-emitting radionuclides that have since been used include Ir-192,[61] Au-198,[62] Cs-131,[63] Pd-103,[64,65] and most commonly, I-125,[66–70] mainly due to its specification in the COMS trials.[58,60] As Co-60, Ir-192 and Au-198 have high energy emissions, which require greater radiation safety precautions and also result in higher doses being delivered to non-involved parts

of the patient as well as the staff performing the treatment, they are rarely used today. Radiological characteristics of each radionuclide are summarized in Table 1.2.

Two beta-emitting radionuclides have been used for ocular brachytherapy: Ru-106/Rh-106 and Sr-90/Y-90. Both of these radionuclides are coated onto a plaque surface as opposed to being contained in an encapsulated seed. The development of plaques coated with Ru-106 by Lommatzsch et al.[71] has led to a long use of Ru-106 for the treatment of uveal melanomas.[72–74] Sr-90 is used less frequently,[75] though Sr-90 applicators are commonly employed for the treatment of pterygium.[76] The ranges of the electrons emitted are much shorter than the mean free paths of the photons emitted from the photon-emitting radionuclides in eye tissues, and so the beta-emitting sources are typically only used for smaller tumours with a maximum height of ~6 mm.[42] Radiological characteristics of these radionuclides are also included in Table 1.2.

Table 1.2 Physical characteristics of radionuclides used for ocular brachytherapy treatment.

Photon emitter	Half-life[a] (d)	Mean energy[a] (keV)	Water TVL[b] (cm)
I-125	59.4	28.4	5.6
Pd-103	16.99	20.7	3.1
Cs-131	9.69	30.4	6.3
Au-198	2.7	412	22.0
Ir-192	73.83	380	21.3
Beta emitter	Half-life[a]	End point beta energy[a] (MeV)	CSDA range in water[c] (mm)
Ru-106/Rh-106	371.8 d	3.541	18.0
Sr-90/Y-90	28.8 y	0.546	2.0

Mean photon energy and TVL (tenth value layer) calculated excluding photon energies < 5 keV
[a]Data from National Nuclear Data Centre (NNDC)[77]
[b]Data from NIST XCOM database[78]
[c]Data from NIST ESTAR database[79]

The most commonly used plaques are the COMS plaques, developed by the COMS group.[80] These come in a range of sizes (10-22 mm in diameter in 2 mm increments), and are made of a 0.5 mm thick gold alloy backing (trade name 'Modulay') which holds a seed carrier called the Silastic insert (made of MDX4-4210 bio-medical grade elastomer; Trachsel Dental Studio, Rochester, MN); both the backing and the insert are hand-cast. Each size of Silastic insert holds a set number of seeds at specific coordinate locations. The inner curvature of the plaques is

based on a standard eye diameter of 24.6 mm, and the insert creates a 1 mm separation between the seeds and the outer scleral surface.[81,82] The COMS plaques can be used with I-125, Pd-103, or Cs-131 seeds, and also come in notched versions which allow closer placement to tumours near the optic nerve. Examples of the COMS plaques are shown in Figure 1.4, and a schematic diagram of the 14 mm plaque is presented in Figure 1.5.

Figure 1.4 COMS plaques, from left to right: 12 mm plaque backing and Silastic insert, 14 mm plaque backing and Silastic insert, 14 mm notched plaque backing and Silastic insert (top two rows), 16 mm plaque backing and Silastic insert, and 16 mm dummy plaque (bottom two rows).
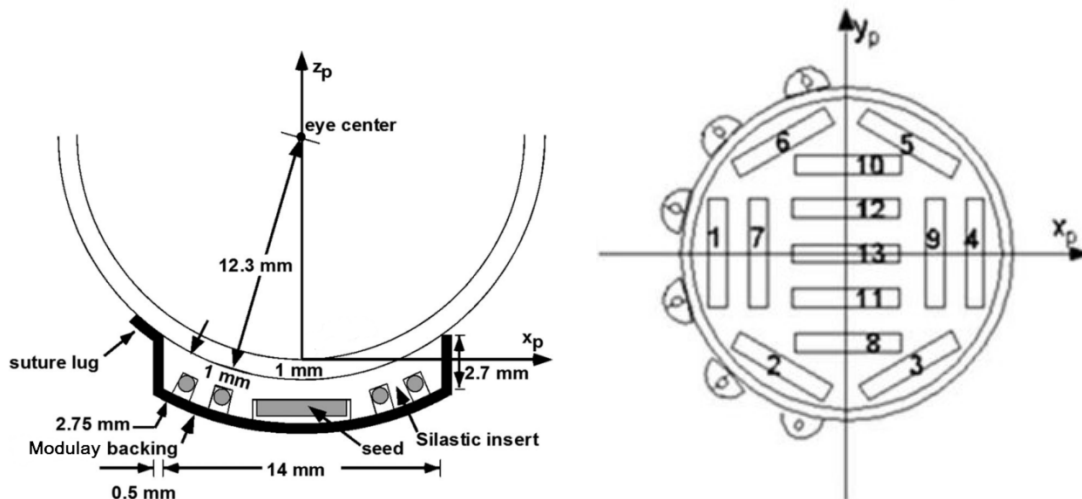
Figure 1.5 Side view of a COMS 14 mm plaque, with plaque backing and Silastic insert with seed slots (left), and corresponding concave view with numbered seed slots (right) (images adapted from Chiu-Tsao *et al.* "Dosimetry of ^{125}I and ^{103}Pd COMS eye plaques for intraocular tumors: Report of Task Group 129 by the AAPM and ABS," Med. Phys. **39**, 6161–6184 (2012)[82] with permission from John Wiley and Sons).

Alternative slotted style plaques are produced by Eye Physics, LLC, based in Los Alamitos, CA. These plaques are primarily characterized by seed slots milled into an 18K gold backing that collimate the radiation emitted by the brachytherapy seeds.[83] The plaques have no seed insert; the seeds are glued directly into the slots. These plaques can also be loaded with I-125, Pd-103, or Cs-131 seeds. Examples are given in Figure 1.6. The 2nd generation of Eye Physics plaques are all manually prototyped, whereas the newest 3rd generation plaques are computer designed, prototyped, and cast from 3D printed molds.

Figure 1.6 Examples of Eye Physics 2nd generation style plaques: model #917 with dummy plaque (upper left), model #2031 with dummy plaque (upper right) (images from www.eyephysics.com), and model #930 with dummy plaque (aka Super9) (bottom).

Somewhat similar in design to the COMS plaques are the ROPES and OSU-NAG plaques. The ROPES plaques consist of a stainless steel backing with a slotted acrylic seed carrier and are produced by the Radiation Oncology Physics and Engineering Services (ROPES) in Australia.[84,85] The OSU-NAG plaques use a gold backing with the same composition as Modulay, but the seeds are glued directly to the plaque backing to eliminate the non-water dosimetric aspect of the Silastic insert. The OSU-NAG plaques also use fewer seeds than the COMS or ROPES plaques.[86] Both the ROPES and OSU-NAG plaques have been used with I-125 and Pd-103 seeds, and both come in a range of sizes and in notched versions. Images of both these types of plaques are shown in Figure 1.7.

Figure 1.7 15 mm ROPES plaque assembly with acrylic insert, plaque backing, dummy plaque, and ejector pin (left) (figure reproduced from http://www.eyephysics.com/ps/ps5/userguide/AssembleROPES.html), and 16 mm OSU-NAG plaque and dummy plaque (right) (figure adapted from Zhang *et al.*, "Comparison of 16 mm OSU-Nag and COMS eye plaques," J. Appl. Clin. Med. Phys. **13**, 166–178 (2012)[86]).

The plaques utilizing Ru-106 are available from Bebig (Eckert & Ziegler BEBIG GmbH, Berlin, Germany). They are made from a thin film of Ru-106 which is encapsulated within a sheet of pure silver, and have a total thickness of 1 mm. The Bebig plaques are available in a range of sizes from 11.6 to 25.4 mm in diameter. An example is shown in Figure 1.8.
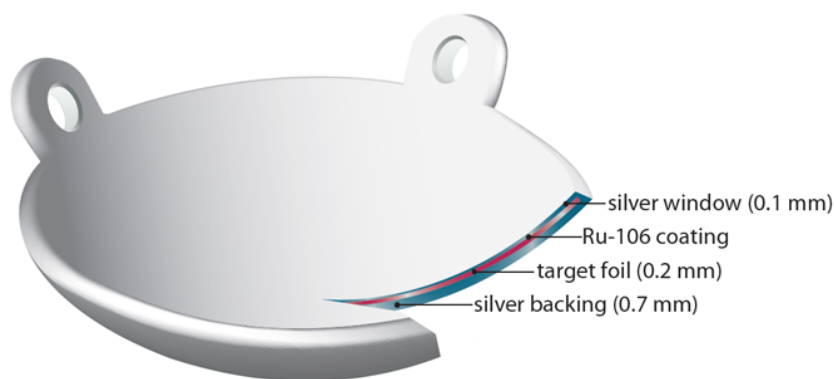
Figure 1.8 Ru-106 Bebig plaque illustrating the location of the Ru-106 coating on the target foil sandwiched between two layers of silver. (Image reproduced from the Ru-106 Bebig plaque product fact sheet: http://www.bebig.com/fileadmin/bebig_neu/user_uploads/Products/Ophthalmic_Brachytherapy/Fact_sheet_Ru-106_Eye_Applicators_Rev.05_English.pdf).

1.3.3 Clinical outcomes: tumour control, survival, and radiation complication rates

The randomized trial conducted by the COMS group, starting in 1985, found that overall survival rates were equivalent between I-125 plaque brachytherapy and enucleation. This led to the understanding that ocular brachytherapy was as effective as enucleation for medium-sized tumours and to an increase in the use of ocular brachytherapy to treat uveal melanomas.[27]

Local tumour control following ocular brachytherapy is generally very good, usually >90%. A summary of outcome results from a selection of clinical studies using Ru-106/Rh-106 plaques, and I-125 or Pd-103 brachytherapy seeds, is shown in Table 1.3 (though there have been several other studies performed). As tumour control rates are generally very high, many of the current goals in ocular melanoma research are to determine means to reduce the normal tissue side-effects following treatment. The main OARs within the eye include the lens, the macula/fovea, the retina, the optic disc, and the optic nerve.

Radiation side-effects from ocular brachytherapy include eyelash loss, dry eye, corneal damage, vitreous hemorrhage, radiation maculopathy, radiation retinopathy, radiation optic neuropathy, cataract, and neovascular glaucoma. Radiation-related vision loss following treatment is usually due to the latter five sequelae as well as exudative retinal detachment.[50] Many of these complications appear to be occurring less frequently since the introduction of lower energy radionuclides (I-125, Pd-103, Ru-106, and Ir-192) to replace Co-60,[12] however the occurrence is still quite high (often >20% for a given complication, see Table 1.4) and strongly depends on both radiation and patient-specific factors. These include: the total dose, dose rate, dose volume, dose to critical structures, tumour size, tumour location, and biological response to radiation.[42] Most radiation effects observed are delayed and worsen over time.[65] Late anterior segment complications include dry eye, iris neovascularization, secondary glaucoma, and cataract, while late posterior segment complications include radiation retinopathy, radiation maculopathy, and optic neuropathy. Acute posterior segment complications include secondary retinal detachment or hemorrhage (vitreous, retinal, or choroidal).[41] Higher radiation doses to the fovea result in a faster onset of chorioretinal atrophy and higher rates of radiation retinopathy and maculopathy, whereas higher radiation doses to the lens result in a higher incidence of cataract formation; both side-effects are related to plaque location.[87–89] Higher doses to the sclera, choroid, and retina were also found to cause higher rates of secondary retinal detachment associated with vision loss.[90] Visual acuity outcomes depend on any pre-existing conditions the

patient had (pre-existing exudative retinal detachment, previous cataract, etc.), on the incidence of the aforementioned radiation side-effects (which are themselves dependent on the position of the tumour and its proximity to the critical structures), and on the radiation dose received throughout the eye. A summary of visual outcomes and occurrence of radiation complications is given in Table 1.4 for the same studies presented in Table 1.3.

Comparing these different studies is difficult given the differences in tumour size, tumour position, length of follow-up, and the lack of uniform dosimetry guidelines and dose prescription/calculation methods. The mean tumour apex doses reported in Table 1.3 are also not directly comparable as some of the dosimetry formalisms changed over time due to the introduction of new source calibration standards and dose calculation methods. These aspects are described further in Section 2.2.

Table 1.3 Clinical outcomes following ocular brachytherapy treatment with either Ru-106, I-125, or Pd-103 (dashed lines indicate values not reported).

Radio-nuclide	Study	Year	No. of Patients	Mean follow-up (months)	Mean tumour size[a] (mm)	Mean apex radiation dose (Gy)	Local control (%)	Metastasis (%)	Overall survival (%)
Ru-106	Lommatzsch et al.[91]	1986	309	80	T1 (mostly small)	100	84 (5yr) 69.9 (6.7yr)	12.9	87
	Kleineidam et al.[92]	1993	184	--	3.5 x 8.0	250	82	13.6	84 (5yr) 74 (10yr)
	Seregard et al.[93]	1997	266	43	4.4 x 10.0	100	83 (4 yr) 82 (5 yr)	11(4 yr) 14 (5 yr)	86
	Damato et al.[73]	2005	458	47	3.2 x 10.2	80-100	99 (2yr) 98 (5yr)	8.1	85.8
I-125	Packer et al.[66]	1992	64	64	--	91	92.2	17.2	82.8
	Quivey et al.[67]	1993	239	35	5.5 x 10.9	71	91.7 (3yr) 82 (5yr)	7.5 (3yr) 12 (5yr)	--
	Shields et al.[69]	2002	354	60	9.0 x 14.0	80	96 (2yr) 91 (5yr)	10 (2yr) 30 (5yr)	--
	COMS[27,94]	2006	657	96	4.8 x 11.6	85	89.7	10 (5yr) 18 (10 yr)	81 (5yr) 65 (10yr)
	Perez et al.[70]	2014	190	49-70[b]	3.9 x 11.0	81	91 (5yr)	10 (5 yr)	84 (5yr)
Pd-103	Finger et al.[64]	2009	400	51	3.8 x 10.5	73	96.7	6 (4.25 yr) 7.3 (5yr) 13.4 (10yr)	87

[a]Tumour size is denoted as: height x basal diameter
[b]Mean follow-up was 49 months for tumour control, 52 months for distant failure, and 70 months for overall survival

Table 1.4 Visual outcomes and radiation complications following ocular brachytherapy treatment with either Ru-106, I-125, or Pd-103 (dashed lines indicate the value was not reported).

Radio-nuclide	Study	Vision >20/200 (%)	Enucleation (%)	Cataracts (%)	Vitreous hemorrhage (%)	Neovascular glaucoma (%)	Radiation maculopathy (%)	Radiation retinopathy (%)	Optic neuropathy/ Optic nerve atrophy (%)	Retinal detachment (%)
Ru-106	Lommatzsch[91]	42.1 (>20/100)	20.7	2	3	1	26.9	--	7.4	6.8
	Kleineidam[92]	--	11.4	--	--	<1	--	--	--	--
	Seregard[93]	--	17	--	--	3	--	--	<1	2
	Damato[73]	75	1.7	--	1	--	--	--	--	<1
I-125	Packer[66]	45.3	17.2	45.3	21.9	10.9	--	23.4	--	--
	Quivey[67]	58	5.4	14	20.8	6.8	18.2	--	11.4	1.3
	Shields[69]	43 (5yr) 11 (10yr)	24 (5yr) 34 (10yr)	66	23	21	24	25	--	--
	COMS[94–96]	57	12.5 (5yr)	83	--	--	--	--	--	--
	Perez[70]	39	6	*						
Pd-103	Finger[64]	79 (5yr) 69 (10yr)	3.5	23	<1	2.5	20.3	22	6	--

*5-year actuarial risk of any radiation complication was 73%, the most common being radiation retinopathy and cataract

1.4 Current challenges, limitations and shortcomings in ocular brachytherapy dosimetry

One of the greatest challenges in ocular brachytherapy is performing accurate dosimetry, whether it is experimental measurements or dose calculations. This is due to the steep dose gradients surrounding the plaque, small volume of interest, use of low-energy photon sources which are very sensitive to material heterogeneities, high sensitivity to experimental set-up uncertainties, and the complexity of the eye itself which has many critical structures. Despite the wide-spread use of ocular brachytherapy to treat uveal melanomas, dosimetry methods have remained rudimentary.[82] Due to the non-standardized procedures with which ocular brachytherapy has been performed and the lack of accurate dose calculations, meaningful inter-comparisons between treatments using different styles of plaques, different radionuclides or seed models, and different dose prescriptions have been limited. As more accurate dose calculation methods become available, these comparisons will become easier to perform.

Because of this, there are several unanswered fundamental questions in ocular brachytherapy, including the optimal prescription dose to achieve tumour control, the optimal treatment dose rate, location of the planning target (the base or the apex of the tumour), and the radiobiological effectiveness radionuclides with different emission energies.

Due to the steep dose gradients, the tumour base receives significantly more dose than the tumour apex.[50] Therefore if prescribing to the tumour apex, two tumours of different heights could have significantly different maximum, mean, and basal doses. This effect is also present when using radionuclides with different energy emissions, particularly for the beta-emitting sources which have a substantially shorter depth of penetration than the photon-emitting sources and therefore a much steeper dose gradient. The dose gradient also has a significant bearing on the dose delivered to the surrounding critical structures. Consequently, it is presently unclear what the minimum dose required to achieve local tumour control is.[82] Equivalent tumour control rates with decreased rates of radiation complications were found by Perez *et al.*[70] when treating with a prescription dose (based on dose calculation to water in water medium) as low as 69 Gy instead of 85 Gy at the tumour apex; however additional dose de-escalation studies are required to determine the minimum dose required to achieve an acceptable level of tumour control.

Although the dose rate dictated by the COMS protocol was 0.43 − 1.05 Gy/h to the prescription point at the tumour apex, reports of dose rates lower than 0.6 Gy/h were reported to have lower tumour control rates.[97] As a result, the latter value was adopted by the ABS-OOTF as the minimum recommended dose rate.[42] The optimal dose rate or the effect of different dose rates has only been studied retrospectively[98] or by theoretical methods,[99,100] and no prospective clinical studies have been performed to investigate this.

On a similar thread, the optimal or required margins around the tumour are also still largely unknown. The size of a radiation therapy treatment margin is typically dictated by the uncertainty in dose delivery, whether it be due to an internal or a set-up variation in geometry, as described in the ICRU-62 report[101] and further discussed for ocular brachytherapy by Gagne and Rivard.[102] For ocular brachytherapy, currently the only recommended margin is a 2-3 mm basal margin to account for plaque placement errors, plaque movement, uncertainty in the location of the tumour edge,[41] and subclinical disease occurring as microscopic spread along the uvea and sclera.[17] Depending on the specific situation, the treatment margin can be adjusted to account for any additional uncertainties.[17] However, the optimal margin around the tumour base is still unknown and depends on the plaque type, as stated in the 2003 ABS report.[41] The 2014 ABS-OOTF report recommends that the tumour diameter should not exceed the diameter of the planning target volume (PTV) so as to avoid a geometric miss.[42]

The COMS protocol helped establish much more uniformity in the treatment procedure, and many improvements have been made to the dose calculation formalism since that time, however there are still many shortcomings. The standard of care for dose calculation in brachytherapy is the TG-43 formalism (more details in Section 2.1.3), and for eye plaques, it is now recommended to also apply some form of correction for the heterogeneous plaque materials (Section 2.2).[82] Even with such a correction, a number of limitations still exist. Several of the TG-43 consensus datasets were obtained using Monte Carlo (MC) codes which have older photon interaction modelling and cross-sectional data, and are based on simplified geometric modelling of the sources. More recent investigations have resulted in relatively large differences in the determined TG-43 parameters (up to 10%).[103,104] Despite this, the consensus datasets have not yet been updated, and older datasets continue to be used. That said, caution should be taken as the newer datasets need to be validated by comparison with the older datasets, against datasets obtained using other MC codes, and with experimental measurements, prior to adoption.

Use of the TG-43 formalism assumes an infinite homogeneous water medium, ignoring the effects of inter-seed attenuation, differing scattering conditions, as well as any non-water materials present in the treatment field (including applicators and patient tissues). The effects of inter-seed attenuation are very small for ocular brachytherapy (~0.5%),[105] but have been found to be non-negligible for other brachytherapy treatment sites such as prostate and breast.[106]

Differences in scattering conditions due to the presence of large air interfaces generally result in an overestimation of the dose using the TG-43 formalism. For ocular brachytherapy, the air interface at the patient's face has been found to cause dose decreases of up to 10% near the interface (corneal/aqueous chamber region).[107] These effects were also observed for breast treatments with Ir-192 by Pantelis *et al.* in which the skin dose was overestimated by up to 10% compared to MC simulations.[108]

The effects of non-water applicator materials and patient tissue heterogeneities have been found to substantially impact the dosimetry for several brachytherapy treatment sites; a detailed analysis is given in the AAPM TG-186 document.[106] For ocular brachytherapy this has only been investigated to a limited extent. Thomson *et al.*[107] studied the effects of replacing a water eye with one made of homogeneous eye material and of lens material, which caused dose decreases throughout the eye of ~2-3% and ~7-9%, respectively.[107] The tissue heterogeneity effects of a realistic eye model on the dose distributions for ocular brachytherapy have been examined by Lesperance *et al.*,[109,110] and resulted in large differences in dose compared to a water eye (more details in Chapter 6).

As dosimetry having greater accuracy is performed for ocular brachytherapy accounting for both plaque and patient heterogeneities, doses to the critical structures within the eye as well as to the tumour can be better understood and more reliably compared between different treatment protocols (different radionuclides, plaque models, prescription criteria, etc.) in order to answer some of the unanswered questions in ocular brachytherapy dosimetry.

1.5 Thesis outline

The research presented in this thesis aims to answer a few of the "unanswered questions" in ocular brachytherapy described above, with the goal of improving the accuracy of dosimetry on multiple fronts: experimental measurements, dose delivery procedures, and dose calculations. The information presented in this chapter provides the foundation of radiation therapy and

brachytherapy for the treatment of uveal melanomas as well as details about the different methods of performing ocular brachytherapy treatments and the motivation for improving the current dosimetry methods. Chapter 2 provides the background information and theoretical basis for the work presented in the subsequent chapters. Chapter 3 describes the methods developed for improving the accuracy of radiochromic film calibration and dose measurement for low-energy brachytherapy sources. These methods were specifically created for experimental ocular brachytherapy dosimetry, but can also be applied to dosimetry studies of other brachytherapy techniques. The radiochromic film dosimetry methods are then applied in Chapter 4, which explores the use of a simple eye phantom for dose measurements with a COMS plaque and one of the Eye Physics plaques. This work establishes the use of a newer model of radiochromic film for ocular brachytherapy dosimetry, provides verification of off-axis dose calculations for the Plaque Simulator treatment planning system (TPS; a planning system specifically for ocular brachytherapy treatments[111]) using MC reference dosimetry data, and introduces some of the sources of uncertainty present in ocular brachytherapy treatments. Chapter 5 provides an in-depth investigation into the sources of uncertainty present in the ocular brachytherapy treatment delivery process. The analysis is used to determine the appropriate size of an apex margin to ensure adequate dosimetric coverage of the tumour, as well as to identify what sources of uncertainty are most significantly impacting the treatment procedure and dosimetry. Chapter 6 investigates the use of a newly available model-based dose calculation algorithm for ocular brachytherapy treatment planning capable of accounting for both the heterogeneous plaque materials and patient tissues, with comparison against MC reference dosimetry to determine the accuracy and limitations of the software. The accuracy of the I-125 source models implemented is also established, as this work presents the first analysis of the examined algorithm for any low energy brachytherapy source. Comparisons are also made to water based (Plaque Simulator) planning to investigate the effects of patient tissues on dose calculations currently performed in the clinic. Lastly, Chapter 7 is the concluding summary chapter that also briefly discusses areas of possible future research.

1.6 References

[1] Canadian Cancer Society's Advisory Committee on Cancer Statistics, *Canadian Cancer Statistics 2016* (Canadian Cancer Society, Toronto, ON, 2016).

[2] Radiological Society of North America, *Introduction to Cancer Therapy (Radiation Oncology)*, (URL: https://www.radiologyinfo.org/en/info.cfm?pg=intro_onco). Last accessed April 19, 2017.

[3] H.E. Johns and J.R. Cunningham, *The physics of radiology*, 4th Ed. (Charles C Thomas, Springfield, IL, IL, 1983).

[4] M.A. Morgan, R.K. Ten Haken, and T.S. Lawrence, "Essentials of Radiation Therapy," in *DeVita, Hellman, and Rosenberg's Cancer: Principles & Practice of Oncology*, 10th ed., edited by V.T. DeVita, T.S. Lawrence and S.A. Rosenberg (Lippincott Williams & Wilkins, Philadelphia, PA, 2015), pp. 136–155.

[5] F.M. Khan, *The physics of radiation therapy*, 5th ed. (Lippincott Williams & Wilkins, Philadelphia, PA, 2014).

[6] R. Nath, "Overview of brachytherapy physics," in *Brachytherapy Physics: Joint AAPM/ABS Summer School*, 2nd ed., edited by B.R. Thomadsen, M.J. Rivard and W.M. Butler (Medical Physics, Madison, WI, 2005), pp. 1–5.

[7] H. Basil, *Brachytherapy, Conquering cancer, The first 100 years* (Best Cure Foundation, Brachytherapy Research & Educational Foundation, Springfield, VA, 2014).

[8] J.N. Aronowitz, S. V Aronowitz, and R.F. Robison, "Classics in brachytherapy: Margaret Cleaves introduces gynecologic brachytherapy," Brachytherapy **6**, 293–297 (2007).

[9] R. Nath, "Sources and delivery systems I: Radionuclides," in *Brachytherapy Physics: Joint AAPM/ABS Summer School*, 2nd ed., edited by B.R. Thomadsen, M.J. Rivard and W.M. Butler (Medical Physics, Madison, WI, 2005), pp. 25–45.

[10] F. Ballester and R. Nath, "Radionuclides in Brachytherapy: Current and Potential New Sources," in *Comprehensive Brachytherapy: Physical and clinical aspects*, edited by J.L.M. Venselaar, D. Baltas, A.S. Meigooni and P.J. Hoskin (Taylor & Francis Group, LLC, Boca Raton, FL, 2013), pp. 29–42.

[11] ICRU, "Prescribing , Recording , and Reporting Brachytherapy for cancer of the cervix," in *ICRU Report No. 89* (ICRU Publications, Bethesda, MD, 2013).

[12] J.A. Shields and C.L. Shields, *Intraocular Tumors. A text and atlas* (WB Saunders, Philadelphia, PA, 1992).

[13] A.D. Singh, M.E. Turell, and A.K. Topham, "Uveal melanoma: Trends in incidence, treatment, and survival," Ophthalmology **118**, 1881–1885 (2011).

[14] C.L. Shields and J.A. Shields, "Ocular melanoma: relatively rare but requiring respect," Clin. Dermatol. **27**, 122–133 (2009).

[15] Cancer.Net, *Eye Cancer: Statistics*, (URL: http://www.cancer.net/cancer-types/eye-cancer/statistics). Last accessed April 11, 2017.

[16] American Joint Committee on Cancer, "Malignant melanoma of the uvea," in *AJCC cancer staging manual*, 7th ed., edited by S.B. Edge, D.R. Byrd, C.C. Compton, A.G. Fritz, F.L. Greene and A. Trotti (Springer, New York, NY, 2010), pp. 547–559.

[17] R. Potter and E. Van Limbergen, "Uveal melanoma," in *The GEC ESTRO handbook of brachytherapy*, edited by A. Gerbaulet, R. Potter, J.J. Mazeron, H. Meertens and E. Van Limbergen (Belgium, 2002), pp. 591–610.

[18] C.L. Shields, J.A. Shields, P. de Potter, J. Carter, D. Tardio, and J. Barrett, "Diffuse choroidal melanoma: Clinical features predictive of metastasis," Arch. Ophthalmol. **114**, 956–963 (1996).

[19] M.D.C. Evans, M.A. Astrahan, and R. Bate, "Tumor localization using fundus view photography for episcleral plaque therapy," Med. Phys. **20**, 769–775 (1993).

[20] Collaborative ocular melanoma study group, "Mortality in patients with small choroidal melanoma. COMS Report No. 4," Arch. Ophthalmol. **115**, 886–893 (1997).

[21] Collaborative Ocular Melanoma Study Group, "The Collaborative Ocular Melanoma Study (COMS) randomized trial of pre-enucleated radiation of large choroidal melanoma II: Initial Mortality Findings. COMS Report No .10," Am. J. Ophthalmol. **125**, 779–796 (1998).

[22] Collaborative Ocular Melanoma Study Group, "The COMS Randomized Trial of Iodine 125 Brachytherapy for Choroidal Melanoma, III: initial mortality findings. COMS Report No. 18," Arch. Ophthalmol. **119**, 969–982 (2001).

[23] Collaborative Ocular Melanoma Study Group, "Factors predictive of growth and treatment of small chroidal melanomas. COMS Report No. 5," Arch. Ophthalmol. **115**, 1537–1544 (1997).

[24] T.G. Murray, "Small choroidal melanoma," Arch. Ophthalmol. **115**, 1577–1578 (1997).

[25] J.J. Augsburger, "Is observation really appropriate for small choroidal melanomas?," Trans. Am. Ophthalmol. Soc. **91**, 147–175 (1993).

[26] J.A. Shields and C.L. Shields, "Management of Posterior Uveal Melanoma: Past, Present, and Future," Ophthalmology **122**, 414–428 (2015).

[27] Collaborative Ocular Melanoma Study Group, "The COMS Randomized Trial of Iodine 125 Brachytherapy for Choroidal Melanoma: V. Twelve-year mortality rates and prognosis factors: COMS Report No. 28," Arch. Ophthalmol. **124**, 1684–1693 (2006).

[28] I.W. McLean, W.D. Foster, and L.E. Zimmerman, "Prognostic factors in small malignant melanomas of choroid and ciliary body," Arch. Ophthalmol. **95**, 48–58 (1977).

[29] C.L. Shields, J. Cater, J.A. Shields, A.D. Singh, M.C. Santos, and C. Carvalho, "Combination of clinical factors predictive of growth of small choroidal melanocytic tumors," Arch. Ophthalmol. **118**, 360–364 (2000).

[30] C.L. Shields, J.A. Shields, H. Kiratli, P. De Potter, and J.R. Cater, "Risk factors for growth and metastasis of small choroidal melanocytic lesions," Ophthalmology **102**, 1351–1361 (1995).

[31] E. Kujala, T. Mäkitie, and T. Kivelä, "Very long-term prognosis of patients with malignant uveal melanoma.," Invest. Ophthalmol. Vis. Sci. **44**, 4651–4659 (2003).

[32] K.M. Egan, L.M. Ryan, and E.S. Gragoudas, "Survival implications of enucleation after definitive radiotherapy for choroidal melanoma," Arch. Ophthalmol. **116**, 366–370 (1998).

[33] T. van den Bosch, E. Kilic, D. Paridaens, and A. De Klein, "Genetics of uveal melanoma and cutaneous melanoma: Two of a kind?," Dermatol. Res. Pract. **2010**, 360136 (13 pp.) (2010).

[34] Collaborative Ocular Melanoma Study Group, "Assessment of metastatic disease status at death in 435 patients with large choroidal melanoma in the Collaborative Ocular Melanoma Study (COMS): COMS report No. 15.," Arch. Ophthalmol. **119**, 670–676 (2001).

[35] M. Diener-West, S.M. Reynolds, D.J. Agugliaro, R. Caldwell, K. Cumming, J.D. Earle, D.L. Green, B.S. Hawkins, J. Hayman, I. Jaiyesimi, J.M. Kirkwood, W.J. Koh, D.M. Robertson, J.M. Shaw, and J. Thoma, "Screening for metastasis from choroidal melanoma: The Collaborative Ocular Melanoma Study Group Report 23," J. Clin. Oncol. **22**, 2438–2444 (2004).

[36] R. Sambuelli, J.D. Luna, V.E. Reviglio, A. Aoki, and C.P. Juarez, "Small choroidal melanoma with massive extraocular extension : invasion through posterior scleral emissary channels," Int. Ophthalmol. **24**, 213–218 (2001).

[37] R. Kath, J. Hayungs, N. Bornfeld, W. Sauerwein, K. Hoffken, and S. Seeber, "Prognosis and treatment of disseminated uveal melanoma," Cancer **72**, 2219–2223 (1993).

[38] D.J. Bell and M.W. Wilson, "Choroidal melanoma: natural history and management options," Cancer Control **11**, 296–303 (2004).

[39] J.A. Shields and C.L. Shields, *Intraocular tumours: an atlas and textbook*, 2nd ed. (Wolters Kluwer, Lippincott Williams & Wilkins, Philadelphia, PA, 2008).

[40] D.H. Char, T. Miller, and J.B. Crawford, "Uveal tumour resection," Br. J. Ophthalmol. **85**, 1213–1219 (2001).

[41] S. Nag, J.M. Quivey, J.D. Earle, D. Followill, J. Fontanesi, and P.T. Finger, "The American Brachytherapy Society recommendations for brachytherapy of uveal melanomas," Int. J. Radiat. Oncol. Biol. Phys. **56**, 544–555 (2003).

[42] The American Brachytherapy Society - Ophthalmic Oncology Task Force, "The American Brachytherapy Society consensus guidelines for plaque brachytherapy of uveal melanoma and retinoblastoma," Brachytherapy **13**, 1–14 (2014).

[43] J.-P. Caujolle, V. Paoli, E. Chamorey, C. Maschi, S. Baillif, J. Herault, P. Gastaud, and J.M. Hannoun-Levi, "Local recurrence after uveal melanoma proton beam therapy: Recurrence types and prognostic consequences," Int. J. Radiat. Oncol. Biol. Phys. **85**, 1218–1224 (2013).

[44] C. Maschi, J. Thariat, J. Herault, and J.-P. Caujolle, "Tumour Response in Uveal Melanomas Treated with Proton Beam Therapy," Clin. Oncol. **28**, 198–203 (2014).

[45] E. Egger, L. Zografos, A. Schalenbourg, D. Beati, T. Böhringer, L. Chamot, and G. Goitein, "Eye retention after proton beam radiotherapy for uveal melanoma," Int. J. Radiat. Oncol. Biol. Phys. **55**, 867–880 (2003).

[46] J.L. Hungerford, A.J.E. Foss, I. Whelahan, R.D. Errington, A. Kacperek, and J. Kongerud, "Side Effects of Photon and Proton Radiotherapy for Ocular Melanoma," Front. Radiat. Ther. Oncol. **30**, 287–293 (1997).

[47] M.W. Wilson and J.L. Hungerford, "Comparison of episcleral plaque and proton beam radiation therapy for the treatment of choroidal melanoma," Ophthalmology **106**, 1579–1587 (1999).

[48] R. Dunavoelgyi, K. Dieckmann, A. Gleiss, S. Sacu, K. Kircher, M. Georgopoulos, D. Georg, M. Zehetmayer, and R. Poetter, "Local Tumor Control, Visual Acuity, and Survival After Hypofractionated Stereotactic Photon Radiotherapy of Choroidal Melanoma in 212 Patients Treated Between 1997 and 2007," Int. J. Radiat. Oncol. **81**, 199–205 (2011).

[49] G. Modorati, E. Miserocchi, L. Galli, P. Picozzi, and P. Rama, "Gamma knife radiosurgery for uveal melanoma: 12 years of experience," Br. J. Ophthalmol. **93**, 40–44 (2009).

[50] P.T. Finger, "Radiation therapy for choroidal melanoma," Surv. Ophthalmol. **42**, 215–232 (1997).

[51] D.H. Char, S.M. Kroll, and J. Castro, "Ten-year follow-up of helium ion therapy for uveal melanoma," Am. J. Ophthalmol. **125**, 81–89 (1998).

[52] A.M. Sarici and H. Pazarli, "Gamma-knife-based stereotactic radiosurgery for medium- and large-sized posterior uveal melanoma," Graefe's Arch. Clin. Exp. Ophthalmol. **251**, 285–294 (2013).

[53] D.H. Char, J.M. Quivey, J.R. Castro, S. Kroll, and T. Phillips, "Helium ions versus iodine 125 brachytherapy in the management of uveal melanoma. A prospective, randomized, dynamically balanced trial," Ophthalmology **100**, 1547–54 (1993).

[54] K. Dieckmann, J. Bogner, D. Georg, M. Zehetmayer, G. Kren, and R. Pötter, "A linac-based stereotactic irradiation technique of uveal melanoma," Radiother. Oncol. **61**, 49–56 (2001).

[55] E. Pilotto, S. Vujosevic, V. De Belvis, R. Parrozzani, B. Boccassini, and E. Midena, "Long-term choroidal vascular changes after iodine brachytherapy versus transpupillary thermotherapy for choroidal melanoma," Eur. J. Ophthalmol. **19**, 646–653 (2009).

[56] R.F. Moore, "Choroidal sarcoma treated by the intraocular insertion of radon seeds," Br. J. Ophthalmol. **14**, 145–156 (1930).

[57] H.B. Stallard, "Radiotherapy for malignant melanoma of the choroid," Br. J. Ophthalmol. **50**, 147–155 (1966).

[58] Collaborative Ocular Melanoma Study Group, "Design and methods of a clinical trial for a rare condition: the Collaborative Ocular Melanoma Study. COMS Report No. 3," Control. Clin. Trials **14**, 362–391 (1993).

[59] S.-T. Chiu-Tsao, "Episcleral eye plaques for treatment of intraocular malignancies and benign diseases," in *Brachytherapy Physics: Joint AAPM/ABS Summer School*, 2nd Ed., edited by B.R. Thomadsen, M.J. Rivard and W.M. Butler (Medical Physics, Madison, WI, 2005), pp. 673–705.

[60] J.D. Earle, R.W. Kline, and D.M. Robertson, "Selection of iodine 125 for the Collaborative Ocular Melanoma Study.," Arch. Ophthalmol. **105**, 763–764 (1987).

[61] C.L. Shields, J.A. Shields, J. Cater, K. Gunduz, C. Miyamoto, B. Micaily, and L.W. Brady, "Plaque radiotherapy for uveal melanoma: Long-term visual outcome in 1106 consecutive patients," Arch. Ophthalmol. **118**, 1219–1228 (2000).

[62] A. Karvat, C. Duzenli, R. Ma, K. Paton, and T. Pickles, "The treatment of choroidal melanoma with ^{198}Au plaque brachytherapy," Radiother. Oncol. **59**, 153–156 (2001).

[63] K.L. Leonard, N.L. Gagne, J.E. Mignano, J.S. Duker, E.A. Bannon, and M.J. Rivard, "A 17-year retrospective study of institutional results for eye plaque brachytherapy of uveal melanoma using 125I, 103Pd, and 131Cs and historical perspective," Brachytherapy **10**, 331–339 (2011).

[64] P.T. Finger, K.J. Chin, and G. Duvall, "Palladium-103 Ophthalmic Plaque Radiation Therapy for Choroidal Melanoma: 400 Treated Patients," Ophthalmology **116**, 790–796 (2009).

[65] P.T. Finger, A. Berson, and A. Szechter, "Palladium-103 plaque radiotherapy for choroidal melanoma: Results of a 7-year study," Ophthalmology **106**, 606–613 (1999).

[66] S. Packer, S. Stoller, M.L. Lesser, F.S. Mandel, and P.T. Finger, "Long-term results of iodine 125 irradiation of uveal melanoma.," Ophthalmology **99**, 767–773; discussion 774 (1992).

[67] J.M. Quivey, D.H. Char, T.L. Phillips, K.A. Weaver, J.R. Castro, and S.M. Kroll, "High intensity 125-iodine (^{125}I) plaque treatment of uveal melanomas," Int. J. Radiat. Oncol. Biol. Phys. **26**, 613–618 (1993).

[68] J. Fontanesi, D. Meyer, S. Xu, and D. Tai, "Treatment of choroidal melanoma with I-125 plaque," Int. J. Radiat. Oncol. Biol. Phys. **26**, 619–623 (1993).

[69] C.L. Shields, M. Naseripour, J. Cater, J.A. Shields, H. Demirci, A. Youseff, and J. Freire, "Plaque Radiotherapy for Large Posterior Uveal Melanomas (≥8-mm thick) in 354 Consecutive Patients," Ophthalmology **109**, 1838–1849 (2002).

[70] B.A. Perez, P. Mettu, L. Vajzovic, D. Rivera, A. Alkaissi, B.A. Steffey, J. Cai, S. Stinnett, J.J. Dutton, E.G. Buckley, E. Halperin, L.B. Marks, P. Mruthyunjaya, and D.G. Kirsch, "Uveal melanoma treated with iodine-125 episcleral plaque: An analysis of dose on disease control and visual outcomes," Int. J. Radiat. Oncol. Biol. Phys. **89**, 127–136 (2014).

[71] P.K. Lommatzsch, "Treatment of choroidal melanomas with ^{106}Ru/^{106}Rh beta-ray applicators," Surv. Ophthalmol. **19**, 85–100 (1974).

[72] L. Bergman, B. Nilsson, G. Lundell, M. Lundell, and S. Seregard, "Ruthenium Brachytherapy for Uveal Melanoma, 1979–2003: Survival and Functional Outcomes in the Swedish Population," Ophthalmology **112**, 834–840 (2005).

[73] B. Damato, I. Patel, I.R. Campbell, H.M. Mayles, and R.D. Errington, "Local tumor control after ^{106}Ru brachytherapy of choroidal melanoma," Int. J. Radiat. Oncol. **63**, 385–391 (2005).

[74] P.K. Lommatzsch, C. Werschnik, and E. Schuster, "Long-term follow-up of Ru-106/Rh-106 brachytherapy for posterior uveal melanoma," Graefe's Arch Clin Exp Ophthalmol **238**, 129–137 (2000).

[75] L. Missotten, W. Dirven, A. Van der Schueren, A. Leys, G. De Meester, and E. Van Limbergen, "Results of treatment of choroidal malignant melanoma with high-dose-rate strontium-90 brachytherapy," Graefe's Arch. Clin. Exp. Ophthalmol. **236**, 164–173 (1998).

[76] S.-T. Chiu-Tsao, "Pterygium brachytherapy physics," in *Brachytherapy Physics: Joint AAPM/ABS Summer School*, 2nd ed., edited by B.R. Thomadsen, M.J. Rivard and W.M. Butler (Medical Physics, Madison, WI, 2005), pp. 707–717.

[77] *NUDAT 2.6, National Nuclear Data Centre, Brookhaven National Laboratory*, (URL: http://www.nndc.bnl.gov/chart/decaysearchdirect.jsp?nuc=125I&unc=nds). Last accessed January 24, 2017.

[78] M.J. Berger and J.H. Hubbell, "XCOM: Photon cross sections on a personal computer," in *Report NBSIR87-3597* (National Institute of Standards Technology (NIST), Gaithersburg, MD, 1987).

[79] M.J. Berger, J.S. Coursey, M.A. Zucker, and J. Chang, *ESTAR, PSTAR, and ASTAR: Computer programs for calculating stopping-power and range tables for electrons, protons, and helium ions (version 1.2.3, online)* (National Institute of Standards and Technology, Gaithersburg, MD, 2005) (available URL: http://physics.nist.gov/Star).

[80] R.W. Kline and P.D. Yeakel, "Ocular melanoma, I-125 plaques," Med. Phys. **14**, 475 (1987).

[81] R.W. Kline, *Coordinate Localization*, (URL: http://rpc.mdanderson.org/rpc/credentialing/Coordinate Localization.doc).

[82] S.-T. Chiu-Tsao, M.A. Astrahan, P.T. Finger, D.S. Followill, A.S. Meigooni, C.S. Melhus, F. Mourtada, M.E. Napolitano, R. Nath, M.J. Rivard, D.W.O. Rogers, and R.M. Thomson, "Dosimetry of ^{125}I and ^{103}Pd COMS eye plaques for intraocular tumors: Report of Task Group 129 by the AAPM and ABS," Med. Phys. **39**, 6161–6184 (2012).

[83] M.A. Astrahan, G. Luxton, Q. Pu, and Z. Petrovich, "Conformal episcleral plaque therapy," Int. J. Radiat. Oncol. Biol. Phys. **39**, 505–519 (1997).

[84] D. Granero, J. Pérez-Calatayud, F. Ballester, E. Casal, and J.M. de Frutos, "Dosimetric study of the 15 mm ROPES eye plaque," Med. Phys. **31**, 3330–3336 (2004).

[85] J. Poder and S. Corde, "I-125 ROPES eye plaque dosimetry: Validation of a commercial 3D ophthalmic brachytherapy treatment planning system and independent dose calculation software with GafChromic® EBT3 films," Med. Phys. **40**, 121709 (11 pp.) (2013).

[86] H. Zhang, F. Davidorf, and Y. Qi, "Comparison of 16 mm OSU-Nag and COMS eye plaques," J. Appl. Clin. Med. Phys. **13**, 166–178 (2012).

[87] P.T. Finger, K.J. Chin, G.-P. Yu, and N.S. Patel, "Risk factors for cataract after palladium-103 ophthalmic plaque radiation therapy," Radiat. Oncol. Biol. **80**, 800–806 (2011).

[88] P.T. Finger, K.J. Chin, and G.-P. Yu, "Risk Factors for Radiation Maculopathy after Ophthalmic Plaque Radiation for Choroidal Melanoma," Am. J. Ophthalmol. **149**, 608–615 (2010).

[89] H. Newman, K.J. Chin, and P.T. Finger, "Subfoveal Choroidal Melanoma: Pretreatment characteristics and response to plaque radiation therapy," Arch. Ophthalmol. **129**, 892–898 (2011).

[90] H. Newman, P.T. Finger, K.J. Chin, and A.C. Pavlick, "Systemic bevacizumab (Avastin) for exudative retinal detachment secondary to choroidal melanoma.," Eur. J. Ophthalmol. **21**, 796–801 (2011).

[91] P.K. Lommatzsch, "Results after -irradiation (^{106}Ru/^{106}Rh) of choroidal melanomas: 20 years' experience," Br. J. Ophthalmol. **70**, 844–851 (1986).

[92] M. Kleineidam, R. Guthoff, and S.M. Bentzen, "Rates of local control, metastasis, and overall survval in patients with posterior uveal melanomas treated with ruthenium-106 plaques," Radiother. Oncol. **28**, 148–156 (1993).

[93] S. Seregard, E. Trampe, I. Lax, E. Kock, and G. Lundell, "Results following episcleral ruthenium plaque radiotherapy for posterior uveal melanoma: The Swedish experience," Acta Ophthalmol. Scand. **75**, 11–16 (1997).

[94] Collaborative Ocular Melanoma Study Group, "The COMS Randomized Trial of Iodine 125 Brachytherapy for Choroidal Melanoma: IV. Local treatment failure and enucleation in the first 5 years after brachytherapy. COMS report no. 19," Ophthalmology **109**, 2197–2206 (2002).

[95] Collaborative Ocular Melanoma Study Group, "Collaborative Ocular Melanoma Study (COMS) randomized trial of I-125 brachytherapy for medium choroidal melanoma: I. visual acuity after 3 years COMS report No. 16," Ophthalmology **108**, 348–366 (2001).

[96] Collaborative Ocular Melanoma Study Group, "Incidence of Cataract and Outcomes after Cataract Surgery in the First 5 Years after Iodine 125 Brachytherapy in the Collaborative Ocular Melanoma Study. COMS Report No. 27," Ophthalmology **114**, 1363–1371 (2007).

[97] J.M. Quivey, J.J. Augsburger, L. Snelling, and L.W. Brady, "^{125}I plaque therapy for uveal melanoma. Analysis of the impact of time and dose factors on local control," Cancer **77**, 2356–62 (1996).

[98] R. Jones, E. Gore, W. Mieler, K. Murray, M. Gillin, K. Albano, and B. Erickson, "Posttreatment visual acuity in patients treated with episcleral plaque therapy for choroidal melanoma: Dose and dose rate effects," Int. J. Radiat. Oncol. Biol. Phys. **52**, 989–995 (2002).

[99] N.L. Gagne, K.L. Leonard, K.E. Huber, J.E. Mignano, J.S. Duker, N. V Laver, and M.J. Rivard, "BEDVH—A method for evaluating biologically effective dose volume histograms: Application to eye plaque brachytherapy implants," Med. Phys. **39**, 976 (2012).

[100] N.L. Gagne, K.L. Leonard, and M.J. Rivard, "Radiobiology for eye plaque brachytherapy and evaluation of implant duration and radionuclide choice using an objective function," Med. Phys. **39**, 3332 (2012).

[101] ICRU, "Prescribing, recording, and reporting photon beam therapy," in *ICRU Report 62 (Supplement to ICRU Report 50)* (ICRU, Washington, DC, 1999).

[102] N.L. Gagne and M.J. Rivard, "Quantifying the dosimetric influences of radiation coverage and brachytherapy implant placement uncertainty on eye plaque size selection," Brachytherapy **12**, 508–520 (2013).

[103] P. Aryal, J.A. Molloy, and M.J. Rivard, "A modern Monte Carlo investigation of the TG-43 dosimetry parameters for an ^{125}I seed already having AAPM consensus data," Med. Phys. **41**, 021702 (10 pp.) (2014).

[104] R.E.P. Taylor and D.W.O. Rogers, "An EGSnrc Monte Carlo-calculated database of TG-43 parameters," Med. Phys. **35**, 4228–4241 (2008).

[105] R.M. Thomson and D.W.O. Rogers, "Monte Carlo dosimetry for ^{125}I and ^{103}Pd eye plaque brachytherapy with various seed models," Med. Phys. **37**, 368–376 (2010).

[106] L. Beaulieu, Å. Carlsson Tedgren, J.-F. Carrier, S.D. Davis, F. Mourtada, M.J. Rivard, R.M. Thomson, F. Verhaegen, T.A. Wareing, and J.F. Williamson, "Report of the Task Group 186 on model-based dose calculation methods in brachytherapy beyond the TG-43 formalism: Current status and recommendations for clinical implementation," Med. Phys. **39**, 6208–6236 (2012).

[107] R.M. Thomson, R.E.P. Taylor, and D.W.O. Rogers, "Monte Carlo dosimetry for ^{125}I and ^{103}Pd eye plaque brachytherapy," Med. Phys. **35**, 5530 (2008).

[108] E. Pantelis, P. Papagiannis, P. Karaiskos, A. Angelopoulos, G. Anagnostopoulos, D. Baltas, N. Zamboglou, and L. Sakelliou, "The effect of finite patient dimensions and tissue inhomogeneities on dosimetry planning of 192 Ir HDR breast brachytherapy: a Monte Carlo dose verification study," Int. J. Radiat. Oncol. Biol. Phys. **61**, 1596–1602 (2005).

[109] M. Lesperance, M. Inglis-Whalen, and R.M. Thomson, "Model-based dose calculations for COMS eye plaque brachytherapy using an anatomically realistic eye phantom," Med. Phys. **41**, 021717 (12 pp.) (2014).

[110] M. Lesperance, M. Martinov, and R.M. Thomson, "Monte Carlo dosimetry for ^{103}Pd, ^{125}I, and ^{131}Cs ocular brachytherapy with various plaque models using an eye phantom," Med. Phys. **41**, 031706 (2014).

[111] M.A. Astrahan, *Plaque Simulator*, (URL: http://eyephysics.com/PS/Index.html). Last accessed May 31, 2017.

Chapter 2 Background and theory

2.1 I-125 brachytherapy sources and dosimetry

2.1.1 I-125 radiation and types of I-125 seeds

Iodine has 37 known isotopes, from I-108 to I-144, all of which are unstable radionuclides with the exception of stable I-127; iodine is therefore a monoisotopic element. I-125 is used in brachytherapy and is produced by the (n,γ) reaction from Xe-124, as shown in Eq. 2.1. I-125 has a half-life of 59.4 days and decays 100% by electron capture to the first excited state of Te-125, which undergoes internal conversion 93.3% of the time and emits a 35.5 keV gamma ray the remaining 6.7% of the time, to reach the ground state of Te-125 (Eq. 2.2 and Figure 2.1). The internal conversion process gives rise to Auger electrons and characteristic x-rays.[1]

$$^{124}_{54}Xe(n,\gamma) \rightarrow {}^{125m\ or\ g}_{\quad\quad 54}Xe \rightarrow {}^{125}_{53}I \tag{2.1}$$

$$^{125}_{53}I + e^- \rightarrow {}^{125}_{52}Te + \gamma \tag{2.2}$$
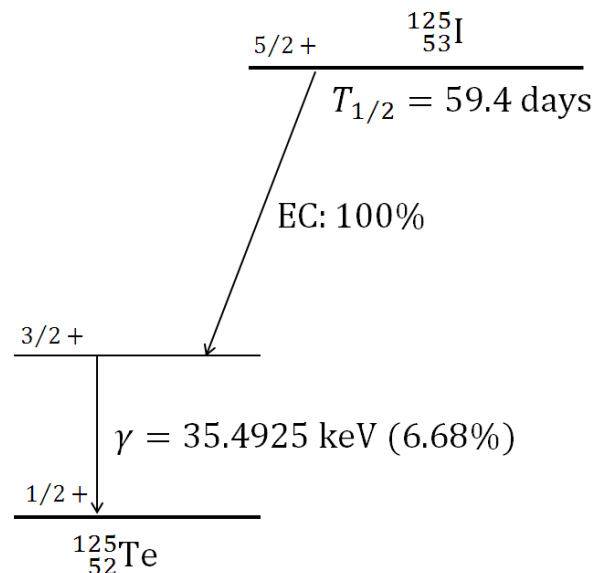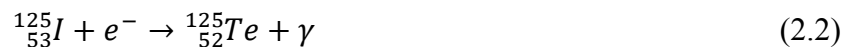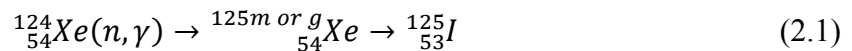
Figure 2.1 Decay scheme for I-125 to Te-125 by electron capture with the release of a 35.5 keV gamma ray.[1]

The photons emitted from I-125 decay are listed in Table 2.1 and have a normalized intensity weighted average energy of 26.06 keV, and a yield of 1.5767 photons/decay. However the 3.77 keV photons are generally not considered in I-125 brachytherapy, as these very low-energy photons are absorbed either by the source encapsulation or within the first few μm outside of the source encapsulation, and therefore do not contribute dosimetrically. Excluding these photons, the average photon energy from I-125 is 28.37 keV.

Table 2.1 I-125 disintegration photon energy spectrum from the NNDC database.[1]

Decay radiation	Energy (keV)	Intensity (%)
XR l	3.77	14.8
XR kα2	27.202	39.6
XR kα1	27.472	73.1
XR kβ3	30.944	6.74
XR kβ1	30.995	13.0
XR kβ2	31.704	3.75
γ	35.4925	6.68
Normalized intensity weighted average energy	26.06	

There are currently nearly 20 different types of I-125 brachytherapy seeds of varying designs, materials, geometries etc. The vast majority consist of an active internal component which contains the radioactive material adsorbed onto some type of radio-opaque substrate (often silver) that can be used for seed localization following patient implantation. The active internal component is contained within a titanium capsule that is sealed at both ends. Depending on the chemical composition of the substrate (most commonly silver but alternatively gold, molybdenum, aluminum, tungsten, platinum, a gold-copper alloy, palladium, or other non-metallic material such as ceramic or polystyrene), the photon emissions from the brachytherapy source also often include fluorescent x-rays emitted following excitation of the high density radio-opaque material through interactions with the I-125 decay photons. This results in a slightly lower average photon energy, around 27-28 keV.[2,3]

2.1.2 Kerma, dose, and charged particle equilibrium

The deposition of energy by photons passing through matter happens via three main interaction events: photoelectric absorption, Compton scattering, and pair-production.[4,5] For the keV energy photons emitted by I-125, the main forms of interaction are photoelectric absorption and Compton scattering, and though it does not result in the transfer of energy, Rayleigh scattering. The probability of a given type of interaction occurring is dictated by the interaction cross-sections, which vary with energy, interaction material, and density (both mass and electron) of the material. The relevant interaction cross-sections for the range of energies present for I-125 decay in water are shown in Figure 2.2 for cross-section data from the XCOM database.[6]
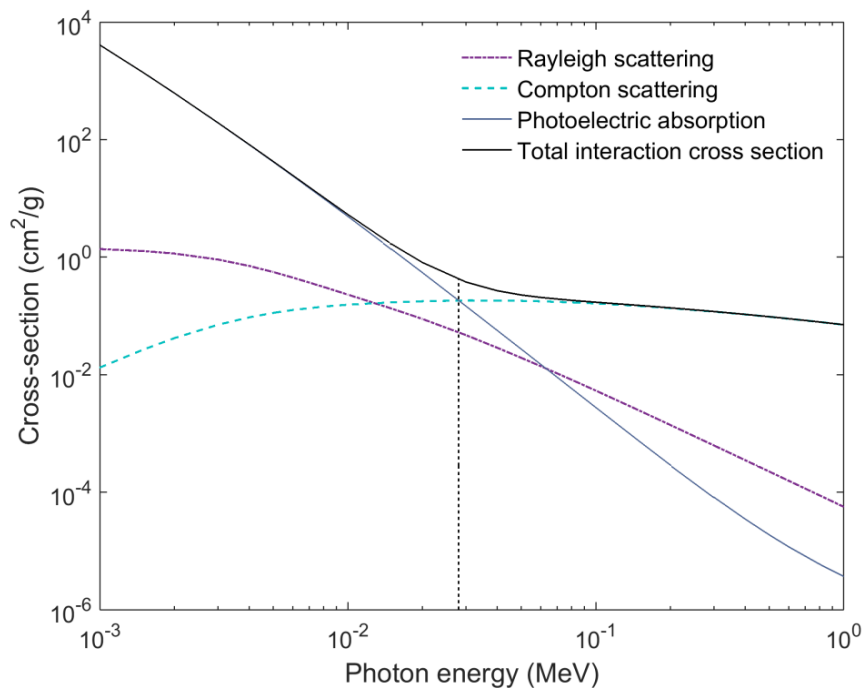
Figure 2.2 Total, photoelectric, Compton scattering (incoherent scattering), and Rayleigh scattering (coherent scattering) interaction cross-sections in water;[6] 28 keV energy is indicated by the dotted line.

The total kinetic energy released to the material by either photoelectric absorption or Compton scattering is known as the Kerma (Kinetic Energy Released per Mass), and is given in

units of J/kg. The total kerma, K, is composed of two components, the collisional kerma, K_c, and the radiative kerma, K_r:

$$K = K_c + K_r \tag{2.3}$$

where the collisional kerma is the net energy transferred to charged particles per unit mass, and the radiative kerma is the kinetic energy per unit mass that is radiated away in charged particle interactions that create other photons. For brachytherapy energies in general, and particularly for the low-energy photons emitted by the decay of I-125, radiative energy losses are negligible ($K_r = 0$), and the total kerma is equal to the collisional kerma.[4,5] The collisional kerma can be related to the particle fluence, Φ, photon energy, E, and the mass energy absorption coefficient, μ_{en}/ρ, as:

$$K_c = \Phi E \frac{\mu_{en}}{\rho} \tag{2.4}$$

Charged particle equilibrium (CPE) exists for a given interaction volume if each charged particle of a given type and energy leaving the volume is replaced by an identical particle entering the volume. If this condition is satisfied, then the collisional kerma is equal to the energy deposited to the medium, which is known as the absorbed dose, D (energy deposited per unit mass), also given in units of J/kg.[4] The range of secondary charged particles produced is estimated by the continuous slowing down approximation (CSDA) range. For electrons set in motion by photons from I-125 decay, the CSDA range is at most approximately 2.3×10^{-3} cm in water (calculated with ESTAR[7]), which is short compared to the corresponding mean free path of I-125 emitted photons (2.19 cm in water), and if using macroscopic-sized volumes such that the range of secondary electrons can be considered short in comparison to the volume, CPE will prevail. In general for brachytherapy, CPE is valid for dose calculation purposes, except very close to the source or at metal-tissue interfaces.[8–11] This is a particularly useful concept for the calculation of dose for low-energy photons, as will be seen in Section 2.5.

2.1.3 TG-43 formalism

The TG-43 dose calculation formalism is described in the 1995 American Association of Physicists in Medicine (AAPM) Task Group (TG)-43 report,[12] and the TG-43U1 and TG-43U1S1 updates,[13,14] and is the worldwide standard for photon brachytherapy dose calculations. The formalism relies on tabulated data based on a geometric dose fall-off framework, and

38

describes dose deposition around a single brachytherapy source located at the centre of a large water phantom.[13] The tabulated data for single sources is derived from Monte Carlo (MC) simulations, thermoluminescent dosimeter (TLD) measurements, or a combination of both, following the specifications outlined in the TG-43U1 report. For multiple sources, the total dose is calculated from the superposition of dose distributions for single sources based on their physical placement and relative dwell times. Implementation of the TG-43 formalism has resulted in significant improvements in the standardization of clinical dose calculations.[13]

The TG-43 dose calculation formalism utilizes multiplicative dose factors to calculate the dose at any point of interest based on its position relative to a reference dose position, given by $P(r_0, \theta_0)$. The geometric set-up is shown in Figure 2.3. The formalism assumes clinical symmetry of the source and uses polar coordinates r and θ, which measure the radial distance away from the source centre and the angle from the source long-axis, respectively. The reference point $P(r_0, \theta_0)$ is at r=1 cm and θ=90°; the reference angle also denotes the transverse axis of the source.
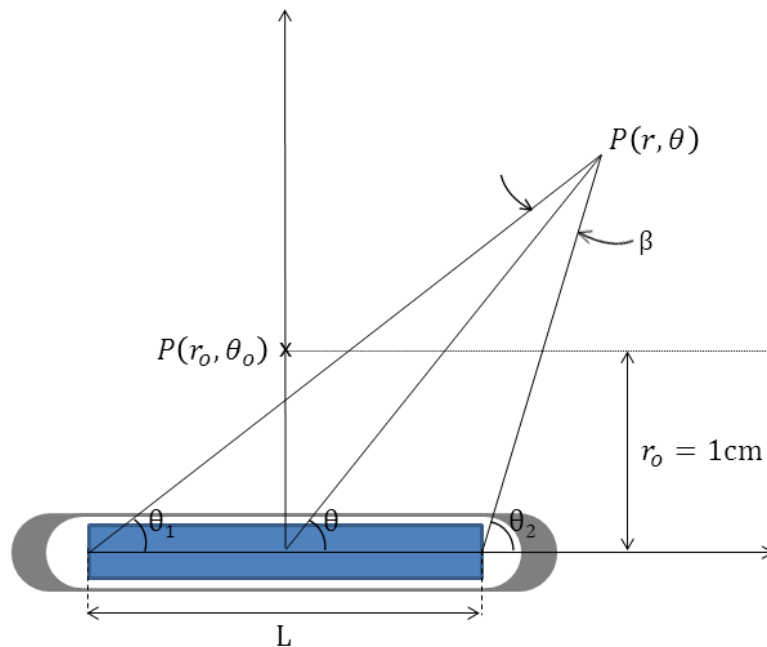
Figure 2.3 Coordinate system used in the 2D TG-43 dose calculation formalism.

The dose rate calculated at any point $P(r, \theta)$ is given by Eq. 2.5:

$$\dot{D}(r, \theta) = S_K \cdot \Lambda \cdot \frac{G_L(r, \theta)}{G_L(r_0, \theta_0)} \cdot g_L(r) \cdot F(r, \theta) \tag{2.5}$$

Each factor in Eq. 2.5 is described in Eqs. 2.6 – 2.11. The air kerma strength, S_K, is the air-kerma rate, $\dot{K}_\delta(d)$, in vacuo, due to photons with energies greater than δ, at a distance d along the transverse axis of the source, multiplied by the square of this distance. The energy cut-off, typically around 5 keV, is introduced to remove the contribution of low-energy photons or contaminants that can increase $\dot{K}_\delta(d)$, but would not contribute to the dose in tissue beyond ~0.1cm (for example, the 3.77 keV photons from I-125 sources, as well as low energy Ti K-shell fluorescent x-rays from the source encapsulation). For low-energy sources, the air-kerma rate is measured using the U.S. National Institute of Standards and Technology (NIST) wide-angle free-air chamber (WAFAC), and the calculated air kerma strength is measured in units of U, where 1 U = 1 cGy·cm² h⁻¹. The WAFAC measures within a ±7.6° conical around the seed's transverse axis, and uses an aluminum filter to remove the low energy photons below 5 keV.

$$S_K = \dot{K}_\delta(d) \cdot d^2 \tag{2.6}$$

$$\Lambda = \frac{\dot{D}(r_0, \theta_0)}{S_k} \tag{2.7}$$

$$G_L(r, \theta) = \begin{cases} \frac{\beta}{L\, r \sin \theta}, & \text{if } \theta \neq 0 \\ (r^2 - L^2/4)^{-1}, & \text{if } \theta = 0 \end{cases} \tag{2.8}$$

$$G_L(r, \theta) = \frac{\cos^{-1}\left(\frac{r \cos \theta - L/2}{\sqrt{r^2 + (L/2)^2 - L\, r \cos \theta}}\right) - \cos^{-1}\left(\frac{r \cos \theta + L/2}{\sqrt{r^2 + (L/2)^2 + L\, r \cos \theta}}\right)}{L\, r \sin \theta}, \text{if } \theta \neq 0 \tag{2.9}$$

$$g_L(r) = \frac{\dot{D}(r, \theta_0)}{\dot{D}(r_0, \theta_0)} \cdot \frac{G_L(r_0, \theta_0)}{G_L(r, \theta_0)} \tag{2.10}$$

$$F(r, \theta) = \frac{\dot{D}(r, \theta)}{\dot{D}(r, \theta_0)} \cdot \frac{G_L(r, \theta_0)}{G_L(r, \theta)} \tag{2.11}$$

The dose rate constant, Λ, is the dose rate to water at a distance of 1 cm on the transverse axis ($\theta = 90°$) for a source with unit air kerma strength ($S_K = 1$U) (Eq. 2.7). It includes the effects of the source geometry, the spatial distribution of the radioactive material in the source, the encapsulation of the source, source self-filtration of emitted photons, and scattering in the water material surrounding the source.[12] The geometry function, $G_L(r, \theta)$, provides an estimate of the

photon fluence fall-off based on a line model of the spatial distribution of radioactivity in the source of active length L. The general form of $G_L(r, \theta)$ is given by Eq. 2.8, while an expanded version is given by Eq. 2.9. The radial dose function, $g_L(r)$, accounts for the effects of scatter and absorption in the water medium along the transverse axis of the source (Eq. 2.10), while the anisotropy factor, $F(r, \theta)$, accounts for the anisotropic dose distribution around the source at locations off of the transverse plane (Eq. 2.11).

2.2 Eye plaque dosimetry

2.2.1 Adoption of and expansion beyond TG-43

Due to the different techniques and radionuclides used for treatment, there was a lack of consensus about the treatment approach for ocular brachytherapy prior to 1985. As mentioned previously, in 1985 the COMS group was created as a multi-institutional cooperative clinical trial sponsored by the National Eye Institute and the National Institute of Health.[15] The randomized trial comparing enucleation against I-125 plaque radiation therapy created a standardized procedure for administering the radiation therapy and for dosimetry calculations. The COMS group recognized the large uncertainties associated with dosimetry, and therefore used a simplified calculation protocol.

In the COMS trial methodology, the prescription point was specified at the tumour apex if the tumour height was ≥5 mm (up to a maximum of 10 mm), or at 5 mm from the inner scleral surface if the tumour height was between 2.5 and 5 mm, with the prescription dose set at 100 Gy.[16] The dose was calculated assuming a point-source approximation of the brachytherapy seed, and no corrections were made for source anisotropy, the plaque or Silastic insert materials (using the COMS style plaques), and photon backscatter or fluorescence photons from the gold-alloy backing. Doses within the eye were calculated using Eq. 2.12:

$$D(r) = A_a \cdot \Gamma_a \cdot f \cdot T(r) \cdot \phi \tag{2.12}$$

where A_a is the apparent activity of the seed in mCi, Γ_a is the exposure rate constant (equal to 1.45 R cm^2/mCi·h for I-125), f is the exposure-to-dose conversion factor (value is seed model dependent), $T(r)$ is the tissue attenuation and scatter factor (tabulated for each seed model, includes a factor of 1/r^2, distinct from the carrier correction factor introduced in Eq. 2.15 that

uses the same symbol; sometimes written as $g(r)/r^2$ where the $1/r^2$ factor is separated out), and ϕ is the anisotropy constant (assumed to be equal to 1 for COMS protocol). The source activity was chosen to maintain a dose rate of $0.42 - 1.05$ Gy/hr, and the plaque size was chosen such that the tumour base plus a 2–3 mm margin was covered by the plaque, and the 100 Gy isodose line passed through the prescription point, encompassed the tumour, and extended to or beyond the edge of the plaque.[16]

The establishment of the TG-43 dose calculation method in 1995 significantly changed the dosimetry calculation formalism for brachytherapy sources, and therefore also impacted the dose calculation for eye plaques. For some I-125 sources, the absorbed dose was lower by up to 17%.[12] Another modification arose from the new NIST 1999 calibration standard using the WAFAC that resulted in seed strengths being reduced by ~10%, which caused an increase in dose rate constants by nearly 10% (the previous NIST standard measurements using the Ritz chamber were contaminated by the low-energy 4.5 keV Ti K-shell characteristic x-rays, as mentioned in Section 2.1.3). These changes were all reflected in the TG-43U1 document.[13]

When the TG-43 method was initially adopted for ocular brachytherapy dose calculations, several assumptions were still made: the source was approximated as a point (point source formalism instead of line source/2D formalism, which also means source anisotropy was ignored), the effects of the gold backing on scatter and attenuation were ignored (treated as water), the Silastic insert was assumed to be water equivalent, and the shielding effects of the plaque lip were also ignored.[16–18] The dose rate at any given point at a distance r from a source was calculated as:

$$\dot{D}(r) = S_k \cdot \Lambda \cdot \left(\frac{r_0^2}{r^2}\right) \cdot g_P(r) \tag{2.13}$$

which is the 1D version of the TG-43 formalism, in which $F(r,\theta) = 1$, $G_P(r,\theta) = r^{-2}$, and the radial dose function is determined assuming a point source ($g_P(r)$) instead of a line source. When the protocol was revised, the effect of the lip, the gold backing and the Silastic insert on a fully loaded plaque were still unknown (dosimetry investigations had only been done on a single centrally loaded seed), and so could not yet be accounted for. For example, the adoption of the TG-43 formalism and updated dose rate constants resulted in a dose decrease of 15% and 11% compared to the original COMS methodology for the Oncura OncoSeed model 6711 and 6702 I-125 seeds (GE Healthcare Inc., Arlington Heights, IL), respectively. The original COMS

protocol prescription dose of 100 Gy was therefore recalculated and changed to 85 Gy. The practice of using a minimum prescription depth of 5 mm was also later eliminated; the tumour apex or point of maximal thickness is now the recommended prescription point, with the requirement that the prescription isodose line encompass the entire tumour.[19,20]

2.2.1.1 Transition to heterogeneous dose calculations

In ocular brachytherapy dosimetry, "heterogeneity" involves two different constituents. The first is the heterogeneity of the metal plaque and insert materials, which will be discussed here, and the second is the heterogeneity of patient tissues, which will be discussed in Section 2.5. Therefore patient tissues are still treated as water equivalent here.

Early studies in the 1990s using TLDs and MC simulations of a single centrally loaded seed in a 20 mm COMS plaque found central axis dose reductions of ~10% and 16% at 10 mm depth and off-axis dose reductions of 15% and 30% for I-125 and Pd-103, respectively.[21–23] These differences were attributed to the non-water equivalence of the Silastic insert which has an effective atomic number, Z_{eff} ~10.7 (Z_{eff} of water is ~7.4), and therefore has more photoelectric interactions with the lower energy photons than water and decreased scatter due to the shielding effect of the gold plaque (a more detailed description of these effects is given in Section 2.2.2.2). This led to applying a correction factor of 0.9 for the tumour dose with I-125 seeds:[24,25]

$$\dot{D}(r) = (0.9) \cdot S_k \cdot \Lambda \cdot \left(\frac{r_0^2}{r^2}\right) \cdot g_P(r) \tag{2.14}$$

Later studies found this constant correction factor to be inadequate for off-axis locations or at depths other than 10 mm. MC studies using BrachyDose[26,27] (EGSnrc-based code) and MCNP5[28,29] found dose differences on the central axis at 5 mm depth of up to 11% and 19% for I-125 and Pd-103, respectively, elsewhere along the central axis of up to 37%, and off-axis differences approaching a factor of 10 between the homogeneous and heterogeneous cases. Rivard et al.[29] found that 85 Gy (based on a homogeneous water assumption) at 5 mm depth actually delivers only 76 Gy and 67 Gy for model 6711 I-125 seeds and Theragenics TheraSeed Model 200 Pd-103 seeds (C.A. Bard Inc., Covington, GA), respectively.

To account for radiation scatter and attenuation by the gold-alloy backing and Silastic insert at depths other than 10 mm, a dose correction factor, $T(r)$, was adopted:[24]

$$\dot{D}(r) = S_k \cdot \Lambda \cdot \left(\frac{r_0^2}{r^2}\right) \cdot g_P(r) \cdot T(r) \tag{2.15}$$

$T(r)$ has limited accuracy as it is determined (using MC simulations) with one centrally loaded seed, and for only one type of brachytherapy seed (the 6711 seed). The correction factor was found to be nearly independent of plaque size, so that the same factor is applied for all COMS plaque sizes.

The AAPM TG-129 report advises that at a minimum, heterogeneity-corrected dose to the prescription point should be calculated in addition to 2D homogeneous dose distributions.[15] Tabulated data for all COMS plaque sizes are provided in the TG-129 document based on the MC results of Thomson *et al*.[26] to convert from a homogeneous dose prescription of 85 Gy to the equivalent heterogeneous dose.

2.2.2 Plaque Simulator: conformal episcleral plaque therapy

The following section describes corrections to the 2D TG-43 dose calculation formalism employed by Melvin Astrahan in the Plaque Simulator software (Eye Physics LLC, Los Alamitos, CA) to improve the accuracy of treatment planning for eye plaques.

2.2.2.1 Collimation algorithms

Collimation algorithms are used to account for the lip of the COMS plaques, as well as the deep seed slots in other plaque designs. The first implementation used a simple "line of sight" shielding algorithm,[30] which assumes complete attenuation of primary radiation, and ignores scatter into shielded regions (which may cause some underestimation of dose in the penumbral regions) (Figure 2.4). The deeply slotted plaques were designed to take advantage of the extra collimation to improve dose homogeneity within the tumour, and to better shield uninvolved structures outside the tumour.

The half-value layer (HVL) of I-125 radiation in gold is ~0.01 mm, so transmission through the 0.5 mm gold plaques can be considered zero. However, to improve the accuracy of the calculated dose within the penumbra, the "line of sight" algorithm is still used but with a more rigorous accounting for the geometry of each seed with respect to the lip of the plaque to determine the fraction of the active length of the brachytherapy source that is visible above the lip horizon (Figure 2.5).[24]

(a)

Tumor
Retina
Sclera
I-125 seeds
Gold shell

(b)

Tumor
Retina
Sclera
Gold
I-125 seeds
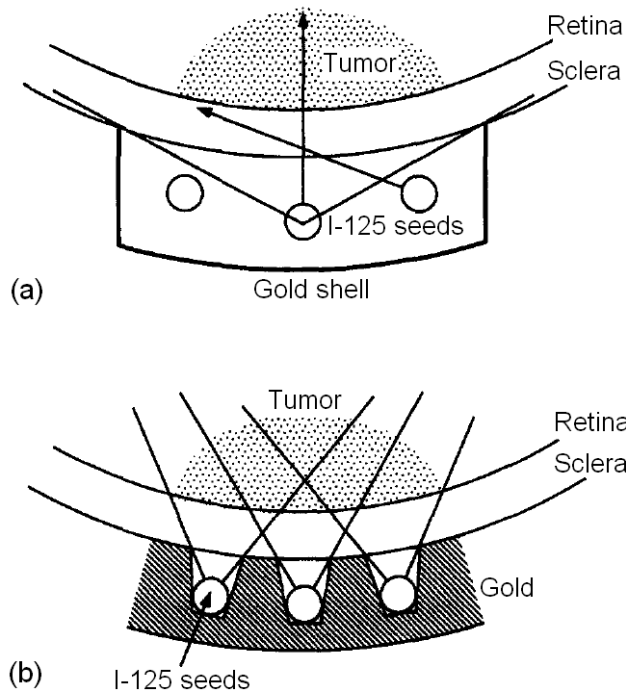
Figure 2.4 Simple "line of sight" collimation algorithm for COMS plaques (a) and slotted plaques (b) (image adapted from M.A. Astrahan, *et al.*, "Conformal episcleral plaque therapy," Int. J. Radiat. Oncol. Biol. Phys. **39**, 505–519 (1997)[30] with permission from Elsevier).

Geometric penumbra
P
Sclera
Gold backing
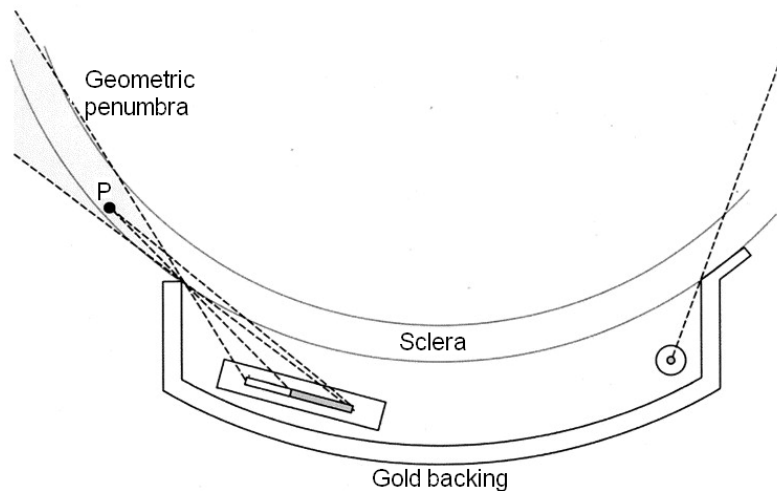
Figure 2.5 Geometric penumbra for a linear source, which varies depending on its proximity and orientation with respect to the lip of the plaque (image adapted from M.A. Astrahan, "Improved treatment planning for COMS eye plaques," Int. J. Radiat. Oncol. Biol. Phys. **61**, 1227–1242 (2005)[24] with permission from Elsevier).

2.2.2.2 Correction factors

As mentioned previously, the dominant photon interaction processes resulting in a transfer of energy to the interacting medium for the low-energy photons emitted from the decay of I-125 are photoelectric absorption and Compton scattering. The effective atomic numbers of water, Silastic, and gold are 7.4, 10.7, and 79, respectively; therefore for water, the probability of Compton scattering compared to photoelectric absorption is approximately 0.5:0.5, while for Silastic it is about 0.25:0.75, and for gold it is essentially 0:1.[24] Using this information, the effects on the dose due to the gold backing and Silastic insert for COMS plaques can be predicted by examining the photon interaction processes as compared to a homogeneous water scenario.

The interaction models in Figure 2.6 outline the expected contributions of photoelectric absorption and Compton scattering in each hemisphere, the front hemisphere being where the eye and tumour would be located. For the water only scenario in Figure 2.6(a), assuming an isotropic point source, half of the photons will be emitted into the front hemisphere and half into the rear hemisphere. Considering the primary photons emitted into the rear hemisphere, in water, half of these will undergo Compton scattering and half will undergo photoelectric absorption. For the I-125 energy range, the average Compton scattering angle is approximately 90° and the energy of once-scattered photons is approximately the same as the primary photon energy for this scattering angle. Now considering these once-scattered photons, approximately half will again undergo Compton scattering and the remaining half will undergo photoelectric absorption. The photons that undergo Compton scattering will again have an average scattering angle of approximately 90°, though now the direction of scattering in relation to the two hemispheres is not symmetric, therefore it is assumed half of these twice-scattered photons will be directed towards the front hemisphere and half further into the rear hemisphere. This simple model predicts that ~12.5% of photons initially emitted into the rear hemisphere will scatter into the front hemisphere. Of these once backscattered photons, a similar fraction could double back and reach the rear hemisphere again. Beyond this many interactions very few photons will remain that have not undergone photoelectric absorption. The net result is that approximately 11% of photons originally emitted into the rear hemisphere will be scattered and absorbed in the front hemisphere, but since that same amount will be scattered out of the front hemisphere, there is equilibrium between the two hemispheres.[24]
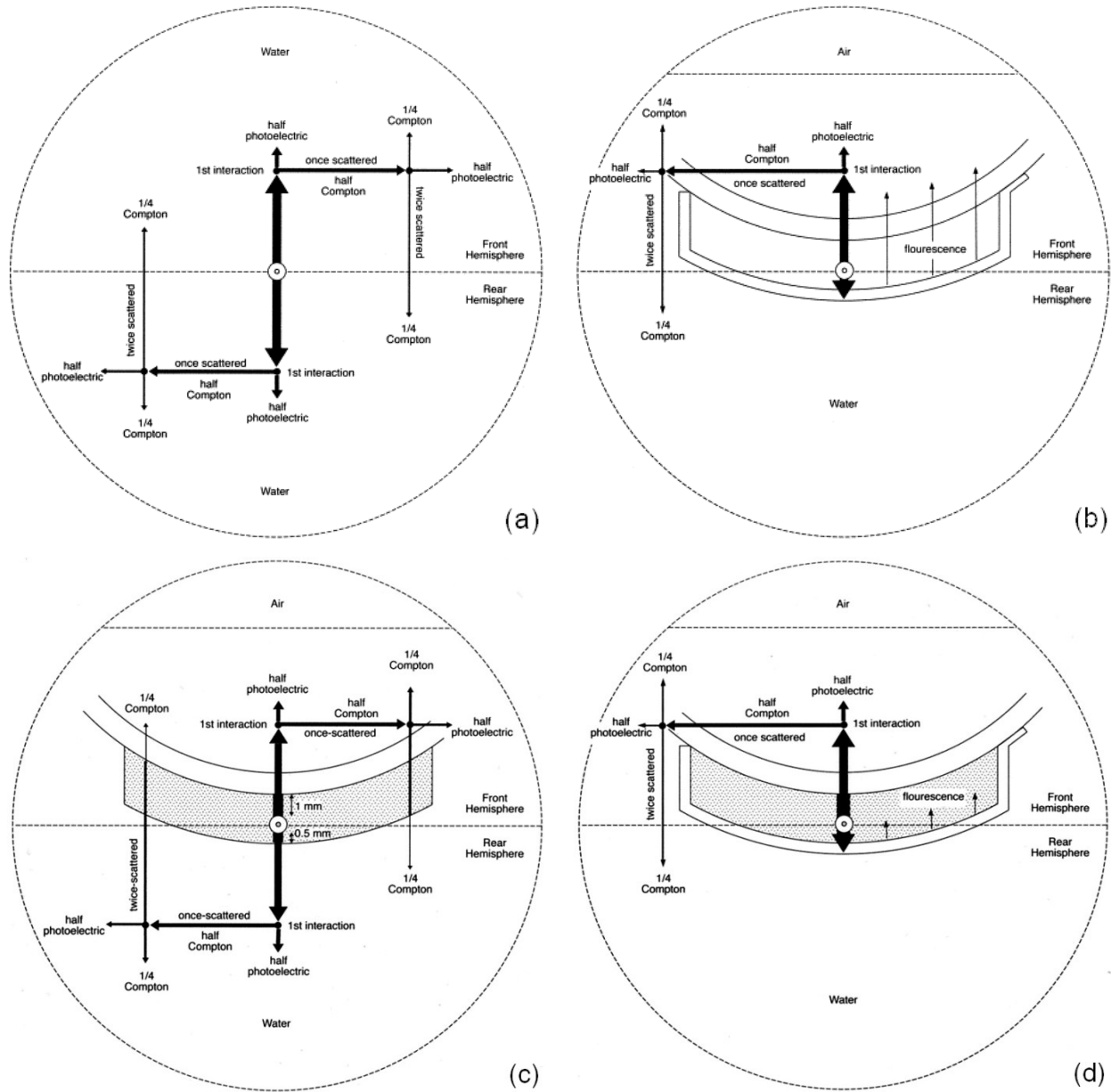
Figure 2.6 Photon interaction processes for (a) water medium only, (b) water with gold plaque and air interface, (c) water with Silastic and air interface, and (d) water with gold plaque and Silastic and air interface (images reproduced from M.A. Astrahan, "Improved treatment planning for COMS eye plaques," Int. J. Radiat. Oncol. Biol. Phys. **61**, 1227–1242 (2005)[24] with permission from Elsevier).

For the gold plaque in water medium scenario [Figure 2.6(b)] the photons that would be scattered back into the front hemisphere are photo-electrically absorbed, predicting ~11% decrease in dose in the front hemisphere. The L-shell fluorescent X-rays result in a small dose

increase very close to the plaque, and photons entering the air are "lost" as a source of scatter so there is also a small dose decrease close to the air interface compared with the water only scenario.

For the Silastic in water medium scenario [Figure 2.6(c)], due to the higher atomic number and density, there is greater photon attenuation in the Silastic than in water, and more of it is by photoelectric absorption. Assuming attenuation is given by $e^{-\mu x}$ for a mean path length of 0.17 cm, in water (μ = 0.46 cm^2/g, x = 0.17 cm) the attenuation is 0.925, and in Silastic (μ = 1.01 cm^2/g, x = 0.17 cm) it is 0.842, such that the ratio of attenuation in water to Silastic is about 0.91. Also, as there is reduced scatter from the rear hemisphere, the Silastic insert is expected to reduce dose in the front hemisphere by ~10%. As with the previous scenario, the air interface creates a small dose decrease close to this interface.

For the gold plaque and Silastic in water medium scenario [Figure 2.6(d)], compared with homogeneous water the combination of the gold plaque and Silastic insert reduces the absorbed dose in the front hemisphere by about 9%, in addition to the 11% due to the loss of backscatter from the rear hemisphere. The air interface further reduces the dose in the immediate vicinity of the interface. There is an approximately 18% maximum decrease in dose 25 mm away from the source,[26] which is well predicted by this simplified model.

In Plaque Simulator, the 2D TG-43 formalism is used with correction factors to account for the increased attenuation through the Silastic insert, the reduced backscatter due to the gold plaque, as well as the air interface at the front of the eye. The dose to a point P is calculated as:

$$D(r,\theta,d,\mu) = D(r,\theta)_{TG-43} \cdot T(r) \cdot t(d,\mu) \cdot A(R) \tag{2.16}$$

where $D(r,\theta)_{TG-43}$ is the 2D TG-43 calculated dose (Eq. 2.5), $T(r)$ accounts for the increased attenuation through the Silastic insert as well as the scatter deficits caused by the gold plaque and is derived from MC simulations, $t(d,\mu)$ accounts for the additional path length, d >1 mm, which is unaccounted for in $T(r)$ as it is derived for a single seed in the central slot, that any photons must travel to reach the dose calculation point compared to water, and is equal to:

$$t(d,\mu) = e^{-\mu_{Silastic}d} / e^{-\mu_{water}d} \tag{2.17}$$

and $A(R)$ accounts for the reduced backscatter from the air interface, where R is the distance from the air interface at the dose calculation point. In Plaque Simulator, if both $T(r)$ and $t(d,\mu)$ are employed, they are combined into one factor and written as $T(r,d,\mu)$.

For the slotted style of plaques there is no seed insert/guide; therefore the only effects are those from collimation, reduced backscatter, and emission of fluorescent x-rays as described in Figure 2.6(b). The effect of the gold plaque backing is accounted for with a backscatter factor ($B(r)$), currently using TLD measured data from Luxton *et al.*[31]

Overall, Plaque Simulator has been found to agree with MC simulated dose distributions in front of the eye plaque very well in a recent analysis,[29] as well as prior to more accurate and updated plaque correction factors being used in the software.[26] Nonetheless, it has a number of limitations. The $T(r)$ data currently used in Plaque Simulator is that determined for a single source loaded in the central slot of the 20 mm COMS plaque, simulated using MC by Thomson *et al.*[26] for one I-125 source model (also given in Table III in the TG-129 document[15]). Similarly, the data used for $A(R)$ is estimated from Figure 8(a) in Thomson *et al.*,[26] which is determined for a fully loaded 20 mm COMS plaque located on the posterior pole. Any deviations from these scenarios could result in inaccuracies in the calculated dose distributions.

The use of different seed models was found to affect the dose distributions minimally for similarly constructed seeds, but larger differences were observed (up to 8%) at points of interest within the eye for distinctly different seed models (for both I-125 and Pd-103 sources).[27] Off-axis dose calculations (at the macula and optic disc) were found to agree well between Plaque Simulator and MC for a fully loaded 12 mm COMS plaque by Thomson *et al.*[26] However, larger differences were observed for a fully loaded 20 mm COMS plaque positioned such that the macula and optic disc were at a further distance from the plaque, but located closer to the central axis. These differences were mainly attributed to the data used to account for the plaque materials and air interface, which at that time came from Chiu-Tsao *et al.*[21] and de la Zerda *et al.*,[23] with implementation described by Astrahan.[24] A more recent comparison by Acar *et al.*[32] of Plaque Simulator calculated doses to Gafchromic film measurements found agreement within 5% along the plaque CAX for most depths and plaque sizes analyzed, and within 7% at most off-axis locations. The exceptions were at shallower depths (within 5 mm of the plaque) on the CAX and in the penumbral zones where differences of up to 12% and 17% were observed, respectively. The differences were attributed to uncertainties in film dosimetry and the plaque collimation algorithm used in Plaque Simulator.[32] The effects of some of these limitations will be addressed in Chapters 4 and 6.

2.3 Radiochromic film dose measurements

Dosimetry measurements for eye plaques introduce many challenges due to the steep dose gradients, small radiation fields, low-energy radiation sources having higher sensitivity to material heterogeneities, larger uncertainties in seed strength compared to external beam calibration/output, as well as many sources of uncertainty in the experimental set-up. Previous experimental dosimetry studies of eye plaques have included a wide variety of dosimeters including TLDs, diodes, radiographic film, radiochromic film, plastic scintillators, polymer gels, small ion chambers, alanine, and diamond detectors. A thorough summary and literature review of these studies are given in the AAPM TG-129 document.[15]

Gafchromic film offers many advantages for brachytherapy dosimetry, and was chosen to explore the feasibility of high-accuracy eye plaque dosimetry due to its capacity for 2D measurement, submillimeter resolution, and excellent reproducibility. These qualities are of particular benefit in small (mm-sized) regions having steep dose gradients, which are characteristic of eye plaque treatments.[33]

Accurate dosimetry measurements using Gafchromic film require developing several procedural elements: scanning protocols, film calibration methods, and film artifact correction methods. The following sections describe the basic theory behind Gafchromic film dosimetry. Methods developed specifically for low-energy brachytherapy dose measurements are described in Chapter 3.

2.3.1 Gafchromic EBT3 film

The film used in this work was Gafchromic® EBT3 (Ashland Specialty Ingredients, Wayne, NJ), which consists of a ~28 μm thick active layer sandwiched between two ~125 μm matte polyester layers, as shown in Figure 2.7. Compared to its predecessors, EBT and EBT2 films, EBT3 film is constructed symmetrically, which eliminates any dependence in the film response due to which side is facing up when scanning the film. The matte polyester layers are specially treated to embed microscopic silica particles, ~5 μm in thickness.[34] The addition of the silica particles frustrates the formation of Newton's rings patterns on the film, which were a noticeable artifact in the older models of Gafchromic film. Newton's rings are interference patterns which occur due to constructive and destructive interference of light passing through two transparent surfaces

separated by a distance less than the magnitude of the wavelength of the light, and appear as dark and light bands in circular patterns in the scanned image. The two surfaces involved in their formation are the glass of the scanner bed, and the polyester layer of the film in contact with it. The addition of the silica particles creates a larger separation between the glass and the polyester layer (order of magnitude larger than the wavelength of light), thereby removing the possibility of light interference causing Newton's rings.[35]
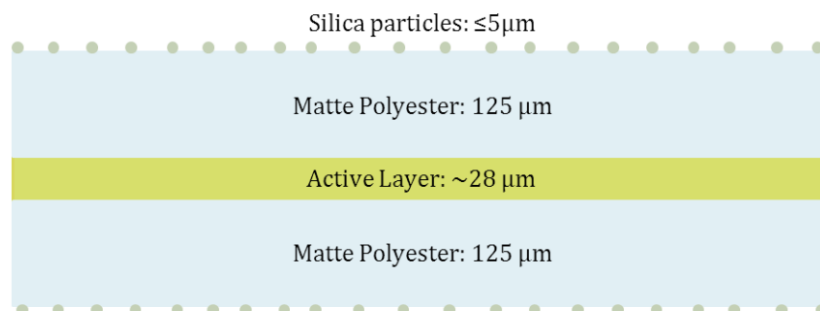
Figure 2.7 Structure of EBT3 Gafchromic film.

The active layer of the EBT model films consists of monomer diacetylene crystals, and differs from pre-EBT models of Gafchromic film (such as MD-55) due to the addition of lithium salt to the active monomer crystal, which is composed of pentacosa-10,12-dyinoic acid (PCDA), to form LiPCDA. This results in the crystals being organized in a more rod- or hair-like structure, which increases the sensitivity of the film, increases the initial polymerization rate, and decreases post-exposure darkening (faster stabilization).[36] However, it also makes the scanner response dependent on the film's orientation (portrait or landscape) due to anisotropic light scattering.[37–39] When exposed to radiation, the crystals undergo polymerization; the polymerized crystals are blue in colour and increase the optical density (OD) of the film.[40,41] The EBT2 and EBT3 film models also have a yellow dye added to the active layer and therefore after radiation exposure appear green in colour. The purpose of adding the yellow dye is to decrease the sensitivity of the film to ambient light and improve its uniformity.[37,42,43] The addition of lithium salt to the PCDA crystal, as well as other medium atomic number additives, makes the film have nearly water-equivalent response over a large range of x-ray beam energies (100 keV to 18

MeV), but work by Sutherland *et al.* suggests EBT-type films have non-unity absorbed dose and intrinsic energy responses at low energy (<100 keV).[44]

2.3.2 Film scanning

In general, film scanning (radiographic or radiochromic) can be done with a densitometer, however flatbed document scanners have gained significant popularity due to the lower cost and their suitability for scanning. Many scanning densitometers utilize lasers as a light source, which provide coherent and polarized light, both of which create two kinds of artifacts in the scanned image: non-reproducible interference patterns, and spreading of transmitted light in regions of high OD gradients (rapidly changing OD's).[45] Although corrections can be made for these effects, flatbed scanners which use non-coherent broadband white light sources do not require them, and are generally simpler to use and more reliable for precise and reproducible measurements.[46]

When using a densitometer, direct OD measurements are made, whereas flatbed document scanners produce pixel value (PV) measurements. Flatbed scanners employ linear amplifiers, whereas densitometers employ logarithmic amplifiers, such that the raw output of transmission flatbed scanners is approximately proportional to the optical fluence exiting the film and incident on the detector, which gives the measured PV. The PV will be some number smaller than the maximum PV (determined by the bit depth of the scanner) as the amount of light will be reduced after passing through the film piece. A measured PV can be converted to an effective OD value for the purpose of film calibration via:

$$OD = -\log_{10} \frac{PV}{2^b - 1} \tag{2.18}$$

where b is the bit depth of the scanned film image.

A commonly used flatbed document scanner is the Epson Expression 10000XL colour image scanner (Seiko Epson Corp., Nagano, Japan). The scanner can be operated in transmission or reflection mode, transmission mode requiring a transparency unit (separate scanner cover which contains a light source). It incorporates a Xenon gas cold cathode fluorescent lamp light source and a double-row three colour charged-coupled device (CCD) array detector, with a maximum resolution of 2400 dpi, a colour depth up to 48 bits (16 bits per colour channel), and

the capability to read a maximum OD of 3.8. The three colour CCD detector results in images composed of three colour channels: red, green, and blue.

Though generally easy to use, inexpensive, and fast, flatbed scanners require carefully developed and precisely implemented protocols. Sources of noise and artifacts present when using flatbed scanners include electronic warm-up, film orientation, and film placement (lateral scanning artifacts). The former two are controlled and minimized by using consistent scanning protocols, while the latter usually requires some form of correction. Lateral scanning artifacts include cross talk, optical path length, and polarization, all of which depend on the scanner construction and type of film. The most significant of these is light polarization due to anisotropic light scattering in the film and the scanner's optical mirror system, the magnitude of which will differ for each colour channel.[47] These effects are minimized by using the central portion of the scanner, orienting film pieces precisely (film rotation of 0°), and by correcting for residual film scanning artifacts.

2.3.3   Film dosimetry methods

Many different methods have been developed for radiochromic film dosimetry, all of which have strengths and weaknesses. Early work with radiochromic film involved performing a double-exposure, first to a known dose, and then to the unknown dose to help correct for film heterogeneities,[48] but these methods have been found to add noise and uncertainty to the film measurements.[49]

When Gafchromic film is manufactured, small variations in the thickness of the active layer occur, which lead to variations in measured dose values. To mitigate this, a variety of film heterogeneity correction methods have been developed, including those utilizing pre- and post-irradiation scans (netOD methods),[46,50–52] many different dose perturbation correction methods of varying complexity (multi-channel methods),[34,53–59] and other methods,[60,61] all of which aim to correct for film thickness variations as well as scanner/film artifacts.

2.3.3.1   netOD methods

The net optical density (netOD) method is extensively described by Devic *et al.*[46] This method of film dosimetry involves pre-scanning all film pieces and determining the change in OD between the pre- and post-irradiated films. When measuring netOD, an average un-irradiated OD value is

subtracted from the irradiated OD values, or registration of the pre- and post-irradiated images is performed such that the un-irradiated OD values are subtracted from the irradiated OD values on a pixel-by-pixel basis, which can be difficult and lead to errors if the films are not scanned in the same area of the scanner, or if they are not well aligned. This method does not account for scan-to-scan variations in the scanner, however, if done properly it accounts for heterogeneity effects of the film due to variations in film thickness and manufacturing and includes an explicit background correction. Due to the linear nature of the amplifiers, when creating calibration curves using netOD the relationship between dose and netOD is not linear as it would be (or nearly so) when using a densitometer; so the typical method for film calibration is to fit a polynomial function to the data to relate measured netOD to dose.[46,62–64]

Above a delivered dose of 4–5 Gy, due to the increasingly non-linear response of the film, fitted polynomial functions can oscillate between data points, which does not physically represent the response of the film to radiation.[34] Film corrections are generally OD dependent, therefore this method will correct well at the dose level of the pre-irradiation scan, which is a blank un-irradiated film (0 Gy), and only correct for some artifacts at other dose levels.[56] Though the netOD method can provide highly accurate dosimetric measurements at moderate doses, these issues as well as the more complicated scanning procedure requiring pre- and post-irradiation scans indicate potential advantages for alternative scanning and dosimetry methods.

2.3.3.2 Triple-channel correction methods

A multitude of dose perturbation correction methods (typically classified as multi-channel methods) exist. The focus here will be on the triple-channel heterogeneity correction method described by the EBT film manufacturer.[34]

For film calibration, this method proposes the use of rational functions to relate dose to measured pixel value (PV), as they were found to represent the characteristics of the film well over a wide dose range. One of the advantages of using a rational function instead of a polynomial to model film dose response is that the parameters in the fitted function can be determined with as few as 4 data points, allowing for efficient calibrations without dozens of dose levels.[34]

The rational functions are also easily inverted, which is beneficial when performing multi-channel heterogeneity correction using all three colour (red-green-blue; RGB) channels (triple-

channel dosimetry) to separate and remove the dose-independent components of the film images, leaving an image that ideally is solely dependent on the absorbed dose.[53]

In general, the triple-channel method utilizes a disturbance value, Δd, in the dose equation which is solved for on a pixel-by-pixel basis such that the differences in the doses calculated from any pair of color channels is minimized.[53] The disturbance value attempts to remove/negate the dose-independent perturbations affecting the measured optical density. The dose-independent components include film active layer non-uniformities and artifacts due to non-uniform scanner output (e.g. noise, lateral scanner artifacts and dust),[53,56] while the dose-dependent component is represented by the calibration of each colour channel where larger areas of film are averaged to minimize or eliminate any variations caused by the dose-independent responses. Triple-channel correction methods have also been found to minimize the effects of lateral scanning artifacts due to non-centrally placed films or wide pieces of film occupying more than the central few centimeters of the scanner.[53,58,59]

The triple-channel method has been found to produce results equivalent to the more conventional netOD method, with a simplified scanning procedure and reduced potential sources of uncertainty arising from image manipulation and noise amplification when subtracting the two images from each other.[56,65] However, it does not correct well for artifacts introduced during film scanning such as fingerprints or dust, and the goodness of curve fitting worsens over larger dose ranges.[56]

2.3.3.3 Other film dosimetry methods

Many other methods have also been studied which use variations of the aforementioned methods. Brown *et al.*[61] converted red channel PVs to "real ODs" using a fifth-order polynomial calibration curve obtained from scanning a NIST calibrated Tiffen Transmission Photographic Step Tablet (The Tiffen Company, Rochester, NY), followed by conversion to netODs. The netODs were then related to dose using a rational function similar to those used by the film manufacturer, and the calibration curve fitting was done using a non-weighted least squares method. Single channel methods without the inclusion of a pre-irradiated film scan have also been investigated in which the measured ODs from the red channel PVs are directly related to dose.[56,66] However, large inaccuracies were found when no corrections were made for film heterogeneities by either the inclusion of a pre-irradiated film scan or the use of a multi-channel

method. Other methods have also been proposed which use the ratio of two colour channels to correct for film heterogeneities,[42,50,54,67] or different colour channels for different dose levels in order to extend the sensitive dose range of the film.[63,68] However, as noted by Mayer *et al.*[54] these methods have yielded partially conflicting results, as some studies found improvements using certain multi-channel methods while others found the same methods degraded results.

2.4 Uncertainties in brachytherapy dosimetry

A recent endeavor in brachytherapy dosimetry has been to standardize the method of reporting uncertainties as described in the joint AAPM and Groupe Européen de Curiethérapie–European SocieTy for Radiotherapy and Oncology (GEC-ESTRO) documents.[69,70] This includes: classifying reported uncertainties as Type A or Type B; distinguishing between variations, uncertainties, and errors or mistakes; using appropriate coverage factors; determining the influence of any measured uncertainties on the absorbed dose for clinically-relevant dose parameters; and following methods in the International Standards Organization *Guide to the expression of Uncertainty in Measurement* (GUM) document and the NIST Technical Note 1297, *Guidelines for Evaluating and Expressing the Uncertainty of NIST Measurements Results*.[71,72]

2.4.1 General uncertainty analysis theory

When presenting measurement uncertainties, components of uncertainty can be classified in two different categories: Type A and Type B. Type A uncertainties are those evaluated by statistical means, for example calculating the standard deviation of the mean of a series of independent observations. Type B uncertainties are those evaluated "by other means" (non-statistical uncertainties). This may include previous measurement data, scientific judgement, experience with the behaviour and properties of relevant materials and instruments, manufacturer's specifications, data provided in calibration and other reports, and uncertainties assigned to reference data taken from handbooks.[72]

The combined standard uncertainty, u_c, represents the standard deviation of a measurement result dependent on other values, all or some of which also have associated standard uncertainties. For a quantity Y determined from N quantities $x_1, x_2,..., x_N$ through a functional relation f:

$$Y = f(x_1, x_2, \dots, x_N) \tag{2.19}$$

the combined standard uncertainty of the measurement result, given by $u_c(y)$ (or σ_Y), is taken to represent the estimated standard deviation of the result, and is the positive square root of the estimated variance $u_c^2(y)$ obtained from:

$$u_c^2(y) = \sum_{i=1}^{N} \left(\frac{\partial f}{\partial x_i}\right)^2 u^2(x_i) + 2 \sum_{i=1}^{N-1} \sum_{j=i+1}^{N} \frac{\partial f}{\partial x_i} \frac{\partial f}{\partial x_j} u(x_i, x_j) \tag{2.20}$$

This is based on a first-order Taylor series approximation of $Y = f(x_1, x_2, \dots, x_N)$ and is referred to as the *law of propagation of uncertainty*. The partial derivatives, $\partial f / \partial x_i$, are referred to as the sensitivity coefficients, $u(x_i)$ is the standard uncertainty associated with the input estimate x_i, and $u(x_i, x_j)$ is the estimated covariance associated with x_i, and x_j. For uncorrelated quantities (all input quantities are independent), $u(x_i, x_j)$ is equal to 0. The combined uncertainty for uncorrelated quantities is therefore:

$$u_c(y) = \sigma_Y = \sqrt{\left(\frac{\partial Y}{\partial x_1}\right)^2 \sigma_{x_1}^2 + \left(\frac{\partial Y}{\partial x_2}\right)^2 \sigma_{x_2}^2 + \dots + \left(\frac{\partial Y}{\partial x_N}\right)^2 \sigma_{x_N}^2} \tag{2.21}$$

The TG-43U1 report expands on this by defining a relative uncertainty propagation factor, defined as:

$$\% \frac{\partial f}{\partial x} \equiv \frac{x}{Y} \frac{\partial Y}{\partial x} \tag{2.22}$$

The total combined percent uncertainty is then:

$$\begin{aligned}
\% \sigma_Y &= \sqrt{\left(\% \frac{\partial Y}{\partial x_1}\right)^2 \% \sigma_{x_1}^2 + \left(\% \frac{\partial Y}{\partial x_2}\right)^2 \% \sigma_{x_2}^2 + \dots + \left(\% \frac{\partial Y}{\partial x_N}\right)^2 \% \sigma_{x_N}^2} \\
&= \sqrt{\% \sigma_{Y|x_1}^2 + \% \sigma_{Y|x_2}^2 + \dots + \% \sigma_{Y|x_N}^2}
\end{aligned} \tag{2.23}$$

where $\% \sigma_{Y|x}$ is the percent standard deviation in Y, due to the uncertainty in the variable x.[13]

For the case where the measured quantity of interest is a simple product of measured or calculated quantities, the combined relative standard uncertainty, $\% u_c$, is calculated by taking the square root of the sum-of-squares of all the relative (%) uncertainties at each step of a measurement traceability chain (all type A and type B uncertainties):

$$\%u_c = \sqrt{(s_i^2 + u_j^2)} \qquad (2.24)$$

where s_i is equal to the relative (%) standard deviation of the mean of replicate/statistical measurements (type A), and u_j is the relative quadrature sum of all type B components of uncertainty.[69]

For normally distributed probability distributions, a measurement $y \pm u_c$ gives an interval within which the true value of y is believed to lie with a 68% level of confidence. For the true value to lie within a larger interval associated with a higher level of confidence, the uncertainty is expanded by multiplying u_c by a coverage factor, denoted by the symbol k. Typically the symbol U is used for expanded uncertainty, but due to the convention of using U for air-kerma strength, the symbol V is used for the expanded uncertainty for brachytherapy applications, thus $V = k \cdot u_c$. Again, when a normal distribution applies, a coverage factor k=2 defines an interval of confidence of ~95%, and k=3 an interval with a level of confidence >99%.

2.4.2 Sources of uncertainty in measurements, Monte Carlo simulations, and treatment planning calculations

2.4.2.1 Measurement uncertainties

All dosimetry measurements in brachytherapy are subject to common intrinsic uncertainties including source activity distribution, and source-to-detector positioning. Most sources are assumed to emit photons uniformly about the circumference of the long axis; however the majority exhibit some variation in the intensity of emissions about this axis due to variation in their activity distribution. This component becomes a systematic uncertainty and propagates to all dosimetric measurements. Intensity variations of 2-20% have been reported for NIST calibrations of low-energy photon emitting sources using the WAFAC chamber.[73] All experimental dosimetry set-ups will have source-to-detector positioning uncertainties, which depend on the nature of the dosimeter (geometry, effective point of measurement, size of sensitive region, etc.) as well as the measurement phantom material/design. Due to the fast dose-rate fall off with distance, the uncertainties may increase as source-to-detector spacing increases due to substantially lower dose-rates. Typically, solid phantoms are used to minimize geometric uncertainties in experimental dosimetry.

The most commonly used dosimeters for brachytherapy dose measurement have been LiF TLDs, radiochromic films, and diamond, diode, and metal-oxide-semiconductor field effect transistor (MOSFET) detectors. The accuracy of results obtained using these dosimeters is dependent on their individual component uncertainties associated with volume averaging, self-attenuation, and absorbed-dose sensitivity.[69] For TLDs, the major sources of uncertainty include the annealing regime and the intrinsic energy dependence. With careful use, an estimate of the overall expanded uncertainty for TLDs is 5.58% (k=2).[74] The main sources of uncertainty for Gafchromic film, also outlined in Section 2.3, include the uniformity of the active component, the accuracy and consistency of the scanning device and scanning procedure, and uncertainties due to handling procedures (exposure to UV light, or widely varying temperatures). For careful handling and scanning procedures, dosimetric uncertainties for film are estimated to be ~3-7% (k=1).[33,52,75] Uncertainties when using diode, diamond, and MOSFET detectors result from the large energy dependence of their absorbed-dose sensitivity, non-linearity, directional dependence, temperature dependence, and bias dependence. As a consequence, the total dosimetric uncertainty for these detectors can exceed 15% (k=1).[76]

2.4.2.2 *Monte Carlo simulation uncertainties*

Often for MC brachytherapy single source dosimetry studies, the only uncertainty reported is the Type A statistical tally uncertainty which decreases as more particles are simulated. This value is usually kept low; however there are many other uncertainties that need to be accounted for. In brachytherapy these include: source construction/geometry, source movable internal components, source emissions/photon spectrum, measurement phantom geometry and composition, radiation transport code physics models, interaction and scoring cross sections, and particle fluence/energy deposition scoring algorithms.

These uncertainties are generally fairly low, usually <1% each. However, the combined uncertainty for the dose rate at 1 cm on the transverse axis of low-energy seed sources has been found to be >1%, which is much larger than the typically stated <0.1% for Type A MC statistical uncertainties. More details are available in the TG-138 document,[69] and a thorough uncertainty analysis for MC derived brachytherapy dosimetry parameters appearing in the TG-43 dose calculation formalism is presented by Aryal *et al.*[77]

2.4.2.3 Uncertainties in TG-43 based treatment planning

Uncertainties in a TG-43 based dose calculation performed by a treatment planning system include uncertainties in each of the dosimetry parameters (air-kerma strength, dose-rate constant, geometry function, radial dose function, anisotropy factor, and any correction factors), as well as uncertainties in the interpolation/extrapolation scheme used by the planning system. Best practice uncertainties for a low-energy brachytherapy source TG-43 calculation are outlined in Table 2.2, following the methods described in the TG-138 document.[69] This uncertainty estimate assumes that the value of the source air-kerma strength obtained from the manufacturer's calibration certificate is used. The dose-rate constant uncertainty assumes that this parameter's value was determined as an average of measured and MC simulated values. Radial dose function and anisotropy factor uncertainties are those reported for MC derived values for low-energy sources (given proper accounting for the uncertainties described in Section 2.4.2.2). The geometry function is dependent on the length of the active component in the seed, L, and is used to determine the values of $g_L(r)$ and $F(r, \theta)$ as well as being included in the TG-43 dose calculation. Therefore, as long as a consistent value for L is used, the (artificial) decoupling of the TG-43 dosimetry parameters results in the geometry function cancelling out, and therefore having no associated uncertainty, i.e. $\%u_{G_L(r,\theta)} = 0$. Uncertainty in TPS interpolation/extrapolation occurs due to the (unavoidable) entry of sparse data into the TPS. Consequently, model fitting and interpolation are utilized, and the associated uncertainty relates to the quality of fit, the implementation of the calculation algorithm, calculation matrix spacing, and the calculation output mechanisms.

Table 2.2 Best practice dosimetric uncertainties for low-energy brachytherapy treatment planning calculations.

Source of uncertainty	Quantity (units)	Relative uncertainty (%)
NIST WAFAC calibration	$S_{K,NIST}$ (U)	0.8
ADCL well ion chamber calibration	$S_{K,NIST}/I_{ADCL}$ (U/A)	0.5
ADCL calibration of source from manufacturer	$S_{K,ADCL}$ (U)	0.57
Dose-rate constant	Λ (Gy/U)	2.0
Radial dose function	$g_L(r)$	1.0
Anisotropy factor	$F(r,\theta)$	1.1
Geometry function	$G_L(r,\theta)$	-
TPS interpolation/extrapolation	-	3.8
Total combined uncertainty (k=1)		4.7
Expanded uncertainty (k=2)		9.4

2.4.3 Treatment site specific uncertainty analysis

Kirisits *et al.* provides example uncertainty estimates for several disease sites and indicates the necessity of similar analyses being performed for other sites or types of treatment, as few estimates are common among the various types of brachytherapy treatment.[70] Performing such an analysis at any given site is required to identify which elements of the treatment contribute most significantly to the overall uncertainty, as well as to determine where improvements can or need to be made to yield lower overall uncertainty in the delivered dose, which can potentially result in improved patient treatments and outcomes.

The uncertainties mentioned in Section 2.4.2.3 (associated with source strength and treatment planning) are generally common to all brachytherapy treatments (though low- and high-energy photon sources differ slightly). However, there are many other components of treatment uncertainty which vary in significance depending on the brachytherapy site and technique (HDR, PDR (pulsed dose rate), permanent implant, type of applicator, etc.), and are typically the largest uncertainty components. Other site specific uncertainty components include heterogeneity effects, positional accuracy, temporal accuracy, imaging inaccuracies, and patient level uncertainties.[70]

Heterogeneity uncertainties for low-energy brachytherapy include inter-seed attenuation, particularly for permanent prostate or partial breast irradiation treatments, differences in scatter

conditions due to finite patient geometry (compared to the assumption of an infinite homogeneous water medium to determine TG-43 parameters), differences in tissue composition and density relative to water (further described in Section 2.5.1), the presence of air-tissue interfaces, and the possible presence of high-Z materials including applicators and shields. Positional accuracies pertain to differences between planned and actual source positions during treatment. This includes the position of a source in an applicator as well as the position of the applicator inside the patient, or the final positions of sources in a patient if no applicator is used during treatment (permanent seed implants). Temporal accuracies include dwell time uncertainties, and transit dose for afterloader (HDR and PDR) based treatments. Imaging uncertainties include variability in anatomical structure contouring (OAR's or PTV/GTV [gross tumour volume]), which can lead to uncertainties in dose calculations, as well as source positioning/placement if using image guidance. Patient level uncertainties are largely dependent on the site/type of treatment and include applicator stability, inter-fraction variations (tumour shrinkage, organ movement), and edema following percutaneous or surgical implantation of seeds.

The various uncertainties present within a particular treatment procedure are often used to determine the size of treatment margin required, to inform the need for post procedure assessment, or to decide if additional considerations are warranted to mitigate specific sources of uncertainty or error. For example, prostate permanent seed implants make use of post-implant imaging and dose planning to account for seed placement/movement uncertainties and to some extent, tissue edema.[78] The specific uncertainties most affecting the dosimetry and dose delivery for ocular brachytherapy are, as of yet, not thoroughly quantified. The work performed in Chapter 5 includes a comprehensive and systematic uncertainty analysis of the delivered dose at the prescription point for ocular brachytherapy to determine an adequate treatment margin. The analysis presents an objective means to identify which component uncertainties are contributing most significantly and determine how they can be minimized.

2.5 Model-based dose calculation algorithms

Model-based dose calculation algorithms (MBDCAs) move away from the water-based calculation approach used by the TG-43 method by taking into account and modelling radiation transport in non-water media (tissues, applicators, air-tissue interfaces). This can result in much

more accurate doses for patient treatment planning, particularly in scenarios where applicators, tissue heterogeneities, and scattering conditions are found to affect the dosimetry.[10] This section therefore looks at the second constituent of heterogeneous dose calculations for ocular brachytherapy, this being the heterogeneity of patient tissues.

2.5.1 Heterogeneity effects for low-energy photons

Mass attenuation (μ/ρ) and mass energy absorption (μ_{en}/ρ) coefficients for various human tissues are comparable to those of water for photon energies above ~200 keV, however at lower energies there are large differences between different tissue compositions, as seen in Figure 2.8. These differences are also observed for tissues within the eye (Figure 2.9), where variations of up to ±10% are seen at the photon energies of interest for ocular brachytherapy.
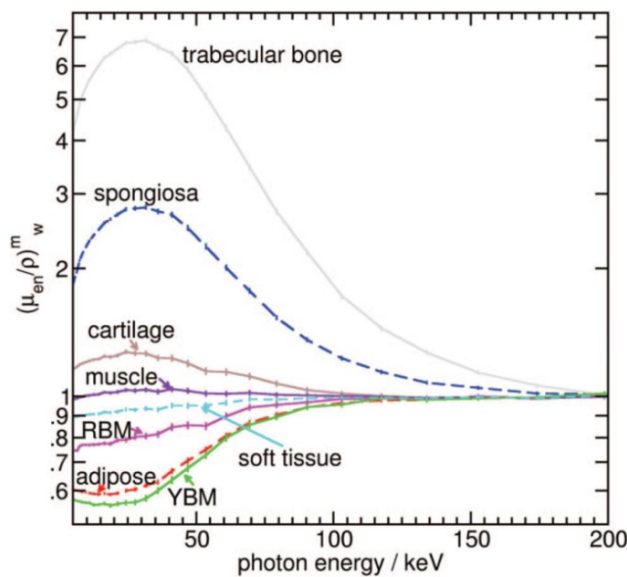
Figure 2.8 Mass energy absorption coefficients relative to water for a number of biological tissues for energies from 5 to 200 keV (values calculated with the EGSnrc user-code 'g'). (Figure reproduced from L. Beaulieu, *et al.*, "Report of the Task Group 186 on model-based dose calculation methods in brachytherapy beyond the TG-43 formalism: Current status and recommendations for clinical implementation," Med. Phys. **39**, 6208–6236 (2012)[79] with permission from John Wiley and Sons and the American Association of Physicists in Medicine).
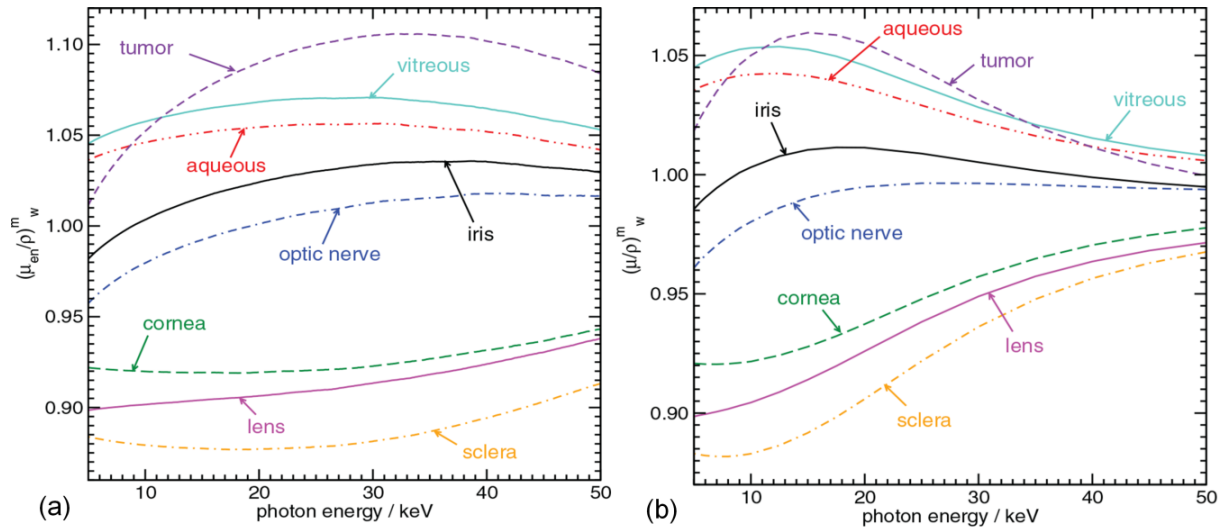
Figure 2.9 Ratios of mass energy absorption coefficients (a) and mass attenuation coefficients (b) for eye tissues relative to those of water for 5-50 keV photon energies. (Figure reproduced from Lesperance *et al.*, "Model-based dose calculations for COMS eye plaque brachytherapy using an anatomically realistic eye phantom," Med. Phys. **41**, 021717 (12 pp.) (2014)[80] with permission from John Wiley and Sons and the American Association of Physicists in Medicine).

An important aspect of clinical dose calculation is therefore also choosing the dose reporting medium. When model-based calculations are available, the possible reporting schemes are: $D_{w,w-\text{TG-43}}$, $D_{w,w/appl/air}$, $D_{m,m}$, and $D_{w,m}$, where the first index indicates the dose deposition medium, and the second index refers to the photon transport medium. Thus $D_{w,w-\text{TG-43}}$ indicates photon transport through unbounded water medium, and reporting dose to water (TG-43 method); any non-water materials (applicators, air interfaces, patient tissues) are not considered. $D_{w,w/appl/air}$ is an absorbed dose-to-water calculation, and accounts for the geometries, compositions and densities of applicators, sources, and air-tissue interfaces, but assumes that all patient tissues are water equivalent. (This is essentially the dose reporting method used by Plaque Simulator, however it relies on pre-calculated applicator correction factors and 1D ray tracing through the Silastic material and is therefore a semi-empirical approach, and not a true MBDCA). $D_{m,m}$ accounts for all non-water tissue/applicator compositions and densities, and reports dose to the local medium. $D_{w,m}$ is similar to $D_{m,m}$ but the dose to medium is converted to dose to water using cavity theory.[79]

For high energy brachytherapy sources, Bragg-Gray (small) cavity theory can be used to convert from dose to medium to dose to water, and differences between these doses are typically found to be very small (a few percent). For low-energy brachytherapy sources, it is unclear whether either the small-cavity or large-cavity regime applies, as the size of the target and the range of secondary charged particles can be comparable, depending on the choice of target.

Assuming large cavity theory (targets are macroscopic), the dose to a target, D_{targ}, made of water is found by:

$$D_{targ}(r) \approx K_{w,m}^{coll}(r) = \overline{(\mu_{en}(r)/\rho)}_m^w \, K_{m,m}^{coll}(r) = \overline{(\mu_{en}(r)/\rho)}_m^w D_{m,m}(r) \qquad (2.25)$$

This assumes that the target is large in comparison to the secondary electron ranges. This is the case for most planning system calculations that use ~mm sized calculation voxels. Due to the large variations in mass attenuation coefficients $(\mu_{en}(r)/\rho)$ for different tissues relative to water for low energy photons, values of dose to water can differ significantly from those for dose to medium.[81]

Assuming small cavity theory (targets are cellular or subcellular size), dose to a water target is found by:

$$D_{targ}(r) \approx D_{w,m}(r) = \left(\overline{\overline{S_{col}}(r)/\rho}\right)_m^w D_{m,m}(r) = \left(\overline{\overline{S_{col}}(r)/\rho}\right)_m^w K_{m,m}^{coll}(r) \qquad (2.26)$$

Here $\left(\overline{\overline{S_{col}}(r)/\rho}\right)_m^w$, the energy averaged mass collisional stopping power, deviates from unity by only a few percent for soft tissues. However, cellular or subcellular targets contain significant mass fractions of proteins, inorganic elements, and lipids, so reporting dose to water may not best represent the target medium. It is unclear how $D_{w,m}$ relates to $D_{m,m}$ for low-energy brachytherapy, and which dose metric better tracks D_{targ}. The current recommendation is to report $D_{m,m}$ as it is conceptually well-defined, whereas $D_{w,m}$ is a theoretical construct and converting to it likely introduces additional uncertainties.[79]

2.5.2 Overview of model-based dose calculation methods

To take non-water-equivalent applicator materials into consideration, simple one-dimensional methods have been used to correct the primary dose for the presence of the applicator based on its "effective attenuation". These methods modify the primary dose contribution, but not the scatter dose which depends on the 3D spatial distribution of heterogeneities present in the

irradiated volume.[79] They also do not account for the heterogeneous tissues present within the patient. More advanced dose calculation methods, a number of which exist and are briefly described here, attempt to account for the various sources of heterogeneity present in the irradiation volume. The goal of any of these methods is to accurately model the stochastic process of radiation transport though matter.

MC methods arrive at a stochastic solution to the Linear Boltzmann transport equation (LBTE) by random sampling from the probability distributions of physical processes underlying photon transport, given a set of input parameters (geometry, materials, and cross-sections) (more details in Section 2.5.3). Several different MC packages (PTRAN, MCNPX, Penelope, EGSnrc, Geant4) have been used for brachytherapy, primarily to determine high-quality single source TG-43 parameter data. In support of brachytherapy treatment planning, several MC-based user codes have been created including MCPI;[82] BrachyDose[83,84] and the recently developed egs_brachy (both EGSnrc based);[85] ALGEBRA (Geant4 based);[86] and BrachyGUI (PTRAN based);[87] as well as user codes which interface with MCNP6 (BrachyGuide and AMIGOBrachy).[88,89]

LBTE solvers use deterministic approaches to construct an approximate solution to the LBTE by systematically discretizing spatial, angular and energy variables. This results in a linear system of equations which can be solved iteratively. As the methods rely on phase-space discretization, they are categorized as grid-based Boltzmann solvers (GBBSs).

For a volume, V, with time-integrated particle radiance $\Phi_{\Omega,E}(\mathbf{r}, E, \widehat{\Omega})$ ($\Phi_{\Omega,E} = d\Phi/d\Omega dE$, and $\Phi = dN/dA$ is the particle fluence), position $\mathbf{r}$, direction $\widehat{\Omega}$, and energy E, the LBTE, along with vacuum boundary conditions is:

$$\widehat{\Omega} \cdot \nabla \Phi_{\Omega,E}(\mathbf{r}, E, \widehat{\Omega}) = Q_{sc}(\mathbf{r}, E, \widehat{\Omega}) + \frac{Q_{prim}(E, \widehat{\Omega})}{4\pi} \delta(\mathbf{r} - \mathbf{r}_p) - \sigma_t(\mathbf{r}, E) \Phi_{\Omega,E}(\mathbf{r}, E, \widehat{\Omega}) \quad (2.27)$$

where $Q_{prim}/4\pi$ is the number of photons per solid angle emitted from a point source at position $\mathbf{r}_p$, σ_t is the macroscopic total cross-section, and Q_{sc} is the photon scattering source. Primary scatter separation (PSS) can be employed, where $\Phi_{\Omega,E} = \Phi_{\Omega,E}^{prim} + \Phi_{\Omega,E}^{sc}$, such that:

$$\hat{\Omega} \cdot \nabla \Phi_{\Omega,E}^{prim} = \frac{Q_{prim}(E,\hat{\Omega})}{4\pi} \delta(\boldsymbol{r} - \boldsymbol{r}_p) - \sigma_t(\boldsymbol{r},E)\Phi_{\Omega,E}^{prim} \tag{2.28}$$

$$\hat{\Omega} \cdot \nabla \Phi_{\Omega,E}^{sc} = Q_{sc} - \sigma_t(\boldsymbol{r},E)\Phi_{\Omega,E}^{sc} \tag{2.29}$$

The primary dose can be calculated analytically, and the scattering source (Q_{sc}) is solved numerically using finite difference methods. For brachytherapy planning, this method is employed by Acuros, a radiation-therapy specific code available as an option in the BrachyVision TPS (Varian Medical Systems, Palo Alto, CA). The Acuros implementation, currently limited to Ir-192 sources, uses a third-order linear discontinuous finite-element method for spatial discretization, discrete-ordinates for angular discretization, and multi-group approximations for energy discretization.[79,90,91]

Superposition/convolution methods are based on superimposing the energy distribution released by a group of photons using a kernel to describe the dose distribution around the site of interaction. Dose deposition kernels are initially generated using MC simulations in a homogeneous water medium, and ray-tracing is used to scale the kernels when calculating radiation transport though non-water media along a photon's path from the source to the point of interest. The collapsed-cone (CC) algorithm improves the calculation speed by "collapsing" the transport of energy released onto cone axes (defined by angular discretization) along a radiation transport grid. For brachytherapy planning purposes, the CC algorithm is integrated in the Oncentra® Brachy (OcB) TPS (Elekta AB, Stockholm, SE) under the name ACE (Advanced Collapsed cone Engine). It currently supports dose calculation for both Ir-192 and Co-60 HDR sources.[92] More details on this calculation method are given in Section 2.5.4.

2.5.3 Monte Carlo method for radiation transport

2.5.3.1 General theory

MC methods for radiation transport are a stochastic alternative to solving the LBTE, relying on the central limit theorem and the law of large numbers. The fundamental elements used for MC simulation of radiation transport are a random number generator, a set of routines for sampling the probability distributions of the physical processes describing particle transport, and a set of input data.[91]

For a given random variable, x, there is an associated probability density function describing the likelihood of each value occurring, given by $p(x)$, which describes the probability of x being between x and $x+dx$, and the integral of $p(x)$ over the domain of x is equal to 1. The probability of x being less than or equal to x' is given by the cumulative distribution function (CDF):

$$P(x') = \int_{-\infty}^{x'} p(x)dx \tag{2.30}$$

The distribution of values of x therefore has an expectation value (or average value) given by:

$$E(x) = \bar{x} = \langle x \rangle = \int_{-\infty}^{\infty} xp(x)dx \tag{2.31}$$

and a variance given by:

$$Var(x) = \langle (x - \langle x \rangle)^2 \rangle = \langle x^2 \rangle - \langle x \rangle^2 \tag{2.32}$$

The standard deviation is equal to the square root of the variance, $\sigma = \sqrt{Var(x)}$.[91]

Given a distribution of x values defined by the probability distribution $p(x)$, if a number N of independent samples of x (x_1, x_2, x_3, etc.) are chosen, then according to the law of large numbers, as N increases, the arithmetic mean of these values tends towards the expectation value of x. According to the central limit theorem, if these N values of x are randomly selected from its probability distribution, the values will be normally distributed. This can be described as:

$$Pr\left(-\frac{\sigma}{\sqrt{N}} < \frac{1}{N}\sum_{i=1}^{N} x_i - \langle x \rangle < \frac{\sigma}{\sqrt{N}}\right) \tag{2.33}$$

which is the probability of the values of x_i being within one standard deviation of the expectation value. This illustrates that as N increases, the spread (σ) of values of x_i decreases and the probability of the average value of the samples being close to the expectation value increases. This is the basic principle behind the MC method and convergence to the desired solution to the LBTE.

Sampling from a probability distribution is done by using a random number generator (in reality a "pseudo" random number generator) and sampling from the CDF. Assuming the CDF is invertible, the random number, r, chosen between 0 and 1, can be used to sample a value of x from it:

$$r = P(x) = \int_a^x p(x')dx' \tag{2.34}$$

The tools are now in place to simulate the "life" of a photon for radiation transport. Given a source of photons, the first step is to determine the direction of the emitted photon (as well as its energy if the source is not monoenergetic), which is done by randomly sampling the CDFs describing each quantity (angular direction and energy). Once this is determined, the next step is to randomly sample the site of the first interaction (step-length the photon will travel before interacting). This is done based on the attenuation coefficient of the photon, given its energy and the medium in which it is travelling:

$$r = P(x) = \int_0^x \mu \exp(-\mu x')dx' = -\exp(-\mu x) + 1 \tag{2.35}$$

which is then inverted to determine x. To determine what type of interaction occurs, which is a discrete event, another random number is used to sample among the relative probabilities of each type of possible interaction, based on their interaction cross-sections. If, for example, the type of interaction selected is Compton scattering, additional random numbers would be used along with the differential cross-section to determine the energy lost by the photon, the new direction it is travelling, and the step-length to the next interaction site. This process assumes that photon transport is modelled as a Markov process (the probability of a given state depends only on the immediately preceding state), and continues until the photon is either photo-electrically absorbed or escapes the boundary of the simulation geometry. The energy lost by the photon at each step is recorded, and the process is then repeated for another photon emitted by the source. Following the basic principles outlined above, the simulation is performed for a very large number of photons, and given accurate physics models, sampling methods, and geometry, will converge on the solution for fluence/energy deposition in the medium of interest.

2.5.3.2 MCNP6 code

This work makes use of the MCNP6 (Monte Carlo N-Particle) general purpose radiation transport code, which is the combination of MCNPX and MCNP5 plus many additional features.[93] The MCNP6 input follows a card structure, which includes cell, surface, and data cards. The simulation geometry is defined by the cell and surface cards using combinatorial geometry elements, in which cells are defined by the intersections, unions, and complements of regions bounded by first- and second-degree surfaces and fourth-degree elliptical tori, as well as

69

simple macrobodies (spheres, boxes, cylinders etc.). The geometry capabilities are further expanded by the use of repeated structures which utilize fill, universe, lattice, and cell translation cards. A single cell or a number of cells can be defined as belonging to a specific universe, which can then be placed within another cell using a fill card or repeated within a lattice structure. A universe can be designated to fill any number of other defined cells in the geometry, or can itself be filled with other defined universes. This facilitates the creation and use of complex geometries having many identical components, and the incorporation of structured and unstructured mesh geometries. The data cards include those specifying materials, physics processes, source characteristics, tally methods, problem termination criteria, and output controls.[94,95]

Incorporated photoatomic and photonuclear data tables are based on the Evaluated Nuclear Data File (ENDF) system and the Evaluated Photon Data Library (EPDL) from the National Nuclear Data Centre (NNDC).[96] The default cross-section library used in MCNP6 based on this data is the MCPLIB84 library. The physics models used in MCNP6 fall under two categories: simple and detailed. Simple physics is used for photon energies above 100 MeV and ignores Rayleigh scattering and fluorescent photon production. Detailed physics includes both of these processes, as well as Doppler broadening (broadening of the discrete Compton scattering energy at each angle into a continuous spectrum to account for the momentum distribution of the bound electron[76]) for more accurate Compton scattering modelling.

The physics modelling is further adjusted using the Mode card, which determines what types of particles will be transported (P=photon, E=electron, N=neutron). For applications in brachytherapy, due to the relatively short ranges of secondary electrons produced which are generally much smaller than the scoring regions of interest, it can be assumed that electrons deposit their energy locally (at the point they are created, through photoatomic interactions), and so do not need to be transported. This significantly reduces the computational time without affecting the accuracy of the results.[97] This simplification is invoked by using Mode P (photon transport only).

MCNP6 offers a number of different tally options. The ones used in this work are the *F4, *FMESH and F6 tallies, all of which are track-length estimators as opposed to analog estimators. Analog estimators record the energy deposited within a scoring region defined by the user only from photon interactions which occur within that volume, whereas track-length estimators score photon energy fluence and calculate absorbed dose by using mass energy absorption coefficients

(or equivalent). Each photon passing through the scoring region contributes to the track-length estimator score of photon fluence. This method gives an estimation of kerma, which for brachytherapy applications can be equated to dose. Similar to using Mode P, track-length estimators significantly reduce computation time as fewer photons can be simulated to achieve a given statistical uncertainty in the scoring tally value.

The *F4 and *FMESH tallies calculate the contribution to the energy fluence as the number of particle track-lengths per unit volume. Therefore, a photon with weight W, energy E, and track-length T within a volume V, will contribute WTE/V to the fluence within the cell. Given an energy and angular distribution of fluence, $\Phi(r, E, \Omega)$, the *F4 and *FMESH tallies calculate the cumulative fluence in a cell as:

$$^*F4 = \frac{1}{V} \int_V dV \int_E dE \int_{4\pi} d\Omega \, E\Phi(r, E, \Omega) \tag{2.36}$$

in units of MeV/cm^2. When using this tally to convert from energy fluence to kerma (and therefore dose), the tally must be multiplied by the cell's mass energy absorption coefficient (μ_{en}/ρ). This is done using the DE/DF cards (Dose Energy and Dose Function cards): a point-wise response function with energy bins (DE) and corresponding conversion values (DF). The *F4 tally is used for specific cells defined by the geometry, while the *FMESH tally overlays a mesh on top of the geometry with position and dimensions specified by the user. The F6 tally is an energy deposition tally, similar to the *F4 and *FMESH tallies, but with an energy-dependent multiplier. The F6 tally is calculated as:

$$F6 = \frac{\rho_a}{V\rho_m} \int_V dV \int_E dE \int_\Omega d\Omega H(E)\sigma_t(E)\Phi(r, E, \Omega) \tag{2.37}$$

where ρ_a and ρ_m are the atomic and mass densities, respectively, H(E) are heating numbers from the nuclear data tables (MeV per collision), and $\sigma_t(E)$ is the microscopic total cross-section in barns. The F6 tally has been found to be equivalent to the *F4 tally within <0.01% when appropriate μ_{en}/ρ values are specified for the same materials.[97] The units are MeV/g which can be converted to J/kg (Gy) using appropriate conversion factors.

The efficiency of simulations can be further improved through the use of phase space files. These files are created using the SSW (source surface write) card to record particles of the type specified by the user (P, E or N, or a combination of these) that cross selected geometric surfaces in specified directions. For a brachytherapy source, this would include all photons leaving the

71

exterior surfaces of the source encapsulation. The created phase-space file can then be used in a later simulation by including the SSR (source surface read) card, and indicating the new surfaces the stored photons will initiate from. The new and original surface geometries must match, but the entire source can be translated to a new position/orientation, and can be replicated at various locations. For I-125 sources, only about half of the photons initiated within the active volume actually exit the source encapsulation, therefore this method allows for an approximately two-fold increase in computational efficiency.

2.5.4 Point kernel superposition/convolution and collapsed-cone approximation

Superposition/convolution principles have a long history of successful use in EBRT,[98] but have only been used more recently for brachytherapy.[99–104] As mentioned previously, this method utilizes energy distributions characterized by a kernel to describe the dose deposition. The kernels are determined from MC simulations, and similarly to LBTE solvers use PSS to separate the components of dose, calculating primary dose analytically and scatter dose using convolution methods.[99,104]

For brachytherapy sources having energies below 700 keV, the contribution of multiply-scattered photons to total scatter dose becomes larger, which makes the conventional single-kernel superposition methods for calculating the scatter dose used in EBRT inadequate (Figure 2.10). Therefore a multiple-scattering or 'successive-scattering' superposition approach is used to improve the accuracy of the scatter dose calculations.[99] The basic method behind this approach will be described.
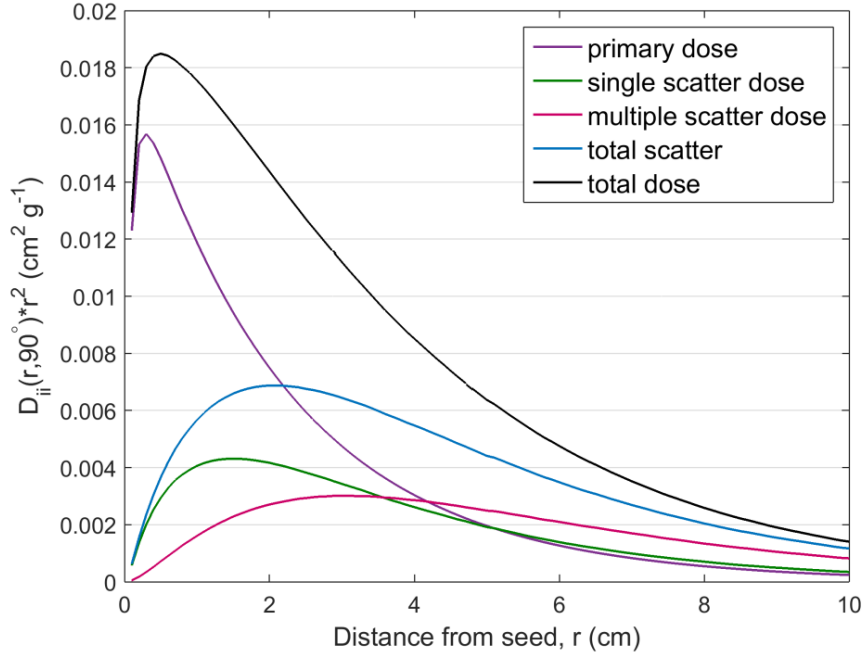
Figure 2.10 Primary scatter separated dose data per radiant energy (D$_{ii}$) multiplied by the radius squared along the transverse axis (θ=90°) for the Oncura model 6711 seed. (Data provided through private communication [R. Thomson].)

The total dose deposited, *D*, per unit of primary radiant energy, *R*, is calculated as:

$$\frac{D}{R} = \frac{D_p + D_{1sc} + D_{msc}}{R} \tag{2.38}$$

where D_p is the dose from primary photons, D_{1sc} is the dose from once scattered photons, and D_{msc} is the multiple-scatter dose from all higher order scattered photons.[105] The primary dose is calculated based on the assumption of CPE (to equate dose to collisional kerma), and is calculated as:

$$\frac{D_p(r)}{R} \cong \frac{K_{c,p}(r)}{R} = \frac{1}{4\pi r^2} \frac{\mu_{en}(r)}{\rho(r)} \exp\left(-\int_0^r \mu(l)dl\right) \tag{2.39}$$

This calculation applies a ray trace/density scaling along the path between the source and the point of dose calculation, ***r***.

The dose from first scattered photons is determined from the distribution of energy transferred from primary photons to first-scattered photons per unit mass, *S*, per unit radiant energy, and is called the 'scerma':

$$\frac{S_{1sc}(\mathbf{r})}{R} = \frac{1}{4\pi r^2} \frac{\mu(\mathbf{r}) - \mu_{en}(\mathbf{r})}{\rho(\mathbf{r})} \exp\left(-\int_0^r \mu(l) dl\right) = \frac{\mu - \mu_{en}}{\mu_{en}} \frac{D_p(\mathbf{r})}{R} \tag{2.40}$$

The first scattered dose is calculated through the convolution of the scerma with the first scattered point kernel, $\tilde{h}_{1sc}$, which describes the spatial distribution of first scattered dose around a primary photon interaction site, and is equal to:

$$\frac{D_{1sc}(\mathbf{r})}{R} = \iiint_V \frac{S_{1sc}(\mathbf{r}')}{R} \tilde{h}_{1sc}(\mathbf{r}', \theta) d^3 r' \tag{2.41}$$

The process is repeated for the multiply-scattered photons:

$$\frac{S_{msc}(\mathbf{r})}{R} = \frac{\bar{\mu}_{1sc} - \bar{\mu}_{en,1sc}}{\bar{\mu}_{en,1sc}} \cdot \frac{D_{1sc}(\mathbf{r})}{R} \tag{2.42}$$

$$\frac{D_{msc}(\mathbf{r})}{R} = \iiint_V \frac{S_{2sc}(\mathbf{r}')}{R} \tilde{H}_{msc}(\mathbf{r}', \theta) d^3 r' \tag{2.43}$$

where $\bar{\mu}_{1sc}$ and $\bar{\mu}_{en,1sc}$ are the spectrum averaged attenuation and energy absorption coefficients for once scattered photons, and $\tilde{H}_{msc}(\mathbf{r}, \theta)$ is the dose deposition kernel for multiple scattered photons. Each dose component is then added together to calculate the total dose per unit of radiant photon energy.

2.5.4.1 Application of the collapsed-cone superposition algorithm

Applying the CC superposition algorithm consists of implementing three main elements.[99,100,104,105] The first is the parameterization of the energy deposition kernels as exponentials over the square of the radius:

$$h_{1sc}(r, \theta) = \frac{B_\theta \cdot e^{-b_\theta \cdot r}}{r^2} \tag{2.44}$$

$$\tilde{H}_{msc}(r, \theta) = \frac{C_\theta \cdot e^{-C_\theta \cdot r} + F_\theta \cdot e^{-f_\theta \cdot r}}{r^2} \tag{2.45}$$

where B_θ, b_θ, C_θ, c_θ, F_θ, f_θ, are parameters fit to the MC derived kernel data for angles θ and distances r from the interaction site. The multiple scatter energy deposition kernel is expressed using bi-exponentials as the second scatter builds up third and fourth scatter and so on, yielding a build-up effect which is not well modeled if parameterized using a single exponential function.

The second element is discretizing the space around the point of energy transfer (point of photon interaction) into a set of cones whose axes are used as transport lines for radiant energy.

For each cone axis, parallel transport lines are arranged throughout the calculation volume so that each voxel is traversed by that cone axis direction.

The third element of the CC approximation is recursive transport of the energy released into a solid angle, $\Delta\Omega$, along the transport lines (cone axes), assuming energy is deposited only along the transport lines. This reduces the dose deposition kernels to the form:

$$\frac{B_\theta \cdot e^{-b_\theta \cdot r}}{r^2} \rightarrow B_\theta e^{-b_\theta \cdot r} \tag{2.46}$$

The energy is then transported recursively along the transport lines from one voxel to the next, which determines the radiant energy available at each step. This approach merges the calculation of both the energy released and the dose deposition into the same step, which helps improve the calculation efficiency.

Compared to a full superposition calculation, using the CC approximation significantly reduces the computation time from $t_{CPU} \sim N^6$ to $t_{CPU} \sim (M_{1sc} + M_{msc}) \cdot N^3$, where N is the number of voxels in the calculation volume, and M_{1sc} and M_{msc} are the number of cones used for first and multiple scatter dose calculations, respectively.[101] Using this algorithm, there is a tradeoff between computational speed and accuracy, which in practice is made by setting the size of the voxels in the calculation matrix and the number of cones/transport directions. The CC approximation is exact very close to a scattering event, as the dose calculation voxel size is larger than the cone opening area ($\Delta\Omega$). However, moving further away from the interaction site, the opening area will become larger than the voxel size, and as energy is only deposited on the cone axis, adjacent voxels contained in the opening area (but that do not contain the cone axis) will receive too little deposited energy. At the same time, voxels containing the cone axis will receive too much energy. This discretization error is known as the ray effect (see Figure 2.11), and is particularly noticeable for brachytherapy dose calculations due to the steep fluence gradients which create large differences in scerma in neighbouring voxels. The ray effect is not observed in EBRT as the scerma in adjacent voxels is similar in magnitude, and therefore these discretization errors tend to wash out.[104] Increasing the dose calculation voxel size or increasing the number of transport directions (M_{1sc} and M_{msc}) reduces the effect; the former decreases computation time while the latter increases it. However, increasing the voxel size results in more volume averaging. Therefore a compromise must be achieved between all of these elements which results in a sufficiently accurate dose calculation within a reasonable computation time.
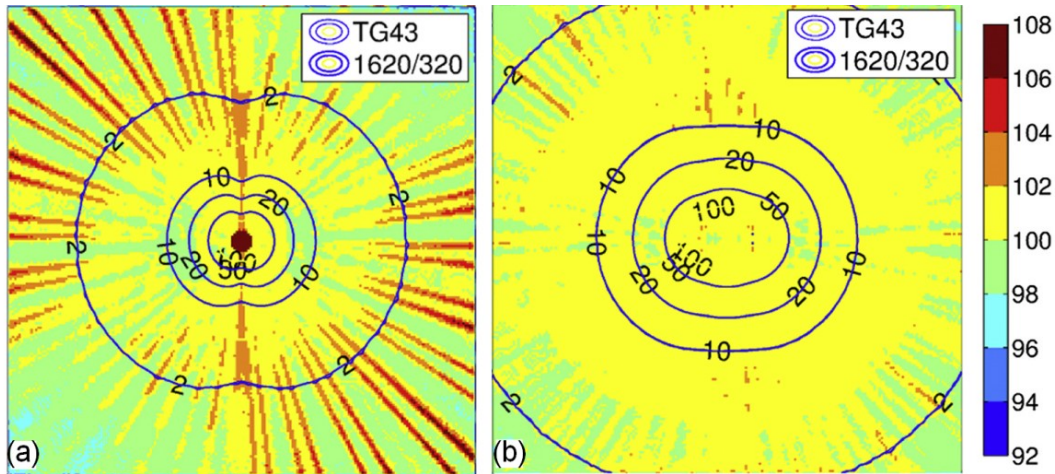
Figure 2.11 Percent dose ratio maps between CC and TG-43 calculated doses for a single dwell position (a), and 8 dwell positions (b) using 1620 and 320 cone axes/transport directions for the first and multiple scattered dose calculations (M_{1sc} and M_{msc}), respectively. Percent isodose lines are superimposed on the images. The ray effect tends to decrease with more cone axes, or with more sources where the overlapping doses wash out the ray artifacts. (Figure adapted from Y. Ma *et al.*, "Validation of the Oncentra Brachy Advanced Collapsed cone Engine for a commercial ^{192}Ir source using heterogeneous geometries," Brachytherapy, **14** 939–952 (2015)[106] with permission from Elsevier).

Adaptations to the original CC algorithm developed for EBRT to render it suitable for use in brachytherapy have been made for steep fluence gradients, scerma distribution very close to the source, beam divergence and kernel alignment/tilting, voxel averaging in the near zone of the source, and high Z applicators/shields.[100,104,105]

2.5.4.2 *Implementation in ACE*

As briefly mentioned in Section 2.5.2, for brachytherapy, the CC algorithm is implemented in the ACE algorithm in OcB. A research version of this software has been used for the work done here (Chapter 6). Although the commercial version of ACE is well described in a white paper[92] and recent journal article,[105] a few elements as specifically implemented in the research version will be described here, including the dose calculation margin and voxel sizes and CC tessellation (accuracy levels), applicator modelling, and material and density assignment.

The software has two accuracy levels, high and standard. Using the high accuracy mode increases the number of cone axes for both first and multiple scattered photons, and decreases the size of the dose calculation voxels; the values of these parameters also depend on the number of dwell positions in the plan. In addition to this, a variably-sized dose calculation grid is implemented in the software, based on bounding boxes and margin sizes, such that smaller calculation voxels are used closer to the source, and larger ones farther away. For the commercial version, the user cannot change the grid parameter values, and those given in the white paper are used by default (the user can only select either high or standard accuracy mode). The research version gives the user the capability to choose the values for all of the above parameters, down to a minimum dose calculation voxel size of 0.1 mm^3 and a maximum number of cone axes of 1620 for both first and residual scatter dose calculations.

The (virtual) applicators available in the OcB software applicator library are tessellated models of 3D CAD (computer-aided drafting) representations, with catheter lines drawn along the source paths. For applicators which contain high Z materials (metals), corrections are made for both intra-voxel presence and dose kernel scaling. For primary dose calculations, each radiation transport step is checked for the presence of tessellation triangles of the applicator, and if present, the step is subdivided and the radiological path length is adjusted for the materials encountered along each sub-step. For scatter dose calculations, the partial volume of an applicator within a voxel is estimated and used to correct the radiation transport.

Material assignments are performed via anatomical structure contouring in the CT images and choosing a material from the ACE material library; if no material is chosen the CT voxel is assumed to contain water. In EBRT, CT/HU numbers are used to calculate electron density, which is adequate for dose calculation in the photon energy regime where Compton scattering dominates, as the Compton interaction cross-section is proportional to the electron density. However, for low-energy brachytherapy, knowledge of both the tissue mass density and atomic number are necessary due to the increased probability of photoelectric absorption. Possible emergent solutions for obtaining these tissue properties involve using dual-energy or spectral CT, but at present the recommended method is to use consensus material definitions.[79,107] The density can then be chosen to be uniform based on the material assigned from the material library, or variable based on the HU values from the CT image. The clinical version of the software implements a standard method of converting from HU to material mass density by first

converting HU to electron density (ρ_{elec}) using a formula from Knöös *et al.*,[108] then converting to mass density based on linear interpolation of tabulated data from a reference CT calibration. The research version, however, allows the user to incorporate their own CT calibration curve to convert directly from HU to mass density.

2.6 References

[1] *NUDAT 2.6, National Nuclear Data Centre, Brookhaven National Laboratory*, (URL: http://www.nndc.bnl.gov/chart/decaysearchdirect.jsp?nuc=125I&unc=nds). Last accessed January 24, 2017.

[2] S.M. Seltzer, P.J. Lamperti, M.G. Mitch, J.T. Weaver, and B.M. Coursey, "New National Air-Kerma-Strength Standards for ^{125}I and [103]Pd Brachytherapy Seeds," J. Res. Natl. Inst. Stand. Technol. **108**, 337–358 (2003).

[3] J. Usher-Moga, S.M. Beach, and L.A. DeWerd, "Spectroscopic output of ^{125}I and [103]Pd low dose rate brachytherapy sources," Med. Phys. **36**, 270–278 (2009).

[4] F.H. Attix, *Introduction to Radiological Physics and Radiation Dosimetry*, 2nd Ed. (Wiley-VCH Verlag GmbH & Co. KGaA, Weinheim, 2004).

[5] H.E. Johns and J.R. Cunningham, *The physics of radiology*, 4th Ed. (Charles C Thomas, Springfield, IL, IL, 1983).

[6] M.J. Berger and J.H. Hubbell, "XCOM: Photon cross sections on a personal computer," in *Report NBSIR87-3597* (National Institute of Standards Technology (NIST), Gaithersburg, MD, 1987).

[7] M.J. Berger, J.S. Coursey, M.A. Zucker, and J. Chang, *ESTAR, PSTAR, and ASTAR: Computer programs for calculating stopping-power and range tables for electrons, protons, and helium ions (version 1.2.3, online)* (National Institute of Standards and Technology, Gaithersburg, MD, 2005) (available URL: http://physics.nist.gov/Star).

[8] F. Ballester, D. Granero, J. Pérez-Calatayud, C.S. Melhus, and M.J. Rivard, "Evaluation of high-energy brachytherapy source electronic disequilibrium and dose from emitted electrons," Med. Phys. **36**, 4250–4256 (2009).

[9] J.F. Williamson, H. Perera, and Z. Li, "Comparison of calculated and measured heterogeneity correction factors of ^{125}I, ^{137}Cs, and ^{192}Ir brachytherapy sources near localized heterogeneities," Med. Phys. **20**, 209–222 (1992).

[10] M.J. Rivard, J.L.M. Venselaar, and L. Beaulieu, "The evolution of brachytherapy treatment planning," Med. Phys. **36**, 2136–2153 (2009).

[11] G. Landry, M.J. Rivard, J.F. Williamson, and F. Verhaegen, "Monte Carlo Methods and Applications for Brachytherapy Dosimetry and Treatment Planning," in *Monte Carlo Techniques in Radiation Therapy*, edited by J. Seco and F. Verhaegen (Taylor & Francis Group, LLC, Boca Raton, FL, 2013), pp. 125–143.

[12] R. Nath, L.L. Anderson, G. Luxton, K.A. Weaver, J.F. Williamson, and A.S. Meigooni, "Dosimetry of interstitial brachytherapy sources: recommendations of the AAPM Radiation Therapy Committee Task Group No. 43. American Association of Physicists in Medicine," Med. Phys. **22**, 209–234 (1995).

[13] M.J. Rivard, B.M. Coursey, L.A. DeWerd, W.F. Hanson, M.S. Huq, G.S. Ibbott, M.G. Mitch, R. Nath, and J.F. Williamson, "Update of AAPM Task Group No. 43 Report: A revised AAPM protocol for brachytherapy dose calculations," Med. Phys. **31**, 633–674 (2004).

[14] M.J. Rivard, W.M. Butler, L.A. DeWerd, M.S. Huq, G.S. Ibbott, A.S. Meigooni, C.S. Melhus, M.G. Mitch, R. Nath, and J.F. Williamson, "Supplement to the 2004 update of the AAPM Task Group No. 43 Report," Med. Phys. **34**, 2187–2205 (2007).

[15] S.-T. Chiu-Tsao, M.A. Astrahan, P.T. Finger, D.S. Followill, A.S. Meigooni, C.S. Melhus, F. Mourtada, M.E. Napolitano, R. Nath, M.J. Rivard, D.W.O. Rogers, and R.M. Thomson, "Dosimetry of ^{125}I and ^{103}Pd COMS eye plaques for intraocular tumors: Report of Task Group 129 by the AAPM and ABS," Med. Phys. **39**, 6161–6184 (2012).

[16] Collaborative Ocular Melanoma Study Group, "COMS Manual of Procedures, Chapter 12: Radiation," in *COMS manual of procedures PB95-179693* (National Technical Information Service, Springfield, VA, 1995).

[17] R.W. Kline and J.D. Earle, "Implications of TG-43 for dose prescription and calculations for I-125 eye plaques," Med. Phys. **23**, 1054 (1996).

[18] S.K. Ray, R. Bhatnagar, W.F. Hartsell, and G.R. Desai, "Review of eye plaque dosimetry based on AAPM task group 43 recommendations," Int. J. Radiat. Oncol. Biol. Phys. **41**, 701–706 (1998).

[19] S. Nag, J.M. Quivey, J.D. Earle, D. Followill, J. Fontanesi, and P.T. Finger, "The American Brachytherapy Society recommendations for brachytherapy of uveal melanomas," Int. J. Radiat. Oncol. Biol. Phys. **56**, 544–555 (2003).

[20] The American Brachytherapy Society - Ophthalmic Oncology Task Force, "The American Brachytherapy Society consensus guidelines for plaque brachytherapy of uveal melanoma and retinoblastoma," Brachytherapy **13**, 1–14 (2014).

[21] S.-T. Chiu-Tsao, L.L. Anderson, K. O'Brien, L. Stabile, and J.C. Liu, "Dosimetry for ^{125}I seed (model 6711) in eye plaques," Med. Phys. **20**, 383–389 (1993).

[22] S.-T. Chiu-Tsao, L. Boulay, I. Kanna, A. de la Zerda, and J.H. Kim, "Dose distribution in the eye for ^{103}Pd seed in COMS eye plaque," Med. Phys. **22**, 923 (1995).

[23] A. de la Zerda, S.-T. Chiu-Tsao, J. Lin, L.L. Boulay, I. Kanna, J.H. Kim, and H.-S. Tsao, "^{125}I eye plaque dose distribution including penumbra characteristics," Med. Phys. **23**, 407–418 (1996).

[24] M.A. Astrahan, "Improved treatment planning for COMS eye plaques," Int. J. Radiat. Oncol. Biol. Phys. **61**, 1227–1242 (2005).

[25] A.L. Krintz, W.F. Hanson, G.S. Ibbott, and D.S. Followill, "A reanalysis of the Collaborative Ocular Melanoma Study Medium Tumor Trial eye plaque dosimetry," Int. J. Radiat. Oncol. Biol. Phys. **56**, 889–898 (2003).

[26] R.M. Thomson, R.E.P. Taylor, and D.W.O. Rogers, "Monte Carlo dosimetry for ^{125}I and ^{103}Pd eye plaque brachytherapy," Med. Phys. **35**, 5530 (2008).

[27] R.M. Thomson and D.W.O. Rogers, "Monte Carlo dosimetry for ^{125}I and ^{103}Pd eye plaque brachytherapy with various seed models," Med. Phys. **37**, 368–376 (2010).

[28] C.S. Melhus and M.J. Rivard, "COMS eye plaque brachytherapy dosimetry simulations for ^{103}Pd, ^{125}I, and ^{131}Cs," Med. Phys. **35**, 3364–3371 (2008).

[29] M.J. Rivard, S.-T. Chiu-Tsao, P.T. Finger, A.S. Meigooni, C.S. Melhus, F. Mourtada, M.E. Napolitano, D.W.O. Rogers, R.M. Thomson, and R. Nath, "Comparison of dose calculation methods for brachytherapy of intraocular tumors," Med. Phys. **38**, 306–316 (2011).

[30] M.A. Astrahan, G. Luxton, Q. Pu, and Z. Petrovich, "Conformal episcleral plaque therapy," Int. J. Radiat. Oncol. Biol. Phys. **39**, 505–519 (1997).

[31] G. Luxton, M.A. Astrahan, and Z. Petrovich, "Backscatter measurements from a single seed of ^{125}I for ophthalmic plaque dosimetry," Med. Phys. **15**, 397–400 (1988).

[32] H. Acar, S.-T. Chiu-Tsao, I. Ozbay, G. Kemikler, and S. Tuncer, "Evaluation of material heterogeneity dosimetric effects using radiochromic film for COMS eye plaques loaded with ^{125}I seeds (model I25.S16)," Med. Phys. **40**, 011708 (2013).

[33] S.-T. Chiu-Tsao, D.C. Medich, and J. Munro, "The use of new GAFCHROMIC EBT film for ^{125}I seed dosimetry in Solid Water phantom," Med. Phys. **35**, 3787–3799 (2008).

[34] D. Lewis, A. Micke, X. Yu, and M.F. Chan, "An efficient protocol for radiochromic film dosimetry," Med. Phys. **39**, 6339 (2012).

[35] R. Serway, C. Vuille, and J. Faughn, *College Physics*, 8th ed. (Brooks/Cole Cengage Learning, Belmont, CA, CA, 2009).

[36] A. Rink, I.A. Vitkin, and D.A. Jaffray, "Characterization and real-time optical measurements of the ionizing radiation dose response for a new radiochromic medium," Med. Phys. **32**, 2510–2516 (2005).

[37] White paper entitled "Gafchromic EBT2: Self-developing film for radiotherapy dosimetry," International Specialty Products, Wayne, NJ, October 2010, http://www.filmqapro.com.

[38] B.D. Lynch, J. Kozelka, M.K. Ranade, J.G. Li, W.E. Simon, and J.F. Dempsey, "Important considerations for radiochromic film dosimetry with flatbed CCD scanners and EBT GAFCHROMIC® film," Med. Phys. **33**, 4551–4556 (2006).

[39] A.A. Schoenfeld, D. Poppinga, D. Harder, K.-J. Doerner, and B. Poppe, "The artefacts of radiochromic film dosimetry with flatbed scanners and their causation by light scattering from radiation-induced polymers.," Phys. Med. Biol. **59**, 3575–97 (2014).

[40] A. Rink, "Point-based ionization radiation dosimetry using radiochromic materials and a fibreoptic readout system" Ph.D. Thesis, University of Toronto, Canada (2008).

[41] A. Niroomand-Rad, C.R. Blackwell, B.M. Coursey, K.P. Gall, J.M. Galvin, W.L. McLaughlin, A.S. Meigooni, R. Nath, J.E. Rodgers, and C.G. Soares, "Radiochromic film dosimetry: Recommendations of AAPM Radiation Therapy Committee Task Group 55," Med. Phys. **25**, 2093–2115 (1998).

[42] T.J. McCaw, J.A. Micka, and L.A. DeWerd, "Characterizing the marker-dye correction for Gafchromic® EBT2 film: A comparison of three analysis methods," Med. Phys. **38**, 5771 (2011).

[43] S. Devic, S. Aldelaijan, H. Mohammed, N. Tomic, L. Liang, F. Deblois, and J. Seuntjens, "Absorption spectra time evolution of EBT-2 model GAFCHROMIC^{TM} film," Med. Phys. **37**, 2207–2214 (2010).

[44] J.G.H. Sutherland and D.W.O. Rogers, "Monte Carlo calculated absorbed-dose energy dependence of EBT and EBT2 film," Med. Phys. **37**, 1110–1116 (2010).

[45] J.F. Dempsey, D.A. Low, A.S. Kirov, and J.F. Williamson, "Quantitative optical densitometry with scanning-laser film digitizers.," Med. Phys. **26**, 1721–1731 (1999).

[46] S. Devic, J. Seuntjens, E. Sham, E.B. Podgorsak, C.R. Schmidtlein, A.S. Kirov, and C.G. Soares, "Precise radiochromic film dosimetry using a flat-bed document scanner.," Med. Phys. **32**, 2245–2253 (2005).

[47] L.J. van Battum, H. Huizenga, R.M. Verdaasdonk, and S. Heukelom, "How flatbed scanners upset accurate film dosimetry," Phys. Med. Biol. **61**, 625–649 (2016).

[48] Y. Zhu, A.S. Kirov, V. Mishra, A.S. Meigooni, and J.F. Williamson, "Quantitative evaluation of radiochromic film response for two-dimensional dosimetry," Med. Phys. **24**, 223–231 (1997).

[49] C.G. Soares, S. Trichter, and S. Devic, "Radiochromic film," in *Clinical dosimetry measurements in Radiotherapy*, edited by D.W.O. Rogers and J.E. Cygler (Medical Physics Publishing, Madison, WI, 2009), pp. 759–813.

[50] T. Aland, T. Kairn, and J. Kenny, "Evaluation of a Gafchromic EBT2 film dosimetry system for radiotherapy quality assurance," Australas. Phys. Eng. Sci. Med. **34**, 251–260 (2011).

[51] B.C. Ferreira, M.C. Lopes, and M. Capela, "Evaluation of an Epson flatbed scanner to read Gafchromic EBT films for radiation dosimetry," Phys. Med. Biol. **54**, 1073–1085 (2009).

[52] S. Devic, N. Tomic, and D. Lewis, "Reference radiochromic film dosimetry: Review of technical aspects," Phys. Medica **32**, 541–556 (2016).

[53] A. Micke, D.F. Lewis, and X. Yu, "Multichannel film dosimetry with nonuniformity correction," Med. Phys. **38**, 2523–2534 (2011).

[54] R.R. Mayer, F. Ma, Y. Chen, R.I. Miller, A. Belard, J. McDonough, and J.J. O'Connell, "Enhanced dosimetry procedures and assessment for EBT2 radiochromic film," Med. Phys. **39**, 2147 (2012).

[55] I. Méndez, P. Peterlin, R. Hudej, A. Strojnik, and B. Casar, "On multichannel film dosimetry with channel-independent perturbations.," Med. Phys. **41**, 011705 (2014).

[56] S.J. van Hoof, P. V Granton, G. Landry, M. Podesta, and F. Verhaegen, "Evaluation of a novel triple-channel radiochromic film analysis procedure using EBT2," Phys. Med. Biol. **57**, 4353–4368 (2012).

[57] J.F. Pérez Azorín, L.I. Ramos García, and J.M. Martí-Climent, "A method for multichannel dosimetry with EBT3 radiochromic films.," Med. Phys. **41**, 062101 (2014).

[58] I. Méndez, "Model selection for radiochromic film dosimetry," Phys. Med. Biol. **60**, 4089–4104 (2015).

[59] A.L. Palmer, D. Bradley, and A. Nisbet, "Evaluation and implementation of triple-channel radiochromic film dosimetry in brachytherapy," J. Appl. Clin. Med. Phys. **15**, 280–296 (2014).

[60] J.A. Martín-Viera Cueto, V. Parra Osorio, C. Moreno Sáiz, F. Navarro Guirado, F.J. Casado Villalón, and P. Galán Montenegro, "A universal dose–response curve for radiochromic films," Med. Phys. **42**, 221–231 (2015).

[61] T.A.D. Brown, K.R. Hogstrom, D. Alvarez, K.L. Matthews, K. Ham, and J.P. Dugas, "Dose-response curve of EBT, EBT2, and EBT3 radiochromic films to synchrotron-produced monochromatic x-ray beams," Med. Phys. **39**, 7412–7417 (2012).

[62] S. Devic, J. Seuntjens, G. Hegyi, E.B. Podgorsak, C.G. Soares, A.S. Kirov, I. Ali, J.F. Williamson, and A. Elizondo, "Dosimetric properties of improved GafChromic films for seven different digitizers.," Med. Phys. **31**, 2392–2401 (2004).

[63] S. Devic, N. Tomic, C.G. Soares, and E.B. Podgorsak, "Optimizing the dynamic range extension of a radiochromic film dosimetry system," Med. Phys. **36**, 429–437 (2009).

[64] S. Devic, "Radiochromic film dosimetry: Past, present, and future," Phys. Medica **27**, 122–134 (2011).

[65] N. Hayashi, Y. Watanabe, R. Malmin, and H. Kato, "Evaluation of triple channel correction acquisition method for radiochromic film dosimetry," J. Radiat. Res. **53**, 930–935 (2012).

[66] L. Paelinck, W. De Neve, and C. De Wagter, "Precautions and strategies in using a commercial flatbed scanner for radiochromic film dosimetry.," Phys. Med. Biol. **52**, 231–242 (2007).

[67] T. Pawlicki, M. Whitaker, and G. Kim, "SU-GG-T-275: On Improving the Accuracy of EBT2 Film Dosimetry Using a Flatbed Scanner," Med. Phys. **37**, 3248–3249 (2010).

[68] C. Andrés, A. del Castillo, R. Tortosa, D. Alonso, and R. Barquero, "A comprehensive study of the Gafchromic EBT2 radiochromic film. A comparison with EBT.," Med. Phys. **37**, 6271–6278 (2010).

[69] L.A. DeWerd, G.S. Ibbott, A.S. Meigooni, M.G. Mitch, M.J. Rivard, K.E. Stump, B.R. Thomadsen, and J.L.M. Venselaar, "A dosimetric uncertainty analysis for photon-emitting brachytherapy sources: report of AAPM Task Group No. 138 and GEC-ESTRO," Med. Phys. **38**, 782–801 (2011).

[70] C. Kirisits, M.J. Rivard, D. Baltas, F. Ballester, M. De Brabandere, R. Van Der Laarse, Y. Niatsetski, P. Papagiannis, T.P. Hellebust, J. Perez-Calatayud, K. Tanderup, J.L.M. Venselaar, and F.A. Siebert, "Review of clinical brachytherapy uncertainties: Analysis guidelines of GEC-ESTRO and the AAPM," Radiother. Oncol. **110**, 199–212 (2014).

[71] Evaluation of measurement data—Guide to the expression of uncertainty in measurement, *International Organization for Standardization (ISO)*, Joint Committee for Guides in Metrology (JCGM 100, 2008), corrected version 2010, http://www.bipm.org/utils/common/documents/jcgm/JCGM_100_2008_E.pdf

[72] B.N. Taylor and C.E. Kuyatt, "Guidelines for Evaluating and Expressing the Uncertainty of NIST Measurement Results," in *NIST Technical Note 1297* (U.S. Government Printing Office, Washington DC, 1994).

[73] M.G. Mitch and S.M. Seltzer, "SU-EE-A2-03: Model-Specific Uncertainties in Air-Kerma Strength Measurements of Low-Energy Photon-Emitting Brachytherapy Sources," Med. Phys. **34**, 2337 (2007).

[74] J.A. Raffi, S.D. Davis, C.G. Hammer, J.A. Micka, K.A. Kunugi, J.E. Musgrove, J.W. Winston, T.J. Ricci-Ott, and L.A. DeWerd, "Determination of exit skin dose for ^{192}Ir intracavitary accelerated partial breast irradiation with thermoluminescent dosimeters," Med. Phys. **37**, 2693–2702 (2010).

[75] S.-T. Chiu-Tsao, J.J. Napoli, S.D. Davis, J. Hanley, and M.J. Rivard, "Dosimetry for ^{131}Cs and ^{125}I seeds in solid water phantom using radiochromic EBT film," Appl. Radiat. Isot. **92**, 102–114 (2014).

[76] J.F. Williamson and M.J. Rivard, "Quantitative dosimetry methods for brachytherapy," in *Brachytherapy Physics: Joint AAPM/ABS Summer School*, 2nd ed., edited by B.R. Thomadsen, M.J. Rivard and W.M. Butler (Medical Physics, Madison, WI, 2005), pp. 233–294.

[77] P. Aryal, J.A. Molloy, and M.J. Rivard, "A modern Monte Carlo investigation of the TG-43 dosimetry parameters for an ^{125}I seed already having AAPM consensus data," Med. Phys. **41**, 021702 (10 pp.) (2014).

[78] Y. Yu, L.L. Anderson, Z. Li, D.E. Mellenberg, R. Nath, M.C. Schell, F.M. Waterman, A. Wu, and J.C. Blasko, "Permanent prostate seed implant brachytherapy: report of the American Association of Physicists in Medicine Task Group No. 64," Med. Phys. **26**, 2054–2076 (1999).

[79] L. Beaulieu, Å. Carlsson Tedgren, J.-F. Carrier, S.D. Davis, F. Mourtada, M.J. Rivard, R.M. Thomson, F. Verhaegen, T.A. Wareing, and J.F. Williamson, "Report of the Task Group 186 on model-based dose calculation methods in brachytherapy beyond the TG-43 formalism: Current status and recommendations for clinical implementation," Med. Phys. **39**, 6208–6236 (2012).

[80] M. Lesperance, M. Inglis-Whalen, and R.M. Thomson, "Model-based dose calculations for COMS eye plaque brachytherapy using an anatomically realistic eye phantom," Med. Phys. **41**, 021717 (12 pp.) (2014).

[81] A. Carlsson Tedgren and G.A. Carlsson, "Specification of absorbed dose to water using model-based dose calculation algorithms for treatment planning in brachytherapy," Phys. Med. Biol. **58**, 2561–2579 (2013).

[82] O. Chibani and J.F. Williamson, "MCPI (c): A sub-minute Monte Carlo dose calculation engine for prostate implants.," Med. Phys. **32**, 3688–3698 (2005).

83 R.E.P. Taylor, G. Yegin, and D.W.O. Rogers, "Benchmarking brachydose: Voxel based EGSnrc Monte Carlo calculations of TG-43 dosimetry parameters," Med. Phys. **34**, 445–457 (2007).

84 R.M. Thomson, G. Yegin, R.E.P. Taylor, J. Sutherland, and D.W.O. Rogers, "Fast Monte Carlo Dose Calculations for Brachytherapy with BrachyDose," Med. Phys. **37**, 3910–3911 (2010).

85 M.J.P. Chamberland, R.E.P. Taylor, D.W.O. Rogers, and R.M. Thomson, "egs_brachy: a versatile and fast Monte Carlo code for brachytherapy," Phys. Med. Biol. **61**, 8214–8231 (2016).

86 H. Afsharpour, G. Landry, M. D'Amours, S. Enger, B. Reniers, E.S. Poon, J.-F. Carrier, F. Verhaegen, and L. Beaulieu, "ALGEBRA: ALgorithm for the heterogeneous dosimetry based on GEANT4 for BRAchytherapy," Phys. Med. Biol. **57**, 3273–3280 (2012).

87 E.S. Poon, Y. Le, J.F. Williamson, and F. Verhaegen, "BrachyGUI: an adjunct to an accelerated Monte Carlo photon transport code for patient-specific brachytherapy dose calculations and analysis," J. Phys. Conf. Ser. **102**, 012018 (2008).

88 E. Pantelis, V. Peppa, V. Lahanas, E. Pappas, and P. Papagiannis, "BrachyGuide: a brachytherapy-dedicated DICOM RT viewer and interface to Monte Carlo simulation software," J. Appl. Clin. Med. Phys. **16**, 5136 (2015).

89 G.P. Fonseca, B. Reniers, G. Landry, S. White, M. Bellezzo, P.C.G. Antunes, C.P. de Sales, E. Welteman, H. Yoriyaz, and F. Verhaegen, "A medical image-based graphical platform-Features, applications and relevance for brachytherapy," Brachytherapy **13**, 632–639 (2014).

90 P. Papagiannis, E. Pantelis, and P. Karaiskos, "Current state of the art brachytherapy treatment planning dosimetry algorithms.," Br. J. Radiol. **87**, 20140163 (2014).

91 P. Papagiannis, L. Beaulieu, and F. Mourtada, "Computational methods for the dosimetric characterization of brachytherapy sources," in *Comprehensive Brachytherapy: Physical and clinical aspects*, edited by J.L.M. Venselaar, D. Baltas, A.S. Meigooni and P.J. Hoskin (Taylor & Francis Group, LLC, Boca Raton, FL, 2013), pp. 85–103.

92 L. Beaulieu, Y. Ma, and B. van Veelen, "ACE Advanced Collapsed cone Engine," White Paper Elekta 1–16 (2014).

93 J.T. Goorley, M. James, T. Booth, F. Brown, J. Bull, J. Cox, and J. Durkee, "Initial MCNP6 Release Overview," Nucl. Technol. **180**, 298–315 (2012).

94 X-5 Monte Carlo Team, *MCNP - A general Monte Carlo N-Particle Transport Code, Version 5, Volume I: Overview and Theory, LA-UR-03-1987* (Los Alamos National Laboratory, 2008).

[95] J.T. Goorley, M.R. James, T.E. Booth, F.B. Brown, J.S. Bull, L.J. Cox, J.W. Durkee, J.S. Elson, M.L. Fensin, R.A. Forster, J.S. Hendricks, H.G. Hughes, R.C. Johns, B.C. Kiedrowski, and S.G. Mashnik, *MCNP6 User's Manual, Version 1.0, LA-CP-13-00634* (Los Alamos National Laboratory, 2013).

[96] M.B. Chadwick, M. Herman, P. Obložinský, M.E. Dunn, Y. Danon, A.C. Kahler, D.L. Smith, B. Pritychenko, G. Arbanas, R. Arcilla, R. Brewer, D.A. Brown, R. Capote, A.D. Carlson, Y.S. Cho, H. Derrien, K. Guber, G.M. Hale, S. Hoblit, *et al.*, "ENDF/B-VII.1 Nuclear Data for Science and Technology: Cross Sections, Covariances, Fission Product Yields and Decay Data," Nucl. Data Sheets **112**, 2887–2996 (2011).

[97] C.S. Melhus and M.J. Rivard, "Approaches to calculating AAPM TG-43 brachytherapy dosimetry parameters for ^{137}Cs, ^{125}I, ^{192}Ir, ^{103}Pd, and ^{169}Yb sources," Med. Phys. **33**, 1729–1737 (2006).

[98] A. Ahnesjö and M.M. Aspradakis, "Dose calculations for external photon beams in radiotherapy," Phys. Med. Biol. **44**, R99–R155 (1999).

[99] Å.K. Carlsson and A. Ahnesjö, "Point kernels and superposition methods for scatter dose calculations in brachytherapy," Phys. Med. Biol. **45**, 357–357 (2000).

[100] A.K. Carlsson Tedgren and A. Ahnesjö, "Accounting for high Z shields in brachytherapy using collapsed cone superposition for scatter dose calculation.," Med. Phys. **30**, 2206–2217 (2003).

[101] Å. Carlsson Tedgren and A. Ahnesjö, "Optimization of the computational efficiency of a 3D, collapsed cone dose calculation algorithm for brachytherapy," Med. Phys. **35**, 1611 (2008).

[102] K.R. Russell, A.K. Carlsson Tedgren, and A. Ahnesjö, "Brachytherapy source characterization for improved dose calculations using primary and scatter dose separation," Med. Phys. **32**, 2739 (2005).

[103] K.R. Russell and A. Ahnesjö, "Dose calculation in brachytherapy for a ^{192}Ir source using a primary and scatter dose separation technique," Phys. Med. Biol. **41**, 1007–1024 (1996).

[104] Å.K. Carlsson and A. Ahnesjö, "The collapsed cone superposition algorithm applied to scatter dose calculations in brachytherapy," Phys. Med. Biol. **27**, 2320–2332 (2000).

[105] A. Ahnesjö, B. van Veelen, and A. Carlsson Tedgren, "Collapsed cone dose calculations for heterogeneous tissues in brachytherapy using primary and scatter separation source data," Comput. Methods Programs Biomed. **139**, 17–29 (2017).

[106] Y. Ma, F. Lacroix, M.-C. Lavallée, and L. Beaulieu, "Validation of the Oncentra Brachy Advanced Collapsed cone Engine for a commercial ^{192}Ir source using heterogeneous geometries," Brachytherapy **14**, 939–952 (2015).

[107] Å. Carlsson Tedgren, F. Verhaegen, and L. Beaulieu, "On the introduction of model-based algorithms performing nonwater heterogeneous corrections into brachytherapy treatment planning," in *Comprehensive Brachytherapy: Physical and clinical aspects*, edited by J.L.M. Venselaar, D. Baltas, A.S. Meigooni and P.J. Hoskin (Taylor & Francis Group, LLC, Boca Raton, FL, 2013).

[108] T. Knöös, M. Nilsson, and L. Ahlgren, "A method for conversion of Hounsfield number to electron density and prediction of macroscopic pair production cross-sections," Radiother. Oncol. **5**, 337–345 (1986).

Chapter 3 Radiochromic film dose measurement for low-energy brachytherapy

*The parts of this chapter pertaining to radiochromic film calibration have been published as: H. Morrison, G. Menon, and R.S. Sloboda, "Radiochromic film calibration for low-energy seed brachytherapy dose measurement," Med. Phys. **41**, 072101 (2014).*

3.1 Introduction

Previous work using Gafchromic film (EBT, EBT2 as well as EBT3 model films [Ashland Specialty Ingredients, Wayne, NJ]) has been primarily focused on its use for intensity modulated radiation therapy (IMRT) plan verification.[1–5] Within this context, the film is typically exposed to MV energy photon beams and to moderate doses of 1-7 Gy, but in some cases has been exposed to high doses as well (up to 34 Gy) for stereotactic body radiotherapy.[6,7]

For brachytherapy source measurements, Gafchromic film calibration methods have been reported for Ir-192 using piece-wise fitting with two different equations for low- and high-dose ranges,[8] using the green channel only due to lower uncertainties up to 50 Gy,[9] as well as using netODs for I-125 sources up to 35 Gy.[10] Performing film calibrations with brachytherapy seeds poses challenges including accurate seed-film placement, relatively low source strength resulting in long exposure times to obtain high doses from a single seed, and much higher uncertainties in radiation output than external beam units. The film manufacturer suggests using large irradiation areas for calibration to reduce the effect of film heterogeneities, which are also difficult to achieve with small brachytherapy sources, and often calibration is performed with a film region as small as 1x1 mm^2,[9] which may not accurately represent the average film response.

In this work, Gafchromic EBT3 film was exposed to low-energy photons from an I-125 brachytherapy seed and doses up to ~35 Gy. This was done to assess the various steps in the film calibration procedure in order to determine the modifications required to achieve high levels of accuracy when deviating from its typical use in external beam radiotherapy (high energy exposure at moderate doses). The accuracy of the calibration curves over the broader dose range was assessed with and without the inclusion of uncertainty in both the measured optical density of the film as well as the reference dose. Accuracy of the calibration curve with a reduced

number of dose levels over the larger dose range was also assessed. This work also establishes a novel film irradiation and measurement method for brachytherapy seeds that yields a larger region of constant dose and thereby reduces the effects of film heterogeneities, and makes comparisons with previous methods. The extent of the energy dependence of the film batch used was also determined as it has been found to vary slightly between earlier film models (EBT and EBT2),[11,12] as well as from batch to batch.[13–15] Though it is well accepted that the film is nearly energy independent above 100 keV,[14] the variation in reported results warrants further investigation, and the energy dependence below an effective energy of 100 keV was of particular interest. Due to the aforementioned challenges when performing calibrations with brachytherapy seeds, the use of a low-energy orthovoltage photon beam of similar effective energy was investigated, and from the results of this work recommendations are made for obtaining accurate film calibrations for low-energy brachytherapy dose measurement over a dose range of $0 - 35$ Gy.

All netOD methods as well as some dose perturbation correction methods require pre-scanning of all films, which can result in additional uncertainties arising from image registration, scan to scan variability, and noise amplification.[16] Therefore a film heterogeneity correction method that does not require pre-scanning of the films was also developed and validated using enhanced dynamic wedge (EDW) fields from a high energy linac.

3.2 Materials and Methods

3.2.1 Film calibration irradiation procedure

The film type used in this study was Gafchromic® EBT3 film (lot # A0318303). The films were stored and handled according to the recommendations made by the American Association of Physicists in Medicine (AAPM) TG-55 report.[17] Film irradiations were performed using three radiation sources: a Varian 21EX linac (Varian Medical Systems, Palo Alto, CA), a Therapax DXT 300 orthovoltage unit (Pantak Inc., East Haven, CT), and an Oncura OncoSeed I-125 model 6711 brachytherapy seed (GE Healthcare Inc., Arlington Heights, IL). Baseline irradiations performed using the Varian 21EX linac were done using a 6 MV beam and an open 10 x 10 cm^2 field with 4 x 4 cm^2 film pieces placed at 100 cm source-to-axis distance (SAD) within 20 x 20 cm^2 slabs of Solid Water (Gammex/RMI, Middleton, WI). A build-up of 1.5 cm

of Solid Water (films were placed at depth of maximum dose, d_{max}) was placed above the film, and 12 cm below for backscatter. Film pieces were irradiated first at 24 different reference dose levels chosen such that they increased in a geometric pattern as recommended by the film manufacturer[18] from 10.1 to 4218 cGy. A second calibration was then obtained using 9 dose levels ranging from 13.2 to 3767 cGy, also increasing in a geometric pattern (the number of required dose levels for accurate determination of calibration parameters was informed by the 24 dose level 6 MV curve – see Section 3.2.3). The output of the Varian 21EX linac is calibrated following the AAPM TG-51 protocol[19] such that 1 cGy/MU is delivered at d_{max} in water (1.5cm) for a 6 MV photon beam. The output of the linac was monitored using a PR-06C Farmer chamber (Capintec, Ramsey, NJ) placed in a plastic quality assurance (QA) output jig (cross-calibrated against the National Research Council of Canada (NRCC) calibrated primary dosimetry system) at the start and end of the film irradiations, and these measurements were used to adjust the nominal reference dose delivered to the film.

Irradiations using the Therapax DXT 300 orthovoltage unit were performed at 75 and 200 kVp using a 10 x 10 cm^2 applicator with a focus-to-surface/skin distance of 30 cm. Half value layers (HVLs) in copper and effective energies are 0.078 mm and 0.921 mm, and 31.1 keV and 77.1 keV for the two beams, respectively. Film pieces cut to 4 x 4 cm^2 were taped to the underside of the applicator and irradiated to 9 different reference dose levels ranging from 17.4 to 3711 cGy (doses to tissue with no backscatter material present), again spaced in a geometric progression. The output of the orthovoltage unit is calibrated following the AAPM TG-61 protocol using the in-air method.[20] The reference doses were verified using a PTW N3004 ion chamber and PTW Unidos E T10009 electrometer (PTW-New York Corp., Brooklyn NY) with National Research Council of Canada (NRCC) calibration factors accurate to ±1% (coverage factor k=2).

The film irradiations performed using the Oncura 6711 I-125 seed were done using a three-piece custom built polymethylmethacrylate (PMMA) phantom (Figure 3.1). The seed used underwent secondary calibration by the vendor, and had a seed strength of 16.01 U at the beginning of the film irradiations with a 1.75% (coverage factor k=1) uncertainty. The seed was placed within a well in the lower part of the central piece (Piece 1) of the phantom, with a small plug placed above it prior to joining the upper and lower parts of the central piece together. Film pieces measuring 4 x 7.5 cm^2 were wrapped length-wise around the second phantom piece (Piece

2) within a machined groove. Piece 1 and 2 were then placed within the 16 cm diameter outer piece (Piece 3) to provide full scatter conditions. The central and second phantom pieces create 1.25 cm separation between the center of the I-125 seed and the centre of the film sensitive layer. The film and seed are aligned vertically such that a strip running length-wise along the film and close to its centre intersects the seed transverse plane ($\theta=90°$), and so will receive the maximum dose. The reference dose was determined using TG-43 tabulated data[21] in water with a conversion factor[22] of 1.14 ± 1.5% applied to account for the PMMA material of the phantom. This set-up was used as opposed to previously described I-125 film calibration methods[10,23] so that any azimuthal variations in the seed construction as well as variations in the film thickness could be averaged, as recommended by the film manufacturer.[18] The films were irradiated to 9 different reference dose levels ranging from 13.4 to 3408 cGy in geometric progression.
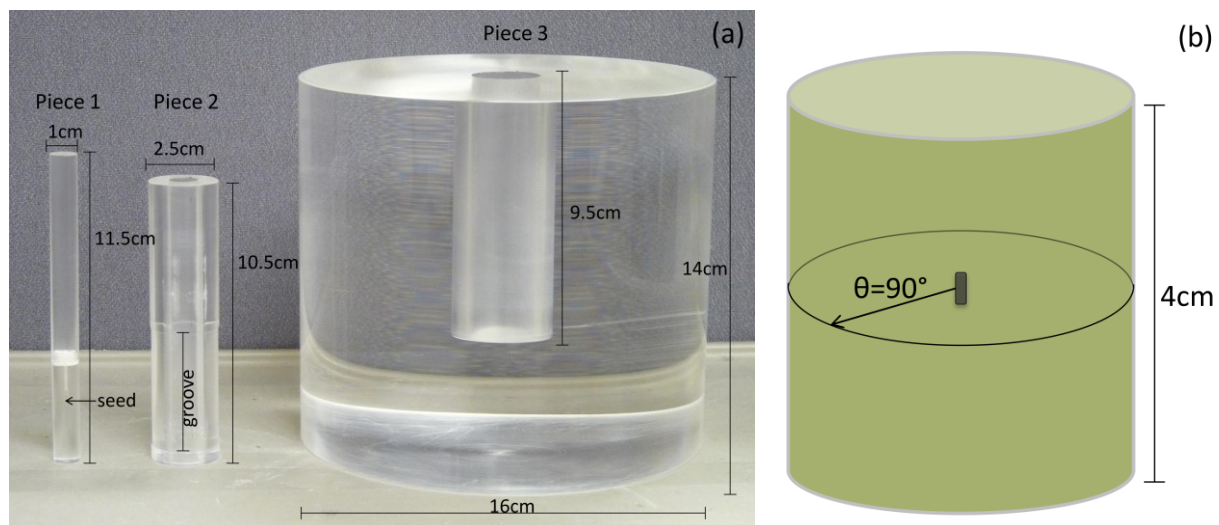
Figure 3.1 PMMA film/seed irradiation phantom, with first, second and third pieces shown from left to right (a); schematic diagram of the film and seed showing where the transverse axis of the seed transects the wrapped film (solid line) and delivers the maximum dose (b). The film is wrapped around Piece 2 in the indicated grooved region.

3.2.2 Film scanning and analysis

All film pieces were scanned using an Epson Expression 10000XL flatbed colour image scanner (Seiko Epson Corp., Nagano, Japan) and the associated Epson Scan v3.49A software. Prior to scanning the films, the scanner was warmed-up for a minimum of 30 minutes, followed by 5-7 preview scans, as this was found to be required to allow appropriate warm-up and stabilization, and is also the suggested protocol.[24,25] If necessary, the film pieces were cleaned with a 70% isopropyl alcohol solution to remove any finger prints, tape residue, or other marks or dust. All film pieces were scanned three times, 24 hours after irradiation, with the scanner in transmission mode (using the transmission adapter), at 72 dpi, 48-bit RGB colour (16 bits per colour), with all colour correction features turned off, and in landscape orientation in the centre of the scanner bed. One to three blank film pieces, cut to the same sizes as the irradiated films, were also scanned to accompany each irradiation energy. The scanner uniformity was also assessed using an un-irradiated piece of film prior to scanning the irradiated films. Within the central region of the scanner bed (larger than the irradiated film pieces), the scanner output was found to be uniform within 0.3%, and as all irradiated film pieces were scanned in the central region of the scanner, the images were not corrected for lateral-scanning artefacts or other non-uniform scanner output effects.

All films were scanned with a piece of glass placed above the films to hold them flat, as suggested by the film manufacturer [A. Micke (private communication)] (with the exception of the first set of 6 MV films irradiated at 24 dose levels, which were scanned without the glass).

The scanned images were saved as Tagged Image File Format (TIFF) images and analyzed using both MATLAB v7.14 (MathWorks, Natick, MA) and FilmQA Pro 2013 (Ashland Specialty Ingredients, Wayne, NJ). The average PVs and standard deviations for each colour channel were measured from a 3.0 x 3.0 cm^2 area in the centre of the film pieces for the films irradiated at 75 kVp, 200 kVp, and 6 MV (film heterogeneity effects were found not to affect the average PV measurements for film regions larger than 2.5 x 2.5 cm^2). For films irradiated with the I-125 seed, a 2.47 mm x 7.4 cm long central region with maximum exposure was measured. Tabulated AAPM TG-43U1 data[21] were used to determine the distance from the transverse axis that resulted in a dose within 0.5% of the maximum dose along the transverse axis, which was found to be 1.2 mm. At 72 dpi this translates to a measurement width of 7 pixels. Including this slightly larger measurement area off of the transverse axis ensured that the measured average PV

was less affected by film thickness variations, while still accurately representing the PV corresponding to the maximum exposure. The average PVs from each of the three scans made per film piece were then averaged together to account for variations in the scanner response. The average measured PVs in each colour channel were converted to optical density (OD) values using Eq. 3.1 and the 16-bit colour channel PV when no film is present (2^{16} -1= 65535).

$$OD = -log_{10}\left(\frac{PV}{65535}\right) \qquad (3.1)$$

A NIST calibrated Tiffen Transmission Photographic Step Tablet #2 (The Tiffen Company, Rochester, NY) was also scanned (with the same scan settings) to compare the effective OD values, obtained using Eq. 3.1, to the NIST calibrated XRITE 361T densitometer (X-Rite Inc., Grand Rapids, MI) measured values and to assess the linearity of the scanner response over a large range of optical densities.

3.2.3 Film calibration and curve fitting

Calibration curves at all energies were determined using FilmQA Pro, as well as a recently published method which includes the uncertainty in reference dose and in measured OD when performing nonlinear least square minimization to determine the calibration fit parameters.[26] The effective variance method solved by direct optimization (EV$_{opt}$) was implemented in a MATLAB code provided by the authors and modified to use a rational linear calibration function. This method, as the name suggests, uses an effective variance in the y variable, calculated using the following formula:

$$\sigma_{y,i,eff}^2 = \sigma_{y,i}^2 + \left(\frac{\partial f(c_j,x)}{\partial x}\right)^2 \sigma_{x,i}^2 \qquad (3.2)$$

where $\sigma_{y,i}$ and $\sigma_{x,i}$ are the standard deviations of y_i and x_i (as used in this study x_i values are reference doses, and y_i values are the corresponding measured ODs), and $\partial f(c_j,x)/\partial x$ is the partial derivative of the function relating the x_i and y_i data with fit parameters c_j.

For the dose range investigated here, the rational linear function suggested by the film manufacturer and used to fit the data is shown in Eq. 3.3.

$$X(D) = (a + bD)/(c + D) \qquad (3.3)$$

93

where *a*, *b,* and *c* are fit parameters, $X(D)$ is the film response in normalized PV (measured PV divided by the maximum value of 65535) and *D* is the dose. If using polynomial functions with netOD over the extended dose range, the fitted functions were found to oscillate between data points, while the rational linear function was found to fit the data well, with the exception of the region with the greatest curvature in the calibration curve (60 – 500 cGy), particularly in the red channel, where there was a larger deviation.

When performing the curve fitting using the Ramos and Pérez[26] nonlinear least squares minimization method, the data was fit three different ways: using equal weightings (i.e. no uncertainty included), including uncertainty in only the OD values, and including uncertainty in both OD and reference dose. For these fittings, the PVs were converted to OD using Eq. 3.1, and the fitting function used to relate OD to reference dose is shown in Eq. 3.4.

$$OD = -log_{10}((a + bD)/(c + D))$$
(3.4)

Fitting was attempted using normalized PVs as well; however for these data the EV_{opt} method gave inconsistent results that were strongly dependent on the initial guesses of the fit parameters. The authors mention that the EV method sometimes gives inaccurate results with some "special" data sets, which may be the case when using this method to perform the calibration fitting with normalized PVs.[26]

Due to the relatively large dose range, piece-wise fitting was also performed using the EV_{opt} method with inclusion of OD and dose uncertainties, by splitting the calibration curve data into low-dose and high-dose ranges demarcated by the center of a transition region in which the slope changes significantly. To ensure a smooth transition between the low-dose and high-dose fitted pieces, there were two overlapping data points in the low- and high-dose ranges. All fitted curves were then inverted (Eq. 3.5) to assess the accuracy of doses determined from measured OD values (hereby called film doses) and the obtained calibration parameters:

$$D = \frac{c \cdot 10^{-OD} - a}{b - 10^{-OD}}$$
(3.5)

This method of piece-wise fitting differs from previous film calibration methods as a full calibration curve (composed of two pieces) is obtained for each colour channel as opposed to using the different colour channels for different dose levels (e.g. red for low dose, green for medium, blue for high dose) based on which has either the lowest relative uncertainty or the

highest sensitivity,[27] and uses the same rational linear calibration function over the entire dose range rather than different functions at low and high dose levels.[8]

When using the rational functions suggested by the film manufacturer to fit the calibration curve, it has been reported that accurate results can be obtained when using only 4 or 5 data points arranged in a geometric progression.[4] This finding, however, has only been validated when performing dosimetry over a narrower dose range with a maximum dose typical for IMRT plans, which is usually on the order of 2-5 Gy. The number of data points used to determine the calibration parameters for the 6 MV and I-125 irradiated films in the present work were systematically reduced while still maintaining an approximate geometric progression to determine how the accuracy of the calibration curve is affected when measuring dose over a greater range.

Due to the spatially non-uniform dose delivery by the I-125 brachytherapy seed, the measurement region was reduced to a smaller 2.47 x 2.47 mm^2 area in the centre of the film within the maximum exposure region to determine the impact this would have on the resulting calibration curve. Previous film measurements using brachytherapy seeds for calibration used regions much smaller than those suggested by the film manufacturer,[9,10,23] who recommends using film pieces at least 25 cm^2 in size.[28] Such a large measurement area is required to ensure an average film response that is not affected by local heterogeneities in the film, which may be a problem if the measurement area is too small.

Using the piece-wise calibration curves, OD values were calculated at each dose level (using Eq. 3.4), and were normalized to the 6 MV OD values to determine the extent of the energy dependence of the film response (Eq. 3.6). Films were also corrected to reflect the same initial zero-dose OD (using the average ODs of the 3.0 x 3.0 cm^2 film regions) since not all films were irradiated and scanned at the same time.

$$normOD = \frac{OD_x}{OD_{6MV}}$$ (3.6)

To assess the error in dose measurements that could result from assuming the film response is independent of irradiation energy, calibration curves obtained from the 75 kVp, 200 kVp, and 6 MV irradiated films were used to calculate dose values from the films irradiated using the I-125 seed. These results were also used to determine whether or not the 75 kVp calibration curve could be used to perform I-125 dosimetry measurements with adequate accuracy.

3.2.4 Film calibration uncertainty analysis

The calculated total uncertainties in the film measurements follow the uncertainty principles outlined in the NIST Technical Note 1297.[29] All uncertainties are grouped as Type A or Type B, and summed in quadrature to determine the total combined uncertainty. Assuming no covariance in the variables, the propagation of uncertainty is found by:

$$\sigma_y^2 = \sum_i \left(\frac{\partial y}{\partial x_i}\right)^2 \cdot \sigma_{x_i}^2 \tag{3.7}$$

where σ_{x_i} and σ_y are the standard deviations of the x_i and y data.

As all film pieces were scanned three times and the average measured PVs from all three scans were used, the standard deviation of the average measured PV (σ_{PV}) was determined from the individual standard deviations ($\sigma_{PV,scan\,i}$) of each film image (Eq. 3.8):

$$\sigma_{PV} = \frac{1}{3}\sqrt{\left(\sigma_{PV,scan1}^2 + \sigma_{PV,scan2}^2 + \sigma_{PV,scan3}^2\right)} \tag{3.8}$$

The standard deviations in the measured PVs (σ_{PV}) as well as the background scanner response, PV$_{blank}$ ($\sigma_{PV_{blank}}$), obtained with no film present in the central part of the scanner, were used to determine the standard deviations in the calculated ODs (σ_{OD}) (Eq. 3.9).

$$\sigma_{OD}(\%) = \sqrt{\left(\frac{\partial OD}{\partial PV}\right)^2 \sigma_{PV}^2 + \left(\frac{\partial OD}{\partial PV_{blank}}\right)^2 \sigma_{PV_{blank}}^2} = \frac{1}{\ln(10)}\sqrt{\left(\frac{\sigma_{PV}}{PV}\right)^2 + \left(\frac{\sigma_{PV_{blank}}}{PV_{blank}}\right)^2} \tag{3.9}$$

When performing dosimetric measurements using the obtained calibration curves, the uncertainty in the film dose is derived from the propagated uncertainty in the measured OD, the uncertainty in the calibration curve, and the uncertainty in the reference doses. The uncertainty in the calibration curve was determined by estimating the uncertainties in the calibration fit parameters such that the uncertainty calculated using Eq. 3.7 (for the calibration fit parameters only) approximately yielded the difference between the reference and film doses. The uncertainties in the reference doses for the linac and orthovoltage units were determined from the output variations obtained from repeated ion chamber measurements (uncertainties in the chamber calibration factors were included), and amounted to 1% for both modalities. For the I-125 seed doses, the uncertainties in the reference doses were determined from the seed strength calibration uncertainty, the uncertainty in the reported dose rate constant (Λ) value,[21] the uncertainty in the PMMA to water dose conversion factor, and the film/seed spacing uncertainty,

which together amounted to a total uncertainty of 5.4% using Eq. 3.7. These uncertainties were then used when including dose uncertainties in the calibration curve fitting. Uncertainties in film/seed spacing were small as the seed phantom was built to high tolerances (±0.05 mm); the dose uncertainty due to film/seed spacing uncertainty was determined by calculating the differences in dose at distance d = 1.25 and d ± 0.05 mm. Uncertainties in irradiation time were deemed negligible as all irradiation times were significantly longer than the timing uncertainty (the shortest irradiation time was over one hour, while the timing uncertainty of placing/removing the seed in the phantom was a few seconds).

The percent standard deviations in the film doses were found using Eq. 3.10:

$$\sigma_{D_{film}}(\%) = \frac{\sqrt{\left(\frac{\partial D_{film}}{\partial OD}\right)^2 \sigma_{OD}^2 + \left(\frac{\partial D_{film}}{\partial a}\right)^2 \sigma_a^2 + \left(\frac{\partial D_{film}}{\partial b}\right)^2 \sigma_b^2 + \left(\frac{\partial D_{film}}{\partial c}\right)^2 \sigma_c^2 + \left(\frac{\partial D_{film}}{\partial D_{ref}}\right)^2 \sigma_{D_{ref}}^2}}{D_{film}} \times 100\% \qquad (3.10)$$

where D_{film} is given by Eq. 3.5, and D_{ref} is the reference dose $\left(\frac{\partial D_{film}}{\partial D_{ref}}\text{is equal to } 1\right)$, and σ_a, σ_b, σ_c are the calibration fitting parameter uncertainties. The uncertainty components are given by:

$$\frac{\partial D_{film}}{\partial OD} = \frac{\ln(10)10^{OD}(a - b\cdot c)}{\left(b\cdot 10^{OD} - 1\right)^2} \qquad (3.11)$$

$$\frac{\partial D_{film}}{\partial a} = \frac{10^{OD}}{1 - b\cdot 10^{OD}} \qquad (3.12)$$

$$\frac{\partial D_{film}}{\partial b} = \frac{10^{OD}\left(a\cdot 10^{OD} - c\right)}{\left(b\cdot 10^{OD} - 1\right)^2} \qquad (3.13)$$

$$\frac{\partial D_{film}}{\partial c} = \frac{1}{b\cdot 10^{OD} - 1} \qquad (3.14)$$

The uncertainty analysis is summarized in Table 3.1 for the red channel dose calculations using the I-125 seed. The same procedure is followed for the other colour channels, and for the 6 MV, 75 and 200 kVp irradiations.

Table 3.1 Uncertainty analysis for dose conversion from optical density for I-125 irradiated films (red channel) (coverage factor k=1 for all values). Values in parentheses are the uncertainties when using the 75 kVp calibration curve to determine I-125 doses.

Source of uncertainty	<20 cGy		20-100 cGy		>100 cGy	
	Type A	Type B	Type A	Type B	Type A	Type B
Propagated uncertainty in dose from OD uncertainty	4.1% (3.2%)		2.2% (1.5%)		1.6% (1.2%)	
I-125 seed air-kerma strength, S_k		1.75% (-)		1.75% (-)		1.75% (-)
Dose rate constant (Λ) (Ref. 8)		4.8% (-)		4.8% (-)		4.8% (-)
PMMA to Water dose conversion factor		1.5% (-)		1.5% (-)		1.5% (-)
External beam reference dose		- (1.0%)		- (1.0%)		- (1.0%)
Film-seed positioning (phantom construction)		0.9% (-)		0.9% (-)		0.9% (-)
OD to dose conversion using calibration curve		9.6% (4.9%)		2.7% (1.7%)		0.9% (0.5%)
Conversion between modalities/energies		- (9.8%)		- (4.4%)		- (1.6%)
Total uncertainty (quadrature sum of all uncertainties)	11.9% (11.5%)		6.5% (5.0%)		5.7% (2.3%)	
Expanded uncertainty: k=2	23.4% (22.9%)		13.0% (10.1%)		11.4% (4.6%)	

3.2.5 Film heterogeneity correction method

The film heterogeneity correction method is based on the methods described by van Hoof *et al.,*[16] Micke *et al.,*[18], and Mayer *et al.*[30]. All of these methods derive from the Beer-Lambert law of absorption, from which it follows that the scanned optical density value at any point is inversely proportional to a dimensionless measure of the thickness of the active layer in the film:[18]

$$OD = \frac{OD_D}{\bar{\tau}/\tau} \qquad\qquad (3.15)$$

This separates the optical density into two components, one dependent only on the exposure/dose (OD_D), and one dependent on the thickness (τ). Given that the film in any batch will have an average thickness, a disturbance value can be defined as the ratio of the average film thickness

for the batch and the film thickness at a given pixel location on a particular film piece ($\bar{\tau}/\tau$). The calibration curves for each channel are derived from large enough pieces of film such that they can be assumed to be unaffected by variations in film thickness, i.e. $\bar{\tau}/\bar{\tau}_{cal} = 1$, which is why they do not require any heterogeneity corrections.

When examining the film on a pixel-by-pixel basis, the dose calculated from any of the three colour channels using the pre-determined calibration curves, given by Eq. 3.16 (where 'k' denotes the colour channel, either R, G, or B), should result in identical values of dose. However, due to the aforementioned dose-independent non-uniformities, slightly different values for dose will be obtained for each colour channel. The differences in dose are attributed to the channel-independent disturbance value, $\Delta d = \bar{\tau}/\tau$, which accounts for the non-uniformities and perturbs the measured optical density, resulting in a slightly different calculated dose as described in Eq. 3.17.

$$D_k = \frac{c_k \cdot 10^{-OD} - a_k}{b_k - 10^{-OD}} = f_k(OD) \tag{3.16}$$

$$D_k = f_k(OD \cdot \Delta d) \tag{3.17}$$

The dose in each channel is now calculated as:

$$D_k = \frac{c_k \cdot 10^{-OD_k \cdot \Delta d} - a_k}{b_k - 10^{-OD_k \cdot \Delta d}} \tag{3.18}$$

Since the actual dose cannot depend on the colour channel used, the dose independent of any film inhomogeneities can be found by minimizing the difference in the calculated dose from all three colour channels through the least squares minimization equation given by Eq. 3.19. The solution for Δd is found by solving the non-linear equation given by Eq. 3.20.

$$\Omega(\Delta d) = \sum_{i \neq j} \left(D_{k_i} - D_{k_j} \right)^2 \rightarrow \frac{min}{\Delta d} \tag{3.19}$$

$$\frac{d}{d\Delta d}\Omega = 0 \tag{3.20}$$

This can be solved iteratively, or by using a brute force approach.[16] The iterative approach was implemented using Newton's method to solve Eq. 3.20, whereas the brute force approach was carried out by calculating the objective function in Eq. 3.19 for a range of disturbance values and accepting the disturbance value resulting in a local minimum following third-order polynomial fitting to the data. Both methods were assessed and resulted in similar corrected values for dose

up to ~15 Gy, beyond which the brute force approach over-estimated the corrected dose. The latter method was found to be strongly dependent on the ability to apply a polynomial fit to the objective function in order to determine the minimum, often giving a local minimum instead of the global minimum (similar problem as using a polynomial function for the calibration curve to relate dose and OD). On the other hand the iterative method matched known dose values consistently up to the maximum dose in the calibration curve.

The iterative approach is performed by first making an initial "guess" for Δd (equal to 1, which assumes the film thickness is equal to the average thickness) to calculate the objective function, in this case $d\Omega/d\Delta d$, which is then used to create a second "guess" and so forth (described by Eq. 3.21 – 3.23) until either the difference between x_{n+1} and x_n is below a threshold value or a pre-set maximum number of iterations have been performed. A threshold value of 10^{-12} and maximum number of iterations of 40 were found to be sufficient to converge on the solution.

$$x: f(x) = 0 \tag{3.21}$$

$$x_1 = x_0 - \frac{f(x_0)}{f'(x_0)} \tag{3.22}$$

$$x_{n+1} = x_n - \frac{f(x_n)}{f'(x_n)} \tag{3.23}$$

For the implementation here, $f(x) = d\Omega/d\Delta d$, and $f'(x) = d^2\Omega/d^2(\Delta d)$.

To minimize the effects of scanner non-uniformities, three scans of each film piece are first averaged together, followed by application of the iterative triple-channel correction method. The optimized disturbance value so determined is then used to calculate the corrected dose in each colour channel. The final dose, D_w, is taken as a weighted mean of the corrected doses in each channel:

$$D_w = w_R \cdot D_R + w_G \cdot D_G + w_B \cdot D_B \tag{3.24}$$

where w_R, w_G, and w_B are applied weights determined by the relative uncertainties in dose in each channel for the given dose level, and D_R, D_G, and D_B are the corrected doses. A number of different dose levels are used in which the relative weights change depending on the sensitivity and uncertainty of each colour channel at a given dose level; see Section 3.2.4. The dose levels are 0-20, 20-80, 80-300, 300-1150, and >1150 cGy, expanding beyond the number of dose levels

used to assess the accuracy of the different calibration methods. The applied weights are determined using Eq. 3.25:

$$W_{R,G,B} = \frac{w_i^{-2}}{\Sigma_{i=1}^3 w_i^{-2}}$$ (3.25)

where w_i is given by:

$$w_i = \left(\frac{\Sigma_{i=1}^3 \sigma_i}{\sigma_i}\right)^{-2}$$ (3.26)

and σ_i is the uncertainty in dose for one colour channel as derived in Section 3.2.4. This results in the colour channel(s) with lower uncertainties having a higher weight and the channel(s) with larger uncertainties having a lower weight in the final weighted mean dose, D_w.

3.2.6 Enhanced Dynamic Wedge (EDW) fields

The iterative triple-channel film heterogeneity correction method was validated using 6 MV 8 x 8 cm^2 60° EDW fields at 5 cm depth from a Varian 21iX linac (Varian Medical Systems, Palo Alto, CA). Film calibration for the EDW fields was performed following the methods outlined in Section 3.2.3 using a 6 MV photon beam from the same linac. Two-piece calibration curves with the inclusion of uncertainties in dose and OD using the EV$_{opt}$ method were created using 9 dose levels (ranging from 13.2 to 3767.4 cGy) and three separate un-irradiated pieces of film.

The EDW treatment plans were created using the Eclipse v.11 TPS (Varian Medical Systems Inc., Palo Alto, CA) to deliver maximum doses (at the toe end of the wedged field) of 2, 10, 20 and 35 Gy. The plans were delivered to 10x10 cm^2 pieces of film at 100 cm SAD in Solid Water with 5 cm of buildup (5 cm depth, 95 cm SSD) and 12 cm of backscatter. Profiles of the wedged fields were obtained by averaging a 7.1 mm wide (20 pixels at 72 dpi) region through the middle of the field.

3.2.7 Iterative triple-channel method uncertainty analysis

Uncertainty calculations for the triple-channel heterogeneity corrected film measurements follow the same methods outlined in Section 3.2.4. The relative uncertainty in the weighted average dose from Eq. 3.24 is:

$$\sigma_{D_w}(\%) = \left[w_R^2\left(\sigma_{D_R}^2\right) + w_G^2\left(\sigma_{D_G}^2\right) + w_B^2\left(\sigma_{D_B}^2\right)\right]^{1/2} \cdot \frac{100}{D_w} \tag{3.27}$$

The consistency of the triple-channel correction, C_{TC}, is equal to:

$$C_{TC} = \frac{1}{3}\sum_{\substack{i,j=1 \\ i \neq j}}^{3}\left|D_i - D_j\right| \tag{3.28}$$

The percent uncertainty in dose for the triple-channel analysis is:

$$\sigma_{TC}(\%) = \frac{1}{3}\sum_{\substack{i,j=1 \\ i \neq j}}^{3}\left|D_i - D_j\right| \cdot \frac{100}{D_w} \tag{3.29}$$

The total Type B uncertainty in the film dose is:

$$\sigma_{B,film}(\%) = \left[\left(\sigma_{D_w}(\%)\right)^2 + \left(\sigma_{TC}(\%)\right)^2\right]^{1/2} \tag{3.30}$$

When taking the average dose ($\overline{D}_w$) from a larger area composed of N pixels that have a standard deviation σ_N, the Type A uncertainty in the average dose is:

$$\sigma_{A,film}(\%) = \frac{\sigma_N}{\sqrt{N}} \cdot \frac{100}{\overline{D}_w} \tag{3.31}$$

The total combined uncertainty for an average dose measurement is:

$$\sigma_{\overline{D}_w}(\%) = \left(\sigma_{A,film}(\%)^2 + \sigma_{B,film}(\%)^2\right)^{1/2} \tag{3.32}$$

3.3 Results

3.3.1 Calibration curves

Measured optical densities for the EBT3 film as a function of absorbed dose in water are shown for each colour channel at each irradiation energy in Figure 3.2. A small difference can be seen for all three colour channels between the different energy irradiations, most noticeably between the 6 MV beam and the other energies, and only very slight differences are observed between the lower energy modalities.

The red channel optical densities obtained for the NIST calibrated Tiffen Transmission Photographic Step Tablet #2 and those reported on the step tablet certificate are shown in Figure 3.3. The scanner was found to have a linear response up to a NIST calibrated OD of approximately 1.7, which was measured to be an OD of 1.13 using Eq. 3.1 and the measured red

channel PV. As can be seen from the red, green and blue channel optical densities measured for the 6 MV irradiations, an OD of 1.13 would occur at a dose greater than 42 Gy, therefore the scanner response is linear within the dose range of interest.

For the various fitting methods used to determine the calibration parameters, all methods result in similar parameters and the overall improvement of one method over another is quite small. In order to quantify the differences between fitting methods, the percent differences between reference and film dose values using Eq. 3.5 with the fitted calibration parameters and the measured ODs were compared, as can be seen in Figure 3.4.
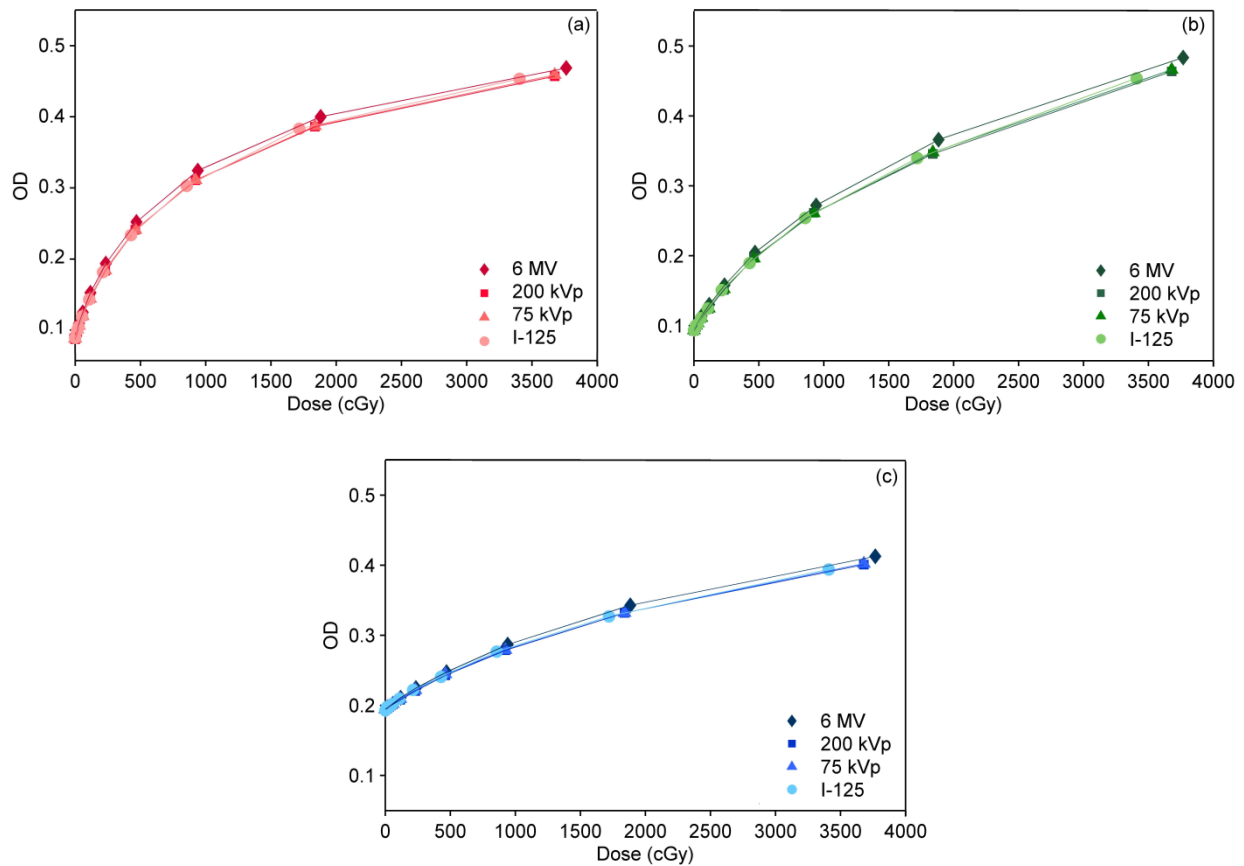
Figure 3.2 Red (a), green (b) and blue (c) channel film responses at each irradiation energy.
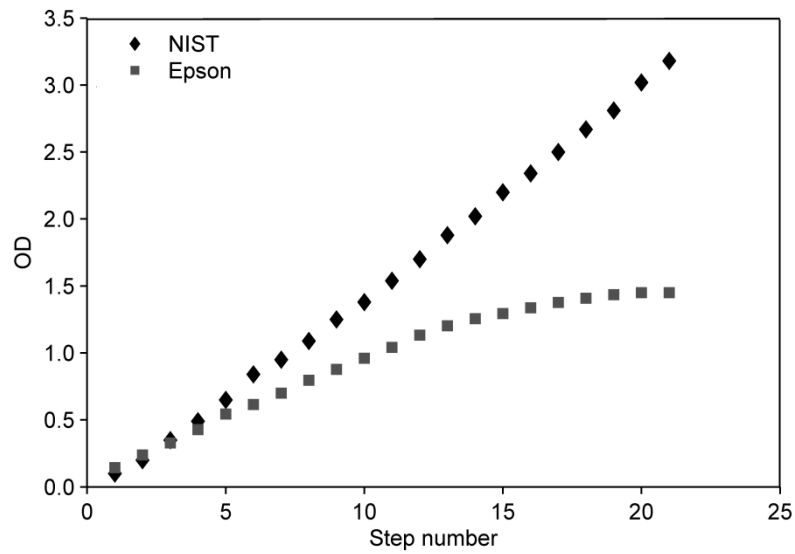
Figure 3.3 Comparison of NIST calibrated Tiffen Transmission Photographic Step Tablet #2 OD and Epson 10000XL measured OD (red channel).
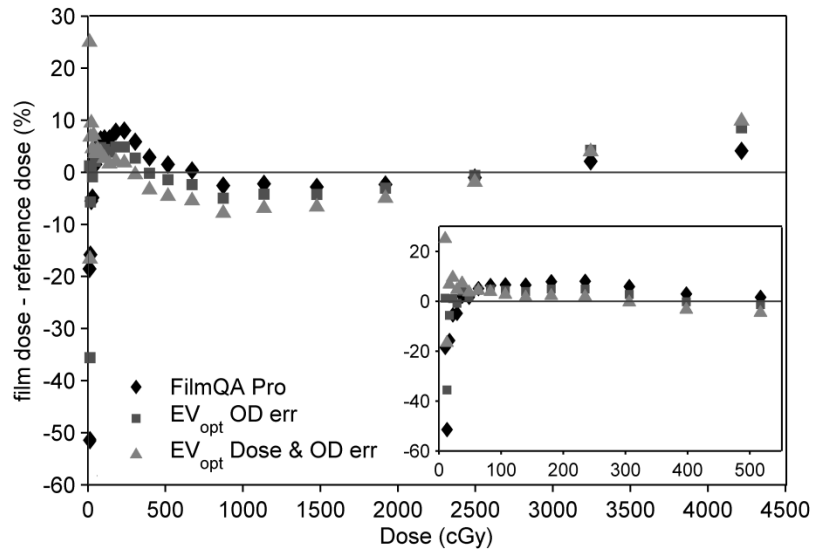
Figure 3.4 Absolute percent difference between reference and film doses for 6 MV irradiations with and without inclusion of uncertainties in OD and dose (6 MV data with 24 dose levels was analyzed). The inset shows the data for the lower doses on an enlarged dose axis.

When including uncertainties in the OD values as well as in the dose values, the most notable difference between the film and reference doses as compared to when no uncertainties are included (equal weighting) is the improvement in fitting at low doses and the worsening of the fit at high doses. For all fitting methods, the fitting in the mid dose range (200-800 cGy, the most "curved" region of the calibration curve), most notably for the red channel and to a lesser extent in the green and blue channels, was not ideal and a greater difference between the reference and film doses was observed. The improvements obtained when using piece-wise fitting with the inclusion of uncertainty in dose and OD (EV_{opt} method) in the red channel, which split the data into low dose (<517 cGy) and high dose (>517 cGy) regions are shown in Figure 3.5. Improvements were found at nearly all dose levels, the most significant being at doses below 30 cGy and in the section of the calibration curve having the greatest curvature between 60 and 500 cGy. Improvements were also found when using piece-wise fitting in the green and blue channels, but to a lesser extent than in the red channel.

When reducing the number of data points from the initial number considered to only 4 or 5, it was found that the accuracy of the resulting calibration curve was not noticeably affected. The average accuracy of the 6 MV calibration curve worsened by 0.9%, while for the I-125 calibration curve there was no average decrease in accuracy as long as the geometric progression was maintained and the highest dose level was included in the calibration curve.

For the I-125 irradiated films, when the measurement area was reduced to a small central region 2.47 x 2.47 mm^2, the calibration parameters obtained using the FilmQA Pro software were only slightly affected. However, when comparing the film doses using the larger 2.47 mm x 7.4 cm area averaged ODs, the accuracy of the film doses was found to be reduced on average by 1.1%, 0.75%, and 2.7% in the red, green and blue channels, respectively, and the percent difference of individual reference points was increased by up to 3.8% in the red channel. This indicates the necessity of averaging over a larger film area when measuring ODs as opposed to netODs (as measuring netODs allows for explicit correction of film heterogeneities if images are registered accurately).
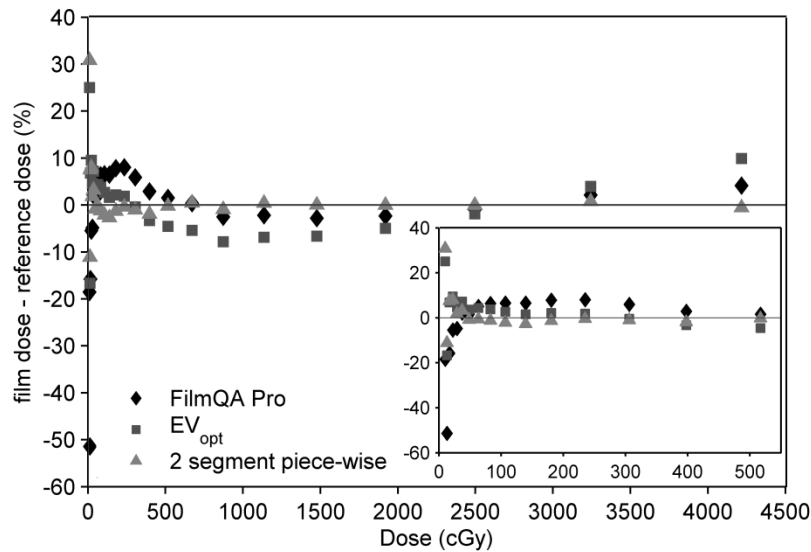
Figure 3.5 Absolute percent difference between reference and film doses for 6 MV irradiations when using one segment (FilmQA Pro (no uncertainties included) and EV_{opt} with inclusion of uncertainties in OD and dose) and two-segment piece-wise fitting (using EV_{opt} method with inclusion of uncertainties in OD and dose). The inset shows the data for the lower doses on an enlarged dose axis.

3.3.2 Energy dependence of film

The normalized OD values calculated from the piece-wise calibration curves are shown in Figure 3.6. At doses above 200 cGy, where the uncertainties are smaller, there is at most a variation in response due to energy of ~3%, which appears to reduce slightly as the dose increases. This trend has been observed in other studies for EBT and EBT3 film,[12,13,31] and may be due to the exponential nature of the polymerization process, or due to some intrinsic energy dependence which varies with dose.[14] However, this assessment warrants careful analysis as the normalized OD values were found to be very sensitive to the initial OD of the un-irradiated films, which will change over time.[4] The energy dependence observed with this film batch was found to be similar to what was observed for EBT3 film by Brown *et al.*,[11] but was less than what was observed by other studies,[13,15] suggesting that the energy dependence of each batch of film may vary and so should be analyzed if the intended application warrants it. The smaller under-response of the I-125 irradiated films compared to the 75 kVp and 200 kVp irradiated films is likely due to the significantly longer irradiation times, which would allow for greater polymerization of the film

106

prior to scanning compared to the other modalities where the dose is delivered in a matter of minutes (as opposed to days).

If the calibration curves obtained from the 200 kVp or 6 MV irradiations are used to determine dose values from I-125 irradiated films, errors in the film dose of up to 4.3% and 7.6% respectively above 1 Gy are obtained. The difference in I-125 doses obtained using the 75 kVp calibration curve is smaller at all dose levels; at doses above 1 Gy it is at most 2.3% (in the blue channel; it is less in the red and green channels). For the EBT3 film lot used in this study, the energy dependence from 200 kVp or 6 MV down to ~28 keV is large enough that neither of these energies should be used for calibration of I-125 irradiation measurements. The 75 kVp calibration curve however could be used to make I-125 dose measurements, but the uncertainties in film doses would need to be increased slightly to account for energy-response differences (uncertainties obtained when using the 75 kVp calibration curve for the I-125 doses are shown in Table 3.1; the additional uncertainty due to conversion between energies/modalities is included).
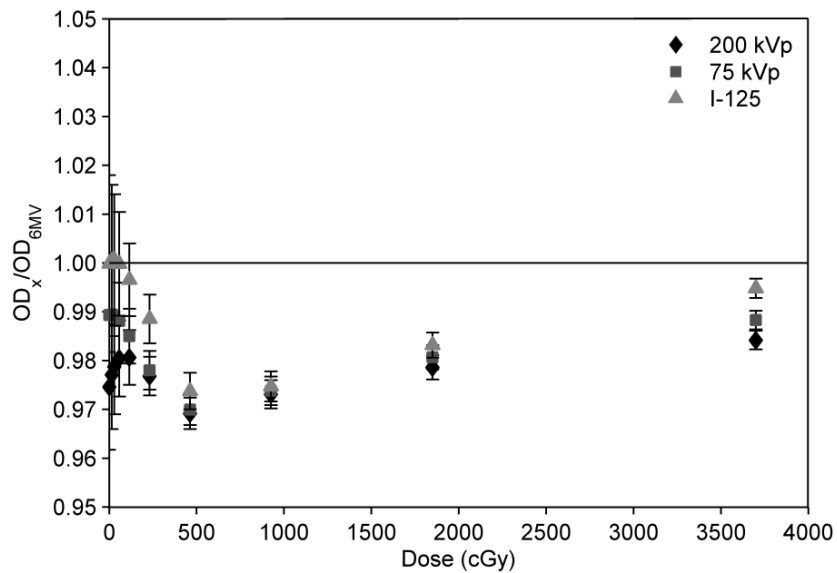
Figure 3.6 Normalized red channel OD values for each irradiation energy.

3.3.3 Film calibration dose uncertainties

For dose measurements performed using a piece-wise calibration curve, the uncertainty in dose was found to depend on the particular dose value in question. Due to the increased inaccuracy of the calibration curves at very low doses, the uncertainties were larger below 20 cGy and progressively decreased at higher dose. The uncertainties for each colour channel at each irradiation energy for low, medium and high dose ranges are summarized in Table 3.2.

Table 3.2 Average percent uncertainties in calculated doses for each color channel and irradiation energy.

Energy	<20 cGy			20-100 cGy			>100 cGy		
	Red	Green	Blue	Red	Green	Blue	Red	Green	Blue
6 MV	9.7	9.3	28.7	3.5	3.1	8.7	1.6	1.5	2.3
200 kVp	7.6	13.2	26.2	3.3	5.0	9.1	1.6	1.6	2.0
75 kVp	7.0	13.2	24.5	3.3	5.8	11.2	1.6	1.6	2.1
I-125	11.9	9.5	19.2	6.5	6.3	8.0	5.7	5.7	5.8

3.3.4 Enhanced Dynamic Wedge (EDW) fields

The film measured doses for the EDW fields agreed with profiles from Eclipse within 1-2% up to ~18 Gy. The 2 and 10 Gy EDW fields agreed with Eclipse over the entire field, while the 20 and 37 Gy fields only showed agreement within less than 2% up to 18 Gy, above which the agreement was within 5-8%. This is larger than the uncertainty in the film measured doses, which range from 3-5% (k=2) depending on the dose level within the main part of the field. The consistency between channels, using Eq. 3.29 but prior to applying the triple-channel correction method, showed larger differences above ~18 Gy. This results in values of $|\Delta d|$ greater than 1.05 (i.e. more than a 5% correction when applying the triple-channel correction method), resulting in over-correction of the dose.

For the 2 and 10 Gy EDW fields, the triple-channel correction method resulted in consistent dose agreement with Eclipse across the field, as shown in Figure 3.7 for the 10 Gy EDW field. The corrected dose distribution and Δd map are shown in Figure 3.8, while the colour channel consistencies prior to and post triple-channel correction are shown in Figure 3.9.
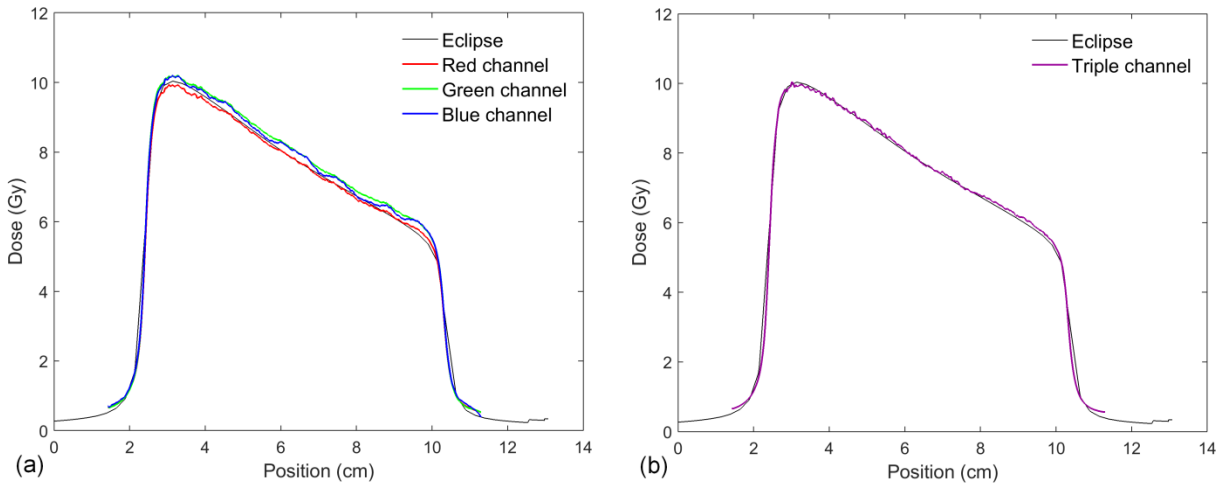
Figure 3.7 Dose profile comparing the planned/expected dose distribution for the 10 Gy 6 MV 60° EDW field from Eclipse with the uncorrected red, green and blue channel doses (a); and the dose profile comparing the planned dose distribution with the doses corrected for film thickness variations using the triple-channel method (b).
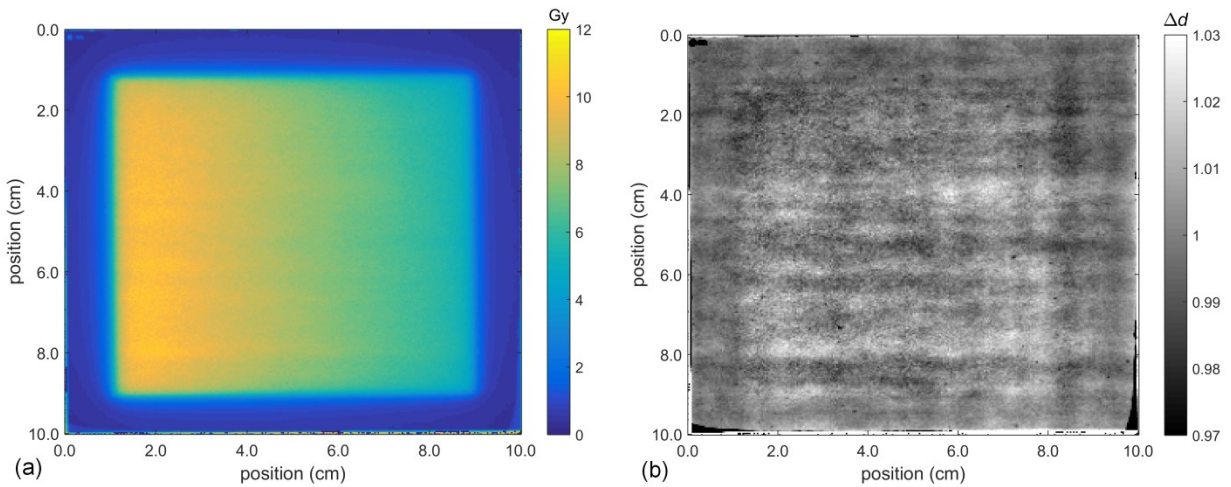
Figure 3.8 Corrected dose map for the 10 Gy 6 MV 60° EDW field (a); disturbance (Δ*d*) map used to correct the dose for thickness variations in the film (b).
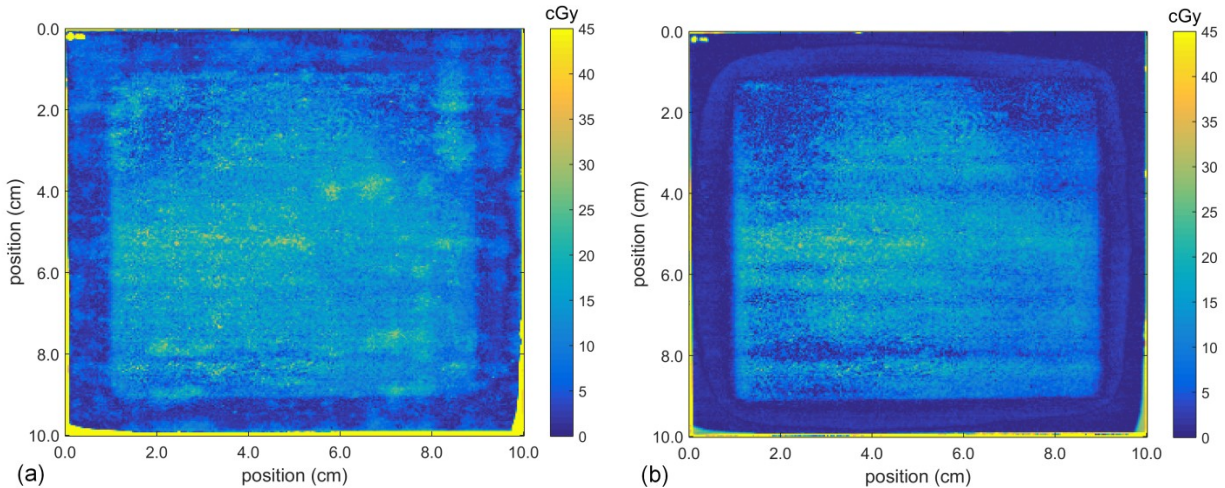
Figure 3.9 Red, green, and blue channel consistency images pre (a) and post (b) triple-channel correction showing the improvement in dose agreement between channels following the application of the triple-channel heterogeneity correction.

3.4 Discussion and conclusions

3.4.1 Film calibration

The method of curve fitting which results in the most accurate calibration curve was found to be two-segment piece-wise fitting with inclusion of OD as well as dose uncertainties. This method was found to best account for variations in the film response (seen in differences in measured ODs) as well as uncertainties in the dose which could affect the measurements. Using this method it is found that the accuracy of a dose estimate derived from a measurement of average OD over an area large enough to be unaffected by film heterogeneities is generally dependent on the dose level, specifically whether it is a low dose below 20 cGy, a moderate dose between 20 and 100 cGy, or a larger dose above 100 cGy. Typically for clinical XRT dosimetry measurements, the doses will be greater than 100 cGy except in certain highly modulated fields; so, the expected uncertainty in the dose will be on the order of 1.6%. The dose uncertainties are considerably higher at doses below 20 cGy as well as in the dose range 20-100 cGy, however they are still only on the order of a few cGy. If more accurate dose measurements are required at low doses, linear interpolation between low-dose calibration points could be performed as the calibration curve is highly linear in this region. The slightly higher dose uncertainty observed

110

when using the low-energy brachytherapy seed is primarily due to the increased uncertainty in the reference doses, this being limited to the accuracy with which the seed strength and dose rate constant can be specified.

When including the uncertainty in the dose values in determining the calibration curve parameters, the smaller uncertainties at low doses (on the order of fractions of cGy as opposed to tens of cGys) create tighter constraints on the fitting at low doses and looser constraints at high doses, which causes improvement in the fit at low doses and increased inaccuracy at high doses. At first glance it may appear that including uncertainties in OD and dose in the curve fitting process creates an overall worse fit. However, it may better represent the variations that can occur in measured optical densities of the film arising from variations in radiation generator output, film heterogeneity, and scanner output.

The calibration curve fitting approach reported by the film manufacturer and others[4,24,27] is, as mentioned, primarily applicable at doses below 5 Gy. When restricting calibrations to these moderate doses, using a single-segment calibration curve results in acceptable accuracy as is seen in the high pass rates obtained when performing plan comparisons using the gamma pass criteria.[2–5,18] However when calibrating across a larger dose range up to ~35 Gy, particularly in the red channel in the region in which the slope changes significantly (100-1000 cGy), the fit is much less accurate. This could result in dose errors of up to 10%, which would be unacceptable when validating treatment plan doses or performing other dosimetry studies. However for two-segment piece-wise fitting over the larger dose range, at doses above 100 cGy, higher levels of accuracy are achievable which are similar to those reported over the smaller dose range for linac irradiated films.[24,27] The dose uncertainties for the brachytherapy doses estimated in this study pertain to a single seed within an irradiation phantom fabricated to high tolerances, and it should be noted that set-up uncertainties in other measurement situations (i.e. multiple sources in a brachytherapy applicator) could increase the dose uncertainties. The I-125 dose determinations performed using the 75 kVp calibration curve were slightly outside the uncertainties in the 75 kVp determined doses. If the percent difference between these values and the actual I-125 reference doses is included as the uncertainty when using the different modality for dose determination, the uncertainty in the I-125 doses is expanded to 2.3% above 1 Gy (as seen in Table 3.1). This expanded uncertainty is less than half that of the I-125 doses determined using the I-125 calibration curve, and therefore the use of the 75 kVp calibration curve to determine I-

125 doses could offer a significant accuracy benefit. This approach lowers the uncertainty in dose for film dosimetry methods compared with those previously published for brachytherapy applications which were shown to have uncertainties ranging from 3-7% above 1 Gy.[10,32] As mentioned earlier, it also has the benefit of requiring much less time to obtain the full calibration curve (a couple of hours as opposed to days and weeks) and also allows for larger film measurement areas to ensure that film heterogeneities are not negatively affecting the calibration curve.

It is, therefore, recommended that when performing dose measurements over a larger range up to or exceeding 35 Gy, whether it is with an external beam modality or a low-energy brachytherapy source, a fitting function that well represents the film characteristics over the larger dose range such as that given by Eq. 3.4 be used. As well, two-segment piece-wise fitting should be performed to obtain dose measurements with lower uncertainties similar to those for low and moderate doses of up to 5 Gy. The number of data points used in creating the calibration curve can be fairly low as suggested by the film manufacturer, however if performing piece-wise fitting the number of data points within each curve segment would still need to be 4-5. So, with a minimum of two overlapping points in the two segments, a minimum of 6 data points plus a blank are required and should be arranged in a geometric progression. If performing low-energy brachytherapy EBT3 film-based dose measurements, a calibration curve can be established using a comparable low-energy external beam x-ray source, keeping in mind that the dose uncertainties may need to be expanded slightly to account for the energy difference. The overall uncertainties will however likely still be lower than if the low-energy brachytherapy source were used for calibration.

3.4.2   Film heterogeneity correction and EDW fields

The sensitivity of each colour channel for EBT type films changes depending on dose, because the light absorption spectrum changes as the film darkens when exposed to radiation.[33] Also, beyond even 10 Gy, the sensitivity of the red channel is significantly lower than the green and blue channels.[27] The significance of this effect will become more pronounced as the time between the irradiation of the calibration films and any experimental films increases. The agreement in the triple-channel correction method was demonstrably more consistent when applied to the films that made up the calibration curve, as there is no time difference between

irradiation of the calibration films and measurement films, both being one and the same. The EDW films were measured approximately 2 months following the creation of the calibration curve, indicating that the calibration curve is useful up to this time, however with a narrower range of useful doses. For the EBT3 film measurements performed in the following chapter (Chapter 4), the 75 kVp calibration curve was obtained within 2 days of the film measurements; therefore this is not of concern for these measurements. The irradiated doses were also below 10 Gy, staying within the validated dose range when using the triple-channel correction method.

3.5 References

[1] O.A. Zeidan, S.A.L. Stephenson, S.L. Meeks, T.H. Wagner, T.R. Willoughby, P.A. Kupelian, and K.M. Langen, "Characterization and use of EBT radiochromic film for IMRT dose verification," Med. Phys. **33**, 4064–4072 (2006).

[2] N. van Wieringen, Y.R.J. van Herten, J.B. van de Kamer, A. Erogluer, A. Bel, and J. Wiersma, "Development of a QA procedure fo IMRT plans using EBT radiochromic film," Radiother. Oncol. **84**, S206 (2007).

[3] A. Mahata and P.B. Ravindran, "Investigation of the use of Gafchromic EBT film for routine IMRT QA," Radiother. Oncol. **84**, S54 (2007).

[4] D. Lewis, A. Micke, X. Yu, and M.F. Chan, "An efficient protocol for radiochromic film dosimetry," Med. Phys. **39**, 6339 (2012).

[5] V. Casanova Borca, M. Pasquino, G. Russo, P. Grosso, D. Cante, P. Sciacero, G. Girelli, M.R. La Porta, and S. Tofani, "Dosimetric characterization and use of GAFCHROMIC EBT3 film for IMRT dose verification," J. Appl. Clin. Med. Phys. **14**, 4111 (2013).

[6] N. Hardcastle, A. Basavatia, A. Bayliss, and W.A. Tomé, "High dose per fraction dosimetry of small fields with gafchromic EBT2 film," Med. Phys. **38**, 4081–4085 (2011).

[7] C. Fiandra, M. Fusella, F.R. Giglioli, A.R. Filippi, C. Mantovani, U. Ricardi, and R. Ragona, "Comparison of Gafchromic EBT2 and EBT3 for patient-specific quality assurance: cranial stereotactic radiosurgery using volumetric modulated arc therapy with multiple noncoplanar arcs," Med. Phys. **40**, 082105 (2013).

[8] E.S. Poon, B. Reniers, S. Devic, T. Vuong, and F. Verhaegen, "Dosimetric characterization of a novel intracavitary mold applicator for ^{192}Ir high dose rate endorectal brachytherapy treatment," Med. Phys. **33**, 4515–4526 (2006).

[9] S. Aldelaijan, H. Mohammed, N. Tomic, L.-H. Liang, F. DeBlois, A. Sarfehnia, W. Abdel-Rahman, J. Seuntjens, and S. Devic, "Radiochromic film dosimetry of HDR ^{192}Ir source radiation fields," Med. Phys. **38**, 6074 (2011).

[10] S.-T. Chiu-Tsao, D.C. Medich, and J. Munro, "The use of new GAFCHROMIC EBT film for ^{125}I seed dosimetry in Solid Water phantom," Med. Phys. **35**, 3787–3799 (2008).

[11] T.A.D. Brown, K.R. Hogstrom, D. Alvarez, K.L. Matthews, K. Ham, and J.P. Dugas, "Dose-response curve of EBT, EBT2, and EBT3 radiochromic films to synchrotron-produced monochromatic x-ray beams," Med. Phys. **39**, 7412–7417 (2012).

[12] P. Lindsay, A. Rink, M. Ruschin, and D.A. Jaffray, "Investigation of energy dependence of EBT and EBT-2 gafchromic film," Med. Phys. **37**, 571–576 (2010).

[13] G. Massillon-JL, "Energy Dependence of the New Gafchromic EBT3 Film: Dose Response Curves for 50 kV, 6 and 15 MV X-Ray Beams," Int. J. Med. Physics,Clinical Eng. Radiat. Oncol. **01**, 60–65 (2012).

[14] J.G.H. Sutherland and D.W.O. Rogers, "Monte Carlo calculated absorbed-dose energy dependence of EBT and EBT2 film," Med. Phys. **37**, 1110–1116 (2010).

[15] E.J. Villarreal-Barajas and R.F.H. Khan, "Energy response of EBT3 radiochromic films: Implications for dosimetry in kilovoltage range," J. Appl. Clin. Med. Phys. **15**, 331–338 (2014).

[16] S.J. van Hoof, P. V Granton, G. Landry, M. Podesta, and F. Verhaegen, "Evaluation of a novel triple-channel radiochromic film analysis procedure using EBT2," Phys. Med. Biol. **57**, 4353–4368 (2012).

[17] A. Niroomand-Rad, C.R. Blackwell, B.M. Coursey, K.P. Gall, J.M. Galvin, W.L. McLaughlin, A.S. Meigooni, R. Nath, J.E. Rodgers, and C.G. Soares, "Radiochromic film dosimetry: Recommendations of AAPM Radiation Therapy Committee Task Group 55," Med. Phys. **25**, 2093–2115 (1998).

[18] A. Micke, D.F. Lewis, and X. Yu, "Multichannel film dosimetry with nonuniformity correction," Med. Phys. **38**, 2523–2534 (2011).

[19] P.R. Almond, P.J. Biggs, B.M. Coursey, W.F. Hanson, M.S. Huq, R. Nath, and D.W.O. Rogers, "AAPM's TG-51 protocol for clinical reference dosimetry of high-energy photon and electron beams.," Med. Phys. **26**, 1847–1870 (1999).

[20] C.M. Ma, C.W. Coffey, L.A. DeWerd, C. Liu, R. Nath, S.M. Seltzer, and J.P. Seuntjens, "AAPM protocol for 40-300 kV x-ray beam dosimetry in radiotherapy and radiobiology," Med. Phys. **28**, 868–893 (2001).

21 M.J. Rivard, B.M. Coursey, L.A. DeWerd, W.F. Hanson, M.S. Huq, G.S. Ibbott, M.G. Mitch, R. Nath, and J.F. Williamson, "Update of AAPM Task Group No. 43 Report: A revised AAPM protocol for brachytherapy dose calculations," Med. Phys. **31**, 633–674 (2004).

22 G. Luxton, "Comparison of radiation dosimetry in water and in solid phantom materials for I-125 and Pd-103 brachytherapy sources: EGS4 Monte Carlo study," Med. Phys. **21**, 631–641 (1994).

23 J. Poder and S. Corde, "I-125 ROPES eye plaque dosimetry: Validation of a commercial 3D ophthalmic brachytherapy treatment planning system and independent dose calculation software with GafChromic® EBT3 films," Med. Phys. **40**, 121709 (11 pp.) (2013).

24 S. Devic, J. Seuntjens, E. Sham, E.B. Podgorsak, C.R. Schmidtlein, A.S. Kirov, and C.G. Soares, "Precise radiochromic film dosimetry using a flat-bed document scanner.," Med. Phys. **32**, 2245–2253 (2005).

25 B.C. Ferreira, M.C. Lopes, and M. Capela, "Evaluation of an Epson flatbed scanner to read Gafchromic EBT films for radiation dosimetry," Phys. Med. Biol. **54**, 1073–1085 (2009).

26 L.I. Ramos Garcia and J.F. Pérez Azorin, "Improving the calibration of radiochromic films by the use of uncertainties in optical density and dose," Med. Phys. **40**, 071726 (2013).

27 S. Devic, N. Tomic, C.G. Soares, and E.B. Podgorsak, "Optimizing the dynamic range extension of a radiochromic film dosimetry system," Med. Phys. **36**, 429–437 (2009).

28 White paper entitled "Gafchromic EBT2: Self-developing film for radiotherapy dosimetry," International Specialty Products, Wayne, NJ, October 2010, http://www.filmqapro.com.

29 B.N. Taylor and C.E. Kuyatt, "Guidelines for Evaluating and Expressing the Uncertainty of NIST Measurement Results," in *NIST Technical Note 1297* (U.S. Government Printing Office, Washington DC, 1994).

30 R.R. Mayer, F. Ma, Y. Chen, R.I. Miller, A. Belard, J. McDonough, and J.J. O'Connell, "Enhanced dosimetry procedures and assessment for EBT2 radiochromic film," Med. Phys. **39**, 2147 (2012).

31 C. Richter, J. Pawelke, L. Karsch, and J. Woithe, "Energy dependence of EBT-1 radiochromic film response for photon (10 kVp-15 MVp) and electron beams (6-18 MeV) readout by a flatbed scanner," Med. Phys. **36**, 5506–5514 (2009).

32 S.-T. Chiu-Tsao, J.J. Napoli, S.D. Davis, J. Hanley, and M.J. Rivard, "Dosimetry for ^{131}Cs and ^{125}I seeds in solid water phantom using radiochromic EBT film," Appl. Radiat. Isot. **92**, 102–114 (2014).

[33] S. Devic, S. Aldelaijan, H. Mohammed, N. Tomic, L. Liang, F. Deblois, and J. Seuntjens, "Absorption spectra time evolution of EBT-2 model GAFCHROMIC^{TM} film," Med. Phys. **37**, 2207–2214 (2010).

Chapter 4 Experimental verification of eye plaque dosimetry using radiochromic film

4.1 Introduction

Many experimental measurements have been performed with TLDs for the COMS and slotted style of eye plaques,[1–9] and with radiochromic (Gafchromic™) film for the COMS or Ropes style eye plaques.[10–13] However, none of the latter measurements used the newest model of Gafchromic film (EBT3) for either the COMS or Eye Physics (slotted) style of plaques. Several of these earlier studies were performed to investigate the impact of plaque heterogeneity effects compared to a homogeneous water scenario (TG-43 based calculations with no correction), whereas more recent studies examined the use of new types of brachytherapy seeds or plaques, or validated treatment planning calculated doses. The work presented in this chapter has a similar goal – to evaluate EBT3 film as an experimental dosimetry tool for eye plaques, but also to address some of the challenges in eye plaque dosimetry in general and to identify shortcomings that might exist in the currently used treatment planning system.

Using the film dosimetry method developed in Chapter 3, dose measurements were performed with EBT3 film in a custom designed eye phantom irradiated with two different styles of eye plaques (16 mm COMS and Super9) suspended in a water tank. Comparisons were made to Plaque Simulator TPS calculations utilizing MC simulated dosimetric parameters to account for the non-water components of the eye phantom. Reference MC simulations mimicking the experimental set-up for the 16 mm COMS plaque were also performed to validate the modified Plaque Simulator dosimetry parameter method, as well as to evaluate the accuracy of both the TPS calculations and the film measurements. In so doing, the accuracy with which eye plaque film measurements can be performed was investigated, some of the challenges that exist in radiochromic film dosimetry for eye plaques were elucidated, and insight was gained into what set-up uncertainties can affect the dose measurements and thus could be affecting patient treatment delivery.

4.2 Methods and Materials

4.2.1 Eye Phantom design and film measurements

A custom designed spherical PMMA eye phantom, 24.6 mm in diameter, was fabricated in house to hold a small piece of film at 6 mm depth (Figure 4.1(a)). The COMS eye plaques are designed based on a standardized eye size of 24.6 mm; with an assumed scleral thickness of 1 mm, 6 mm depth will be at a reference tumour height of 5 mm.

At 6 mm depth, the PMMA eye phantom holds a circular piece of film 16 mm in diameter. A 16 mm diameter cylindrical template was used to trace the circular piece of film. Small notches were cut into the film piece matching two notches in the PMMA eye phantom to keep the film from rotating or moving during irradiation. For irradiations, the eye phantom was sealed with plasticine to keep the film dry, and suspended in the centre of a water tank (WxHxD = 20.2 x 15.2 x 15.2 cm^3) to provide full backscatter conditions for I-125 sources (Figure 4.1(b)).
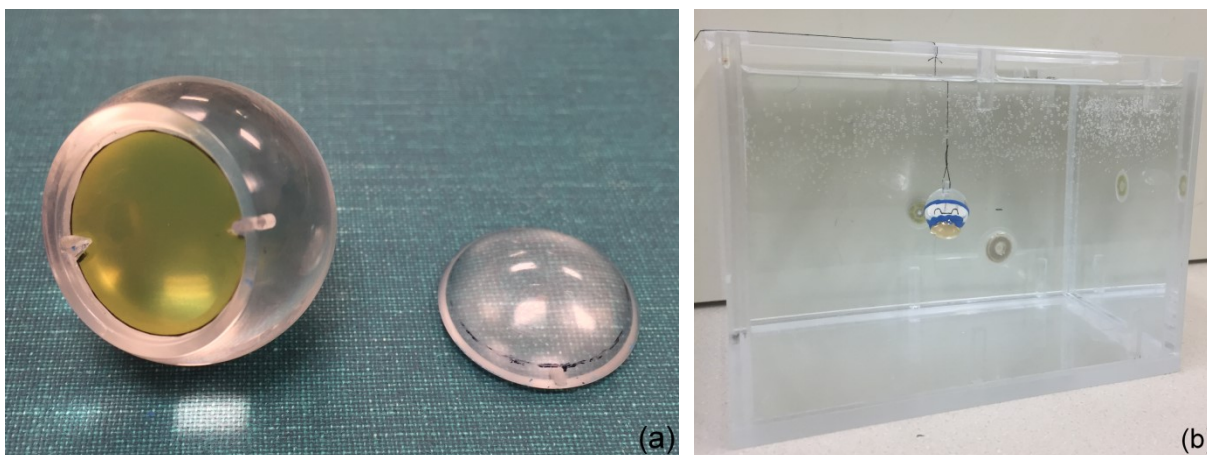
Figure 4.1 PMMA eye phantom designed to hold a piece of film at 6 mm depth (a), and phantom suspended in water tank with attached 16 mm COMS plaque (b).

Two different plaque types were used: a 16 mm COMS plaque (Trachsel Dental Studio, Rochester, MN) and a Super9 plaque (also known as a model #930 plaque) (Eye Physics LLC, Los Alamitos, CA)). The latter is frequently used at our facility for very posterior, juxta- or peri-papillary tumours due to its notched design accommodating the optic nerve sheath. The COMS plaque consists of a dome-shaped gold alloy (Modulay) backing which holds a seed carrier

(Silastic – MDX4-4210 bio-medical grade elastomer), while the Super9 plaque is made of standard 18K gold and has 7 mm long milled seed slots.

Film measurements using EBT3 film (lot # A0318303) were performed using a fully loaded 16 mm COMS plaque containing 13 I-125 seeds of 3.29 mCi average apparent activity at assay, and a nearly fully loaded Super9 plaque containing 26 seeds (of a possible 29) of 2.47 mCi average apparent activity at assay. For the latter, the middle slot in the central groove and the two slots next to the notch were empty, and seeds in the loaded slots were glued into the centers of the slots. The seeds used were model IAI-125A I-125 seeds (IsoAid LLC, Port Richey, FL). Each plaque was centered on the PMMA phantom above the film, attached using plasticine on the suture eyelets, and left in place to deliver ~7 Gy to the film centre. Due to the extended length and heavier weight of the Super9 plaque, it required additional plasticine on the notch ends to hold it in place, whereas the 16 mm COMS plaque was fixed only at the suture eyelets.

Film calibration was performed following the methods outlined in Chapter 3, with a 75 kVp photon beam from a Therapax DXT 300 Orthovoltage unit (Pantak Inc., East Haven, CT). Two-piece calibration curves with the inclusion of uncertainties in dose and OD using the EV_{opt} method were created using 8 dose levels ranging from 22.6 to 1311.6 cGy, and three separate un-irradiated pieces of film.

Two irradiations were performed for each style of plaque. The films were scanned 24 hours post-irradiation, and corrected doses were calculated using the triple-channel method described in Section 3.2.5. Due to the small size of the film pieces, they were scanned at 96 dpi and the central dose was determined from a region 1.85 x 1.85 mm^2 in size (size of region chosen to decrease film heterogeneity effects without undue dose averaging).

4.2.2   Plaque Simulator dosimetry parameters

For comparison with Plaque Simulator (version 6.2.1, Eye Physics LLC, Los Alamitos, CA), the physics file with the source data for the IsoAid IAI-125A seed was altered to calculate dose to water in PMMA. This was done by simulating TG-43 parameters for the IsoAid seed using MCNP6 (version 6.1),[14] scoring dose to water with particle transport through PMMA. The seed geometry was modelled based on Simulation condition 11 from Aryal *et al.*,[15] and the source photon spectrum was taken from the NNDC database,[16] though the 3.77 keV photons were not included.

To simulate the air kerma strength (S_K) in MCNP6 the seed was positioned in the centre of a vacuum sphere and the deposited energy was scored within a ±7.6° conical region around the transverse plane in a 0.00002 mm thick shell at a distance of 30 cm from the centre of the source with a cut-off energy of 5 keV. This setup mimics the sampling geometry of the National Institute of Standards Technology (NIST) wide angle free air chamber (WAFAC),[17] which better represents the clinical method for low-energy source calibration as compared with a point source measurement.[18] The deposited energy was scored using the *F4 track-length estimator and a DE/DF card containing values of mass energy-absorption coefficients in dry air from the NIST database[19] was used to convert the energy fluence to air kerma.

To calculate the TG-43 parameters, the seed was centered in a 30 cm radius sphere of PMMA with a density of 1.19 g/cm³. The dose rate constant, Λ, radial dose function, $g_L(r)$, and anisotropy factor, $F(r,\theta)$, were determined from dose data obtained by dividing the sphere into concentric spheres and conics, similar to the geometry used by Rivard *et al.*,[20] and scoring the deposited energy per unit mass in each subdivided region using the F6 track-length estimator. The parameters were then calculated using the equations in Section 2.1.3. Further details of the simulation geometry are provided in Section 6.2.2.1. To convert the scored dose in PMMA to dose in water, the F6 tally was modified by a DE/DF card containing the ratio of mass energy-absorption coefficients for water and PMMA using the values from the NIST XCOM database.[19] This approach assumes large cavity theory in which the dose to a different medium is found by:

$$D_{w,m} = K_{w,m} = (\mu_{en}(r)/\rho)_m^w \cdot K_{m,m} \tag{4.1}$$

where $K_{w,m}$ and $D_{w,m}$ are the collisional kerma and dose, respectively, to water (w) for photons transported through medium (m), and $K_{m,m}$ is equal to the F6 tally. The scoring regions are significantly larger than the range of secondary electrons, therefore the target is macroscopic in size, and large cavity theory applies (see Section 2.5.1).[21]

Similarly, parameters were determined for the Plaque Simulator transmission factor $T(r)$ and backscatter factor $B(r)$ for the COMS and Eye Physics slotted style plaques, respectively, from two simulations: one with the plaque materials defined, and one with all plaque materials set to PMMA. The energy deposited in water for radiation transport through PMMA ($D_{w,m}$) was scored in 0.5 x 0.5 x 0.5 mm³ voxels along the plaque CAX. $T(r)$ was determined using a single I-125 seed in the centre of a 12 mm COMS plaque (further details in Section 6.2.3.1), while $B(r)$

was determined using a single I-125 seed in a slot with dimensions matching those used in Plaque Simulator v6.2.1 for the Super9 plaque. The slot dimensions are shown in Figure 4.2. The plaque backing has a maximum thickness of 1.2 mm and an inner radius of curvature of 12.5 mm, leaving a 0.2 mm gap between the inner surface of the plaque and the eye, while the centre of the seed sits in contact with the eye (a sphere 24.6 mm in diameter). The plaque material is 18K gold (Au:Ag:Cu = 75%:15%:10% by weight) with a density of 15.58 g/cm^3.[22]
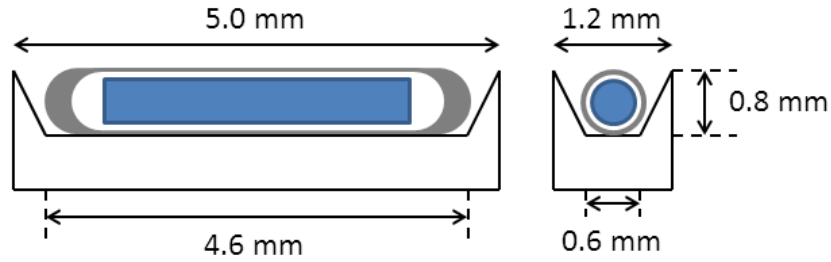
Figure 4.2 Geometric slot design of the Super9 plaque as modelled in Plaque Simulator.

Simulations of the IsoAid I-125 seed in PMMA to calculate the TG-43 parameters were done with 5×10^8 particles resulting in statistical uncertainties of 0.1% in the region of dosimetric interest (within a standard eye). Simulations for $T(r)$ and $B(r)$ were performed with 5×10^9 starting particles for each scenario (all PMMA, and with plaque materials in PMMA), resulting in statistical uncertainties of <0.15% at 6 mm depth. Simulations for $T(r)$ and $B(r)$ were also performed in water (instead of PMMA) for comparison with previously published values,[3,23] and agreed within 0.5% up to 25 cm from the source for $T(r)$, and within 0.6% up to 10 mm from the source for $B(r)$.

Simulating all TG-43 parameters and plaque heterogeneity corrections in this manner enables the dose to be calculated at any point as follows:

$$D_{w,m}(r,\theta) = S_k \cdot \Lambda_{w,m} \cdot g_L(r)_{w,m} \cdot F(r,\theta)_{w,m} \cdot \frac{G_L(r,\theta)}{G_L(r_o,\theta_o)} \cdot \begin{cases} t(d,\mu) \cdot T(r)_{w,m} & \text{COMS} \\ B(r)_{w,m} & \text{Super9} \end{cases} \quad (4.2)$$

In this way, the calculated dose at the film depth will be the dose to water (for which the film is calibrated) for photon transport through PMMA (the eye phantom material). Though Eq. 4.2

does not specifically account for the water medium surrounding the PMMA eye phantom, the dose contribution at the film center from scattered photons returning from outside the phantom, following the simple interaction model outlined by Astrahan,[24] will be ~<2% for each seed due to the high attenuation and rapid fluence fall-off of the low-energy photons. The difference in attenuation over two mean free paths (assuming a round-trip to make it back into the PMMA eye phantom) of I-125 photons in water (mean free path is 2.19 cm) compared with I-125 photons in PMMA is ~1.5%. For the <2% dose contribution from each seed, this means a difference in dose of <0.1%; therefore the effect of the different medium outside the eye phantom was deemed negligible.

The film depth was measured from high resolution microCT imaging of the eye phantom (details in Section 5.2.3) and the centre of the active layer of the film was found to be at a depth of 6.19 ± 0.09 mm from the outer surface of the phantom. Therefore, for dose calculation purposes the tumour height was set to 5.19 mm (accounting for the standard 1 mm scleral thickness) and treatment start and end times, and the I-125 source strengths, were set to those used for each film irradiation.

4.2.3   MCNP6 reference dose simulation at the film plane

An additional MCNP6 simulation was performed for the 16 mm COMS plaque fully loaded with IsoAid I-125 seeds, scoring dose to water in a thin layer of water at a depth of 6.19 mm ± 14 μm (the same thickness as the film active layer) in the PMMA eye phantom immersed in the experimental water tank [Figure 4.1(b)]. The *FMESH tally was used to create a 2D scoring grid in the water layer having scoring voxels of size 0.26 x 0.26 mm^2 (to match the scanned film resolution) x 28 μm. The *FMESH tally was modified by a DE/DF card containing mass-energy absorption coefficients for water to convert from photon fluence to dose to water using the NIST XCOM database.[19] Due to the small film thickness, some difference may be observed due to electrons not being tracked; however, a water layer with twice the thickness was also simulated and was found to result in equivalent values of scored dose within statistical uncertainties. More details on the geometry of the seeds and plaque in the MCNP6 simulation are given in Sections 6.2.2 and 6.2.3. The simulation was performed with 1×10^9 starting particles per seed, resulting in statistical uncertainties of <0.25% within the region matching the film location. This 2D reference dose distribution was used for comparison with both of the COMS plaque film

measurements, and as an independent validation of the implementation of the modified TG-43 parameters in Plaque Simulator.

To verify that the different medium outside the eye phantom was not affecting the doses within the eye region using the TG-43 $D_{w,m}$ method in Section 4.2.2, the above simulation was repeated, but with PMMA material outside of the eye instead of water.

4.2.4 Uncertainty analysis

Uncertainty calculations follow the same methods outlined in Section 3.2.7, using a 75 kVp calibration curve for I-125 irradiated film measurements, with the addition of uncertainties in film positioning, plaque placement and plaque tilt. The uncertainty in film positioning accounts for the difference in dose due to the uncertainty in the depth of the film. This was calculated in Plaque Simulator from the change in dose when moving ± 0.09 mm in depth at a tumour apex height of 5.19 mm. An estimate of the accuracy with which the plaques were centered on the eye phantom, as well as the amount of tilt occurring during irradiation were also included. The dosimetric effects of these were calculated in Plaque Simulator from the change in dose at the tumour apex with plaque movement or tilt. It was assumed that the plaques were centered on the phantom within 0.25 mm for both plaque types. The tilt in the COMS plaque was estimated to be 0.4 mm (a rotation of the plaque is also applied to bring the eyelets back in contact with the eye surface); for the Super9 plaque it was assumed to be zero due to the additional plasticine used to hold the plaque in place. Plaque placement and tilt uncertainties are based on the uncertainty analysis findings in Chapter 5.

The uncertainty in Plaque Simulator calculated dose follows the values outlined in the AAPM TG-138 document[25] and the methods in Aryal *et al.*[15] Uncertainties in the TPS calculated dose include: the source air kerma strength, which is taken from the manufacturer's assay; uncertainties in each TG-43 parameter and in the plaque heterogeneity correction factors [$T(r)$ and $B(r)$], all of which are derived from the MCNP6 simulations; and TPS interpolation/extrapolation uncertainties.

The uncertainties in the MCNP6 reference dose simulation at the film plane include those associated with tally statistics, mass-energy absorption coefficients for conversion from fluence to dose, the physics of the MC code, phantom composition, the source photon spectrum, and

mass attenuation coefficients for phantom attenuation (values adopted from Aryal *et al*. for the IsoAid I-125 seed).[15]

4.3 Results

4.3.1 Plaque Simulator, film, and MCNP6 dose comparison

Film measured dose distributions for one each of the 16 mm COMS and Super9 trials are shown in Figure 4.3, and Plaque Simulator calculated and film measured doses along the plaque CAX for all four trials are given in Table 4.1.

The tumour apex doses calculated using Plaque Simulator for the 16 mm COMS plaque agreed within 0.06% with the MCNP6 calculated doses at the centre of the 2D film scoring region for the simulation with the fully loaded 16 mm COMS plaque, PMMA eye phantom and water tank. Dose profiles across this tumour apex plane in the eye showed overall good agreement as well, with slightly larger differences at farther off-axis positions (Figure 4.4).

The difference in dose at the centre of the eye at a tumour apex height of 5.19 mm for the simulation fully in PMMA medium compared to that with the PMMA eye phantom surrounded by water was 0.28% (as described in Section 4.2.3). As predicted, simulating the TG-43 parameters and eye plaque heterogeneity parameters in PMMA compared to the PMMA eye phantom surrounded by water has negligible effect at the tumour apex. However, this is no longer true at farther off-axis positions, where the differences in dose were up to 2% between the two simulations at 10.5 mm away from the central tumour apex location.
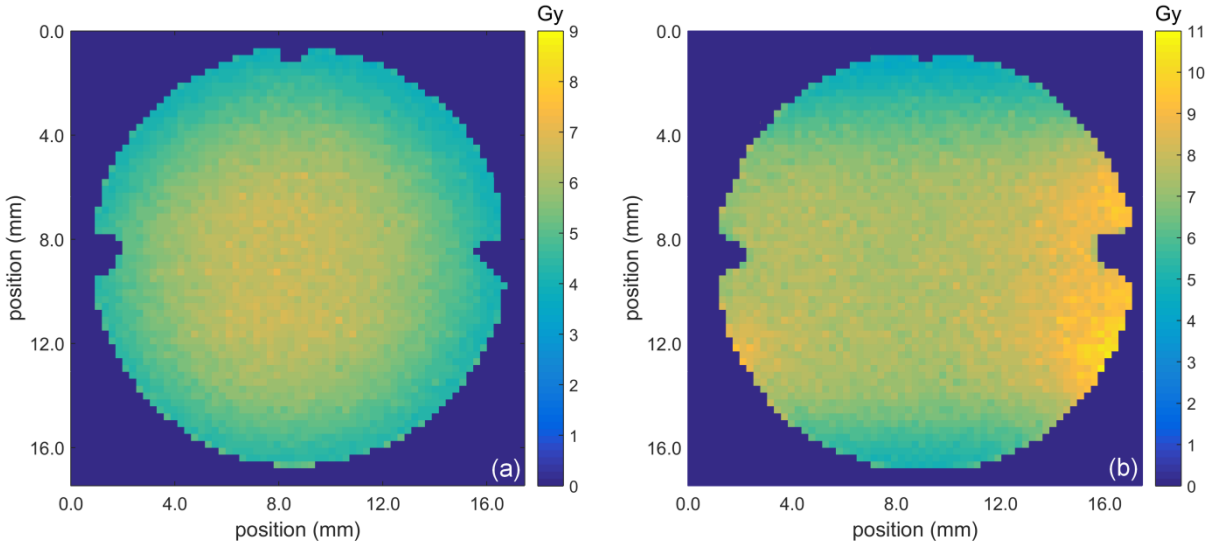
Figure 4.3 Measured film dose distributions for the 16 mm COMS plaque (trial 1) (a), and the Super9 plaque (trial 1) (b). The dose values in pixels located outside the film pieces in the scanned images were set to zero.
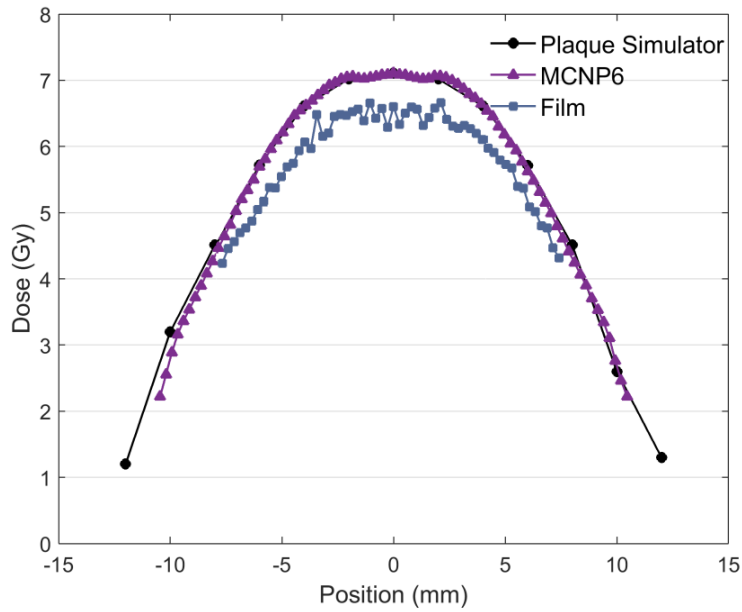
Figure 4.4 Dose profiles in the tumour apex plane at 6.19 mm depth for the fully loaded 16 mm COMS plaque. Profiles are horizontal with respect to the film images in Figure 4.3.

Table 4.1 Calculated and measured doses at 6.19 mm depth along the plaque CAX in the spherical PMMA eye phantom (uncertainties are for coverage factor k=2).

Trial	Plaque Simulator dose (Gy)	Film dose (Gy)	% difference
16 mm COMS #1	7.1 ± 8.8%	6.5 ± 15.7%	-8.1%
16 mm COMS #2	7.1 ± 8.8%	6.6 ± 15.6%	-8.4%
Super9 #1	7.0 ± 8.8%	7.5 ± 4.5%	7.7%
Super9 #2	7.0 ± 8.8%	7.6 ± 5.1%	8.0%

Note that for the Super9 plaque the slots are 7 mm long, whereas in Plaque Simulator they are modelled to be 5 mm long (see Figure 4.2). For the film measurements, the seeds were glued into the centre of the slots, whereas Plaque Simulator places the shorter slots closer to the outer edge of the plaque. The extent to which this affects the dose is described in Section 5.3.3.2 and results in expected Plaque Simulator doses ~6% higher than what is shown in Table 4.1, thus reducing the percent differences from film measured doses to 1.7-2.0 %.

4.3.2 Uncertainty analysis

Uncertainties in film measurements are summarized in Table 4.2 for the first 16 mm COMS trial. The uncertainties for the second trial and the Super9 plaque trials are similar, with small variations occurring due to differences in the film active layer consistency/nominal thickness, and differences in uncertainties in film positioning. The uncertainty in film positioning was equal to 1.8% for the 16 mm COMS plaque, and 1.2% for the Super9 plaque. The uncertainty in plaque placement was 0.05% for the 16 mm COMS plaque, and 0.11% for the Super9 plaque.

126

Table 4.2 Uncertainty in film dose (values given are for the 16 mm COMS trial #1; similar values were determined for the other trials).

Uncertainty component	Type A	Type B
Variation within 1.85x1.85 mm^2 measurement area (7x7 pixels; N=49)	$2.7\%/\sqrt{N}$	
Calibration curve & weighted dose		1.6%
Triple-channel consistency (σ_{TC})		0.79%
Film positioning		1.8%
Plaque placement		0.05%
Plaque tilt		7.4%
Total combined uncertainty (k=1)	7.8%	
Expanded uncertainty (k=2)	15.7%	

Uncertainties in the expected doses calculated using Plaque Simulator are shown in Table 4.3. They include the uncertainties in: the source air kerma strength which is taken from the manufacturer's assay; the dose rate constant, which is adopted from Aryal *et al*;[15] $g_L(r)$ and $F(r,\theta)$ using the recommended values from TG-138[25] that include uncertainties in phantom composition and geometry, mass attenuation coefficients for phantom attenuation, tally volume averaging, and Type A statistical uncertainties; tally volume averaging and statistical uncertainties in $T(r)$ and $B(r)$; and the extrapolation/interpolation uncertainty taken from TG-138 for low-energy sources.

Table 4.3 Uncertainty in Plaque Simulator calculated dose (all uncertainties are Type B).

Uncertainty component	Uncertainty Value
Source strength (S_K)	1.1%
Treatment planning calculations:	
Λ	1.2%
$g_L(r)$	1.0%
$F(r,\theta)$	1.1%
$T(r)$ or $B(r)$	0.16%
Extrapolation/interpolation	3.8%
Total combined uncertainty (k=1)	4.4%
Expanded uncertainty (k=2)	8.8%

Agreement between film measured and Plaque Simulator calculated doses is generally within the estimated uncertainties, though there are other uncertainties currently unaccounted for which could explain the remaining differences observed (see Section 4.4).

The total uncertainty in the MCNP6 reference dose simulation at the film plane amounts to <0.9% (k=1) in each scoring voxel. The components of uncertainty are summarized in Table 4.4.

Table 4.4 Uncertainty in MCNP6 reference dose simulation at the film plane.[15]

Uncertainty component	Type A	Type B
Tally statistics	<0.3%	
μ_{en}/ρ for dose calculation	0.07%	0.77%
μ/ρ for phantom attenuation		0.28%
Physics of MC code		0.1%
Phantom composition		0.05%
Source photon spectrum		0.03%
Total combined uncertainty (k=1)	<0.88%	
Expanded uncertainty (k=2)	<1.8%	

4.4 Discussion and conclusions

Though the differences between the film measured doses and the doses calculated using Plaque Simulator for all trials are within the calculated uncertainties, the 16 mm COMS film doses are consistently lower than the calculated doses, while the Super9 film doses are higher than the calculated doses. For the COMS plaque, this could be due to the plaque being tilted away from the surface of the PMMA eye phantom during irradiation, as the plaque was only fastened to the phantom on one side (at the suture eyelets), compared to the Super9 plaque which required plasticine on the eyelets and the notches to hold it in place. The amounts of tilt that would cause the observed decreases in dose for the COMS plaques are 0.44 mm for trial 1, and 0.45mm for trial 2, slightly higher than the estimated 0.4 mm. With actual sutures on a patient's eye and surrounding orbital tissues to help hold the plaque in place, the plaques would ideally be held on more securely in the clinical setting.

Due to the very steep dose gradients, even a small amount of tilt can create large differences in dose, indicating the necessity for a highly controlled experimental set-up. Given that the average reproducibility between trials for both plaque types was very good (0.2% after accounting for irradiation time differences including source decay), the differences between film doses and Plaque Simulator doses could be due to something that did not change between trials. This could include the positions of seeds within the slots (imperfect placement of the seeds in the slots) or variations in source strengths, as one source strength was applied for all seeds in Plaque Simulator whereas in reality the strengths will vary within the manufacturer's specified tolerance. The amount of plaque tilt and offset may not be the same for each trial, whereas since the same seeds and plaque were used (without re-gluing seeds or removing the Silastic insert) the uncertainties in seed strength and seed positioning in the plaques would remain the same between trials.

As mentioned for the Super9 plaque, the difference between film measured and Plaque Simulator calculated doses is most likely due to the seeds being glued into the centres as opposed to the outer edges of the 7 mm long slots, thereby moving the seeds closer to the tumour apex for the measurements. The estimated dose for seeds glued into the centres of the slots brings the dose differences well within the calculated uncertainties.

The high level of agreement between Plaque Simulator calculated doses and the MCNP6 simulations for the 16 mm COMS plaque in the plane of the film indicates that using seed specific dosimetry data with correct material assignments (water for actual treatment planning as opposed to PMMA) results in high accuracy dose calculations even though Plaque Simulator uses several approximations, such as $T(r)$ values obtained for a single central seed for one size of plaque. At off-axis positions the level of agreement was less (13.4% different at -10 mm and 6.8% at +10 mm), though this could be partly due to differing scatter conditions between the two scenarios (dose difference between PMMA everywhere and PMMA eye surrounded by water is 1.1% at ±10 mm off-axis).

The slight increases in dose off the central axis at ±2 mm seen in Figure 4.4 for the MCNP6 simulation arising from the two centre seeds (the 16 mm plaque does not have one central seed) is not observable in the Plaque Simulator calculated doses (possibly due to the approximation used for $T(r)$), though the difference is very small and would not be clinically relevant. At locations very close to the plaque lip (in the penumbra) or at farther off-axis positions, the

129

agreement between Plaque Simulator and MC simulations has been shown to be worse,[26] though within the central region away from the edge of the eye (within ±6 mm) the agreement here has been found to be very good, within 1.4%.

There are other additional uncertainty components which were either not explicitly assessed or not comprehensively assessed here. These include: seed positioning in the plaques (briefly mentioned above); variations in plaque construction (silastic insert thickness, slot dimensions etc.); source activity distribution and azimuthal fluence differences (variations in the coating of the active layer on the inner component of the seeds); and uncertainties in plaque placement and tilt on the eye. These uncertainties and the extent to which they each affect dosimetry are further investigated in Chapter 5.

Though resulting in a similar level of agreement as previous studies using TLDs and earlier models of Gafchromic film, or other plaque and seed types, and showing overall good reproducibility, highly accurate EBT3 film measurements for eye plaques are challenging and can be affected by many variables. They do however offer validation of treatment planning and MC calculations, and help elucidate the various set-up uncertainties that are most likely to affect actual patient treatments.

4.5 References

1 S.-T. Chiu-Tsao, L.L. Anderson, K. O'Brien, L. Stabile, and J.C. Liu, "Dosimetry for ^{125}I seed (model 6711) in eye plaques," Med. Phys. **20**, 383–389 (1993).

2 M.A. Astrahan, G. Luxton, Q. Pu, and Z. Petrovich, "Conformal episcleral plaque therapy," Int. J. Radiat. Oncol. Biol. Phys. **39**, 505–519 (1997).

3 G. Luxton, M.A. Astrahan, and Z. Petrovich, "Backscatter measurements from a single seed of ^{125}I for ophthalmic plaque dosimetry," Med. Phys. **15**, 397–400 (1988).

4 G. Luxton, M.A. Astrahan, P.E. Liggett, D.L. Neblett, D.M. Cohen, and Z. Petrovich, "Dosimetric calculations and measurements of gold plaque ophthalmic irradiators using iridium-192 and iodine-125 seeds," Int. J. Radiat. Oncol. **15**, 167–176 (1988).

5 A. de la Zerda, S.-T. Chiu-Tsao, J. Lin, L.L. Boulay, I. Kanna, J.H. Kim, and H.-S. Tsao, "^{125}I eye plaque dose distribution including penumbra characteristics," Med. Phys. **23**, 407–418 (1996).

[6] S.-T. Chiu-Tsao, L. Boulay, I. Kanna, A. de la Zerda, and J.H. Kim, "Dose distribution in the eye for ^{103}Pd seed in COMS eye plaque," Med. Phys. **22**, 923 (1995).

[7] K.A. Weaver, "The dosimetry of ^{125}I seed eye plaques," Med. Phys. **13**, 78–83 (1986).

[8] W. Alberti, B. Pothmann, P. Tabor, K. Muskalla, K.-P.P. Hermann, and D. Harder, "Dosimetry and physical treatment planning for iodine eye plaque therapy," Int. J. Radiat. Oncol. Biol. Phys. **20**, 1087–1092 (1991).

[9] A. Wu, E.S. Sternick, and D.J. Muise, "Effect of gold shielding on the dosimetry of an ^{125}I seed at close range," Med. Phys. **15**, 627–628 (1988).

[10] A. Wu and F. Krasin, "Film dosimetry analyses on the effect of gold shielding for iodine-125 eye plaque therapy for choroidal melanoma," Med. Phys. **17**, 843–846 (1990).

[11] A.L. Krintz, W.F. Hanson, G.S. Ibbott, and D.S. Followill, "Verification of Plaque Simulator Dose Distributions Using Radiochromic Film," Med. Phys. **29**, 1220–1221 (2002).

[12] H. Acar, S.-T. Chiu-Tsao, I. Ozbay, G. Kemikler, and S. Tuncer, "Evaluation of material heterogeneity dosimetric effects using radiochromic film for COMS eye plaques loaded with ^{125}I seeds (model I25.S16)," Med. Phys. **40**, 011708 (2013).

[13] J. Poder and S. Corde, "I-125 ROPES eye plaque dosimetry: Validation of a commercial 3D ophthalmic brachytherapy treatment planning system and independent dose calculation software with GafChromic® EBT3 films," Med. Phys. **40**, 121709 (11 pp.) (2013).

[14] J.T. Goorley, M. James, T. Booth, F. Brown, J. Bull, J. Cox, and J. Durkee, "Initial MCNP6 Release Overview," Nucl. Technol. **180**, 298–315 (2012).

[15] P. Aryal, J.A. Molloy, and M.J. Rivard, "A modern Monte Carlo investigation of the TG-43 dosimetry parameters for an ^{125}I seed already having AAPM consensus data," Med. Phys. **41**, 021702 (10 pp.) (2014).

[16] *NUDAT 2.6, National Nuclear Data Centre, Brookhaven National Laboratory*, (URL: http://www.nndc.bnl.gov/chart/decaysearchdirect.jsp?nuc=125I&unc=nds). Last accessed January 24, 2017.

[17] S.M. Seltzer, P.J. Lamperti, M.G. Mitch, J.T. Weaver, and B.M. Coursey, "New National Air-Kerma-Strength Standards for ^{125}I and ^{103}Pd Brachytherapy Seeds," J. Res. Natl. Inst. Stand. Technol. **108**, 337–358 (2003).

[18] R.E.P. Taylor and D.W.O. Rogers, "An EGSnrc Monte Carlo-calculated database of TG-43 parameters," Med. Phys. **35**, 4228–4241 (2008).

[19] J.H. Hubbell, and S.M. Seltzer. (2004), *Tables of X-Ray Mass Attenuation Coefficients and Mass Energy-Absorption Coefficients* (version 1.4). National Institute of Standards and Technology, Gaithersburg, MD. (URL: http://physics.nist.gov/xaamdi). Last accessed January 24, 2017.

[20] M.J. Rivard, "Monte Carlo radiation dose simulations and dosimetric comparison of the model 6711 and 9011 ^{125}I brachytherapy sources," Med. Phys. **36**, 486–491 (2009).

[21] A. Carlsson Tedgren and G.A. Carlsson, "Specification of absorbed dose to water using model-based dose calculation algorithms for treatment planning in brachytherapy," Phys. Med. Biol. **58**, 2561–2579 (2013).

[22] P. Aryal, J.A. Molloy, and M.J. Rivard, "Independent dosimetric assessment of the model EP917 episcleral brachytherapy plaque," Med. Phys. **41**, 092102 (11 pp.) (2014).

[23] S.-T. Chiu-Tsao, M.A. Astrahan, P.T. Finger, D.S. Followill, A.S. Meigooni, C.S. Melhus, F. Mourtada, M.E. Napolitano, R. Nath, M.J. Rivard, D.W.O. Rogers, and R.M. Thomson, "Dosimetry of ^{125}I and ^{103}Pd COMS eye plaques for intraocular tumors: Report of Task Group 129 by the AAPM and ABS," Med. Phys. **39**, 6161–6184 (2012).

[24] M.A. Astrahan, "Improved treatment planning for COMS eye plaques," Int. J. Radiat. Oncol. Biol. Phys. **61**, 1227–1242 (2005).

[25] L.A. DeWerd, G.S. Ibbott, A.S. Meigooni, M.G. Mitch, M.J. Rivard, K.E. Stump, B.R. Thomadsen, and J.L.M. Venselaar, "A dosimetric uncertainty analysis for photon-emitting brachytherapy sources: report of AAPM Task Group No. 138 and GEC-ESTRO," Med. Phys. **38**, 782–801 (2011).

[26] R.M. Thomson, R.E.P. Taylor, and D.W.O. Rogers, "Monte Carlo dosimetry for ^{125}I and ^{103}Pd eye plaque brachytherapy," Med. Phys. **35**, 5530 (2008).

Chapter 5 Delivered dose uncertainty analysis at the tumour apex

A version of this chapter has been published as: H. Morrison, G. Menon, M.P. Larocque, H.-S. Jans, E. Weis, and R.S. Sloboda, "Delivered dose uncertainty analysis at the tumor apex for ocular brachytherapy," Med. Phys. **43**, *2891-4902 (2016).*

5.1 Introduction

For ocular brachytherapy, currently the only recommended PTV margin is a 2-3 mm basal margin. As discussed in Section 1.4, this margin is introduced to account for plaque placement errors, plaque movement, uncertainties in the location of the tumour edge,[1] and subclinical disease occurring as microscopic spread along the uvea and sclera.[2] However, the optimal margin around the tumour base is still unknown. Investigations into the effect of plaque placement variations on the basal coverage and volumetric dose have been performed,[3] and the effects of plaque tilt and positioning accuracy have also been investigated.[4–7] However, a full analysis of dosimetric uncertainty at the tumour apex has yet to be performed. There is currently no recommendation on the size of a treatment margin to be applied at the tumour apex, as guidelines simply state that the prescription point should be at the tumour apex (with no added margin). However, in clinical practice some centers apply a margin at the tumour apex along the tumour CAX to account for uncertainty in tumour height measurement, and prescribe the dose to this point (private communication [A. Wilkinson, A. Beiki-Ardakani, M. Astrahan, and J. Emrich]).

Given the recent endeavor in brachytherapy dosimetry to standardize the method of reporting uncertainties (as described in the joint AAPM and GEC-ESTRO documents),[8,9] as recently demonstrated by Kirisits *et al.*[9] wherein the uncertainties present in the treatments of a number of different disease sites were examined, a similar analysis was performed for ocular brachytherapy. This was motivated by: 1) the lack of understanding/knowledge of the uncertainties present and their dosimetric effects in the ocular brachytherapy treatment process; 2) the lack of consensus on tumour apex margin sizes; and 3) the results of the experimental radiochromic film measurements performed in Chapter 4.

The study presented in this chapter examines various sources of dosimetric uncertainty at the tumour apex in ocular brachytherapy treatments (the dose at the prescription point being the clinically-relevant quantity) for two different types of plaques, in order to determine what sources of uncertainty are contributing most significantly, to ascertain where improvements to reduce these could be made, and to estimate an appropriate uncertainty-based treatment margin at the tumour apex.

5.2 Materials and Methods

The total dosimetric uncertainty was assessed for three tumour heights, 3, 5, and 10 mm, measured along the plaque CAX from the inner sclera, representing small, medium, and large sized tumours, and all dosimetric uncertainties were determined at these depths. The uncertainties were assessed for two plaque types: a 16 mm COMS plaque and a Super9 plaque (also known as a model #930 plaque) (Eye Physics LLC, Los Alamitos, CA), which is frequently used at our facility (the Cross Cancer Institute; CCI) for very posterior, juxta- or peri-papillary tumours due to the potential dose distribution offered. The COMS plaques consist of a dome-shaped gold alloy (Modulay) backing which holds a seed carrier (Silastic – MDX4-4210 bio-medical grade elastomer) (Trachsel Dental Studio, Rochester, MN), whereas the Super9 Eye Physics plaque is made of standard 18K gold and has 7 mm long milled seed slots.

The primary sources of dosimetric uncertainty assessed were those arising from seed construction, source strength, plaque assembly, dose calculations, tumour contouring/tumour dimension measurements, plaque positioning, and plaque tilt. Although inherently larger variations can be present in a given treatment situation depending on surgical skill, location or shape of the tumour, circumstances creating tilt (ocular muscle beneath the plaque, sub-plaque hemorrhage), individual patient response to the surgery (swelling or other complications), etc., the most common tumour shape, a simple dome-shape, was simulated to assess the tumour height measurement, plaque positioning, and plaque tilt uncertainties. All treatment planning calculations were done using Plaque Simulator v5.7.6 (Eye Physics LLC, Los Alamitos, CA), a dedicated ophthalmic treatment planning system which performs 3D dose calculations using a modification of the TG-43 formalism for the line-source approximation. Heterogeneity corrections for the plaque materials were used for all Plaque Simulator calculations. This

includes $T(r)$, the carrier modifier factor for the COMS plaques,[10] and $B(r)$, the scatter/fluorescence modifier factor for the Eye Physics slotted style of plaques[11] – discussed in more detail in Section 5.2.4. Although the air interface factor,[10] $A(R)$, can also be used, it was not included in order to keep the dose calculations independent of the exact position of the tumour and its position relative to the air surface. To determine an appropriate treatment margin to apply at the tumour apex on the plaque/tumour central axis (CAX), the doses along the CAX were compared to the tumour apex dose. The following sections outline the methods used to assess each source of uncertainty.

5.2.1 Seed construction

The majority of uncertainties associated with brachytherapy seed construction are reflected in the uncertainties in the dosimetry parameters for each seed model [S_K, $g_L(r)$, Λ, $F(r,\theta)$, etc.]. These include the source specifications (capsule dimensions and composition, end-weld thickness, distribution of the active material), movable components, and the source emissions,[8] which should be accounted for in computational simulations when determining seed dosimetry parameters and will be reflected in variations observed in experimental measurements. For seeds that are constructed symmetrically about the azimuthal axis (the long-axis of the source as described in Rivard *et al.*[12]) the dosimetry is considered to be symmetric about this axis. Consequently, dose variations are only determined for the radial distance and for the angle away from the long-axis of the source (r and θ in the TG-43 formalism). Due to non-uniform/imperfect distribution of the active material on internal components as well as their movement, there can be variation along the azimuthal direction (azimuthal/rotational anisotropy – not to be confused with the anisotropy factor, $F(r,\theta)$). For interstitial irradiation this effect can in most cases be assumed to be negligible, as the average tissue dose surrounding the seed will not be affected. However, for eye plaque therapy, the irradiation is mainly occurring from one side of each seed, and can therefore be affected by azimuthal variations. Though an internal dynamic component can and will move throughout treatment, the variation in the dose delivered to the tumour apex from each seed will be bounded by the measured azimuthal variation and will not necessarily average out for a small number of seeds. Accordingly, the azimuthal anisotropy was determined for three I-125 seed models using Gafchromic EBT3 film (lot# A0318303; Ashland Specialty Ingredients, Wayne, NJ) and the cylindrical three piece custom built polymethylmethacrylate (PMMA)

phantom shown in Figure 3.1. These variations have also been measured using a wide-angle free air chamber by rotating the seed about its long axis.[8,13,14]

Film calibration methods followed those outlined in Chapter 3, using the same calibration curve as for the eye phantom measurements (Section 4.2.1). The measured doses were determined using the iterative triple-channel method described in Section 3.2.5.

The azimuthal anisotropy irradiations were performed using 4 x 7.5 cm^2 pieces of film scanned at 72 dpi. The dose along the seed's transverse axis was measured along a central 2.47 mm wide region of the film (± 5.6° about the transverse axis) and normalized to determine the azimuthal variations in radiation output from the seed. Azimuthal anisotropy was measured for four Advantage™ I-125 model IAI-125A brachytherapy seeds (IsoAid LLC, Port Richey, FL) which is the seed type used for our clinical treatments, as well as one Oncura OncoSeed I-125 model 6711 seed (GE Healthcare Inc., Arlington Heights, IL), and one BEBIG I-125 IsoSeed® I25.S16 seed (Eckert & Ziegler, Berlin, Germany) for comparison, both of which have a similar structure to the IAI-125A seed (titanium capsule with end-welds, active material adsorbed on an inner mobile rod).

5.2.2 Source strength

The source strength, in units of air-kerma strength, S_K, is taken from the manufacturer's Accredited Dosimetry Calibration Laboratory (ADCL) calibrated assay. As plaques for patient treatment are assembled in house and seeds are received loose, all seeds are assayed to verify that each individual seed is within ±6% of the ordered seed strength, and the batch average seed strength is within ±3% as per AAPM guidelines.[15] The IAI-125A seeds undergo routine NIST calibration, which is then transferred to the ADCLs following the process described in TG-138; therefore the uncertainty in the manufacturer provided source strength for each seed is given by row 3 of Table I in TG-138, and is the value used.[8]

5.2.3 Plaque assembly

Uncertainties associated with plaque assembly include the placement of seeds within slots in the plaques, placement of the Silastic insert in the plaque backing (COMS plaques), and plaque component variations. Uncertainties in seed placement within the plaques were determined using high resolution CT scanning with a Siemens Inveon microPET/CT scanner (Siemens Medical

Solutions USA Inc., Knoxville, TN). Image volumes were acquired with 80 kVp X-ray tube voltage and consist of isotropic voxels with a side length of 21.3 μm. To prevent the occurrence of significant metal artifacts in the images, IsoAid IAI-125A I-125 seed shells (no silver core or radioactive material in the Ti shells), having the same dimensions and outer surface properties as actual seeds, were used. Due to the low-energy x-ray source, the gold/Modulay plaques could also not be imaged directly (due to metal artifacts). For the 16 mm COMS plaque, a photopolymer 3D printed plaque was created using SolidWorks 2014 (Dassault Systèmes SolidWorks Corporation, Waltham, MA), and a positive impression of the Super9 plaque was created using alginate impression and dental stone casting materials. As the Super9 plaque is a manually prototyped plaque and due to its irregular shape, it is not easily re-designed using 3D CAD software. The plaque replicas are shown in Figure 5.1 (a) and (b). The 16 mm COMS Silastic insert and the Super9 plaque were loaded as per usual clinical practice; the 16 mm COMS Silastic insert was inserted into the 3D printed plaque, while the seed shells were glued directly into the Super9 mold with super glue (cyanoacrylate). The COMS insert was fully loaded (13 seeds), whereas for the Super9 plaque the central 8 slots on each side were loaded (16 slots in total – the replicated mold was not fully loaded due to a limited number of seed shells). The plaques were then positioned on a custom built 24.6 mm diameter spherical PMMA eye phantom for imaging.
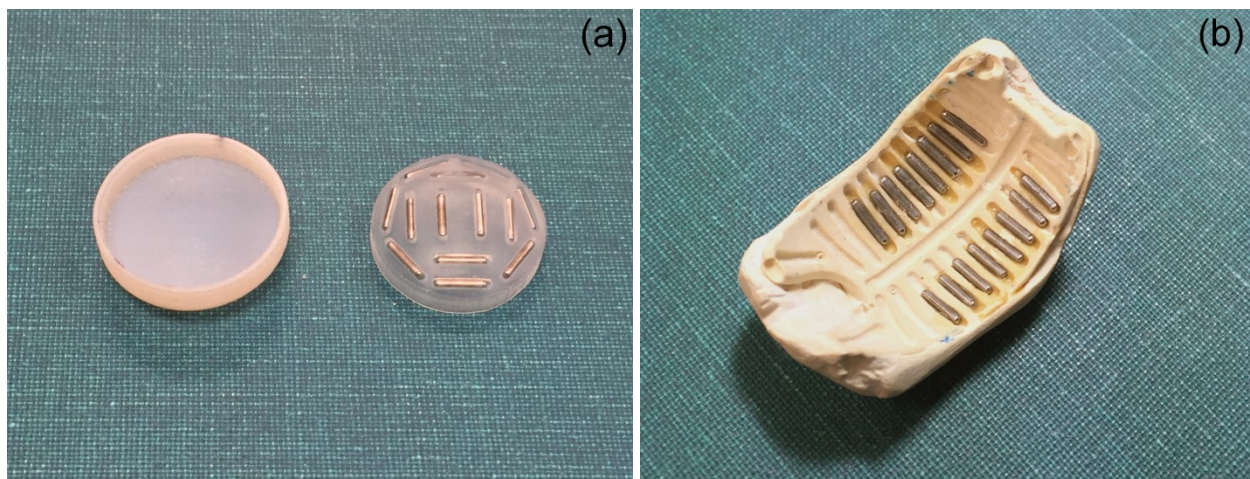
Figure 5.1 Photopolymer 3D printed plaque and 16 mm Silastic insert containing Ti seed shells (a), Super9 impression mold with Ti seed shells glued into the central 16 slots (b).

Three different 16mm COMS Silastic inserts were imaged (Figure 5.2), as they were found to vary in overall thickness, and two molds of the Super9 plaque were imaged (one empty and one containing seed shells (Figure 5.3)). All microCT images were analyzed using ImageJ v1.48 (US National Institutes of Health). Seed/slot coordinates were measured from the images in order to alter the standard slot positions defined within Plaque Simulator using the slot editor. The slot positions in Plaque Simulator are described using: the angle alpha (α) or the distance r from the angle α's projection onto the YZ plane; the angle β; the tilt of the slot; and the source offset, which describes the distance of the seed/slot from the inner plaque surface (Figure 5.4).[16] For the COMS Silastic insert the distance r to the centre of each seed and the angle β were measured from the coronal CT images. The source offsets were measured from the source centre to the surface of the PMMA phantom in the sagittal and transverse plane images, using the plane in which the seed axis was not parallel (e.g. a seed slot parallel to the Z-axis would be measured in the XY-plane) to ensure the measured offset is along the radial line towards the centre of the sphere defined by the radial curvature of the Silastic insert. For any slots that were at a 45° angle to both the sagittal and transverse planes, the source offset was taken as the average measurement in both planes. The seed center positions were determined from the position of the minimum pixel value between the two peaks indicating the Ti shell walls in a profile through the image, whereas PMMA phantom/Silastic interface positions were determined from half-maximum pixel values between the material boundaries. The COMS inserts are designed to hold the seeds at a 1 mm radial offset from the inner Silastic surface (surface in contact with the eye/phantom), i.e. 1.4 mm to the seed centre for a 0.8 mm diameter seed. The COMS inserts are designed such that the tilt angles of all slots are 90°. Due to the lack of slot collimation and the concentric arrangement of the seeds such that the seed transverse axes bisect the plaque central axis, any small variation in slot tilt has no dosimetric effect at the tumour apex, so the tilt was not measured.
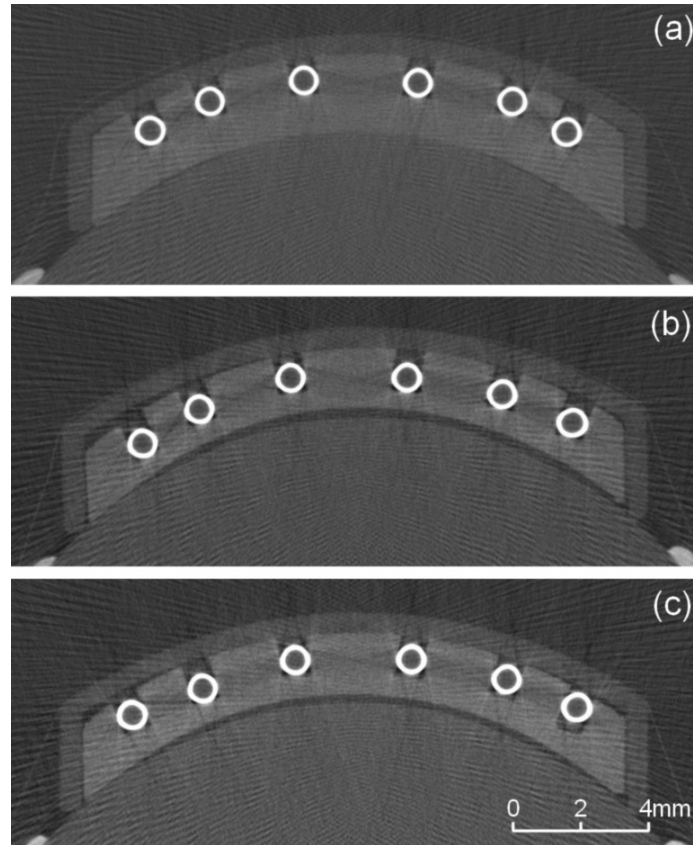
Figure 5.2 microCT images of 16 mm COMS Silastic insert #1 (a), insert #2 (b), and insert #3 (c), mounted on the PMMA eye phantom. Visible deviations from the ideal geometry are a small gap between the outer Silastic surface and the inner 3D printed COMS plaque surface in the upper left corner in images (b) and (c), the gap between the inner Silastic surface and the PMMA phantom in images (b) and (c), and the right-most seed shell not placed fully into the Silastic slot in image (c).

COMS inserts are designed to be 2.25 mm thick, with 1 mm of material beneath each seed, i.e. slots are designed to be 1.25 mm deep. The total Silastic thickness (in the center and at two outer edges) and thickness beneath each seed was measured for comparison with Silastic insert design specifications. The Silastic thickness beneath the slots was used to calculate ratios of photon attenuation for Silastic vs. water, compared to the expected attenuation through 1 mm of Silastic vs. water.[17] For example, for I-125 radiation, the ratio of attenuation for 1 mm of Silastic compared to water (using the poly-energetic I-125 brachytherapy seed emission spectrum including silver fluorescent x-rays[13,14] and attenuation cross-sections from the XCOM database[18]) is 0.8034, whereas if the Silastic thickness beneath the seed slots is on average 1.08

mm (Silastic insert #1), the ratio is 0.7996. The change in attenuation is then +0.48%. The total thicknesses of seven 16 mm Silastic inserts were measured with calipers for comparison, all of which were in the range of thicknesses of the three imaged inserts. Assuming the latter represent the production range of Silastic insert thicknesses, the associated uncertainty can be represented by a rectangular distribution, centered on a value of 1 mm (the expected Silastic thickness beneath the slots).
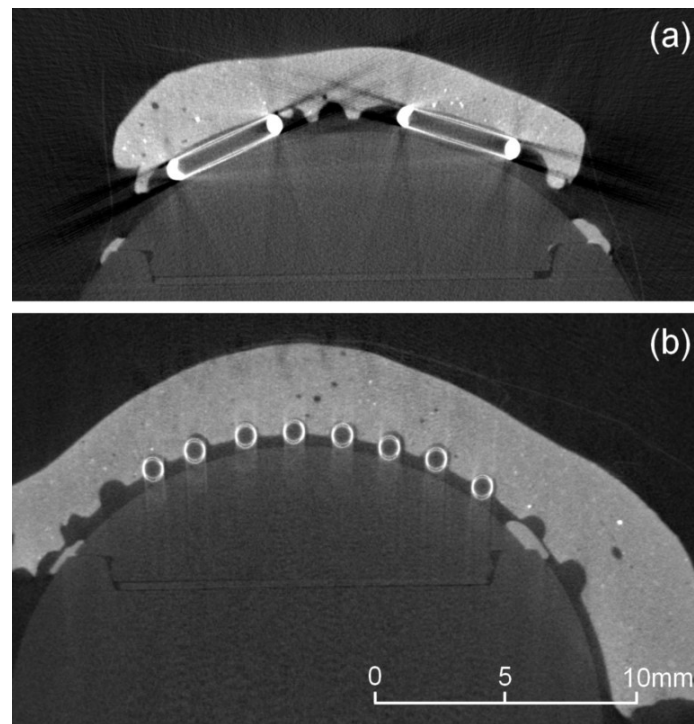
Figure 5.3 microCT images of the Super9 impression mold containing Ti seed shells on the PMMA eye phantom in transverse (a), and sagittal views (b).
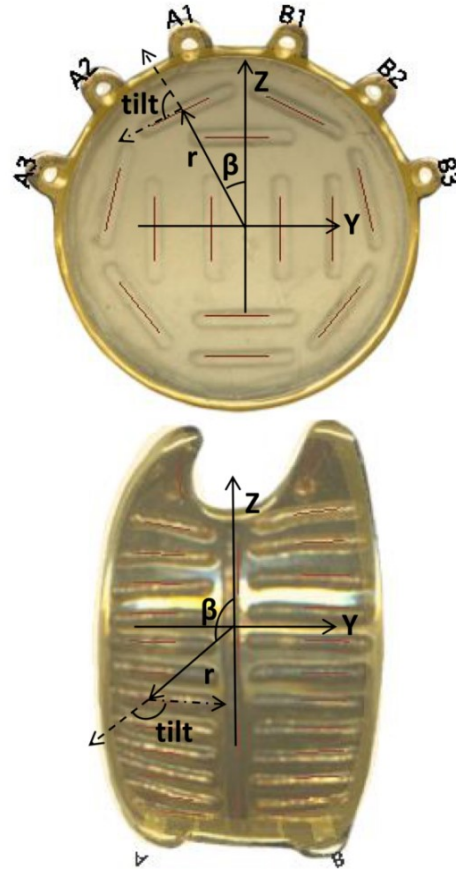
Figure 5.4 Plaque Simulator coordinate system with coordinates r, β, and tilt overlaid on the 16 mm COMS (top) and Super9 (bottom) plaques (X-axis points out of the page).

As the Super9 plaque holds the seeds in contact (or very nearly) with the eye, the original source offset values were used (0.4 mm). The radial distance r, angle β, and tilt were measured from the coronal images. Large variations in source positioning can occur when placing the 4.5 mm long seeds in the 7 mm long slots. The modelled seed positions in Plaque Simulator are in the outer part of the slots. However, due to the large variation in possible seed placement, the coordinates of seeds glued in the centers of the slots, as well as at the inner edges of the slots, were measured and used to alter the seed positions in Plaque Simulator. CAX and tumour apex doses were compared between the modified plaque models and the original un-altered plaque model.

5.2.4 Treatment planning calculations

All treatment planning calculations were performed using Plaque Simulator and consensus dosimetry data for the IsoAid IAI-125A I-125 seed.[19–21] The dose rate at a distance r from a given seed is calculated using the 2D TG-43 formalism[22,23] with correction factors C_i for the plaque materials:

$$\dot{D}(r,\theta) = S_K \cdot \Lambda \cdot \frac{G_L(r,\theta)}{G_L(r_0,\theta_0)} \cdot g_L(r) \cdot F(r,\theta) \cdot \prod_i C_i \qquad (5.1)$$

The correction factors include $T(r)$ for the COMS plaques,[10] $B(r)$ for the Eye Physics slotted style of plaques,[11] and $A(R)$ for both plaque types (which here was set to 1, but actual values could be used).[10]

The consensus dose rate constant, $_{CON}\Lambda$, is the average of both experimental (EXP) and Monte Carlo (MC) derived values, and the combined uncertainty is calculated using Eq. 19 from TG-43U1[23] and the values for $_{EXP}\Lambda$ and $_{MC}\Lambda$ from Solberg *et al.* and Meigooni *et al.*[20,21] All values and uncertainties are listed in Section E.1. of the Appendix in the TG-43U1S1 document.[19]

Uncertainties in the line source radial dose function, $g_L(r)$, the anisotropy function, $F(r,\theta)$, and TPS interpolation were taken from approximate and recommended values from TG-138 due to the absence of explicit published uncertainties for these consensus values. As $g_L(r)$ and $F(r,\theta)$ are determined from the same Monte Carlo dataset from Solberg *et al.*,[20] they are not statistically independent variables. Therefore if they are being multiplied together the combined uncertainty should not be taken as the quadrature sum of the individual percent uncertainties,[24] but will be approximated as the uncertainty of one of these parameters. In this case the uncertainty for $g_L(r)$ will be used, as it would be larger than the uncertainty in $F(r,\theta)$ at the tumour apex. Uncertainties for the plaque specific correction factors $T(r)$ (for the COMS style plaque), $B(r)$ (for the Eye Physics style plaque), as well as $A(R)$ (for both plaque types) are also included.[10,11]

5.2.5 Tumour dimension measurements

For tumour dimension measurements, the minimum uncertainty in apical height will be the inherent resolution of the ultrasound unit. Modern imaging units, such as the Eye Cubed[TM] ultrasound (Ellex Medical Lasers Ltd., Adelaide, SA, Australia) which is used for all patient

planning at our center, has an inherent A-scan resolution of 50 μm, and B-scan axial and lateral resolutions of 50 and 100 μm, respectively. The actual uncertainty in an apical height measurement is however larger due to potential difficulties distinguishing the tumour and scleral surface, the calibration of the ultrasound probe, and differences between subsequent A- and B-scan measurements, and is typically assumed to be ±0.5 mm.[25–28] Tumour basal dimensions can be measured with indirect ophthalmoscopy, ultrasound B-scan images, and from transillumination shadows, which range in accuracy from ±0.3 mm up to ±1 mm; differences larger than these are assumed to represent documented growth.[25,29] These values can differ depending on the exact shape of the tumour, whether the tumour apex is offset from the radial axis through the centre of mass of the tumour (non-symmetric tumour), if there is retinal detachment, extrascleral extension etc. However, these values are representative for a simple dome-shaped tumour. Additional uncertainties could be added to the tumour dimensions to account for tumour growth between imaging and treatment, though this can be minimized if imaging is performed shortly before treatment (a few days), at which point additional growth is unlikely.[25]

All repeated apex height measurements from ultrasound images are expected to agree within ±0.5 mm, which would indicate a large coverage factor. For a conservative estimate, it will be assumed that this uncertainty has a coverage of over 95%, i.e. k=2. The unexpanded uncertainty in tumour height measurements will be taken as ±0.25 mm for k=1 for a simple dome-shaped tumour. The CAX doses of fully loaded plaques were used to assess the change in dose due to this change in tumour apex height.

5.2.6 Plaque placement and tilt

Plaque placement, both position on the spherical surface of the eye and the tilt of the plaque, has been studied previously,[4–7] and in general has been found to be acceptable for the majority of patients. Sub-optimally placed plaques, or those that required repositioning were most often associated with peri- or juxta-papillary, or very posteriorly located tumours. Similarly, tilting occurred more frequently in papillary tumours than with equatorial or anterior tumours. Again, using a simple dome-shaped tumour that is not close to the optic nerve, it is our ophthalmologist's expert opinion that sutures/eyelets can be placed accurately within 0.25 mm of their planned positions using calipers and toric axis markers for tumours located ≤8 mm back

from the limbus, and within 0.4 mm when >8 mm back from the limbus. These values are consistent with general published findings of good plaque placement with no uncovered basal margins for tumours located away from the optic nerve.[4–7] Due to possible variations in these values a conservative 0.5 mm shift in plaque positioning (eyelet position) was used and the change in dose at the tumour apex for fully loaded plaques was recorded.

Plaque tilt can be accounted for in treatment planning calculations if detected at plaque insertion or expected during planning (e.g. if the plaque is to be positioned on top of an ocular muscle). Uncertainty arises if the amount of tilt differs from what is expected, or if it changes throughout the course of treatment. In the study performed by Almony *et al.* the average change in plaque tilt from insertion to removal was +0.82 mm (positive movement being an increase in the amount of tilt).[4] No plaque displacement was measured in repeat intraoperative echograms by Tabandeh *et al.*,[7] and an average change in the seed-to-tumour apex distance of +0.5 mm was determined by Finger *et al.* using 3D ultrasonography.[6] In all studies, plaque tilt was strongly associated with decreased distance to the fovea or optic disc, particularly for peri- or juxta-papillary tumours, or for notched plaques. A median increase in plaque tilt of 0.4 mm for a tumour located away from the optic nerve was used to assess the change in dose at the tumour apex for the two fully loaded plaque types.

5.3 Results

5.3.1 Seed construction

The azimuthal variation in dose around a seed was found to be ±1.46% (k=1) for the IsoAid IAI-125A I-125 seed. In comparison, the azimuthal variations for the Oncura 6711 and BEBIG I25.S16 seeds were 2.06% and 1.58% (both k=1), respectively, which are similarly constructed seeds. The azimuthal variation in radiation output of seeds has been reported to vary up to ±15%,[13,14] though for symmetrically constructed seeds it is expected to be much lower. The measured variation for the IAI-125A seed is consistent with variations for other similarly constructed seeds.

5.3.2 Source strength

The uncertainty in the manufacturer provided source strength for each seed from row 3 of Table I in TG-138 is 1.1% (k=1).[8] This is then equivalent to a dosimetric uncertainty of 1.1% (k=1).

5.3.3 Plaque assembly

5.3.3.1 16 mm COMS plaque

The total thickness of the three Silastic inserts imaged was 2.27, 1.78, and 1.82 mm, and the average thickness of Silastic material beneath the seeds was 1.08, 0.52, and 0.55 mm for inserts #1, #2, and #3, respectively. Using a rectangular distribution and approximating the asymmetric distribution as symmetric to determine the dosimetric uncertainty at the tumour apex,[30,31] with a mean expectation value of 1 mm, the uncertainty is equal to: $u_{Silastic\ thickness} = |b_+ + b_-|/2\sqrt{3} = |a_+ - a_-|/2\sqrt{3} = |1.08 - 0.52|/2\sqrt{3} = 0.16\ mm.$ The changes in attenuation/dose for $1 - 0.16 = 0.84$ mm and $1 + 0.16 = 1.16$ mm are $\pm 0.97\%$.

When changing all 13 seed coordinates to those measured from the microCT images, the difference in dose at the tumour apex for the 5 mm tumour (medium sized tumour) was -2.36%, +3.59%, and +0.91% for Silastic inserts #1, #2, and #3, respectively, as can be seen in Figure 5.5(a). The average seed depth (measured from the seed centre radially toward the centre of the eye) was 1.40 ± 0.15 mm. Though the total Silastic thickness as well as the thickness beneath the slots varied, the average seed depth from the surface of the eye was equal to the expected value of 1.40 mm. Silastic insert #1, which was slightly thicker, fully filled the 3D printed COMS plaque and no gap was visible between the Silastic surface and the eye phantom, whereas there was a visible radial gap (see Figure 5.2 (b) and (c); mean: 0.24 mm, range: 0.14 – 0.37 mm, beneath each seed slot) between the eye phantom and the Silastic surface for the other two inserts due to their being thinner than the expected 2.25 mm. The COMS Silastic inserts are hand-made by pressing the silicone liquid into a two-part mold which has the open seed slots facing down;[32] thus the majority of variation will not be in the depths of the seed slots themselves but in the thickness of Silastic beneath the seeds, which is consistent with our findings. For inserts #2 and #3, the variations cause the entire plaque and seeds to sit slightly closer to the surface of the eye phantom, but if the Silastic insert is pressed fully into the plaque, the seeds will be close to their expected positions. For comparison, if the seed depths were measured from the inner Silastic

surface (neglecting the gap to the PMMA surface) the dose increases at the tumour apex would be much larger: +9.60% and +6.24% for inserts #2 and #3, respectively. A gap would however likely be maintained in a patient treatment in this scenario due to the rigid nature of the eye, and the space between the Silastic surface and eye would fill with fluid.
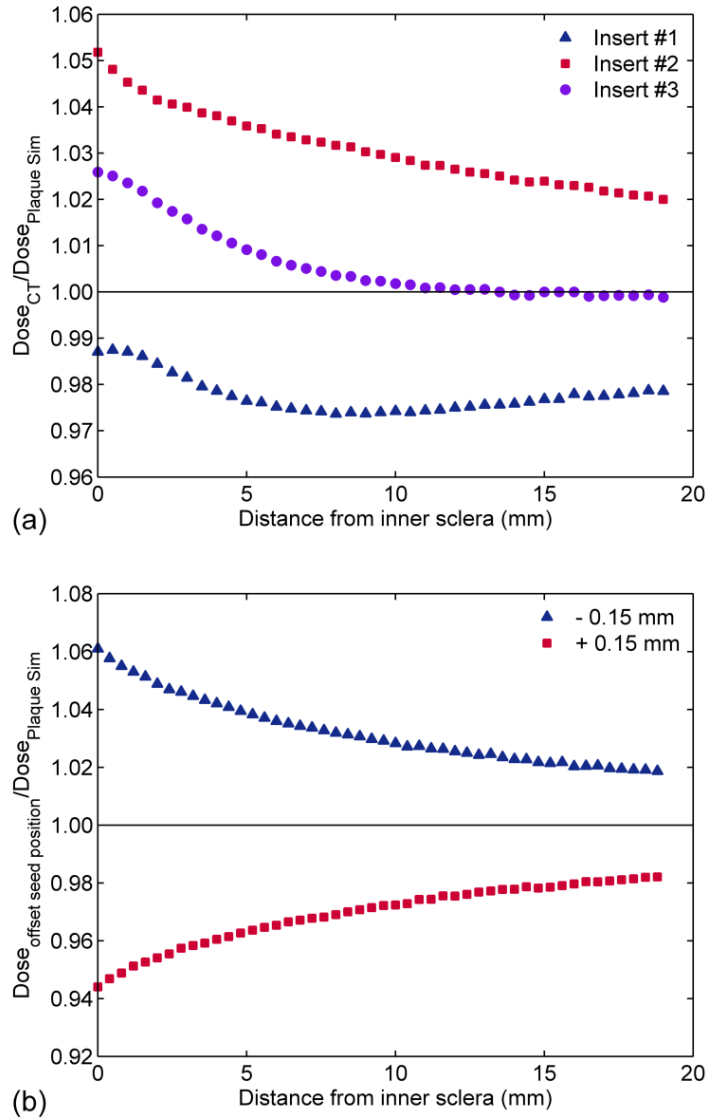
Figure 5.5 Ratio of CAX doses for the measured seed coordinates in Silastic inserts #1, #2, and #3 from the CT images ($Dose_{CT}$), compared to the original positions ($Dose_{Plaque\ Sim}$) (a); and ratio of CAX doses for an average offset position of ±0.15 mm for all seeds ($Dose_{offset\ seed\ position}$) from the expected position of 1.4 mm ($Dose_{Plaque\ Sim}$) (b).

As the Silastic does not collimate the radiation, the largest dosimetric change is due to a change in the seed offset distance, and possible associated changes in Silastic attenuation (changes in β or tilt will have less effect). Setting all seed offset positions to $1.40 - 0.15 = 1.25$ mm and $1.40 + 0.15 = 1.55$ mm, the dose at the tumour apex ranges from $+3.90$ to -3.67%; the change in dose along the CAX is illustrated in Figure 5.5(b). As it is less of a clinical concern if the tumour is over-dosed compared to under-dosed, to account for this uncertainty, the decrease in dose will be used, i.e. $\pm 3.67\%$. The uncertainty due to seed placement in the 16 mm COMS Silastic insert is therefore taken as the quadrature sum of the uncertainty due to thickness variation and seed offset position: $\%u_{COMS\ seed\ position} = \sqrt{(0.97\%)^2 + (3.67\%)^2} = 3.8\%$.

5.3.3.2 Super9 plaque

Adjusting the positions of the 16 seeds to the centres of each slot resulted in a 5.8% increase in dose at the tumour apex for the 5 mm tumour height, and with the seeds located at the inner edge of the slots there was a 15.8% increase in dose, compared to the seeds in the standard positions used in Plaque Simulator (outer edges of the slot), as seen in the CAX doses in Figure 5.6. As the seeds can be purposefully glued in a given position, and assuming the inner/outer positions will be less likely than the central positions, a triangular distribution was used to determine the uncertainty in dose due to seed positions for the Super9 plaque. For a prescription dose of 70 Gy using the standard outer seed slot positions, the expected dose in this case is the dose with the seeds in the central positions (5.8% larger than 70 Gy), 74.1 Gy, and the distribution ranges from 70 Gy to 81.1 Gy ($+15.8\%$). The uncertainty is equal to: $u_{Super9\ seed\ placement} = |b_+ + b_-|/2\sqrt{6} = |a_+ - a_-|/2\sqrt{6} = |81.1 - 70.0|/2\sqrt{6} = 2.27$ Gy. The percent uncertainty is $\%u_{Super9\ seed\ placement} = \pm 3.06\%$, centered on a $+5.8\%$ bias.
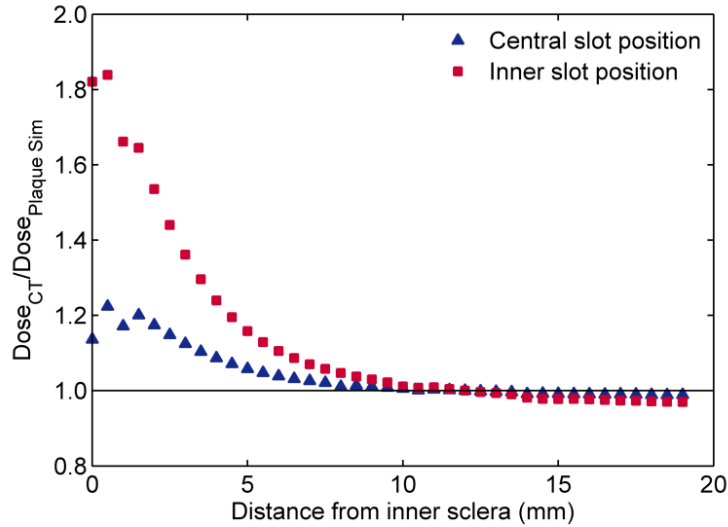
Figure 5.6 Ratio of CAX doses for seed positions at the centers and inner edges of the slots in the Super9 plaque as measured from the CT images (Dose$_{CT}$) compared to the standard outer positions used in Plaque Simulator (Dose$_{Plaque\ Sim}$).

5.3.4 Treatment planning calculations

The average experimental and Monte Carlo derived dose rate constants are $_{EXP}\Lambda = 0.990 \pm 0.047$ cGy h^{-1} U^{-1} and $_{MC}\Lambda = 0.971 \pm 0.015$ cGy h^{-1} U^{-1}. Using Eq. 19 from TG-43U1[23], $_{CON}\Lambda$ is equal to 0.981 ± 0.025 cGy h$^{-1}\cdot$U^{-1}, with an associated percent uncertainty, %$\sigma_{_{CON}\Lambda}$, of ±2.58%. From the TG-138 document, for MC-simulated data, the uncertainty in $g_L(r)$ for 0.5 cm ≤ r ≤ 5 cm (which is the case at the tumour apex) for low-energy photon-emitting brachytherapy sources is 1%.[8] Uncertainty in interpolation/extrapolation, termed %u_{TPS} in TG-138, for low-energy sources is equal to 3.8%.[8] The uncertainties in the correction factors are equal to ±0.1% for $T(r)$ and $A(R)$ from Thomson *et al.*[10], and ±2% for $B(r)$ from Luxton *et al.*[11] The total combined uncertainty due to treatment planning parameters is ±4.70% for the 16 mm COMS plaque, and ±5.11% for the Super9 plaque.

5.3.5 Tumour dimension measurement

A difference in tumour height of ±0.25 mm for a 5 mm tall tumour equates to a change in dose of +5.33% to -5.00% for the 16 mm COMS plaque and +3.79% to -3.60% for the Super9 plaque.

148

Again, the decrease in dose will be used as the dose uncertainty, i.e. ±5.00% and ±3.60% for the 16 mm COMS and Super9 plaques, respectively.

5.3.6 Plaque placement and tilt

The basal diameter coverage is very sensitive to plaque placement,[3] whereas the dose at the tumour apex is much less sensitive to changes in plaque position on the eye. A 0.5 mm shift in plaque positioning (eyelet position) results in 0.1% and 0.3% decreases in dose at the tumour apex at 5 mm depth for fully loaded 16 mm COMS and Super9 plaques, respectively. The shift in position for the Super9 plaque is a lengthwise shift; changes in dose due to lateral shifts in plaque position are much smaller, -0.08% for a 0.5 mm shift in eyelet position.

A median increase in plaque tilt of 0.4 mm results in a 7.7% and 3.9% decrease in dose at the tumour apex for the 16 mm COMS and Super9 plaques, respectively. Uncertainties in both plaque placement and plaque tilt create decreases in dose at the tumour apex which could be mitigated by using a minimum apex margin, while the uncertainties described in the previous sections (Sections 5.3.1– 5.3.5) could be accounted for by applying an additional margin. For the 16 mm COMS and Super9 plaques, apex margins of 0.4 and 0.3 mm, respectively, would compensate for uncertainties in both plaque position and plaque tilt.

5.3.7 Total dosimetric uncertainty

The uncertainties from Sections 5.3.1 – 5.3.5 for both the 16 mm COMS and Super9 plaques for a 5 mm tall tumour are summarized in Table 5.1.

Table 5.1 Dosimetric uncertainties at the tumour apex for fully loaded 16 mm COMS plaque and Super9 plaques (values in the center are common for the two types of plaques).

	Plaque	
Source of uncertainty	16 mm COMS	Super9
Source azimuthal fluence	1.46%	
Source strength (S_K)	1.1%	
Seed placement	3.67%	3.06%
Silastic thickness	0.97%	-
Treatment planning calculation:		
Λ	2.58%	
$g_L(r)$	1.0%	
$T(r)$, $A(R)$, and $B(r)$*	0.14%	2.0%
Extrapolation/interpolation	3.8%	
Tumour height	5.00%	3.60%
Total combined uncertainty (k=1)	8.07%	7.19%
Expanded uncertainty (k=2)	16.1%	14.4%

*Uncertainties in $T(r)$ and $A(R)$ are included for the COMS plaque, and $B(r)$ and $A(R)$ for the Super9 plaque.

The margins to account for all uncertainties excluding plaque placement and plaque tilt are determined from the total dosimetric uncertainties outlined in Table 5.1. The expanded uncertainties (k=2) to be accounted for are 16.1% and 14.4%, which require margins of 0.9 and 1.1 mm for the 16 mm COMS and Super9 plaques, respectively. These margins, in addition to the margin to account for plaque tilt and positioning, result in total apex margins of 1.3 and 1.4 mm for the two plaque types, respectively (the dose gradient is less steep for the Super9 plaque, therefore a larger margin is required).

All previously described uncertainties were also determined at tumour apex heights of 3 and 10 mm depths for the two types of plaques, using the same methods as for a tumour height of 5 mm. The uncertainties as well as the required treatment margins to ensure adequate dosimetric coverage at the tumour apex are summarized in Table 5.2 for all three tumour heights.

Table 5.2 Total dosimetric uncertainties at the three tumour apex heights (3, 5 and 10 mm) for fully loaded 16 mm COMS plaque and Super9 plaques, as well as the required margins to ensure adequate dosimetric coverage for a simple dome-shaped tumour.

Uncertainty components and required margins	16 mm COMS			Super9		
	3 mm	5 mm	10 mm	3 mm	5 mm	10 mm
Total combined uncertainty* (%) (k=1)	8.63	8.07	7.11	9.09	7.19	6.55
Expanded uncertainty (%) (k=2)	17.3	16.1	14.2	18.2	14.4	13.1
Margin for expanded uncertainty (mm)	0.9	0.9	1.0	1.5	1.1	1.0
Plaque placement/tilt margin (mm)	0.4	0.4	0.4	0.3	0.3	0.2
Total Margin (mm)	1.3	1.3	1.4	1.8	1.4	1.2

*As described in Table 5.1.

5.4 Discussion

The prescription convention aims to cover 100% of the tumour (as modelled in the TPS) with the isodose line representing 100% of the prescribed dose. However, due to uncertainties in the dose delivery process, the actual dose delivered may be different than planned. Cold spots within the tumour volume may be of particular clinical concern. As the tumour apex is receiving the lowest dose within the tumour, this is most commonly the location of a potential cold spot. A planning margin on the apex may be used to ensure that it is covered by the prescribed dose. The optimal size of this margin has not been previously established; therefore various sources of uncertainty were analyzed at the prescription point to determine an adequate margin size.

In general, the assessed uncertainties are dependent on the dose gradient at the depth of interest, and are therefore larger when the dose gradient is steeper. However, this in turn also means that a relatively smaller margin may be needed. This trend is found for the 16 mm COMS plaque, for which the dose gradient along the CAX gradually decreases with depth making the relative uncertainties larger at shallower depth, but requiring close to the same treatment margins to account for them. For the Super9 plaque, due to the collimating seed slots, the CAX dose first increases and then plateaus at just over 2 mm from the outer scleral surface, at which point it begins to decrease and is in general less steep than the dose gradient for the 16 mm COMS plaque. The dosimetric uncertainties are therefore in general lower for the Super9 plaque than for

the 16 mm COMS plaque, with the exception of the seed positioning uncertainty at the 3 mm tumour apex height at which point the dose is very sensitive to seed positioning.

For the Super9 plaque, the increase in dose observed when gluing the seeds into the centers of the slots may also partly compensate for the decrease in dose due to uncertainties in plaque positioning and plaque tilt. For a plaque loaded with the central 16 seeds (as in Section 5.2.3), the margin to account for plaque tilt and plaque positioning (line 4 in Table 5.2) could be eliminated for the 3 mm tumour, and reduced to 0.1 mm for the 5 mm tumour (there was no change for the 10 mm tumour). This however would require examining a fully loaded plaque to verify if a reduction in apex treatment margin is appropriate.

These margins can be used as a guide for determining an appropriate apex margin for a given treatment, which can be chosen based on the specific tumour height. The required margin may however need to be increased for more complex scenarios (mushroom shaped tumours, tumours close to the optic nerve, etc.) than the simple dome-shaped tumour presented here, and should be evaluated on a case-by-case basis.

For example, partially loaded and eccentrically placed plaques are frequently used for patient treatments at the CCI as they allow for a number of advantages including: more conformal doses around the basal edges of the tumour; easier suture attachment and plaque placement as the eyelets are brought more anterior on the eye compared to using a smaller plaque size centered on the tumour; and the potential for dose sparing to critical structures in the eye. Consequently, the uncertainties in the patient treatment plans using a 16 mm COMS plaque that was partially loaded and eccentrically placed over the tumour were also assessed. Due to steeper dose gradients when using fewer seeds as well as higher sensitivity to plaque placement and tilt, the required apex margins to account for the dosimetric uncertainty were slightly larger, ranging from 1.3 to 1.75 mm for small to medium sized tumours.[33]

5.4.1 Possible means to minimize uncertainty in the delivered dose

The largest sources of uncertainty are due to seed placement within the plaque, treatment planning calculations, tumour height measurement, and plaque tilt. For the slotted type of plaques, the uncertainty in seed placement is particularly large for the Super9 plaque due to the long seed slots. The manufacturer stated slot lengths are shorter for most of the other 2nd generation Eye Physics plaques; therefore this uncertainty could be smaller for other slotted

plaques. To minimize seed placement uncertainty in the COMS plaques, seeds need to be carefully loaded. This may be beyond the control of centers which receive plaques pre-loaded and sterilized. Nevertheless, plaques should be visually inspected to determine if any seeds appear misplaced.

The current treatment planning calculations are based on TG-43 dosimetry parameters from consensus datasets. For the IsoAid IAI-125A seed, these parameters have recently been re-analyzed.[34–36] The newer parameters have been determined using MC simulations with improved physics models and related cross-section libraries, as well as with more rigorous accounting of various source construction details (I-125 coating thickness, coating mass density, end-weld construction, etc.). The more recently determined dosimetry parameters for the IsoAid IAI-125A seed also have lower uncertainties than those in the older currently used consensus dataset due to improvements in the MC simulations (smaller scoring volumes, decreased statistical uncertainties, more accurate cross-section libraries and photon spectra, etc.), and if used would reduce the uncertainties in treatment planning calculations. In addition, if the dosimetry parameter data is determined at small enough increments, the interpolation and extrapolation uncertainty could be reduced.

Though not included in the present assessment of total uncertainties, compared to the more recently determined TG-43 parameters for the IAI-125A seed the consensus TG-43 data over-estimates the dose. The parameters determined by Taylor *et al.*[34] and Zimmerman *et al.*[36] were substituted into Plaque Simulator (the Aryal *et al.*[35] data was not used due to a lack of $g_L(r)$ values at small values of r, though the data is very similar to that of Taylor *et al.*) and resulted in dose decreases at the 5 mm tumour apex of 5.2% and 2.1% for the 16 mm COMS plaque, respectively, and 5.2% and 2.0% for the Super9 plaque, respectively. Using up to date TG-43 dosimetry parameters would improve both the accuracy and precision of the dose calculations. Accurate MC simulations of the backscatter factor employed for the Eye Physics plaques, $B(r)$, to replace the TLD measured values, would also further reduce the dose calculation uncertainty for these styles of plaques.

Due to the difficulty in distinguishing the tumour-scleral interface, and with variation in the scleral thickness which is generally assumed to be 1 mm but can vary from 0.3-1 mm,[2] the current method employed by our group is to measure the tumour height from the outer sclera. The tumour height for treatment planning purposes is then taken as the measured value minus 1

mm, which is then added in Plaque Simulator as the standard 1 mm scleral thickness. In this way the measured distance from the outer sclera to the tumour apex is preserved, and uncertainty in tumour height measurement is minimized.

Minimizing plaque tilt during plaque insertion can be achieved by verifying plaque position during surgery using, for example, intraoperative ultrasonography, as has been done in previous studies.[4,6,7] If the plaque needs to be placed over an ocular muscle, uncertainty in the thickness of the ocular muscle will lead to uncertainty in the estimated amount of plaque tilt, which can be minimized by removing the ocular muscle (and subsequent reattaching it after plaque removal) if clinically acceptable. However minimizing any change in plaque tilt throughout treatment is much more difficult to achieve, as it has been found to depend on tumour position (proximity to the optic nerve, ocular muscle involvement etc.), whether or not a notched plaque is used, which suture eyelets are used, the amount of swelling, and the possible occurrence of an episcleral hematoma.[4]

5.4.2 Uncertainties requiring further research

Additional uncertainties which require further research to accurately quantify include those associated with radiation transport and dose deposition media, both for patient tissue and plaque materials. For I-125, at 5 mm depth from the inner sclera, the difference in dose for a single seed in a Silastic insert in a pure gold backing compared to a Modulay backing is approximately 1.4% (Thomson *et al*. Fig. 3(a)).[10] The difference arises due to the copper and silver content in the gold alloy. Both Modulay and 18K gold alloys exhibit variations in their exact composition, and although the difference would be smaller than the difference when compared with pure gold, it would alter the dose at the tumour apex. Similarly, variations in the Silastic composition can also affect the dose.[37]

Variations arising from considerations of patient tissue composition have been examined by Lesperance *et al*., who reported an increase in dose to the tumour apex of 7.9% for I-125 when including various ocular media ($D_{w,w}$ vs. $D_{m,m}$).[38] These calculations were performed using one possible melanoma tumour composition, whereas simulations for a second, less water-equivalent, melanoma tumour composition resulted in a further 5% increase in dose to the tumour apex compared to a plaque in water. It is noted however that the exact composition of uveal melanoma is not currently available, and that variations in elemental composition are

expected to exist within the patient population. Individualized model-based dose calculations would be necessary to account for the different ocular media present in each patient.[39] Exploring this possibility is the purpose of the work performed in the following chapter.

5.5 References

[1] S. Nag, J.M. Quivey, J.D. Earle, D. Followill, J. Fontanesi, and P.T. Finger, "The American Brachytherapy Society recommendations for brachytherapy of uveal melanomas," Int. J. Radiat. Oncol. Biol. Phys. **56**, 544–555 (2003).

[2] R. Potter and E. Van Limbergen, "Uveal melanoma," in *The GEC ESTRO handbook of brachytherapy*, edited by A. Gerbaulet, R. Potter, J.J. Mazeron, H. Meertens and E. Van Limbergen (Belgium, 2002), pp. 591–610.

[3] N.L. Gagne and M.J. Rivard, "Quantifying the dosimetric influences of radiation coverage and brachytherapy implant placement uncertainty on eye plaque size selection," Brachytherapy **12**, 508–520 (2013).

[4] A. Almony, S. Breit, H. Zhao, J. Garcia-Ramirez, D.B. Mansur, and J.W. Harbour, "Tilting of radioactive plaques after initial accurate placement for treatment of uveal melanoma," Arch. Ophthalmol. **126**, 65–70 (2008).

[5] J.W. Harbour, T.G. Murray, S.F. Byrne, R. Hughes, E.K. Gendron, F.J. Ehlies, and A.M. Markoe, "Intraoperative echographic localization of iodine 125 episcleral radioactive plaques for posterior uveal melanoma," Retina **16**, 129–134 (1996).

[6] P.T. Finger, J.M. Romero, R.B. Rosen, R. Iezzi, R. Emery, and A. Berson, "Three-dimensional ultrasonography of choroidal melanoma: localization of radioactive eye plaques," Arch. Ophthalmol. **116**, 305–312 (1998).

[7] H. Tabandeh, N.A. Chaudhry, T.G. Murray, F. Ehlies, R. Hughes, I.U. Scott, and A.M. Markoe, "Intraoperative echographic localization of iodine-125 episcleral plaque for brachytherapy of choroidal melanoma," Am. J. Ophthalmol. **129**, 199–204 (2000).

[8] L.A. DeWerd, G.S. Ibbott, A.S. Meigooni, M.G. Mitch, M.J. Rivard, K.E. Stump, B.R. Thomadsen, and J.L.M. Venselaar, "A dosimetric uncertainty analysis for photon-emitting brachytherapy sources: report of AAPM Task Group No. 138 and GEC-ESTRO," Med. Phys. **38**, 782–801 (2011).

[9] C. Kirisits, M.J. Rivard, D. Baltas, F. Ballester, M. De Brabandere, R. Van Der Laarse, Y. Niatsetski, P. Papagiannis, T.P. Hellebust, J. Perez-Calatayud, K. Tanderup, J.L.M. Venselaar, and F.A. Siebert, "Review of clinical brachytherapy uncertainties: Analysis guidelines of GEC-ESTRO and the AAPM," Radiother. Oncol. **110**, 199–212 (2014).

[10] R.M. Thomson, R.E.P. Taylor, and D.W.O. Rogers, "Monte Carlo dosimetry for ^{125}I and ^{103}Pd eye plaque brachytherapy," Med. Phys. **35**, 5530 (2008).

[11] G. Luxton, M.A. Astrahan, and Z. Petrovich, "Backscatter measurements from a single seed of ^{125}I for ophthalmic plaque dosimetry," Med. Phys. **15**, 397–400 (1988).

[12] M.J. Rivard, C.S. Melhus, and B.L. Kirk, "Brachytherapy dosimetry parameters calculated for a new ^{103}Pd source," Med. Phys. **31**, 2466–2470 (2004).

[13] S.M. Seltzer, P.J. Lamperti, M.G. Mitch, J.T. Weaver, and B.M. Coursey, "New National Air-Kerma-Strength Standards for ^{125}I and ^{103}Pd Brachytherapy Seeds," J. Res. Natl. Inst. Stand. Technol. **108**, 337–358 (2003).

[14] S.M. Seltzer, P.J. Lamperti, R. Loevinger, M.G. Mitch, J.T. Weaver, and B.M. Coursey, "Erratum: New National Air-Kerma-Strength Standards for ^{125}I and ^{103}Pd Brachytherapy Seeds," J. Res. Natl. Inst. Stand. Technol. **109**, 301 (2004).

[15] W.M. Butler, W.S. Bice, L.A. DeWerd, J.M. Hevezi, M.S. Huq, G.S. Ibbott, J.R. Palta, M.J. Rivard, J. Seuntjens, and B.R. Thomadsen, "Third-party brachytherapy source calibrations and physicist responsibilities: report of the AAPM Low Energy Brachytherapy Source Calibration Working Group," Med. Phys. **35**, 3860–3865 (2008).

[16] M.A. Astrahan, G. Luxton, G. Jozsef, T.D. Kampp, P.E. Liggett, M.D. Sapozink, and Z. Petrovich, "An interactive treatment planning system for ophthalmic plaque radiotherapy," Int. J. Radiat. Oncol. Biol. Phys. **18**, 679–687 (1990).

[17] M.A. Astrahan, "Improved treatment planning for COMS eye plaques," Int. J. Radiat. Oncol. Biol. Phys. **61**, 1227–1242 (2005).

[18] M.J. Berger and J.H. Hubbell, "XCOM: Photon cross sections on a personal computer," in *Report NBSIR87-3597* (National Institute of Standards Technology (NIST), Gaithersburg, MD, 1987).

[19] M.J. Rivard, W.M. Butler, L.A. DeWerd, M.S. Huq, G.S. Ibbott, A.S. Meigooni, C.S. Melhus, M.G. Mitch, R. Nath, and J.F. Williamson, "Supplement to the 2004 update of the AAPM Task Group No. 43 Report," Med. Phys. **34**, 2187–2205 (2007).

[20] T.D. Solberg, J.J. DeMarco, G. Hugo, and R.E. Wallace, "Dosimetric parameters of three new solid core I-125 brachytherapy sources," J. Appl. Clin. Med. Phys. **3**, 119–134 (2002).

[21] A.S. Meigooni, J.L. Hayes, H. Zhang, and K. Sowards, "Experimental and theoretical determination of dosimetric characteristics of IsoAid ADVANTAGE ^{125}I brachytherapy source," Med. Phys. **29**, 2152–2158 (2002).

[22] R. Nath, L.L. Anderson, G. Luxton, K.A. Weaver, J.F. Williamson, and A.S. Meigooni, "Dosimetry of interstitial brachytherapy sources: recommendations of the AAPM Radiation

Therapy Committee Task Group No. 43. American Association of Physicists in Medicine," Med. Phys. **22**, 209–234 (1995).

[23] M.J. Rivard, B.M. Coursey, L.A. DeWerd, W.F. Hanson, M.S. Huq, G.S. Ibbott, M.G. Mitch, R. Nath, and J.F. Williamson, "Update of AAPM Task Group No. 43 Report: A revised AAPM protocol for brachytherapy dose calculations," Med. Phys. **31**, 633–674 (2004).

[24] D.C. Medich, M.A. Tries, and J.J. Munro, "Monte Carlo characterization of an ytterbium-169 high dose rate brachytherapy source with analysis of statistical uncertainty," Med. Phys. **33**, 163–172 (2006).

[25] C.L. Shields, J.A. Shields, H. Kiratli, P. De Potter, and J.R. Cater, "Risk factors for growth and metastasis of small choroidal melanocytic lesions," Ophthalmology **102**, 1351–1361 (1995).

[26] S.F. Byrne and R.L. Green, *Ultrasound of the eye and orbit* (Mosby Year Book Inc., St. Louis, MO, 1992).

[27] Collaborative Ocular Melanoma Study Group, "Echography (ultrasound) procedures for the collaborative ocular melanoma study (COMS), Report No.12, Part II," J. Ophthalmic Nurs. Technol. **18**, 219–232 (1999).

[28] D.J. Coleman, D.H. Abramson, R.L. Jack, and L.A. Franzen, "Ultrasonic diagnosis of tumors of the choroid," Arch. Ophthalmol. **91**, 344–354 (1974).

[29] D.G. Godfrey, R.G. Waldron, and A. Capone, "Transpupillary thermotherapy for small choroidal melanoma," Am. J. Ophthalmol. **128**, 88–93 (1999).

[30] Evaluation of measurement data—Guide to the expression of uncertainty in measurement, International Organization for Standardization (ISO), Joint Committee for Guides in Metrology (JCGM 100, 2008), corrected version 2010, http://www.bipm.org/utils/common/documents/jcgm/JCGM_100_2008_E.pdf.

[31] B.N. Taylor and C.E. Kuyatt, "Guidelines for Evaluating and Expressing the Uncertainty of NIST Measurement Results," in *NIST Technical Note 1297* (U.S. Government Printing Office, Washington DC, 1994).

[32] S. McCauley Cutsinger, K.M. Furutani, and S. Corner, "A Method to Verify Eye Plaque Seed Coordinates Using the FARO Edge," Brachytherapy **14**, S68–S69 (2015).

[33] H. Morrison, M.P. Larocque, G. Menon, H.-S. Jans, E. Weis, and R.S. Sloboda, "Delivered dose uncertainty analysis for partially loaded and eccentrically placed 16 mm COMS plaques compared to fully loaded plaques for brachytherapy treatment of uveal melanoma," International Society of Ocular Oncology (ISOO) Bienniel Conference (URL: http://isoo2017.com/ISOO abstracts/Saturday sessions/Saturday 115 - 225/Saturday 115pm to 225pm_4.pdf) (2017).

[34] R.E.P. Taylor and D.W.O. Rogers, "An EGSnrc Monte Carlo-calculated database of TG-43 parameters," Med. Phys. **35**, 4228–4241 (2008).

[35] P. Aryal, J.A. Molloy, and M.J. Rivard, "A modern Monte Carlo investigation of the TG-43 dosimetry parameters for an ^{125}I seed already having AAPM consensus data," Med. Phys. **41**, 021702 (10 pp.) (2014).

[36] L.W. Zimmermann, A. Amoush, and D.A. Wilkinson, "Episcleral eye plaque dosimetry comparison for the Eye Physics EP917 using Plaque Simulator and Monte Carlo simulation," J. Appl. Clin. Med. Phys. **16**, 226–239 (2015).

[37] C.S. Melhus and M.J. Rivard, "COMS eye plaque brachytherapy dosimetry simulations for ^{103}Pd, ^{125}I, and ^{131}Cs," Med. Phys. **35**, 3364–3371 (2008).

[38] M. Lesperance, M. Inglis-Whalen, and R.M. Thomson, "Model-based dose calculations for COMS eye plaque brachytherapy using an anatomically realistic eye phantom," Med. Phys. **41**, 021717 (12 pp.) (2014).

[39] L. Beaulieu, Å. Carlsson Tedgren, J.-F. Carrier, S.D. Davis, F. Mourtada, M.J. Rivard, R.M. Thomson, F. Verhaegen, T.A. Wareing, and J.F. Williamson, "Report of the Task Group 186 on model-based dose calculation methods in brachytherapy beyond the TG-43 formalism: Current status and recommendations for clinical implementation," Med. Phys. **39**, 6208–6236 (2012).

Chapter 6 Model-based dose calculations for COMS eye plaques using ACE

A version of this chapter has been submitted as two articles to Medical Physics: H. Morrison, G. Menon, M.P. Larocque, E. Weis and R.S. Sloboda, "Collapsed-cone dose calculations in water medium for I-125 seeds and COMS eye plaques," and (same author list) "Collapsed-cone dose calculations in tissue media for COMS eye plaques loaded with I-125 seeds."

6.1 Introduction

The currently recommended dosimetry protocol for eye plaques supports a supplementary calculation that includes corrections for heterogeneous plaque materials (gold backing and Silastic inserts), as they cause significant reductions in dose within the eye.[1] Though many studies contributed to this improvement in dose calculation accuracy,[2–6] tissues in the eye are still assumed to be entirely water. This assumption can cause substantial dose calculation inaccuracies, as recently demonstrated using MC simulations for a voxelized geometric model of the eye and a COMS eye plaque where differences of up to 10% within a choroidal melanoma and 14% within the lens of the eye were reported.[7] Given that ocular brachytherapy does not always achieve local tumour control and that metastases or secondary radiation effects can often occur, more accurate clinical dosimetry is warranted.

With the recent advent of commercially available model-based dose calculation algorithms, the possibility of moving away from traditional TG-43 water-based dose calculation in clinical practice now exists.[8] These algorithms allow for consideration of patient scatter conditions that differ from the infinite homogeneous medium assumed in TG-43 single source dosimetry parameter determination, patient tissue heterogeneities as opposed to homogeneous water medium, and non-water-equivalent applicator materials (including plastics and metal shields). All of these are expected to impact ocular brachytherapy dosimetry due to the presence of the air interface at the patient's face, the low-energy photons emitted by the radiation sources which are highly sensitive to material composition (values of absorbed dose and radiation attenuation), and the high-Z gold plaques.[8,9]

159

With the goal of improving the accuracy of dose calculations and accounting for all these effects, the Oncentra Brachy (OcB) TPS with the Advanced Collapsed cone Engine (ACE) algorithm was assessed for its potential to be used for ocular brachytherapy. The ACE algorithm has previously only been applied to Ir-192 and Co-60 high-dose-rate brachytherapy treatment planning. Therefore, to perform patient-specific model-based dose calculations with ACE for ocular brachytherapy, a low-energy radiation source as well as eye plaques first needed to be incorporated into the treatment planning software.

The work presented in this chapter outlines the procedure for incorporating two I-125 seed types and three sizes of COMS eye plaques into the software, and describes the subsequent evaluation of the ACE algorithm in a research version of OcB (v4.6). The ACE algorithm was assessed in four stages: (1) for a single seed in water (TG-186 level 1 commissioning[8]); (2) for the three sizes of COMS eye plaques in water; (3) using a voxelized eye phantom containing various ocular structures and materials with different densities for each structure; and (4) using a patient CT dataset with a realistic variability in tissue densities throughout the entire patient model. MC simulations using MCNP6 were used to obtain reference dosimetry for comparison with all ACE calculated doses. The ACE and MCNP6 doses were also compared to water-based dosimetry obtained using the Plaque Simulator TPS to explore the effects of including the heterogeneous tissues. Through this approach, the accuracy of ACE was evaluated and current shortcomings in both OcB and ACE were identified. This work presents the first implementation of model-based dose calculations for eye plaques using a commercial software platform to account for heterogeneous eye tissues as well as plaque materials, potentially allowing for routine clinical dose calculations beyond the TG-43 formalism.

6.2 Materials and Methods

6.2.1 Monte Carlo simulations

MCNP6 (v.1)[10] is used for all simulations presented in this chapter. The general theory behind MCNP6 is presented in Section 2.5.3.2. Additional details will be provided here and throughout the following sections. The default photon cross-section library, MCPLIB84 (84p), was used for all simulations. The I-125 photon spectrum was taken from the NNDC database,[11] as shown in Table 2.1, though as discussed previously the 3.77 keV photons were not included as they are not

found to contribute dose beyond ~0.1 cm in tissue[12] and only increase the simulation time. All simulations were performed using Mode P (electrons deposit energy locally) as the electron ranges are significantly shorter than the size of the scoring cells (approximately one hundredth or less).

As mentioned in Section 2.5.3.2, *F4, *FMESH, and F6 tallies are used to calculate energy deposition within a specified cell per starting particle, with conversion factors (μ_{en}/ρ) required for the *F4 and *FMESH tallies to convert energy fluence to energy deposited per unit mass.

In general, the numbers of particles simulated were chosen such that the statistical uncertainty in dose rate within each scoring cell remained below approximately 0.5% within the regions of interest.

6.2.2 Seed modelling

6.2.2.1 Implementation in MCNP6

Three I-125 brachytherapy seeds were created for simulations in MCNP6. This involved first creating the seed geometry and benchmarking it against previously published dose data, which was done by calculating TG-43 parameters for each of the three seeds. To accomplish this, the seed (the specifics of the geometry for each seed to be discussed following) was positioned centrally within a 30 cm radius water sphere with a hydrogen-to-oxygen atomic ratio of 2:1 and a mass density of 0.998 g/cm^3. The spherical water volume surrounding the seed was divided into a contiguous sampling space bounded by spheres and conics, similar to the geometry described by Rivard *et al.*[13] The first sphere was 0.05 cm thick at a distance of 0.1 cm, after which additional spheres were created at 0.1 cm increments up to a radius of 1 cm, and then 0.5 cm increments (with 0.1 cm thickness) up to a radius of 10 cm. Cones were created in 2° increments (space between cones was 1°), centered on integer values of polar angle. The F6 tally was used to score energy deposition in water (converted to dose to water) at 5° intervals from 0° to 90° for each radius (0.1 to 10 cm). The ratios of scored dose were used to calculate the TG-43 parameters $g_L(r)$ and $F(r, \theta)$ using equations 2.9 – 2.11. Simulations in water were performed with 5×10^8 starting particles, resulting in at most 0.5% statistical uncertainties for θ > 15° at 10 cm (and slightly larger uncertainties ~0.1-5% at θ ≤ 15°). Statistical uncertainties were 0.06% at 1 cm and 0.1% at 3 cm on the transverse axis (for a coverage factor of k=1).

The dose rate constant (Λ) was calculated using an additional simulation to determine the air-kerma strength, S_K. To determine S_K, the seed was positioned in vacuum and the energy deposition in air (using a *F4 tally and μ_{en}/ρ values for air from the NIST database[14] on a DE/DF card with a 5 keV cutoff energy) was scored in a 0.00002 mm thick spherical shell centered at 30 cm radial distance within a ±7.5946° wide conical region to mimic the NIST WAFAC chamber[15] on the transverse plane of the seed.[16] The energy deposited per mass is equal to the air-kerma rate, $\dot{K}_\delta(d)$, which is used to calculate S_K using equation 2.6 at a radial distance (d) of 30 cm. This value, in combination with the dose rate from the water simulation at $(r, \theta) = (1$ cm, 90°) is used to calculate Λ using equation 2.7. The simulations in vacuum were performed with 1×10^9 starting particles, resulting in statistical uncertainties of 0.07% for S_K and 0.09% for Λ.

The I-125 seeds implemented for MCNP6 include the model IAI-125A (IsoAid LLC, Port Richey, FL) (used for simulations in Chapter 4), the Nucletron selectSeed model 130.002 (Elekta AB, Stockholm, SE), and the Oncura OncoSeed model 6711 (GE Healthcare Inc., Arlington Heights, IL). As stated in Chapter 4, the design of the IAI-125A seed is based on the dimensions used by Aryal *et al.* in their Simulation condition 11,[16] and is briefly described here and shown in Figure 6.1. The capsule is composed of titanium with a density of 4.54 g/cm^3, and houses an inner silver rod of density 10.5 g/cm^3 which is coated with AgI with a density of 6.003 g/cm^3, and the remaining space in the capsule is filled with argon gas with a density of 0.001662 g/cm^3. The end welds are defined by two ellipses. All other dimensions are specified in Table 6.1.

The dimensions used for the selectSeed model 130.002 I-125 seed were taken from Karaiskos *et al.*[17] and Taylor and Rogers[18] (also presented in the Carleton Laboratory for Radiation Physics (CLRP) TG-43 parameter database[19]). The titanium capsule and silver rod are of the same density as the corresponding components of the IAI-125A seed. The end welds are hemispherical in shape and the remaining space in the capsule is filled with dry air (NIST composition and density[14]). A schematic of the seed is shown in Figure 6.2, and the dimensions are given in Table 6.1.

The dimensions used for the OncoSeed model 6711 seed were taken from Dolan *et al.*[20] and Taylor and Rogers[18] (also presented in the CLRP TG-43 parameter database[19]). The titanium capsule and silver rod have the same density as those for the other two seeds. The 6711 seed also has hemispherical end welds and the capsule is also filled with dry air. The main difference is the

45° bevelled edges of the silver rod; the inner diameter of the bevelled edges is 0.35 mm. A schematic of the seed is shown in Figure 6.3 and all other dimensions are given in Table 6.1.
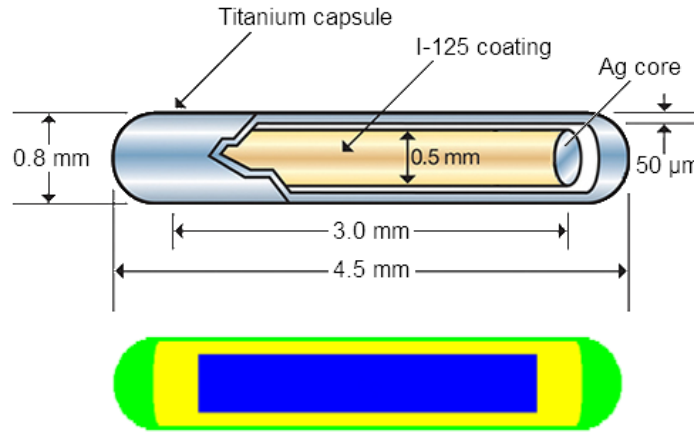
Figure 6.1 Schematic diagram of the model IAI-125A seed. The top image shows the nominal seed design from the seed manufacturer (image reproduced from http://www.eyephysics.com/ps/PS6/UserGuide/OrderSeeds.html), whereas the bottom image shows the geometry used in MCNP6 from the geometry plotter.
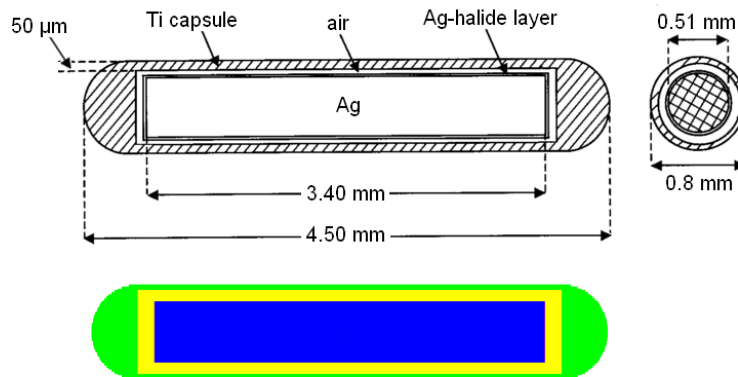
Figure 6.2 Schematic diagram of the selectSeed model 130.002 seed. The top image shows the nominal seed design (adapted from Karaiskos *et al*., "Monte Carlo dosimetry of the selectSeed 125 I interstitial brachytherapy seed," Med. Phys. **28**, 1753–1760 (2001)[17] with permission from John Wiley and Sons and the American Association of Physicists in Medicine) whereas the bottom image shows the geometry used in MCNP6 from the geometry plotter (end-welds and Ag rod diameter are not shown to scale in the top image).
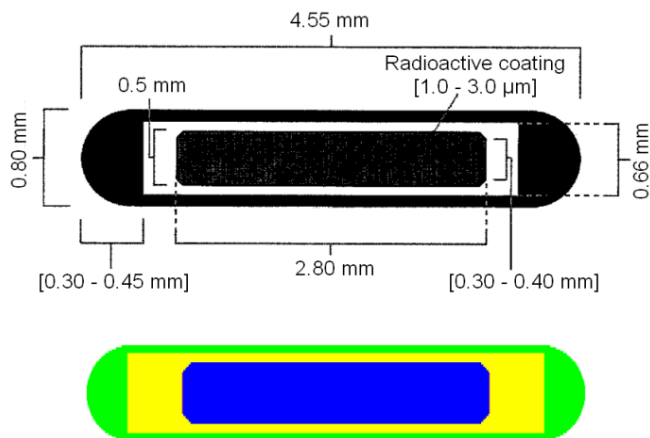
Figure 6.3 Schematic diagram of the model 6711 seed. The top image shows the nominal seed design (adapted from Dolan *et al*., "Monte Carlo and experimental dosimetry of an ^{125}I brachytherapy seed," Med. Phys. **33**, 4675–4684 (2006)[20] with permission from John Wiley and Sons and the American Association of Physicists in Medicine) whereas the bottom image shows the geometry used in MCNP6 from the geometry plotter (end-welds are displayed with the maximum thickness of 0.45 mm in the top image, and the average thickness of 0.375 mm in the bottom image).

Table 6.1 Dimensional characteristics of the model IAI-125A, selectSeed 130.002 and 6711 I-125 seeds (all dimensions are given in mm unless otherwise specified).

Parameter	Source model		
	IAI-125A	selectSeed 130.002	6711
Ag rod length	3.00	3.40	2.80
Ag rod bevel at 45°	0.00	0.00	0.05
Ag rod diameter	0.50	0.51	0.50
Capsule outer length	4.50	4.50	4.55
Capsule inner length	3.70	3.70	3.80
Capsule outer diameter	0.80	0.80	0.80
Capsule inner diameter	0.70	0.70	0.66
Capsule endweld thickness	0.35	0.40	0.375
Coating thickness	0.5 μm	3.0 μm	1.75 μm
Coating composition	AgI	AgCl:AgI = 1:1	AgBr:AgI = 2.5:1
Coating density	6.003 g/cm^3	5.6 g/cm^3	6.2 g/cm^3

6.2.2.2 Implementation in ACE

The seeds incorporated for use in OcB for ACE calculations include the Nucletron selectSeed model 130.002 and the OncoSeed model 6711. This requires TG-43 dosimetry parameters, as well as the primary scatter separated (PSS) data described in Section 2.5.4 and shown in Figure 2.10 for the 6711 seed. Any photons that leave the Ti source encapsulation are considered primary photons, whereas those that undergo one interaction (without being absorbed) are first-scattered photons and those that undergo any number of subsequent interactions are multiply-scattered photons. The PSS data for both types of seed were created by the CLRP group using BrachyDose[18,21] for the selectSeed, and a recently rewritten version, egs_brachy,[22] for the model 6711 seed (the data for the selectSeed are available in the CLRP online database[19]).

The TG-43 data for the selectSeed were taken from Karaiskos *et al.* and the PSS data were determined at 1 mm/1° increments from 0.1 cm to 10 cm and 0° to 90°. The TG-43 data for the 6711 seed were determined using egs_brachy and provided by the CLRP group. These data were re-interpolated onto a regularly spaced grid [1 mm increments for $g_L(r)$, and 1 mm/1° increments for $F(r,\theta)$]. The PSS data for the 6711 seed were determined at higher resolution within the first 2 cm from the source: radially at 0.1 mm increments up to 1 cm from the source, then at 0.5 mm increments for 1 cm < r < 2 cm; and angularly at 1° increments, for the primary, first scattered, and multiply-scattered dose contributions. The PSS data are used to create the parameterized dose deposition kernel data (as described in Section 2.5.4.1), which are then normalized to match the TG-43 calculated dose at 1 cm from the source on the transverse axis based on the total dose determined using the ACE algorithm in a 15 cm radius spherical water phantom.

To perform the superposition and collapsed-cone calculation, the dose in each step is calculated per radiant energy available, which is ultimately determined from the energy weighted photon spectrum for a given radiation source. The energy weighted photon spectrum is scored in bins as:

$$\frac{(dR(E_j)/dE)}{R} = \sum \frac{E_i}{(\Delta E \cdot R)} \tag{6.1}$$

where E_j is the energy in the centre of a bin, E_i is the energy of the ith photon escaping the source encapsulation with energy between $E_j \pm \Delta E/2$, and ΔE is the bin width. The energy weighted

photon spectrum is normalized to the total radiant photon energy, R (total energy of photons escaping the source encapsulation). The units of the energy weighted photon spectrum are therefore MeV^{-1}. The spectra for the selectSeed and 6711 I-125 seeds are shown in Figure 6.4.
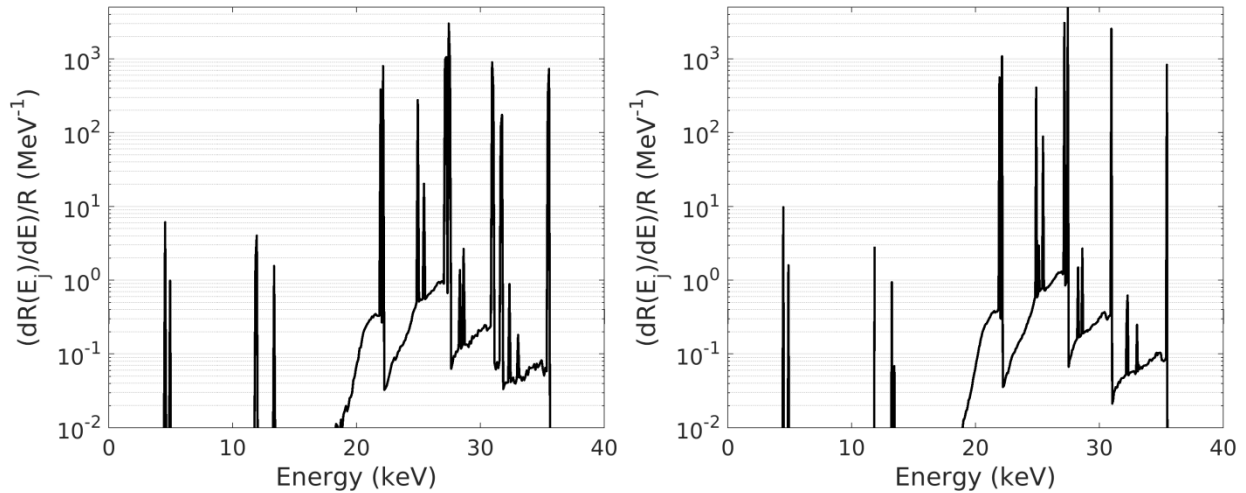
Figure 6.4 Energy weighted spectrum of primary photons used in ACE to determine the energy per radiant photon energy for the selectSeed (left) and 6711 seed (right). (Data for the selectSeed available on the CLRP TG-43 parameter database,[19] data for the 6711 seed provided through private communication [R. Thomson]).

All other aspects of the dose calculation by ACE follow methods outlined in relevant publications;[23,24] no additional or different methods are used compared to high energy HDR source calculations with the exception of the size of dose calculation grid, which in the research version of OcB (v4.6) was set to 0.5 x 0.5 x 0.5 mm^3. The default number of cones/transport directions for collapsed-cone calculation of first- and multiply-scattered dose in the high accuracy mode setting (hACE) was used for all ACE dose calculations (1620/320 for a single dwell position, and 720/240 for more than one dwell position).

Both the selectSeed and 6711 seed were incorporated into OcB as sources for a Flexitron afterloader (to be compatible with the current catheter-afterloader set-up in OcB). The sources were added to the source database in OcB with an initial calibration source strength of 3.81 U (the current maximum source strength possible for I-125 seeds in OcB). All treatments were planned to start at the source calibration time, and therefore used the initial source strength of 3.81 U.

Initial validations of ACE calculated doses for both seeds were performed using a single seed in a water box of dimensions 15 x 15 x 15 cm^3 (level 1 commissioning) by comparing the dose distribution around the seed to both TG-43 and MCNP6 simulated doses. The TG-43 and ACE dose data were exported from OcB using a grid size of 0.5 x 0.5 x 0.5 mm^3 centered on the source, and dose was scored around the sources in MCNP6 using a *FMESH tally of the same dimensions and position around the source. The irradiation time was set to deliver 5 Gy at 1 cm on the transverse axis of the source based on the TG-43 calculation, and the same total dwell time was used for the ACE calculation. The *FMESH data gives the energy deposited per starting particle. The total dose for comparison with OcB is determined by calculating the dose rate per starting particle $\left(_{SP}\dot{D}\right)$ (*FMESH tally value) per source air-kerma strength per starting particle $\left(_{SP}S_K\right)$ (from single source simulation in vacuum as described in Section 6.2.2.1), and multiplying by the source air-kerma strength $\left(_{source}S_K\right)$ and total dwell time (T) required in OcB:

$$D_T = \frac{_{SP}\dot{D}}{_{SP}S_K} \cdot {_{source}S_K} \cdot T \tag{6.2}$$

The value for $_{source}S_K$ was always 3.81 U. The default dose calculation setting in OcB does not include a correction for source decay, so a constant dose rate is used to calculate the total dose. These simulations used 5×10^9 starting particles, resulting in an average of 0.5% statistical uncertainty within the 6 x 6 x 6 cm^3 region used for comparison around the seed and a maximum statistical uncertainty of 1.3% at the furthest distance from the source examined.

For comparisons between ACE, TG-43, and MCNP6 calculated doses, both for single seed and plaque dosimetry, 3D local (%ΔD$_{LOCAL}$) and global (%ΔD$_{GLOBAL}$) percent differences were used and are defined as:[25]

$$\%\Delta D_{LOCAL} = \frac{D(r) - D_{ref}(r)}{D_{ref}(r)} \cdot 100 \tag{6.3}$$

$$\%\Delta D_{GLOBAL} = \frac{D(r) - D_{ref}(r)}{D_{ref}(r_{ref})} \cdot 100 \tag{6.4}$$

where r_{ref} for the calculation of %ΔD$_{GLOBAL}$ is located at 1 cm from the source on the transverse axis. These parameters are used to assess the accuracy of ACE calculated doses as well as the clinical relevancy of dose differences.

167

Due to the increased resolution of the PSS data for the 6711 seed (and higher level of agreement, as will be shown in Section 6.3.1.2), it was used for most of the following work presented in this chapter. In order to improve MCNP6 simulation efficiency, a phase space file for the 6711 seed was created using the SSW card (as explained in Section 2.5.3.2) with 1×10^9 starting particles. The number of tracks recorded in the phase space file was 4.5×10^8, indicating that less than half of the initially simulated particles leave the source encapsulation. Use of a phase space file results in a speed up of over two-times in the simulations for the 6711 seed. All simulations for this seed incorporated into a COMS eye plaque were performed using an SSR card (see Section 2.5.3.2) (though only one seed was "active" at a time) such that 1×10^9 starting particles were effectively simulated for each source location in the plaque.

6.2.3 COMS plaque modelling

6.2.3.1 Implementation in MCNP6

Standard COMS eye plaques with diameters of 12, 16, and 20 mm were modelled in MCNP6 using the standard geometry, seed coordinates, and material properties provided in TG-129.[1] COMS plaques are designed based on a standard eye diameter of 24.6 mm with all seed centres located at a radial distance of 1.4 mm from the outer sclera on the surface of a sphere of radius 13.7 mm. The plaque backings were created from segments of two bounding spheres with an outer diameter of 15.55 mm and inner diameter of 15.05 mm, contained within a cylinder of the appropriate diameter and cap height to create the appropriate lip height (Figure 6.5). The plaque backings were composed of Modulay, which has a mass composition of 77%, 14%, 8%, and 1%, of gold, silver, copper, and palladium, respectively, and a density of 15.8 g/cm^3. The Silastic insert was created to fill the space between the Modulay backing and eye sphere, and was made of 39.9%, 28.9%, 24.9%, 6.3%, and 0.005%, of silicone, oxygen, carbon, hydrogen, and platinum by weight, respectively, with a density of 1.12 g/cm^3.
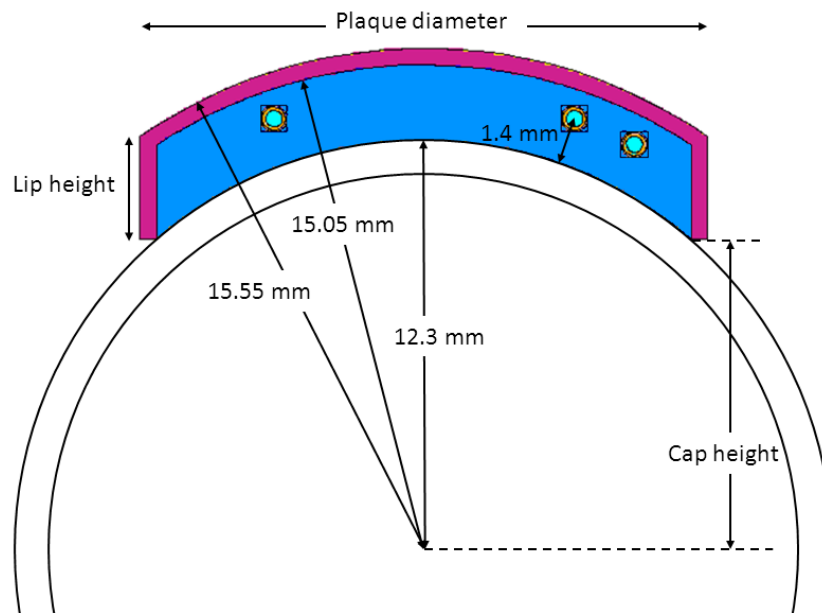
Figure 6.5 Side view of a COMS plaque as modelled in MCNP6, showing the plaque backing in magenta, Silastic insert in blue, inserted I-125 seeds, and relevant dimensions.

The I-125 sources (as described in Section 6.2.2.1) were inserted into the Silastic medium using MCNP6 universe and fill cards, which were copied and translated into the various locations for each COMS plaque size with a cell translation card, based on the seed coordinates from TG-129 and documentation by Kline.[1,26] The plaque eyelets were not modelled, as they are assumed to have a negligible dosimetric effect due to their small size and the low dose within their vicinity.[5] The eye plaques were centered in a sphere of water with a radius of 20 cm.

For all three types of I-125 seeds, simulations were performed for a single seed in the central slot (SS-COMS) of the plaque (for the 12 and 20 mm plaques; 16 mm does not have a central slot) and with all seed positions loaded (fully loaded 12, 16, and 20 mm plaques; FL-COMS). The simulations performed with one centrally located seed used 5×10^9 starting particles, resulting in statistical uncertainties of at most 0.6% in the eye region in front of the plaque or along the plaque CAX up to 30 mm from the Silastic surface. Simulations with fully loaded plaques (8, 13, and 24 seeds for the 12, 16, and 20 mm plaques, respectively) were performed with 1×10^9 starting particles per source (for the 6711 source, the same phase space file and a different seed for the random number generator (RNG) were used for each source, with a slight

169

rotation between each source due to the way in which they were replicated using the cell translation card). For the fully loaded plaques, only one source was made "active" at a time, but all the other sources were modelled such that inter-seed effects were included in the FL-COMS simulations. The resulting statistical uncertainties for all FL-COMS simulations were < 0.3% in the eye region in front of the plaques.

Benchmarking for the COMS plaque simulations was performed in two ways. The first involved running simulations for the heterogeneous and homogeneous material cases (plaque materials defined as Modulay and Silastic, and plaque materials (backing and insert) set to water) to calculate the COMS carrier correction factor, $T(r)$, to compare to published values.[1,5] This was done for all three I-125 seed types with a single seed loaded in the central slot of the 12 and 20 mm plaques. Dose along the CAX of the plaque was scored in 0.5 x 0.5 x 0.5 mm^3 voxels located from 0.5 to 27.5 mm from the outer scleral/Silastic surface. The second benchmarking test was performed for plaques fully loaded with 6711 seeds and involved comparison to data available on the CLRP eye plaque database.[27] The *FMESH tally was used to create a mesh of the same size and dimensions as that used in the CLRP database (array of 0.5 x 0.5 x 0.5 mm^3 voxels extending in a 2.5 x 2.5 x 2.5 cm^3 volume in front of the plaque). Total doses were calculated by summing the dose per starting particle from each simulated source and normalizing by the air-kerma strength per starting particle ($_{SP}S_K$), yielding values in units of Gy h^{-1} U^{-1}. Statistical uncertainties were summed in quadrature. This ignores the correlation between particles when re-using the phase space file which will result in a small underestimation of statistical uncertainty,[22] however the amount of correlation will be small.

6.2.3.2 Implementation in ACE

The three COMS plaques (12, 16, and 20 mm diameter) were incorporated into the OcB applicator library by creating 3D CAD drawings of each plaque and Silastic insert in SolidWorks 2014 (Dassault Systèmes SolidWorks Corporation, Waltham, MA), again using the dimensions and seed/slot coordinates specified in TG-129 and by Kline.[1,26] In order to make the applicator models compatible with the afterloader in OcB, virtual catheter lines were created, offset by 0.4 mm along the surfaces of the seed slots in the Silastic insert in PTC Creo 3.0 CAD software (PTC, Needham, MA). The final assembly of plaque and insert was saved as a CAD STEP file, which was used by Elekta to create an applicator file to add to the Applicator Modelling module

(a library containing the geometry of the available applicators) in OcB. The latter operation involved creating high resolution tessellations of the assembled plaque and incorporating both the tessellated plaque and catheter data into a single applicator model. To preserve the correct seed orientation, three dwell positions are available along each catheter line for each slot in the Silastic insert, though only the first available dwell position (located at the centre of each Silastic insert slot) is to be activated. The materials assigned to the COMS plaque applicators for the plaque backing and seed insert were the same as those used for Modulay and Silastic as described in Section 6.2.3.1.

Initial dosimetric comparisons were performed by positioning the plaques in the centre of a 15 x 15 x 15 cm^3 water box in OcB. Dose distributions were calculated for the 12 and 20 mm SS-COMS plaques and for the 12, 16 and 20 mm FL-COMS plaques. For all plans the dose was normalized at a reference position 6 mm from the Silastic surface along the plaque CAX (this location is representative of a 5 mm standard tumour height, assuming 1 mm scleral thickness). Total dwell times were determined using TG-43 calculations to deliver 5 Gy to the reference point for the SS-COMS plan and 70 Gy for the FL-COMS plans. Calculations using both the selectSeed and 6711 seeds were performed assuming an initial source activity of 3.81 U in all cases. ACE calculations were performed using the same dwell times and source strengths as for the TG-43 calculations.

Doses along the plaque CAX were determined at 0.5 mm increments starting at 0.5 mm from the outer scleral surface, and 3D dose grids consisting of 0.5 x 0.5 x 0.5 mm^3 voxels centered at the middle (central source position) of the plaque were exported. The same 3D dose grids were created in MCNP6 using a *FMESH tally for comparative purposes, as were the CAX dose data used to calculate $T(r)$ as described in the previous section. Doses within a 24.6 mm diameter spherical region in front of the COMS plaques (location of a standard sized eye) extracted from the 3D dose grids were also used to assess the accuracy of ACE within the region of interest (the eye) for ocular brachytherapy treatments.

MCNP6 dose rates per starting particle for each activated source (for FL-COMS plans) were summed together to calculate a total dose rate per starting particle, and total doses for both the SS-COMS and FL-COMS scenarios were determined using Eq. 6.2 for the same total dwell time as in the ACE calculations and the same value for $_{source}S_K$ of 3.81 U.

For the 16 mm FL-COMS plan, additional ACE calculations were performed to investigate if either increasing the number of cones/transport directions or increasing the dose calculation resolution would improve accuracy. First, the ACE calculation was repeated with the number of cones/transport directions increased to 1620/320 for the first- and multiply-scattered doses (default numbers for a single dwell position). Then, the calculation was repeated with the maximum possible resolution given the available computer memory (0.2 mm^3 voxels up to 20 mm from the sources). Dose was exported on the usual 0.5 x 0.5 x 0.5 mm^3 grid for comparison with MCNP6.

6.2.4 Voxelized eye phantom

6.2.4.1 Implementation and validation in MCNP6

Following verification of the accuracy of the dose distributions for individual I-125 sources and all three COMS plaques in both MCNP6 and ACE, a voxelized eye phantom was used to assess the ability of ACE to account for heterogeneous materials and densities within the eye – in particular, for a large number of different materials assigned to very small anatomical structures. For this scenario, the density within each contoured structure was kept constant; the added complexity of variable density structures is examined in the next scenario presented in Section 6.2.5. Both scenarios utilize only the model 6711 seed.

The voxelized eye phantom was provided by Lesperance *et al.*[7] as an EGSnrc based egsphant file.[28] The phantom contains a detailed model of the right eye embedded in the voxelized ICRP Reference Female computational phantom.[29] The ICRP female phantom was chosen over the male phantom due to a higher resolution of voxels (1.75 x 1.75 x 4.84 mm^3 in left-right, anterior-posterior, superior-inferior directions, respectively). The media defined in the ICRP phantom are based on segmentation of high resolution, full body CT scans, modified to correspond with the geometry and composition of the Reference Female given in the ICRP Report 89 document.[30] Elemental compositions for the assigned media are given in the ICRP Report 110 document.[29] The eye phantom embedded within the Reference Female phantom was created at a higher resolution, with 0.5 x 0.5 x 0.5 mm^3 voxels.

The voxelized phantom as presented in the egsphant file format was reformatted for incorporation into MCNP6, which required creating a universe for each different material

present, and creating a lattice that is filled in raster format with the defined universes. To incorporate the portions of the phantom with different voxel sizes, the entire phantom was re-sampled onto the larger grid size of the ICRP female phantom (this results only in a re-sampling of the eye model onto the larger voxel grid). The embedded portion containing higher resolution voxels was then defined on a separate lattice in MCNP6, overlying and replacing the re-sampled part of the larger lattice. In similar fashion, the 16 mm COMS plaque fully loaded with model 6711 seeds was created to be contained within another universe, and overlaid on the voxelized eye and head model, thereby replacing the underlying eye and head materials. The plaque was placed such that the Silastic surface to tumour apex distance was 5.8 mm (5 mm tumour, 0.5 mm scleral thickness, 0.3 mm space between flat/voxelized sclera and Silastic surface, see Figure 6.6).

To validate the implementation of this model in MCNP6, the materials and densities used by Lesperance *et al.* were replicated and the total dose was calculated using the source strength required to deliver 85 Gy at the tumour apex for a completely homogeneous water scenario ($D_{TG-43sim}$ as described in Lesperance *et al.*) in 100 hours,[5,31] based on the value simulated for S_K for the model 6711 source and accounting for source decay. Mean doses within the various structures in the eye (tumour, lens, vitreous, and sclera) as well as doses at points of interest (POI) (tumour apex, centre of the lens, optic disc, and fovea) were compared to the $D_{m,m}$ values given in Table II in Lesperance *et al.* for the I-125 seed. As the optic nerve extended beyond the embedded eye phantom and dose was not determined outside this higher resolution lattice in MCNP6, the maximum nerve dose was compared instead of the mean nerve dose.

The effects of replacing the tissues surrounding the eye (from the ICRP female phantom) with water (with and without a planar air boundary) were generally found to cause negligible differences in the mean doses to the ocular structures as determined by Lesperance *et al.*, with the exception of the far side of the sclera, lens maximum and mean doses, and minimum vitreal dose; these differences were minimized when including the planar air interface. As a small step beyond these two simplified scenarios (all water and water with a flat planar air interface), the entire shape and dimensions of the ICRP Reference Female phantom were preserved, however all materials outside the eye were set to either water or air. In this way the air boundary still wraps conformally around the front of the eye and the half-closed eyelid in the phantom is still present, but is now made of water as shown in Figure 6.6. The simulation in MCNP6 was

repeated and doses were compared to those obtained using the full ICRP Reference Female phantom materials.
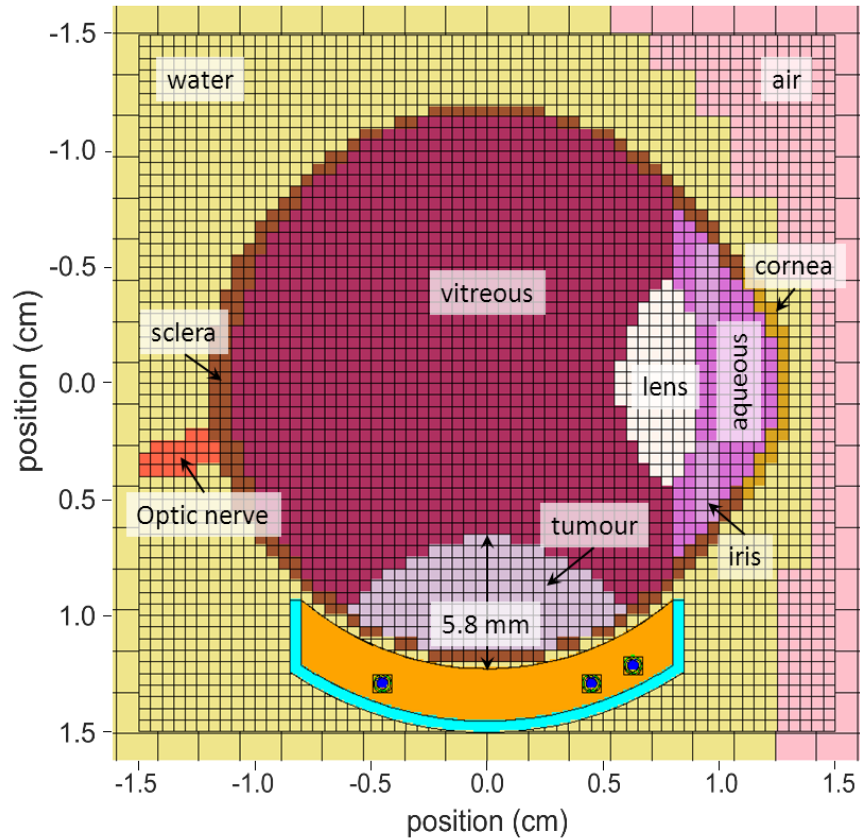
Figure 6.6 Voxelized eye phantom with the 16 mm COMS plaque fully loaded with model 6711 seeds with surrounding water and air materials. All ocular anatomical structures are labeled and the inner plaque surface to tumour apex distance of 5.8 mm is indicated. The boundaries between the higher and lower resolution lattices are visible at the ±1.5 cm positions.

6.2.4.2 Implementation in ACE

To incorporate the voxelized eye phantom into OcB, for simplicity (and based on negligible differences), the eye phantom with surrounding water materials and conformal air boundary was used as described in the preceding paragraph. The entire model was converted to a 3D dataset containing the equivalent densities within each voxel, which was then re-sampled onto a uniform 0.5 x 0.5 x 0.5 mm^3 grid using nearest-neighbour interpolation. No interpolation was required for

the portion containing the embedded eye phantom which was already at this resolution, whereas the surrounding water and air materials were essentially partitioned into smaller voxels. The density within each voxel was then used to convert to a Hounsfield unit (HU) value via the CT calibration curve shown in Figure 6.7, using linear interpolation between nearest points on the curve. The CT calibration curve was for a Toshiba Aquillon-64 scanner (Toshiba Medical Systems, Inc., Tustin, CA), used to acquire the patient CT dataset described in the next section (Section 6.2.5), and was obtained from an axial scan of a Catphan 600 phantom (The Phantom Laboratory, Inc., Salem, NY). The voxelized eye phantom represented as a CT image dataset was then imported into OcB.
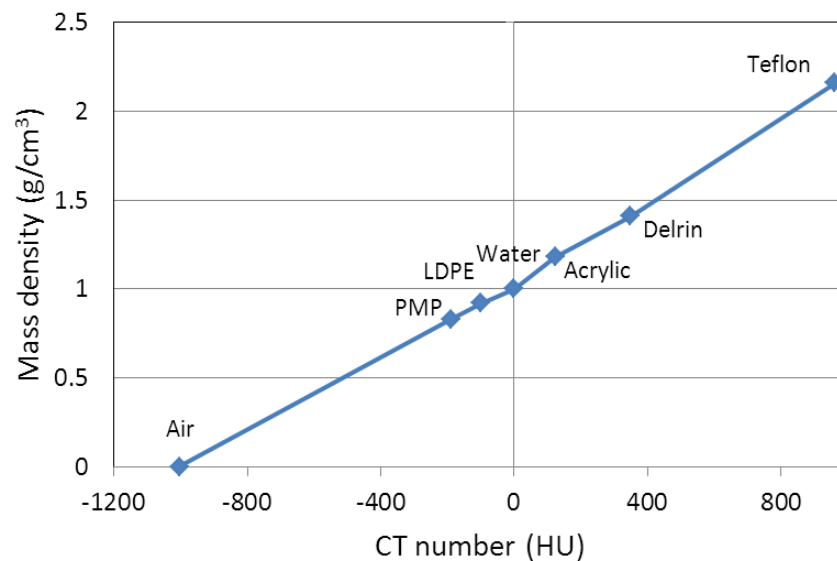
Figure 6.7 CT calibration curve for a Toshiba Aquillon-64 scanner obtained using a Catphan 600 phantom.

All structures in the eye phantom were then contoured in OcB on a slice-by-slice basis, materials were assigned to each structure, and their densities were determined from the HU values in the image (using the supplied CT calibration curve from Figure 6.7). Due to the limited material library in OcB, mass attenuation coefficients from the XCOM online database[32] were compared for all available materials and the materials used by Lesperance *et al*. The material most closely matching over the energy range of interest (5 − 35 keV) was assigned to the

corresponding structure in OcB (see Figure 6.8). Assigned materials and densities are summarized in Table 6.2. The materials assigned in OcB were also used in MCNP6 for comparison. The 16 mm COMS plaque was then placed adjacent to the tumour, maintaining the previously specified distance of 5.8 mm from the Silastic surface to the tumour apex. The total dwell time required to deliver 85 Gy to the tumour apex for a TG-43 calculation with a source strength of 3.81 U assuming a constant dose rate (no source decay, as is the default in OcB) was determined. Doses within the same structures and at the same POIs examined previously, as well as doses along the plaque CAX, were used to compare ACE with MCNP6.
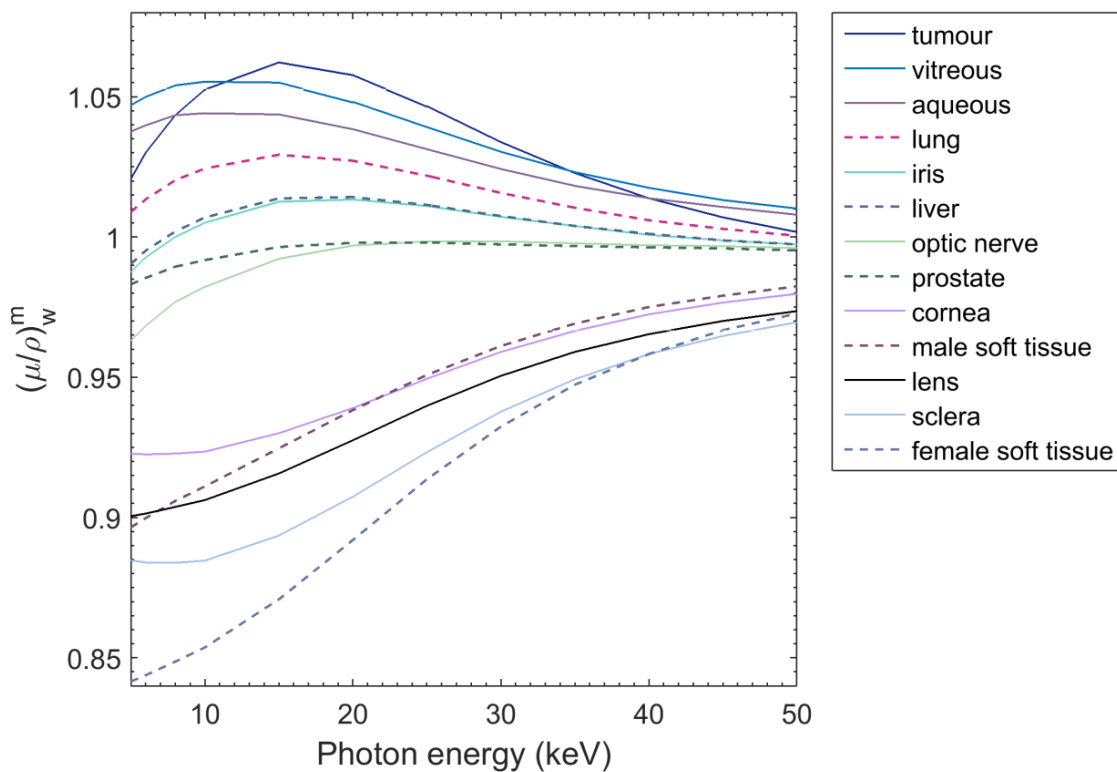
Figure 6.8 Ratios of mass attenuation coefficients for tissues in the eye from Lesperance *et al.*[7] (solid lines) and the closest matching tissue in the OcB material library (dashed lines) to those of water. The lens material compositions were the same in both instances.

Table 6.2 Material assignment in OcB for the voxelized eye phantom

Eye structure	Assigned material	Material density (g/cm^3)
Lens	Lens	1.07
Tumour	Inflated lung	1.04
Sclera	Female soft tissue	1.05
Cornea	Male soft tissue	1.05
Vitreous	Inflated lung	1.007
Aqueous	Inflated lung	1.003
Optic nerve	Prostate	1.04
Iris	Liver	1.05

All MCNP6 simulations with the voxelized eye phantom were performed using 1×10^9 starting particles per source, through use of the model 6711 seed phase space file, with corresponding statistical uncertainties of <0.3% within the structures of the eye. Doses to water were also scored using a *FMESH tally and DE/DF cards providing mass energy absorption coefficient values.

6.2.5 Patient CT dataset

To assess ACE's ability to accurately calculate dose in a scenario with clinically realistic variability in densities as well as materials, a second case scenario was examined using a patient CT dataset, following a similar procedure as for the voxelized eye phantom. The CT dataset was obtained using a high resolution helical scanning protocol on a Toshiba Aquillon-64 scanner yielding 0.5 x 0.5 x 0.5 mm^3 voxels. A medium-sized dome shaped tumour (5 mm in height and 12 mm basal diameter) was added to the CT dataset in the left non-cancerous eye. The tumour was positioned at 9 o'clock (nasal side) and 13.5 mm from the limbus. This centered the tumour on the left-right axis of the CT dataset (as the equator of the eye was not aligned with the left-right axis of the dataset) and helped with ease of plaque placement, as shown in Figure 6.9. The HU value for the tumour was chosen such that the density was the same as that for the tumour in the voxelized eye model (1.04 g/cm^3) based on the CT calibration curve (Figure 6.7).
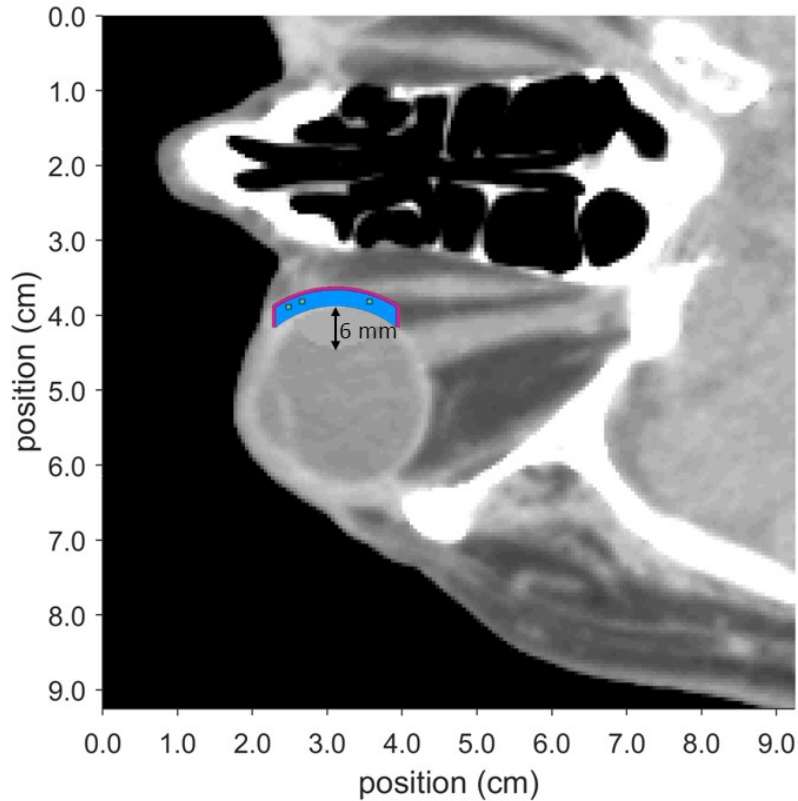
Figure 6.9 Visualization of the patient CT dataset with the 16 mm COMS plaque fully loaded with model 6711 seeds overlaid on the image with an inner plaque surface to tumour apex distance of 6 mm.

Due to poorer image contrast in the CT dataset compared to the voxelized eye model, anatomical structures were contoured in OcB based on relative density thresholds. Voxels with $\rho \leq 0.4$ g/cm^3 were assigned air, 0.4 g/cm$^3 < \rho < 0.95$ g/cm^3 water, 0.95 g/cm$^3 \leq \rho < 1.03$ g/cm^3 female soft tissue, 1.03 g/cm$^3 \leq \rho \leq 1.15$ g/cm^3 male soft tissue, 1.15 g/cm$^3 < \rho < 1.3$ g/cm^3 also water, and $\rho \geq 1.3$ g/cm^3 cortical bone. Material compositions are available in the ICRU Report 46[33] and in Table III of the TG-186 document.[8] This resulted in all materials in the eye being assigned as either female or male soft tissue in OcB, allowing for some variation in material composition dependent on density compared to only using one type of soft tissue with variable density. The density within each individual voxel used for ACE calculation was determined from the CT number within the voxel. Therefore, this scenario presents a larger variation in densities within the eye compared to the voxelized eye phantom, though with fewer materials and material interfaces. The 16 mm COMS plaque was then positioned adjacent to the tumour with the same

178

rotational orientation as in the voxelized eye phantom (seed slot #10 is at the anterior side of the eye), with a distance of 6 mm from the Silastic surface to the tumour apex, as shown in Figure 6.9. The total dwell time was determined based on a dose of 70 Gy to the tumour apex using a source strength of 3.81 U as calculated in Plaque Simulator (details in Section 6.2.6 following), using the equivalent dwell time to account for the lack of source decay in OcB.

The patient CT dataset was then replicated for input into MCNP6 using the same materials and densities, with the 16 mm COMS plaque fully loaded with model 6711 seeds placed at the same location on the eye. Densities within each voxel were determined at 0.1 g/cm^3 intervals and used to assign corresponding materials as applied in ACE, as described above. The total dose was calculated using Eq. 6.2 with the same dwell time and source strength as used for the ACE calculation. Doses along the plaque CAX were compared between ACE and MCNP6, as well as at POIs (tumour apex, centre of the lens, optic disc, and fovea).

As with the voxelized eye phantom, the MCNP6 simulation was performed using 1×10^9 starting particles per source drawn from the model 6711 seed phase space file, resulting in statistical uncertainties of <0.35% within the eye. Doses to water were also scored using a *FMESH tally and DE/DF cards providing mass energy absorption coefficient values.

6.2.6 Comparisons with Plaque Simulator

To compare to the current standard clinical procedure used at the CCI, corresponding treatment plans for the voxelized eye model and patient CT dataset were also created in the Plaque Simulator TPS (v6.2.1). A new model 6711 I-125 source was created in Plaque Simulator with updated TG-43 data determined by the CLRP group using egs_brachy (the same data implemented in OcB). The sources were calibrated to have a source strength of 3.81 U and the treatment start times were the same as the source calibration time. The COMS carrier correction factor $T(r)$ was used for all calculations, and comparisons were made with and without the air interface factor $A(R)$.

The central CT image slice was imported into Plaque Simulator and the generic eye model was adjusted to match the image (in this way the lens, fovea, and optic disc are in the correct position relative to each other and the tumour), as shown in Figure 6.10. For the voxelized eye phantom, the tumour height and basal diameter were set to 4.8 mm and 12 mm, respectively, and for the patient CT dataset they were 5.0 mm and 12 mm, respectively. As Plaque Simulator

assumes 1 mm of scleral thickness, these tumour heights create the same plaque to tumour apex distance as that used in the ACE and MCNP6 calculations for each scenario.
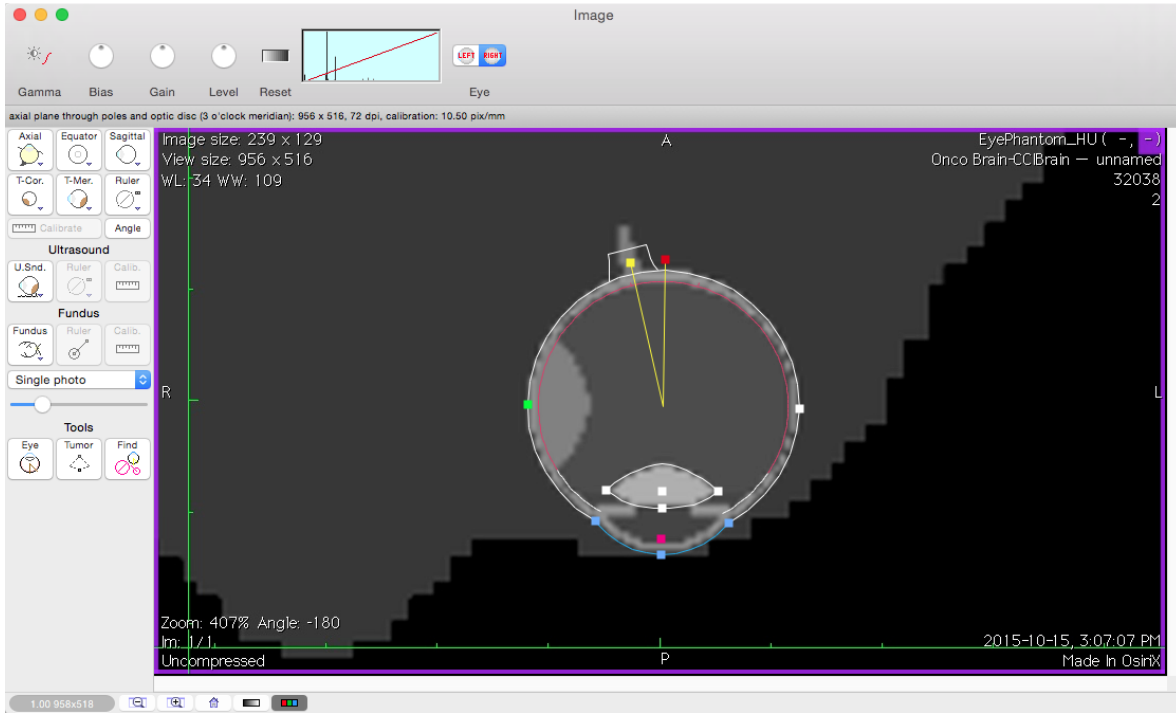
Figure 6.10 CT slice for the voxelized eye phantom imported into Plaque Simulator to adjust the generic eye model to match the eye phantom.

As Plaque Simulator accounts for source decay, equivalent dwell times for the 3.81 U sources were calculated using equations 6.5 – 6.8. The total dose (D_T) is calculated using Eq. 6.5 with a dwell time of T_1 when source decay is accounted for, and with Eq. 6.6 with a dwell time of T_2 when source decay is excluded.

$$D_T = \frac{\dot{D}_o}{\lambda}\left(1 - e^{-\lambda \cdot T_1}\right) \tag{6.5}$$

$$D_T = \dot{D}_o \cdot T_2 \tag{6.6}$$

Setting Eq. 6.5 equal to Eq. 6.6 and solving for both T_1 and T_2 gives:

$$T_1 = \frac{(1 - e^{-\lambda \cdot T_2})}{\lambda} \qquad (6.7)$$

$$T_2 = -\frac{1}{\lambda} \ln(1 - T_1 \cdot \lambda) \qquad (6.8)$$

The total dwell time required for the voxelized eye phantom calculation in ACE was 119.62 hours, while in Plaque Simulator the equivalent time including source decay was 123.24 hours. For the patient CT dataset, the corresponding times were 115.59 and 118.97 hours, respectively.

Doses at the tumour apex, centre of the lens, optic disc, and fovea, and along the inner sclera (basal margin) were compared to those obtained with ACE and MCNP6 for both cases, in order to determine the extent of the effect of the patient tissue materials on doses of clinical interest within the eye.

6.3 Results and discussion

6.3.1 Single seed dosimetry in water

6.3.1.1 MCNP6 benchmarking

The majority of TG-43 parameters were within 2% of values obtained from either the main literature reference (Aryal *et al.*,[16] Karaiskos *et al.*,[17] and Dolan *et al.*[20]) or from Taylor and Rogers[18] (as presented in the CLRP TG-43 parameter database[19]). The comparison of dose rate constants is presented in Table 6.3.

Table 6.3 Dose rate constants, Λ (in cGy h^{-1} U^{-1}), for the three simulated seed models, with comparison to the reference literature and CLRP TG-43 seed database WAFAC values, and percent differences with respect to the primary reference data (Aryal *et al.*[16] for the IAI-125A seed, and the CLRP database for the other two seeds). Data for the 6711 seed generated using both BrachyDose (first value; from the online database), and egs_brachy (second value; obtained through correspondence [R. Thomson]) was available from the CLRP group.

Source model	Data source			Percent difference from primary reference
	MCNP6	Literature	CLRP	
IAI-125A	0.909	0.922	0.925	-1.38%
selectSeed	0.911	0.954	0.917	-0.67%
6711	0.918	0.942	0.924 / 0.931	-0.64% / -1.38%

For the model IAI-125A seed, the average difference in the radial dose function, $g_L(r)$, compared to the values for Simulation condition 11 in Aryal et $al.$[16] is 0.14%, with a maximum difference of 1.08%. The difference in values of the anisotropy factor, $F(r,\theta)$, is on average 0.60%.

For the selectSeed, the Karaiskos et $al.$[17] data showed good agreement with the simulated MCNP6 parameters; however there was a higher level of agreement with the CLRP data. The difference in dose rate constant with respect to the Karaiskos data was 4.6% and the average percent difference in $g_L(r)$ was 0.34%. The anisotropy data could not be directly compared without re-interpolation as the Karaiskos data was determined at half-degree intervals; however it showed larger differences compared to the CLRP data. The average percent differences for $g_L(r)$ and $F(r,\theta)$ values with respect to the CLRP data were 0.02% and 0.2%, respectively.

Similar levels of agreement were found for the 6711 seed with respect to both the main literature reference (Dolan et $al.$[20]) and the CLRP database. The MCNP6 simulated dose rate constant differed by 2.54% relative to the value given by Dolan et $al.$, and average percent differences for $g_L(r)$ and $F(r,\theta)$ were 1.15% and 0.03%, respectively. The average agreement with respect to the CLRP database (using BrachyDose) for $g_L(r)$ and $F(r,\theta)$ was 0.09% and 0.33%, respectively. Relative values of $g_L(r)$ and $F(r,\theta)$ for the 6711 seed are shown in Figures 6.11 and 6.12; similar results were found for the other seed models. Most MCNP6 simulated values agreed to within 1% of CLRP database or Aryal et $al.$ values for the IAI-125A seed.
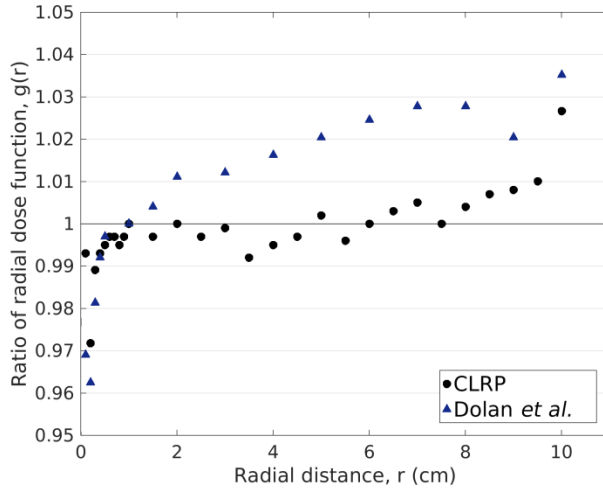
Figure 6.11 Ratio of the value of the radial dose function, $g_L(r)$, simulated using MCNP6 to the value from the CLRP seed database[18,19] and from Dolan *et al.*[20]
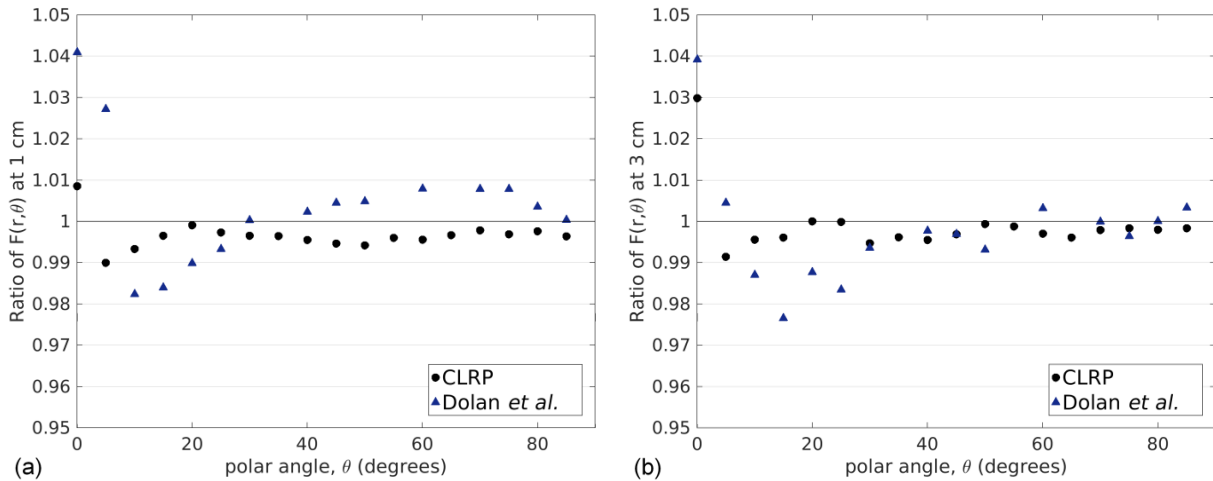
Figure 6.12 Ratio of the value of the anisotropy factor, $F(r,\theta)$, simulated using MCNP6 to the value from the CLRP seed database[18,19] and from Dolan *et al.*[20] at 1 cm (a), and 3 cm (b).

6.3.1.2 Comparison with ACE

For the Nucletron selectSeed, the average difference within a 6 x 6 x 6 cm³ region around the source between MCNP6 and TG-43 calculated doses was $(3.7 \pm 3.0)\%$ (mean $\pm$ standard deviation). However, there were large differences adjacent to the end welds of the seeds (>30%).

Slightly better agreement was found between TG-43 and ACE calculated doses, for which the average difference was (0.78 ± 2.3)%, but the large differences (>20%) were still present adjacent to the end-welds (Figure 6.13(a)). The average difference between ACE and MCNP6 calculated doses was (4.4 ± 2.1)%, again with larger differences near the end welds (>10%), however within a much smaller region more closely matching the projected width beyond the welds (Figure 6.13(b)). Important to note is that OcB sets a maximum dose value of 8x the prescribed dose. Therefore all voxels within ~3 mm of the source are assigned this maximum dose, which is seen in the large dose differences in this region in Figure 6.13, though in actuality the agreement is much better.

For both comparisons, ray-artifacts due to the collapsed-cone approximation are seen. The minimum radial distance and radial increments for $g_L(r)$ and $F(r, \theta)$ in OcB were 5 mm, and the polar angle increments were 5°. As the Karaiskos *et al.*[17] and MCNP6 simulated TG-43 parameters showed larger differences, larger differences in the dose distribution were generally expected for the selectSeed. These differences are less for the ACE data compared to MCNP6. However, as the ACE data is normalized to match the TG-43 data at 1 cm on the transverse axis, a bias can be introduced which potentially caused the 0.7% larger average difference in dose between ACE and MCNP6 compared to TG-43 and MCNP6.
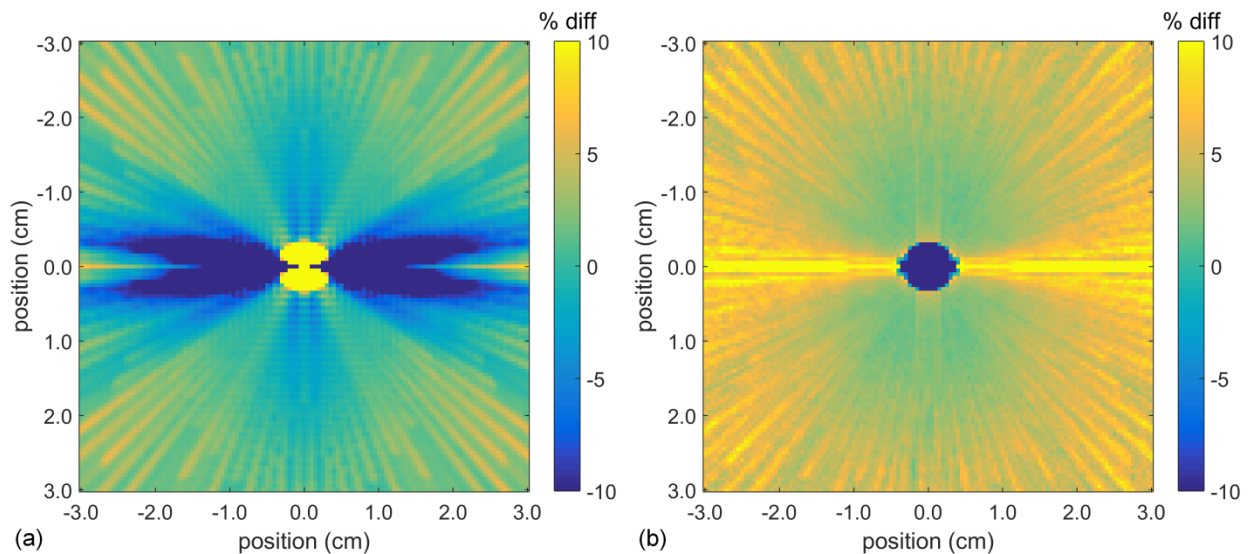
Figure 6.13 Percent dose differences for a single Nucletron selectSeed in water in the longitudinal plane (seed sits length-wise left-right) for ACE compared to TG-43 (a) and MCNP6 (b).

184

These results motivated the use of higher resolution TG-43 and PSS data for the model 6711 seed, as well as more up to date TG-43 data determined using similar means as the PSS data. With such data the accuracy of the ACE algorithm itself, without confounding extraneous differences, could be better examined.

Figure 6.14 Percent dose differences for a single model 6711 seed in water in the longitudinal plane (seed sits length-wise left-right) for ACE vs. TG-43 (a), and histogram of percent dose differences for ACE vs. TG-43 for 6 x 6 x 6 cm^3, 4 x 4 x 4 cm^3, and 2 x 2 x 2 cm^2 regions centered on the seed, showing higher level of agreement closer to the source (b).

For the model 6711 source, a noticeable improvement in the agreement compared to the selectSeed was observed, particularly beyond the end-welds and within close proximity to the source. For the single seed in water, the average difference between ACE and TG-43 within the 6 x 6 x 6 cm^3 region surrounding the seed was slightly larger: (3.7 ± 1.5)%. However, within smaller regions closer to the source, the agreement improved substantially. Within an inner 2 x 2 x 2 cm^3 region, the average difference was (0.6 ± 1.3)% (Figure 6.14). As the PSS data was determined at much higher resolution within the first 2 cm from the source there is less interpolation required during the ACE calculation, particularly when using the smaller 0.5 x 0.5 x 0.5 mm^3 calculation grid, thus resulting in the higher level of agreement. This can be observed in the marked reduction in ray artifacts within the first ~1-2 cm from the source, whereas beyond

this distance the ray artifacts are clearly visible. These differences are summarized in Table 6.4. Beyond the 6 x 6 x 6 cm^3 region examined the differences between ACE and TG-43 decreased, i.e. the 6 x 6 x 6 cm^3 region included the largest relative dose differences. Large differences beyond the end welds were still observed (>10%), however they were confined within polar angles of approximately $\pm$ 5°.

Table 6.4 Percent differences between TG-43, ACE, and MCNP6 for a single 6711 seed in water for three different ROI sizes centered on the seed.

| ROI size | Average percent differences and standard deviations within ROI | | |
	ACE vs TG-43	MCNP6 vs TG-43	ACE vs MCNP6
6 x 6 x 6 cm^3	3.7 $\pm$ 1.5	-0.9 $\pm$ 0.7	4.7 $\pm$ 1.7
4 x 4 x 4 cm^3	2.5 $\pm$ 1.3	-0.9 $\pm$ 0.8	3.4 $\pm$ 1.4
2 x 2 x 2 cm^3	0.6 $\pm$ 1.3	-0.8 $\pm$ 1.8	1.4 $\pm$ 1.3

Local and global percent differences between ACE and TG-43 up to a maximum radial distance from the centre of the seed of 4.3 cm (within a 5 x 5 x 5 cm^3 volume) are shown in Figure 6.15. The larger differences and spread in values in %ΔD_{LOCAL} at radial distances of 3-4 cm due to the ray artifacts and collapsed-cone approximation, and the improved agreement within 2 cm of the source due to the higher resolution PSS data, are seen. The global differences, %ΔD_{GLOBAL}, normalized to 5 Gy (dose at 1 cm on the transverse axis), show approximately the same differences within the first 1 cm from the source (values within the range [-3%, +1.8%]). Beyond 2 cm, the global percent differences are less than 0.75%. Though the local percent differences are larger in magnitude, they will have reduced clinical significance for ocular brachytherapy due to the small doses at these distances. In practice, the maximum distance of interest will be approximately 2.5 cm which roughly corresponds to the opposite side of the eye, and at these distances the dose fall-off is substantial. Dose differences within the eye are examined more thoroughly for the voxelized eye phantom and patient CT dataset.
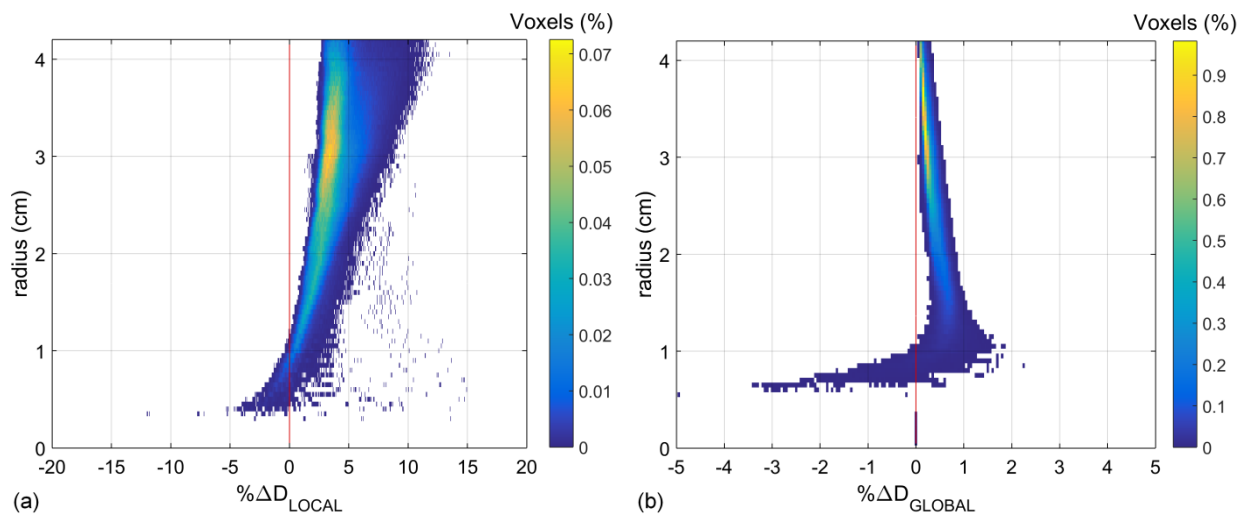
Figure 6.15 2D histogram of distance to the source centre (radius (cm)) vs. local (%ΔD$_{LOCAL}$) (a) and global (%ΔD$_{GLOBAL}$) (b) percent dose differences for ACE compared to TG-43 calculated dose values for a single OncoSeed model 6711 source in water. The reference point for %ΔD$_{GLOBAL}$ is at a distance of 1 cm on the transverse axis of the source.

Dose differences in the central plane of the seed for TG-43 and ACE compared to MCNP6 are shown in Figure 6.16. The agreement between TG-43 and ACE calculated doses compared with MCNP6 doses are summarized in Table 6.4. Agreement between MCNP6 and TG-43 is excellent, with the only main differences occurring near the end welds. Though these differences are smaller than what is observed for ACE, there does appear to be a small bias of approximately <1%. This is also visible in the comparison between ACE and MCNP6 which shows a ~1% larger difference compared to ACE vs. TG-43. Local and global percent differences between ACE and MCNP6 are nearly identical to those between ACE and TG-43, but with a ~1% bias in results. As the ACE doses are normalized to match the TG-43 doses at 1 cm on the transverse axis, this difference is expected to propagate to the ACE data. Overall, the agreement between ACE and both TG-43 and MCNP6 is within the uncertainties seen in the TPS calculations (4.7% for k=1 for TG-43 based planning (Table 2.2), and ~5% for ACE calculations[34–36]). The 5% uncertainty in ACE calculations was determined based on single source TG-186 level 1 commissioning[8] results for the generic high-dose rate Ir-192 source.[35,36] The differences observed for the model 6711 seed are similar, being in the range [-2%, +4%] for the region of interest for ocular brachytherapy (differences for the Ir-192 source were in the range [-2%,

187

+3%]). These differences are found within a 3D volume around the source as compared with the 2D planes used by Ballester *et al.*,[36] and therefore involve a much larger number of voxels. Given the similar level of agreement for the 6711 source as compared with the generic Ir-192 source, the same level of uncertainty for ACE calculations of 5% will be adopted.
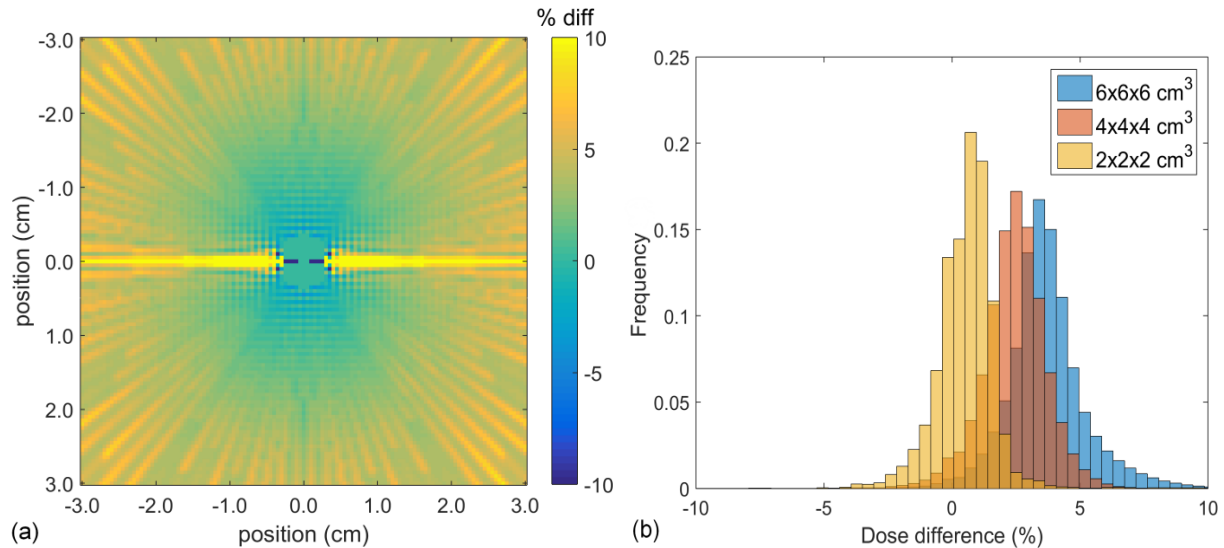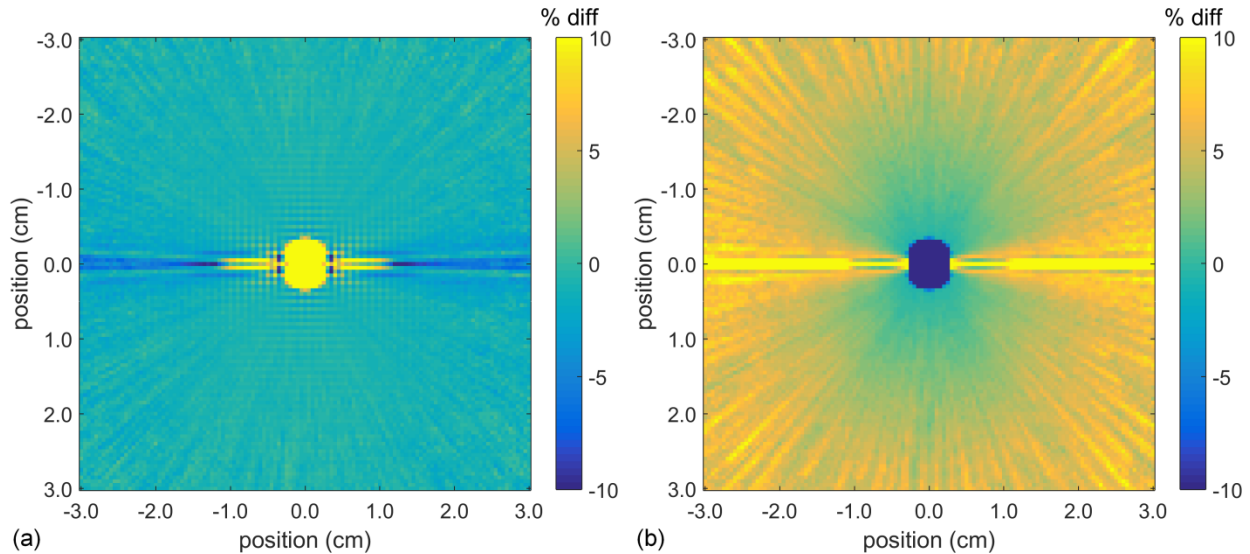

Figure 6.16 Percent dose differences for a single 6711 seed in water in the longitudinal plane (seed sits length-wise left-right) for MCNP6 compared to TG-43 (a), and ACE compared to MCNP6 (b).

6.3.2 COMS plaque dosimetry in water

6.3.2.1 MCNP6 benchmarking

Values of $T(r)$ determined for the 12 mm COMS plaque with one centrally loaded seed for all three I-125 seed models are shown in Figure 6.17. All three seed types agree closely with each other and with tabulated data from TG-129[1] for both the 12 and 20 mm COMS plaques, to within at most 2.0%. This finding is expected as all three seeds have a similar construction (solid Ag core with Ti encapsulation), and is consistent with what was found by Thomson *et al.*,[5,6] where $T(r)$ values for the model 6711 and IAI-125A seeds varied by a similar amount for a single seed in a 20 mm COMS plaque and differences between different plaque sizes were small.
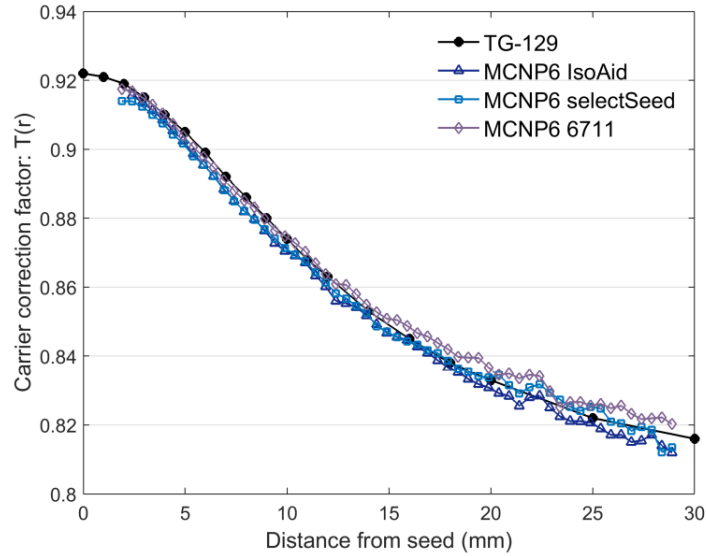
Figure 6.17 COMS plaque carrier correction factor, $T(r)$, determined from the ratio of dose along the plaque CAX for a single seed in the centre slot of the 12 mm COMS plaque to the dose for the same seed in water (plaque backing and insert are made of water) for three I-125 seed types compared to reference data from TG-129.[1] Uncertainties in simulated values of $T(r)$ are at most 0.8% at a distance of 29 mm from the source.
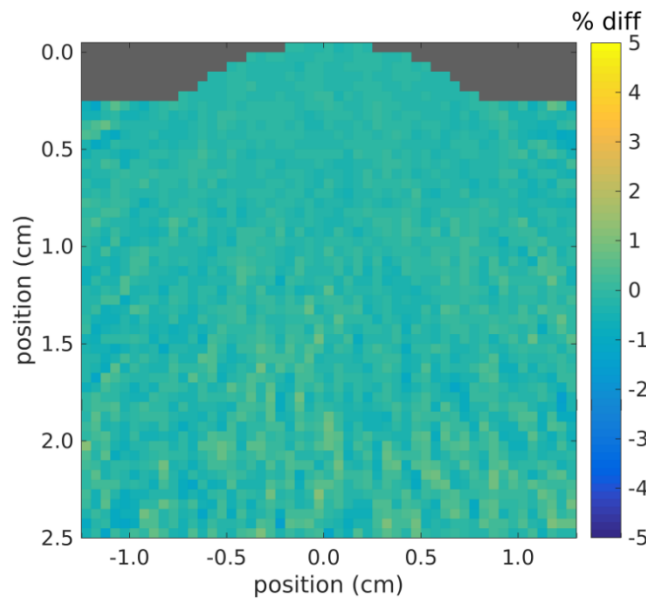
Figure 6.18 Percent difference between MCNP6 and CLRP Eye Plaque Database[27] dose rates in the central plane for a 16 mm COMS plaque fully loaded with model 6711 I-125 seeds in water. Regions with zero scored dose rate in the CLRP database are greyed out.

For the fully loaded plaques, the average difference in dose rate per air-kerma strength (Gy h^{-1}U^{-1}) in a 2.5 x 2.5 x 2.5 cm^3 volume directly in front of the plaque was at most 0.16% with a maximum standard deviation of 1.1% for the 12, 16, and 20 mm COMS plaques (excluding regions behind the plaque and where the dose was <1% of the dose at 6 mm depth), compared to the CLRP Eye Plaque Database data.[27] The percent difference in dose rate for the 16 mm COMS plaque in a plane passing through the centre of the plaque is shown in Figure 6.18.

The high level of agreement along the plaque CAX as well as in the 3D distributions in front of plaques provided sufficient validation of the plaque models and their implementation in MCNP6 for use in more complex scenarios and investigations.

6.3.2.2 Comparison with ACE

An example of the set-up in OcB is illustrated in Figure 6.19, which shows a SS-COMS plan using the 12 mm plaque with TG-43 calculations compared to ACE (denoted TG-186) calculations for the same dwell time. As can be seen, the ACE calculations predict nearly complete shielding by the Modulay plaque backing, as well as a decrease in dose in front of the plaque manifest as a shift in the isodose lines closer to the Silastic surface. The ACE algorithm also shows a slight perturbation in dose at an adjacent slot in the Silastic insert, which would be filled with the background material (in this case water). The calculation in this case was performed using a larger ACE calculation grid size (1 x 1 x 1 mm^3) compared to all other results presented. Consequently, the less than 100% effective shielding of the plaque backing observed could be due to the backing (which is only 0.5 mm thick) being averaged with the adjacent water during the ACE calculation. This observation, along with initial comparisons using the larger calculation grid size (which showed noticeable differences at the edges of the plaque and inner Silastic surface compared to MCNP6 simulated doses) and the inaccurate interpolation observed when examining point doses within the larger dose calculation voxels (due to the extremely sharp dose gradients), pointed to the necessity of using a smaller dose calculation grid size for ocular brachytherapy applications.
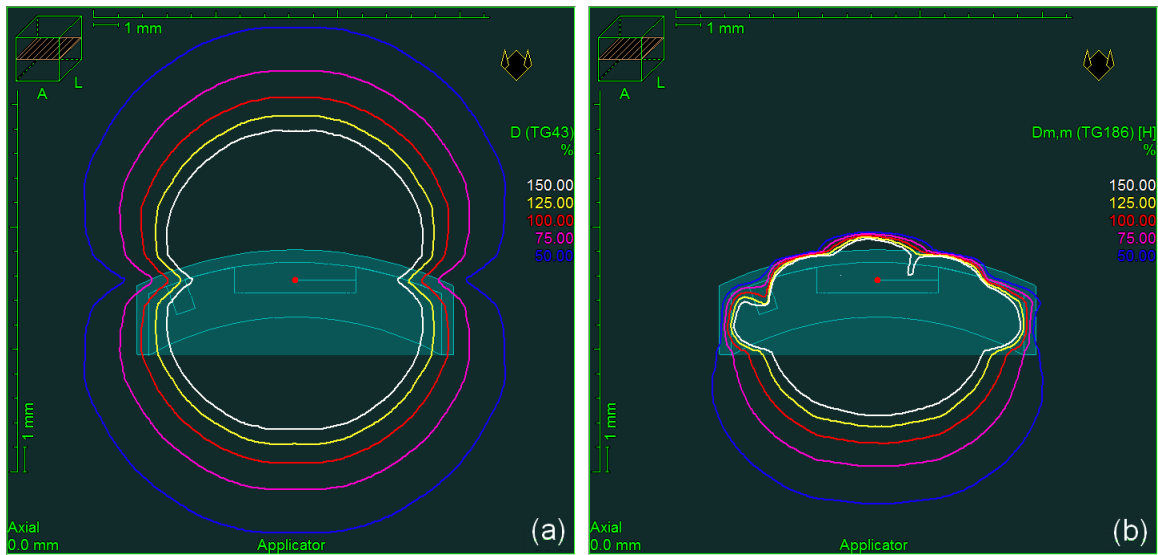
Figure 6.19 Isodose plots in OcB for a single selectSeed in a 12 mm diameter COMS plaque using TG-43 calculation (a), and ACE calculation (b).

Percent differences along the plaque CAX for the SS- and FL-COMS plans for the selectSeed and model 6711 seed are shown in Figure 6.20. Important to note is the difference in the y-axis scale for each seed type and the maximum differences at the outer scleral surface. The latter differences for the selectSeed were up to 5 times larger than for the 6711 seed. This is attributed to the lower resolution of the PSS data for the selectSeed compared to the 6711 seed, as well as to the use of older TG-43 data which showed poorer agreement with MCNP6. As previously mentioned the PSS/ACE data is normalized to the TG-43 dose at 1 cm on the transverse axis; therefore differences between MCNP6 and TG-43 doses will manifest as a bias between the ACE and MCNP6 data, which was observed for both seed types. Differences beyond ~10 mm are similar for both sources, increasing slightly when moving further away from the sources/plaque (beyond ~20 mm) as the collapsed-cone approximation becomes less accurate. This trend was also observed for the single seed data in water along the source transverse axis. However, differences are consistently lower for the 6711 seed for the entire distance range examined along the plaque CAX. For both seed models, ACE calculated doses for the 16 mm COMS plaque showed better agreement with MCNP6 doses compared to the other plaque sizes, even at shallow depths. A likely cause of this is the lack of a central source position in this plaque, such that any position on the CAX is at a greater average distance to the sources

compared to the other plaques which have a central source. For this plaque, the differences between ACE and MCNP6 doses are within ±1.5% from 0.5 to 27.5 mm from the outer scleral surface, with an average difference of 0.3%.
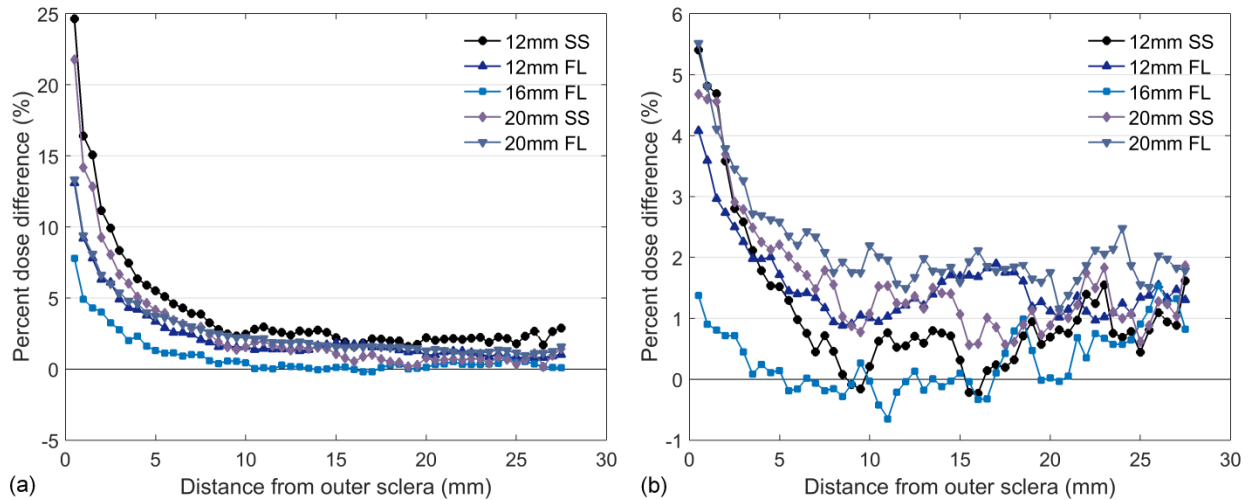
Figure 6.20 Percent dose difference along the plaque CAX between ACE and MCNP6 for single seed (SS) and fully loaded (FL) COMS plaques for the Nucletron selectSeed (a), and Oncura 6711 seed (b).

The percent differences for all plaque plans (SS- and FL-COMS) and for all three plaque sizes within the spherical eye region in front of the plaque showed overall good agreement. Values for both seed models are summarized in Table 6.5. Similarly to the dose along the CAX, the agreement for the model 6711 seed is slightly better than for the selectSeed. The percent dose difference between ACE and MCNP6 in the central plane of the 16 mm COMS plaque fully loaded with 6711 seeds is shown in Figure 6.21(a), with a histogram of the dose difference distribution within the spherical region indicated in Figure 6.21(b). For the most part, within the standard spherical eye region the agreement between ACE and MCNP6 is within the uncertainty of ACE dose calculation (5%), however larger differences are observed in the penumbral shadow of the plaque, where dose differences vary from [-12%, +8%]. These latter differences are likely due to the intra-voxel presence of the plaque within the background water material, which for primary dose is handled quite carefully but involves larger approximations for scattered dose.[24] Other contributing factors are the simplifications made in radiation source modelling and angular

discretization of photon transport in ACE. The PSS data used by ACE is determined for a line source, however radiation sources are implemented as point sources, with corrections to account for this.[24] The combined effect is seen as single high and low percentage difference streaks near the plaque lip for the SS-COMS plans, and multiple streaks (due to multiple seeds) for the FL-COMS plans. Large percent differences are observed behind the plaque, however the doses are extremely low and these differences are not of clinical concern.

Table 6.5 Average percent dose differences between ACE and MCNP6 within a 3D spherical eye region in front of the plaque for the 12, 16, and 20 mm COMS plaques loaded with the selectSeed and model 6711 seed.

Plaque plan	Percent difference and standard deviation (%)	
	selectSeed	6711
12 mm SS	1.5 ± 6.7	1.2 ± 6.5
12 mm FL	2.1 ± 6.8	1.6 ± 6.4
16 mm FL	0.8 ± 5.0	0.5 ± 5.4
20 mm SS	2.7 ± 16.3	2.5 ± 12.8
20 mm FL	1.1 ± 13.5	2.5 ± 9.4
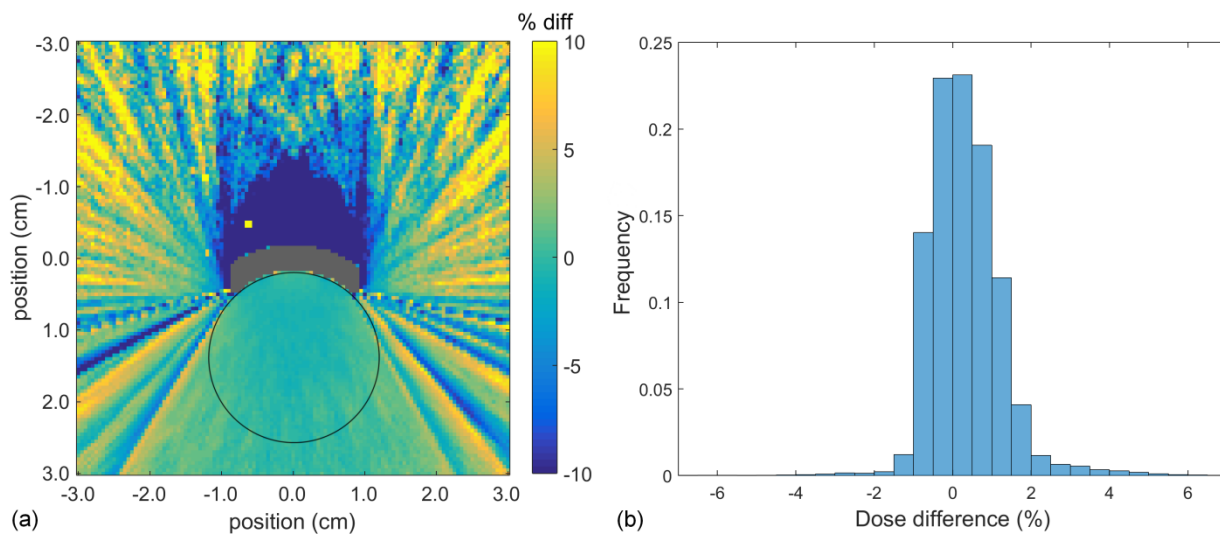
Figure 6.21 Percent dose differences between ACE and MCNP6 in the central plane for a 16 mm COMS plaque (the pixels containing the plaque are greyed out) fully loaded with 6711 seeds; circular region shows the location of a standard spherical eye (a), and histogram of percent dose differences within the spherical eye region (b).

Increasing the number of cones/transport directions as well as decreasing the calculation voxel size resulted in negligible changes in the ACE doses, with the exception of an improvement in dose agreement immediately surrounding the entire plaque (behind the Modulay plaque backing and in front of the Silastic insert). At these locations there would be less voxel averaging between plaque and water material, but this improvement was only seen within ~0.5-1.0 mm from the plaque. Ray artifacts were more evident with the smaller dose calculation grid. The default number of cones with multiple dwell positions (720/240) is therefore sufficient, and negligible gains are achieved by increasing the dose calculation resolution. Also, both of these changes result in a ~2-3 times increase in dose calculation time.

From the examination of plaque dosimetry in water, expected differences when moving forward to more complex scenarios will be at the penumbral edges of the plaque. Depending on the position of the plaque relative to the optic nerve, optic disc, and fovea, these sensitive structures could be located in the plaque penumbra, and therefore the accuracy of ACE in these regions would be of concern and will warrant careful examination. Doses within a tumour (the region adjacent to the plaque), and along the plaque CAX are expected to agree well.

6.3.3   Voxelized eye phantom

6.3.3.1 MCNP6 benchmarking

Doses within the various structures in the eye determined using MCNP6 and corresponding doses given by Lesperance *et al.*[7] are summarized in Table 6.6. Average doses as well as doses at POIs agreed quite closely, the maximum percentage difference being 4.8% for the optic disc. The largest absolute dose difference of 1.5 Gy was at the tumour apex. The source strength determined by Lesperance *et al.* to deliver 85 Gy to the tumour apex for the $D_{TG-43sim}$ scenario was not reported, therefore the differences in dose could be due to minor variations in values used in the final dose calculations: MC simulated source air kerma strength; I-125 source photon spectrum (Lesperance *et al.* used the TG-43U1 spectrum[12]); and energy deposition calculated by different MC codes which use different physics databases and scoring methods. Given these possible variations, the dose differences between MCNP6 and Lesperance *et al.* are quite small, particularly for low-energy photon sources for which such variations can have a notable impact on results.

Table 6.6 Average doses to volumes and doses to POIs (in Gy) for ocular structures in the voxelized eye model with materials and densities from Lesperance *et al.* Structures with 'avg' indicated are average doses within the entire structure, whereas the rest are averages within 1-4 voxels that make up the POI.

Ocular structure	MCNP6 dose	Lesperance *et al.*[7] dose	Percent difference (%)
Tumour (avg)	148.1	147.6	0.3
Tumour apex	82.1	80.6	1.8
Lens (avg)	15.0	14.7	1.7
Centre of lens	14.1	13.7	3.2
Vitreous (avg)	23.4	23.2	1.0
Max nerve dose	15.9	16.5	-3.9
Optic disc	14.8	14.1	4.8
Sclera (avg)	23.5	24.3	-3.2
Fovea	9.8	9.7	1.2

Replacing the ICRP materials in the Reference Female computational phantom with either water or air resulted in at most a 0.5% change in the average dose to any of the ocular structures. This largest change was for the average nerve dose. In the full computational phantom, the nerve is almost entirely surrounded by adipose tissue, such that changing all extra-ocular materials to water has a relatively larger impact on the scattering conditions in the small nerve structure. Maintaining the shape of the water-air interface reduced the differences in dose observed when changing the ICRP materials to water as compared with the planar air interface examined by Lesperance *et al*. For the latter scenario a 5% difference in minimum vitreal dose was observed between the full and material replaced phantoms, whereas using the conformal air interface the difference is reduced to 0.3%.

6.3.3.2 *Comparison with ACE*

For the version of the voxelized eye phantom incorporated into OcB, differences in dose between ACE and MCNP6 within the same ocular structures and at the POIs are given in Table 6.7. Average doses within most of the structures agreed quite well, ranging between 2.5–14.3%, the largest difference being for the average scleral dose. Though structures were contoured on every slice of the phantom their 3D reconstructions in OcB were imperfect due to the small and irregular contour shapes, making differences for the sclera and at various tissue interfaces larger

than within other parts of the eye, as seen in Figure 6.22. The differences at the POIs (tumour apex, centre of the lens, optic disc (defined in the sclera), and fovea (also defined in sclera)) were quite small (at most 3.9%) with the exception of the fovea, which showed a 20.9% difference. The fovea is located at a tissue interface in one of the regions showing larger differences; adjacent voxels in the vitreal fluid agreed within 7.6%. Both the fovea and optic disc are also located near the penumbral edges of the radiation field where larger percent difference streaks are seen. Therefore, depending on the position of these structures relative to both the plaque edge and tissue interfaces, large differences could be observed. Differences along the plaque CAX ranged from 0.7–7.8%, following a trend similar to that observed for the plaque in water, and are shown in Figure 6.23.

Table 6.7 Average doses to volumes and doses to POIs (in Gy) for ocular structures in the voxelized eye model calculated by ACE and MCNP6. Structures with 'avg' indicated are average doses within the entire structure, whereas the rest are averages within 1-4 voxels that make up the POI.

Ocular structure	ACE dose	MCNP6 dose	Percent difference (%)
Tumour (avg)	147.0	143.2	2.5
Tumour apex	81.1	79.7	1.7
Lens (avg)	16.1	15.3	5.2
Centre of lens	15.7	15.4	1.9
Vitreous (avg)	24.3	23.5	3.3
Optic disc	15.6	15.0	3.9
Sclera (avg)	27.0	23.6	14.3
Fovea	12.0	9.9	20.9
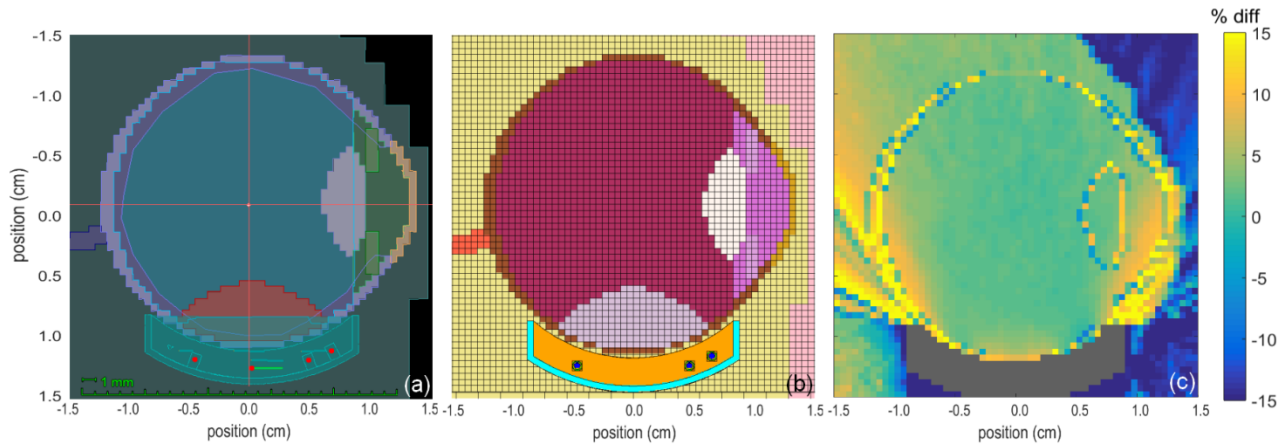
Figure 6.22 Central slice of the voxelized eye phantom as incorporated into OcB with anatomical structure contours (a), MCNP6 model input with matching material assignments (b), and percent difference map between ACE and MCNP6 doses for the slice (pixels containing the plaque are greyed out).
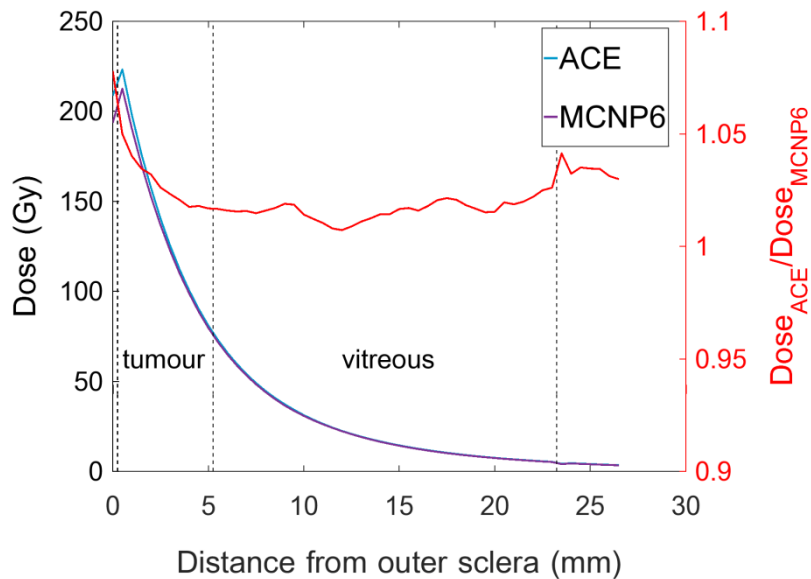
Figure 6.23 Plaque CAX doses and their ratio along the CAX for ACE and MCNP6 for the voxelized eye phantom.

The effects of the non-water tissues in the eye on dosimetry are quite large, as seen in the comparison with Plaque Simulator calculated doses. The doses to POIs calculated using Plaque Simulator and MCNP6 are given in Table 6.8. Isodose contours comparing Plaque Simulator,

197

ACE, and MCNP6 calculated doses are shown in Figure 6.24. Lesperance *et al.* determined a 7.9% increase in dose to the tumour apex for the heterogeneous scenario compared to the plaque in water scenario ($D_{m,m}$ vs. $D_{w,w}$), whereas in this study a difference of 0.4% was observed. The inflated lung material assigned to tumour in the ACE and MCNP6 calculations is slightly more water equivalent than the tumour material used by Lesperance *et al.*, such that the tumour apex dose is only slightly affected. However, the lens, optic disc, and fovea doses are more affected, due to differences in attenuation of the radiation passing through the tissue materials compared to water, as well as scoring dose to medium as opposed to water. The differences can be seen in Figure 6.24 at the various tissue interfaces, and noticeably in the lens. In this case, the doses at the inner scleral edge are quite similar for both Plaque Simulator and MCNP6, though the 100% isodose line is up to 0.26 mm closer to the basal edge of the tumour for MCNP6 than the 100% line calculated using Plaque Simulator. Depending on the choice of tissue material, to obtain a desired margin around the basal edge of the tumour the margin planned using Plaque Simulator may need to be increased slightly.

Table 6.8 Comparison of Plaque Simulator and MCNP6 calculated doses to POIs (in Gy) for ocular structures in the voxelized eye model. The MCNP6 tumour apex dose is taken as the average dose in the 8 voxels at the top of the tumour and the adjacent ones in vitreous, to more closely match the dose to a point calculated by Plaque Simulator.

Ocular structure	Plaque Simulator	MCNP6	Percent difference (%)
Tumour apex (at point)	75.5	75.8	-0.4
Lens	18.0	15.4	16.8
Optic disc (in same plane as fovea and tumour apex)	18.4	13.4	37.0
Fovea	13.3	9.9	34.0
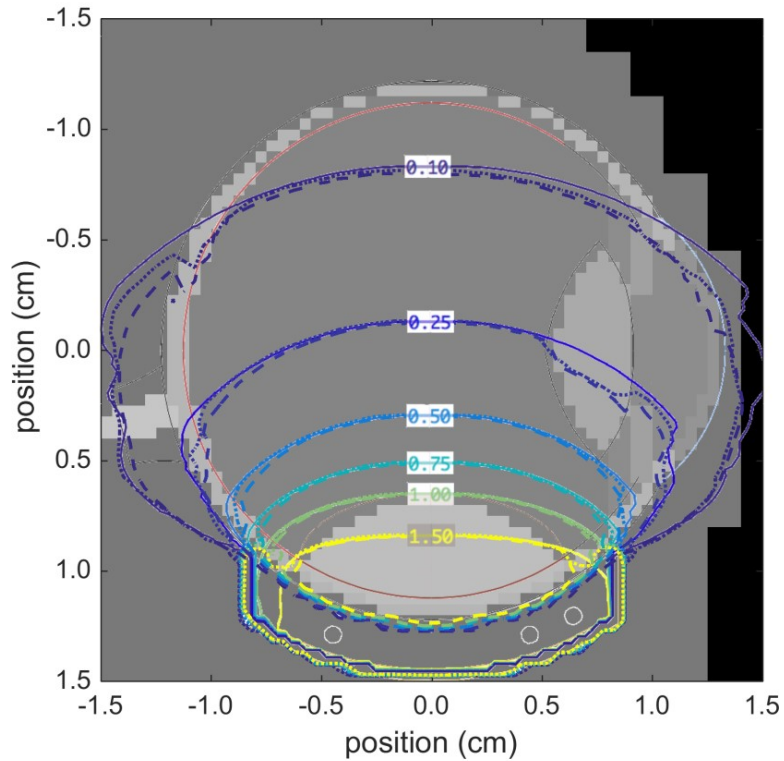
Figure 6.24 Isodose contours for the voxelized eye phantom from Plaque Simulator (solid lines), ACE (dotted lines), and MCNP6 (dashed lines) for the central slice through the eye. All compared plans have the same total reference air kerma. Isodose line values are normalized to the Plaque Simulator tumour apex dose of 75.5 Gy.

The doses scored to water for radiation transported through medium, $D_{w,m}$, at each POI are given in Table 6.9. The value of $D_{m,m}$ at the tumour apex (Table 6.8) is closer to the Plaque Simulator dose than the value of $D_{w,m}$, whereas the opposite is true for the other POIs. The choice of tissue materials and their densities, as well as interaction cross-sections, mass attenuation coefficients, and mass energy-absorption coefficients, can play competing roles in either increasing or decreasing dose when calculating $D_{w,m}$ or $D_{m,m}$.

Table 6.9 Comparison of Plaque Simulator and MCNP6 calculated doses to POIs (in Gy) for ocular structures in the voxelized eye model. Doses are calculated in water for radiation transported through medium ($D_{w,m}$).

Ocular structure	Plaque Simulator	MCNP6	Percent difference (%)
Tumour apex (at point)	75.5	72.9	3.6
Lens	18.0	17.1	5.4
Optic disc (in same plane as fovea and tumour apex)	18.4	15.6	17.5
Fovea	13.3	11.6	15.1

Turning the air interface factor on in Plaque Simulator only had an effect on the lens dose, which decreased to 17.7 Gy, 14.9% different from the MCNP6 dose to medium ($D_{m,m}$ in Table 6.8). Though still a large difference, applying the air interface factor improved the accuracy of the lens dose calculation in Plaque Simulator. Turning on the air interface factor also moved the 10% isodose line closer to the cornea and to the MCNP6 isodose line, thereby improving the accuracy of the dose calculation in this region as well.

6.3.4 Patient CT dataset

For the patient CT dataset, ACE accounted for the non-uniform densities within the various structures in the eye quite well. The dose differences observed at interfaces for the voxelized eye model were also visible here, but with fewer tissue interfaces, to a much lesser extent. The contoured structures within the patient CT model were smoother than those in the voxelized eye model, such that the 3D reconstructions in OcB matched the contours better, and consequently led to the ACE calculation being more accurate at the tissue interfaces. ACE and MCNP6 dose differences at the POIs exhibited a similar level of agreement to that found for the voxelized eye phantom with the exception of the fovea, which showed much better agreement; these values are summarized in Table 6.10. For the fovea and optic disc, the accuracy of ACE dosimetry greatly depends on the position of the plaque; though both POIs agreed well with MCNP6, nearby voxels in the optic nerve showed differences of up to 30%. Dose differences within the central plane of the CT dataset are shown in Figure 6.25. Differences in the plaque penumbra were similar to those observed for the plaques in water and in the voxelized eye phantom, as were average differences within the central part of the eye. Large differences were also seen within

and beyond the contoured bone on the lateral side of the head. The ACE algorithm does not account for changes in the spectrum of scattered photons in different media (the initial energy spectrum [Figure 6.4] is used for all dose calculations), and similar differences around bony structures have also been observed for high energy HDR dose calculations using Ir-192.[35,37–39] Differences along the plaque CAX ranged from -2.8–1.2% (Figure 6.26). The large difference observed at the plaque/sclera/tumour interface for the voxelized phantom was not observed for the CT dataset, likely due to the same material being assigned for the sclera and tumour (i.e. there was no material interface adjacent to the Silastic insert).

Table 6.10 Comparison of ACE and MCNP6 calculated doses to POIs (in Gy) for ocular structures in the patient CT dataset. Doses are averages within 1-4 voxels that make up the POI.

Ocular structure	ACE	MCNP6	Percent difference (%)
Tumour apex	67.5	68.5	-1.4
Centre of lens	12.7	13.6	-6.2
Optic disc	25.2	23.9	5.4
Fovea	15.6	15.2	3.6
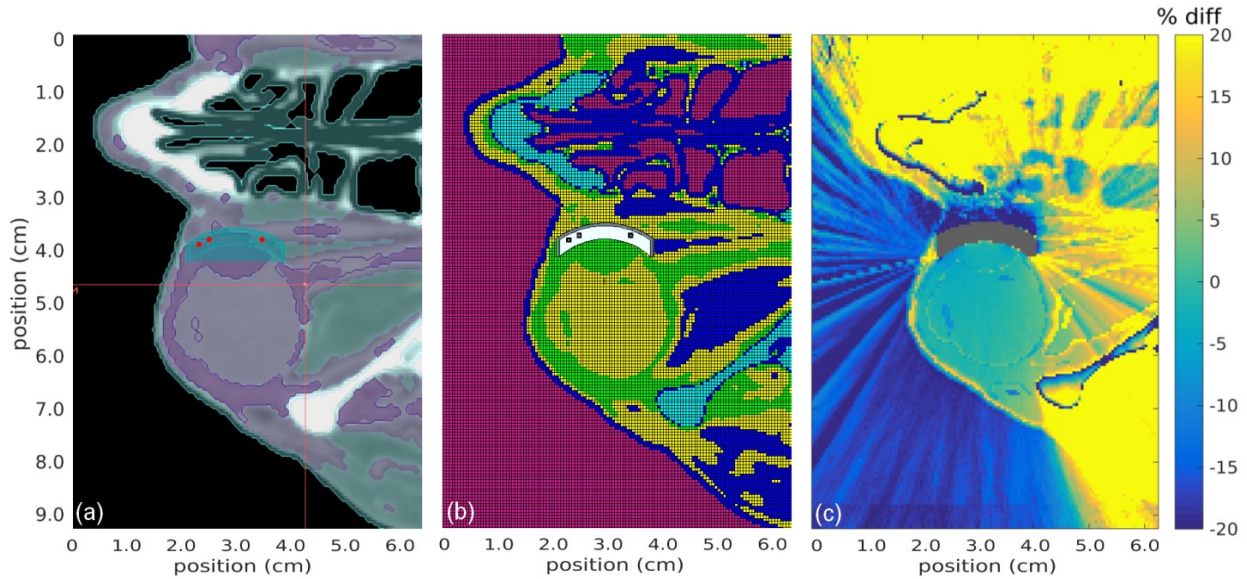
Figure 6.25 Central slice of the patient CT dataset imported into OcB with structure contours based on density values (black is air, blue is water, light purple is female soft tissue, dark purple is male soft tissue, white is cortical bone) (a), MCNP6 with matching material assignments (magenta is air, dark blue is water, yellow is female soft tissue, green is male soft tissue, and light blue is cortical bone) (b), and percent dose difference map between ACE and MCNP6 doses for the slice (pixels containing the plaque are greyed out) (c).
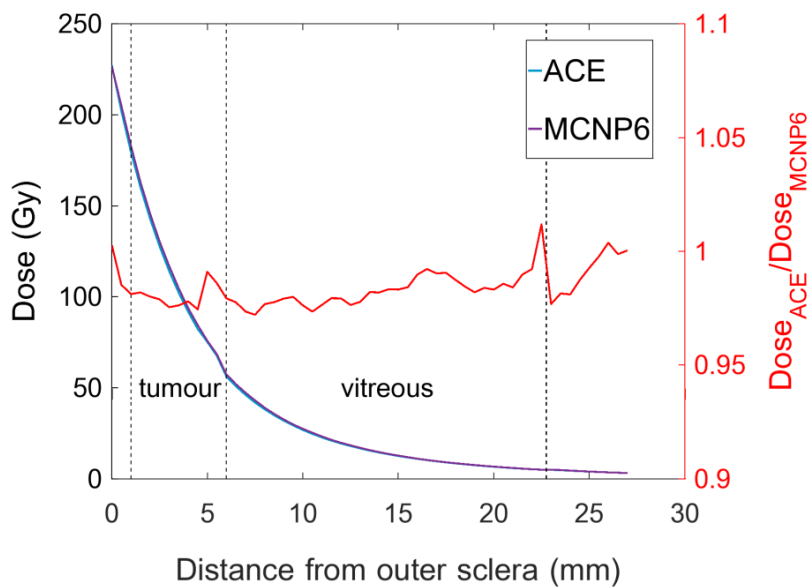
Figure 6.26 Plaque CAX doses and their ratio along the CAX for ACE and MCNP6 for the patient CT dataset.

202

Similarly to the voxelized eye phantom, the effects of the non-water tissues in the eye on dosimetry are quite large when compared to Plaque Simulator calculated doses. The doses to the POIs determined using Plaque Simulator are given in Table 6.11, and isodose contours comparing Plaque Simulator, ACE, and MCNP6 calculated doses are shown in Figure 6.27. The mass attenuation and mass-energy absorption coefficients for both the female and male soft tissue are lower than those for water, therefore compared to using the inflated lung material for the voxelized eye phantom, the dose at the tumour apex is decreased more with respect to the water-based (Plaque Simulator) value. The lens, optic disc, and fovea are all composed of male soft tissue, and the radiation traverses similar amounts of male soft tissue but differing amounts of female soft tissue to reach each of these structures. Though the male soft tissue has a higher density, it is slightly more water equivalent than the female soft tissue. Therefore, there are again competing processes occurring to change the dose to medium compared to the dose to water. The largest difference was found for the optic disc, which is located at the shortest distance to the plaque surface (12.0 mm), whereas the lens had the smallest difference and is the furthest distance away from the plaque surface (15.6 mm) (for comparison, the distance to the fovea was 14.9 mm). The longer distance traversed by photons through female soft tissue to reach the POI apparently reduced the effects of the tissue heterogeneities on dose, however this trend was not observed for the voxelized eye phantom with lung material assigned to the vitreous fluid. The reductions in dose at the inner scleral edges are larger for this scenario than for the voxelized eye phantom. The 100% isodose line is at most 0.36 mm closer to the basal edge of the tumour for the MCNP6 calculation than the 100% line calculated by Plaque Simulator. Again, depending on the choice of tissue materials, the basal margin planned using Plaque Simulator may need to be adjusted.

Table 6.11 Comparison of Plaque Simulator and MCNP6 calculated doses to POIs (in Gy) for ocular structures in the patient CT dataset. The MCNP6 tumour apex dose is the average dose in the voxel at the top of the tumour and the adjacent one in vitreous (2 voxels) to more closely match the dose to a point calculated by Plaque Simulator.

Ocular structure	Plaque Simulator	MCNP6	Percent difference (%)
Tumour apex (at point)	70.0	62.9	11.3
Centre of lens	14.4	13.6	5.8
Optic disc	28.2	23.9	17.8
Fovea	16.7	15.2	9.5
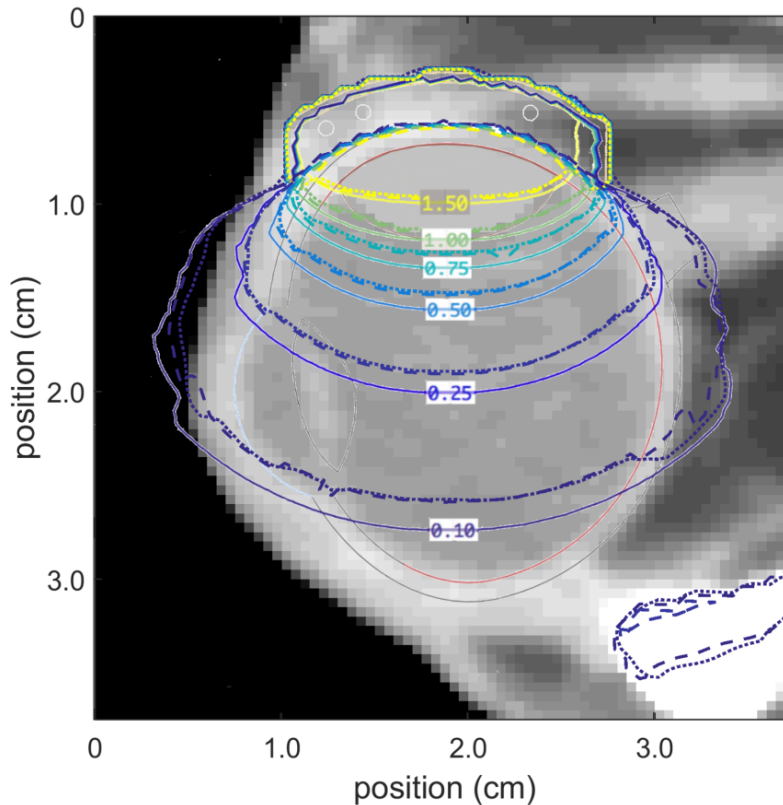
Figure 6.27 Isodose contours for the CT dataset from Plaque Simulator (solid lines), ACE (dotted lines), and MCNP6 (dashed lines) for the central slice through the eye. All compared plans have the same total reference air kerma. Isodose line values are normalized to the Plaque Simulator tumour apex dose of 70.0 Gy.

The doses scored to water for radiation transported through medium, $D_{w,m}$, at each POI are given in Table 6.12. For this scenario, all values of $D_{w,m}$ were closer to those calculated using Plaque Simulator than corresponding $D_{m,m}$ values (Table 6.11), and all values of $D_{w,m}$ were larger than corresponding values of $D_{m,m}$ (due to the ratio of mass energy-absorption coefficients being less than 1). The values of $D_{m,m}$ and $D_{w,m}$ for the patient CT dataset are in general closer to the Plaque Simulator doses than the corresponding values for the voxelized eye phantom, though using two different soft tissue materials throughout the eye is less realistic than the larger number of materials used for the voxelized eye phantom. The choice of materials strongly influences the doses calculated throughout the eye, indicating the need for adequate knowledge of the materials in the eye to perform realistic and accurate dosimetry.

Table 6.12 Comparison of Plaque Simulator and MCNP6 calculated doses to POIs (in Gy) for ocular structures in the patient CT dataset. Doses are calculated in water for radiation transported through medium ($D_{w,m}$).

Ocular structure	Plaque Simulator	MCNP6	Percent difference (%)
Tumour apex (at point)	70.0	70.7	1.0
Centre of lens	14.4	14.8	-2.7
Optic disc	28.2	26.0	8.3
Fovea	16.7	16.6	0.7

Turning on the air interface factor in Plaque Simulator again only affected the lens dose, which decreased to 14.0 Gy, reducing the difference between the Plaque Simulator and MCNP6 lens doses ($D_{m,m}$ from Table 6.11) to 2.9%. Again, using the air interface factor improved the accuracy of the lens dose calculation in Plaque Simulator. However, applying this factor makes the difference between the Plaque Simulator and MCNP6 $D_{w,m}$ values for the lens dose larger, in contrast to the voxelized eye phantom which yielded a larger difference for $D_{m,m}$ compared to Plaque Simulator. The voxelized eye phantom used lens tissue for the lens, so a comparison of lens doses is more realistic for this scenario, however the changes in dose that occur from traversing non-water vitreal fluid (whether it be constituted of inflated lung or female soft tissue) affect these values as well.

6.4 Summary discussion and conclusions

6.4.1 Single source and plaque dosimetry in water

For the single source dosimetry, a clear improvement in the accuracy of the ACE calculation was obtained by using higher resolution PSS data and more current/accurate TG-43 data that better matches the PSS data. This difference was evident between the selectSeed and the model 6711 seed. A further improvement could potentially be realized if the PSS data were determined at higher resolution 0.1 mm/1° intervals for the entire region up to 2 cm from the source (or up to 2.5 cm for ocular brachytherapy applications), although given the small values of global percent differences at 2 cm and beyond, any clinical advantage would be minimal considering how quickly the dose falls off with increasing distance from the source.

For the plaques in water, ACE accounted for the heterogeneous plaque materials very well, with the advantage that no correction factors such as those implemented in Plaque Simulator are needed. Currently in Plaque Simulator, the same COMS plaque carrier correction factor is used for all I-125 source models, whereas it has been shown that different models will have slightly different dose reductions in front of the plaque.[6] By providing source specific PSS data in OcB for the ACE calculation, differences caused by the length of the inner active rod, distribution of activity, construction of the source etc., are inherently accounted for. Although these differences are generally quite small, particularly when compared to other systematic uncertainties present in the dose calculations and dose delivery, they do represent an advantage when using ACE.

The doses along the plaque CAX and within the central part of the eye agreed well within the uncertainties in the ACE calculations (<5%). However, a distinct limitation of ACE was found at the plaque penumbra, where there were differences of up to 12%. Depending on the plaque position, critical structures could be located in this region, and therefore the accuracy of the dose calculated within these structures could be questionable. That being said, depending on the distance of a critical structure to the plaque, these doses could be quite low. Therefore, a ~10% uncertainty in dose might not be clinically significant, particularly if the maximum dose is well below the threshold tolerance dose for the critical structure in question. Global percent differences for the fully loaded 16 mm COMS plaque (with model 6711 seeds) relative to the dose at 5 mm from the inner sclera (reference tumour apex location) are shown in the central plane of the plaque in Figure 6.28. The differences within the penumbra are within ±1.5%, and

the largest difference immediately adjacent to the plaque is ~5%. This comparison is useful to more fully assess the observed differences in order to determine whether or not they might have a clinical impact.
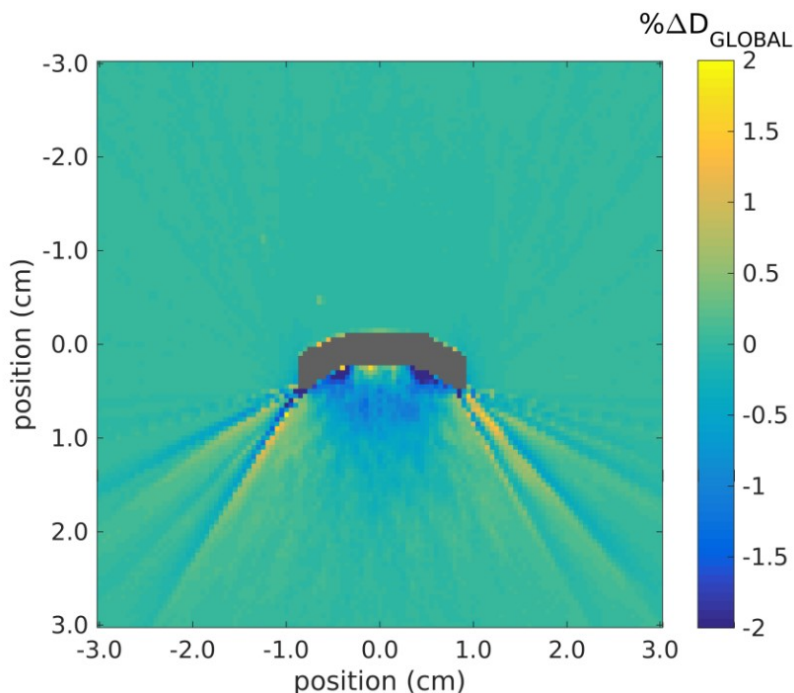
Figure 6.28 Global percent dose differences between ACE and MCNP6 doses in the central plane of the eye plaque for a fully loaded 16 mm COMS plaque in water relative to the dose at 5 mm from the inner sclera (the pixels containing the plaque are greyed out).

The larger differences in the plaque penumbra for the COMS plaques are limited to a conical shell volume around the eye, and it is expected that similarly constructed plaques would show similar effects (e.g. ROPES plaques [stainless steel backing with acrylic insert],[40] COMS type plaques with thin acrylic inserts or no inserts[41–43]). However, if a slotted style of plaque (e.g. Eye Physics plaques such as the Super9[44]) was incorporated into OcB, each seed would be located adjacent to a smaller interior plaque edge, and penumbral differences could potentially be larger and affect a larger volume of the eye region. Different styles of plaques would need to be individually evaluated to determine how well ACE could handle the dose modifying effects of the applicator.

6.4.2 Heterogeneous tissue material dosimetry

Overall, ACE was able to account for the presence of heterogeneous eye tissues and variable tissue densities quite well. The main limitations, manifest as regions with the largest dosimetric inaccuracy, occurred near the plaque penumbra (as seen for the plaques in water) and at tissue interfaces (combined up to 21% different at a POI). Examining global percent differences yielded results similar to those for the plaque in water, but the differences immediately adjacent to the plaque were somewhat larger, being [-2%, +17%] for the voxelized eye phantom and [-20%, +8%] for the patient CT dataset. Further away from the plaque, values for $\%\Delta D_{GLOBAL}$ were within ±3% with the exception of the cortical bone for the patient CT dataset (as expected due to unaccounted for spectral changes). Improvements in how OcB/ACE handles the intra-voxel presence of applicator materials could mitigate some of these differences, particularly at the plaque penumbra. The larger differences seen for the voxelized eye phantom at tissue interfaces present an extreme case as anatomical structures are voxelized and OcB 3D reconstructions of the contoured structures are inaccurate. In reality structures are not shaped like this and would be smoother; for the patient CT dataset these differences were smaller, as expected. Contouring a patient CT dataset with as many structures as were delineated for the voxelized eye phantom would likely be unfeasible due to limitations in structure visibility/contrast in the image. However, ideally at least the tumour, vitreous, and lens could be contoured and appropriate tissue compositions assigned to carry out a dose calculation that would give clinically relevant results and move beyond water-based dose calculations.

Compared to water-based treatment planning calculations using Plaque Simulator, both of the heterogeneous tissue scenarios indicate that water-based planning could result in underdosing the tumour (by up to 11%) and overestimating the dose to various critical structures in the eye (by up to 37%). In both scenarios the ACE doses for almost all POIs were closer to the MCNP6 doses than the Plaque Simulator doses, even in regions where the ACE dose calculations were less accurate. The accuracy of ACE was therefore sufficient to demonstrate the general effects of heterogeneous tissues in the eye on dose compared to water-based planning.

For both scenarios the air interface factor in Plaque Simulator slightly overestimates the dose reduction at the corneal surface if the eyelid is closed, therefore the improved agreement when using the air interface factor may not be due to more closely matching the scattering conditions, but coincidentally matching the dose reductions in one instance due to reduced

backscatter at the air interface (Plaque Simulator) and in the other instance due to the lower mass energy absorption coefficients of lens or soft tissue compared to water (MCNP6).

An important outstanding issue is however choosing the appropriate composition for each tissue in the eye. As already briefly discussed, the dose greatly depends on the tissues chosen and how the associated values of μ/ρ, μ_{en}/ρ, and density of the assigned tissues compare to water. The tissues specified by Lesperance *et al.* are likely closer to actual eye tissues than the tissue choices available in OcB, and therefore should yield more accurate comparisons between $D_{w,w}$ and $D_{m,m}$. For I-125, the 100% isodose line penetrates deeper for $D_{m,m}$ than for $D_{w,w}$ for the tissues used by Lesperance *et al.* as shown in Figure 4(a) in their work, such that a 2 mm basal margin deemed adequate for water-based planning would also be adequate for tissue-based planning. This is the opposite of what was found here for both the voxelized eye phantom and the patient CT dataset. The challenge is that the actual compositions of certain tissues in the eye are still unknown, such as that of ocular melanoma. Therefore, further investigation into the compositions of different structures in the eye is needed. As shown by Lesperance *et al.*, using a less water equivalent material for the tumour results in larger differences in dose to the tumour compared to the water-based scenario. When prescribing dose to the tumour apex this will also change the dose received in all other parts of the eye, demonstrating the importance of accurate material compositions for low-energy brachytherapy, a detail that is not nearly as critical for high-energy treatments.[8,45–48]

Transitioning from the traditional TG-43 dose reporting scheme (augmented with corrections for the plaque materials) to a dose to medium reporting scheme is expected to result in more accurate knowledge of doses to various structures in the eye. However, understanding the underlying factors that cause the changes in dose compared to water-based planning will be important to appreciate the clinical implications of implementing model-based dose calculations. The choice of tissue compositions for eye structures should be investigated further before transitioning to a model-based dose calculation method. That being said, once tissue compositions are known with greater certainty the OcB material library could be expanded. Then, ACE could present an informative tool for determining the effect of heterogeneous tissues on dosimetry within the eye and deciding if changes in TG-43 based prescription protocols are warranted.

More accurate dose calculations within the eye reporting dose to medium may also result in more accurate correlations between the prescribed dose and tumour control rate, and between doses to critical structures and toxicity rates, and thereby could improve the consistency of multi-institutional dose prescription. The use of a model-based dose calculation algorithm such as ACE would also allow for volumetric based planning, which represents an important step forward for ocular brachytherapy.

6.5 References

[1] S.-T. Chiu-Tsao, M.A. Astrahan, P.T. Finger, D.S. Followill, A.S. Meigooni, C.S. Melhus, F. Mourtada, M.E. Napolitano, R. Nath, M.J. Rivard, D.W.O. Rogers, and R.M. Thomson, "Dosimetry of ^{125}I and ^{103}Pd COMS eye plaques for intraocular tumors: Report of Task Group 129 by the AAPM and ABS," Med. Phys. **39**, 6161–6184 (2012).

[2] H. Acar, S.-T. Chiu-Tsao, I. Ozbay, G. Kemikler, and S. Tuncer, "Evaluation of material heterogeneity dosimetric effects using radiochromic film for COMS eye plaques loaded with ^{125}I seeds (model I25.S16)," Med. Phys. **40**, 011708 (2013).

[3] M.J. Rivard, S.-T. Chiu-Tsao, P.T. Finger, A.S. Meigooni, C.S. Melhus, F. Mourtada, M.E. Napolitano, D.W.O. Rogers, R.M. Thomson, and R. Nath, "Comparison of dose calculation methods for brachytherapy of intraocular tumors," Med. Phys. **38**, 306–316 (2011).

[4] C.S. Melhus and M.J. Rivard, "COMS eye plaque brachytherapy dosimetry simulations for ^{103}Pd, ^{125}I, and ^{131}Cs," Med. Phys. **35**, 3364–3371 (2008).

[5] R.M. Thomson, R.E.P. Taylor, and D.W.O. Rogers, "Monte Carlo dosimetry for ^{125}I and ^{103}Pd eye plaque brachytherapy," Med. Phys. **35**, 5530 (2008).

[6] R.M. Thomson and D.W.O. Rogers, "Monte Carlo dosimetry for ^{125}I and ^{103}Pd eye plaque brachytherapy with various seed models," Med. Phys. **37**, 368–376 (2010).

[7] M. Lesperance, M. Inglis-Whalen, and R.M. Thomson, "Model-based dose calculations for COMS eye plaque brachytherapy using an anatomically realistic eye phantom," Med. Phys. **41**, 021717 (12 pp.) (2014).

[8] L. Beaulieu, Å. Carlsson Tedgren, J.-F. Carrier, S.D. Davis, F. Mourtada, M.J. Rivard, R.M. Thomson, F. Verhaegen, T.A. Wareing, and J.F. Williamson, "Report of the Task Group 186 on model-based dose calculation methods in brachytherapy beyond the TG-43 formalism: Current status and recommendations for clinical implementation," Med. Phys. **39**, 6208–6236 (2012).

[9] M.J. Rivard, J.L.M. Venselaar, and L. Beaulieu, "The evolution of brachytherapy treatment planning," Med. Phys. **36**, 2136–2153 (2009).

[10] J.T. Goorley, M. James, T. Booth, F. Brown, J. Bull, J. Cox, and J. Durkee, "Initial MCNP6 Release Overview," Nucl. Technol. **180**, 298–315 (2012).

[11] *NUDAT 2.6, National Nuclear Data Centre, Brookhaven National Laboratory*, (URL: http://www.nndc.bnl.gov/chart/decaysearchdirect.jsp?nuc=125I&unc=nds). Last accessed January 24, 2017.

[12] M.J. Rivard, B.M. Coursey, L.A. DeWerd, W.F. Hanson, M.S. Huq, G.S. Ibbott, M.G. Mitch, R. Nath, and J.F. Williamson, "Update of AAPM Task Group No. 43 Report: A revised AAPM protocol for brachytherapy dose calculations," Med. Phys. **31**, 633–674 (2004).

[13] M.J. Rivard, C.S. Melhus, and B.L. Kirk, "Brachytherapy dosimetry parameters calculated for a new ^{103}Pd source," Med. Phys. **31**, 2466–2470 (2004).

[14] J.H. Hubbell, and S.M. Seltzer. (2004), *Tables of X-Ray Mass Attenuation Coefficients and Mass Energy-Absorption Coefficients* (version 1.4). National Institute of Standards and Technology, Gaithersburg, MD. (URL: http://physics.nist.gov/xaamdi). Last accessed January 24, 2017.

[15] S.M. Seltzer, P.J. Lamperti, M.G. Mitch, J.T. Weaver, and B.M. Coursey, "New National Air-Kerma-Strength Standards for ^{125}I and ^{103}Pd Brachytherapy Seeds," J. Res. Natl. Inst. Stand. Technol. **108**, 337–358 (2003).

[16] P. Aryal, J.A. Molloy, and M.J. Rivard, "A modern Monte Carlo investigation of the TG-43 dosimetry parameters for an ^{125}I seed already having AAPM consensus data," Med. Phys. **41**, 021702 (10 pp.) (2014).

[17] P. Karaiskos, P. Papagiannis, L. Sakelliou, G. Anagnostopoulos, and D. Baltas, "Monte Carlo dosimetry of the selectSeed ^{125}I interstitial brachytherapy seed," Med. Phys. **28**, 1753–1760 (2001).

[18] R.E.P. Taylor and D.W.O. Rogers, "An EGSnrc Monte Carlo-calculated database of TG-43 parameters," Med. Phys. **35**, 4228–4241 (2008).

[19] R.E.P. Taylor and D.W.O. Rogers, *The CLRP TG-43 Parameter Database for Brachytherapy*, (URL: http://www.physics.carleton.ca/clrp/seed_database). Last accessed March 16, 2017.

[20] J. Dolan, Z. Lia, and J.F. Williamson, "Monte Carlo and experimental dosimetry of an ^{125}I brachytherapy seed," Med. Phys. **33**, 4675–4684 (2006).

[21] R.E.P. Taylor, G. Yegin, and D.W.O. Rogers, "Benchmarking brachydose: Voxel based EGSnrc Monte Carlo calculations of TG-43 dosimetry parameters," Med. Phys. **34**, 445–457 (2007).

22 M.J.P. Chamberland, R.E.P. Taylor, D.W.O. Rogers, and R.M. Thomson, "egs_brachy: a versatile and fast Monte Carlo code for brachytherapy," Phys. Med. Biol. **61**, 8214–8231 (2016).

23 L. Beaulieu, Y. Ma, and B. van Veelen, "ACE Advanced Collapsed cone Engine," White Paper Elekta 1–16 (2014).

24 A. Ahnesjö, B. van Veelen, and A. Carlsson Tedgren, "Collapsed cone dose calculations for heterogeneous tissues in brachytherapy using primary and scatter separation source data," Comput. Methods Programs Biomed. **139**, 17–29 (2017).

25 Y. Ma, J. Vijande, F. Ballester, A. Carlsson Tedgren, D. Granero, A. Haworth, F. Mourtada, G.P. Fonseca, K. Zourari, P. Papagiannis, M.J. Rivard, F.-A. Siebert, R.S. Sloboda, R. Smith, M.J.P. Chamberland, R.M. Thomson, F. Verhaegen, and L. Beaulieu, "A generic TG-186 shielded applicator for the commissioning of model-based dose calculation algorithms for high-dose-rate 192Ir brachytherapy," Med. Phys. Accepted (2017).

26 R.W. Kline, *Coordinate Localization*, (URL: http://rpc.mdanderson.org/rpc/credentialing/Coordinate Localization.doc).

27 R.M. Thomson, R.E.P. Taylor, and D.W.O. Rogers, *The CLRP Eye Plaque Database*, (URL: http://www.physics.carleton.ca/clrp/eye_plaque). Last accessed March 14, 2017.

28 B. Walters, I. Kawrakow, and D.W.O. Rogers, *DOSXYZnrc Users Manual* (National Research Council Canada, Ottawa, Canada, 2005).

29 ICRP, "Adult reference comutational phantoms," in *ICRP Report No. 110* (ICRP, Washington, DC, 2009).

30 ICRP, "Basic anatomical and physiological data for use in radiological protection: reference values," in *Annals of the ICRP 89* (ICRP, Washington, DC, 2002).

31 M. Lesperance, M. Martinov, and R.M. Thomson, "Monte Carlo dosimetry for ^{103}Pd, ^{125}I, and ^{131}Cs ocular brachytherapy with various plaque models using an eye phantom," Med. Phys. **41**, 031706 (2014).

32 M.J. Berger and J.H. Hubbell, "XCOM: Photon cross sections on a personal computer," in *Report NBSIR87-3597* (National Institute of Standards Technology (NIST), Gaithersburg, MD, 1987).

33 ICRU, "Photon, electron, proton and neutron interaction data for body tissues," in *ICRU Report No. 46* (ICRU Publications, Bethesda, MD, 1992).

34 B. Cawston-Grant, H. Morrison, G. Menon, and R.S. Sloboda, "Experimental verification of Advanced Collapsed-cone Engine for use with a multichannel vaginal cylinder applicator," J. Appl. Clin. Med. Phys. **18**, 16–27 (2017).

[35] P. Papagiannis, E. Pantelis, and P. Karaiskos, "Current state of the art brachytherapy treatment planning dosimetry algorithms.," Br. J. Radiol. **87**, 20140163 (2014).

[36] F. Ballester, Å. Carlsson Tedgren, D. Granero, A. Haworth, F. Mourtada, G.P. Fonseca, K. Zourari, P. Papagiannis, M.J. Rivard, F.-A. Siebert, R.S. Sloboda, R.L. Smith, R.M. Thomson, F. Verhaegen, J. Vijande, Y. Ma, and L. Beaulieu, "A generic high-dose rate 192Ir brachytherapy source for evaluation of model-based dose calculations beyond the TG-43 formalism," Med. Phys. **42**, 3048–3062 (2015).

[37] A.K. Carlsson Tedgren and A. Ahnesjö, "Accounting for high Z shields in brachytherapy using collapsed cone superposition for scatter dose calculation.," Med. Phys. **30**, 2206–2217 (2003).

[38] G. Anagnostopoulos, D. Baltas, P. Karaiskos, E. Pantelis, P. Papagiannis, and L. Sakelliou, "An analytical dosimetry model as a step towards accounting for inhomogeneities and bounded geometries in ^{192}Ir brachytherapy treatment planning," Phys. Med. Biol. **48**, 1625–1647 (2003).

[39] Y. Ma, F. Lacroix, M.-C. Lavallée, and L. Beaulieu, "Validation of the Oncentra Brachy Advanced Collapsed cone Engine for a commercial ^{192}Ir source using heterogeneous geometries," Brachytherapy **14**, 939–952 (2015).

[40] D. Granero, J. Pérez-Calatayud, F. Ballester, E. Casal, and J.M. de Frutos, "Dosimetric study of the 15 mm ROPES eye plaque," Med. Phys. **31**, 3330–3336 (2004).

[41] H. Zhang, F. Davidorf, and Y. Qi, "Comparison of 16 mm OSU-Nag and COMS eye plaques," J. Appl. Clin. Med. Phys. **13**, 166–178 (2012).

[42] M.A. Astrahan, A. Szechter, and P.T. Finger, "Design and dosimetric considerations of a modified COMS plaque: the reusable 'seed-guide' insert," Med. Phys. **32**, 2706–2716 (2005).

[43] P.T. Finger, A. Berson, and A. Szechter, "Palladium-103 plaque radiotherapy for choroidal melanoma: Results of a 7-year study," Ophthalmology **106**, 606–613 (1999).

[44] M.A. Astrahan, G. Luxton, Q. Pu, and Z. Petrovich, "Conformal episcleral plaque therapy," Int. J. Radiat. Oncol. Biol. Phys. **39**, 505–519 (1997).

[45] D.E. Hyer, A. Sheybani, G.M. Jacobson, and Y. Kim, "The dosimetric impact of heterogeneity corrections in high-dose-rate 192Ir brachytherapy for cervical cancer: Investigation of both conventional Point-A and volume-optimized plans," Brachytherapy **11**, 515–520 (2012).

[46] K. Zourari, T. Major, A. Herein, V. Peppa, C. Polgar, and P. Papagiannis, "A retrospective dosimetric comparison of TG43 and a commercially available MBDCA for an APBI brachytherapy patient cohort," Phys. Medica **31**, 669–676 (2015).

[47] J. Hofbauer, C. Kirisits, A. Resch, Y. Xu, A. Sturdza, R. Pötter, and N. Nesvacil, "Impact of heterogeneity-corrected dose calculation using a grid-based Boltzmann solver on breast and cervix cancer brachytherapy.," J. Contemp. Brachytherapy **8**, 143–9 (2016).

[48] D. Jacob, M. Lamberto, L. DeSiyza Lawrence, and F. Mourtada, "Clinical transition to model-based dose calculation algorithm: A retrospective analysis of high-dose-rate tandem and ring brachytherapy of the cervix," Brachytherapy **16**, 624–629 (2017).

Chapter 7 Summary, conclusions, and future work

Ocular melanoma is a relatively rare, but often deadly form of cancer. The treatment of this disease using plaque based brachytherapy has been found to be as effective as enucleation in terms of overall survival; however, the occurrence of radiation side-effects in the eye affecting visual outcome, and therefore quality of life, remain high. The long-term survival of the patient is also strongly dependent on whether or not local tumour control is achieved. Therefore, there exists a fine balance between achieving local control while reducing radiation complications in the eye, a goal that is challenged due to the difficulty of performing accurate dosimetry for ocular brachytherapy. The steep dose gradients, small volume of interest, high sensitivity to material heterogeneities, and complexity of the eye structure contribute to this challenge.

Ocular brachytherapy has been commonly performed since the 1980s; however, it continues to be administered using a multitude of different methods and dosimetric protocols which makes outcome comparisons between different methods difficult. The current recommended dosimetry protocol for ocular brachytherapy is given in the American Brachytherapy Society – Ophthalmic Oncology Task Force 2014 report, with specific guidelines for the Collaborative Ocular Melanoma Study (COMS) style of plaques in the American Association of Physicists in Medicine Task Group (TG) 129 report. Though these reports facilitate some standardization in the treatment procedure, a number of limitations and shortcomings still exist in ocular brachytherapy dosimetry. The work performed in this thesis provides a number of dosimetric advancements including improvements to experimental dosimetry techniques, dose delivery and treatment planning protocols, as well as dose calculation methods.

To improve experimental dosimetry methodology, a modified procedure for performing EBT3 Gafchromic film calibration and absolute dose measurement was established for low-energy brachytherapy sources for irradiations up to 35 Gy in Chapter 3. Comparisons were made with irradiations from higher energy external photon beams, and variations in the film energy response of up to 3% above 2 Gy were observed, which could cause dose errors of up to 8%. Therefore, film calibration should be done with an appropriately low-energy source having a comparable effective energy when performing low-energy brachytherapy dose measurements. For the batch of film studied, the 75 kVp photon beam had an effective energy close to that of

the I-125 seed and could be used for calibration, while differing energy responses for the 200 kVp and 6 MV photon beams made these modalities demonstrably less suitable for low-energy seed calibration. Various fitting methods were also evaluated due to the large dose range investigated in this study. Two-segment piece-wise fitting with inclusion of uncertainties in measured optical density as well as delivered reference dose was found to result in the most accurate calibration curves. Above doses of 100 cGy, dose measurements can be made to within 5.7% (k=1) for I-125 seed irradiations if using the I-125 source for calibration, which is comparable to other brachytherapy Gafchromic film dosimetry studies. However, measurement uncertainty can be reduced to 2.3% (k=1) if using the 75 kVp photon beam for calibration. A triple-channel film heterogeneity correction method was also developed that does not require pre-scanning of films prior to irradiation, and therefore simplifies the procedure compared to other predominantly used methods for brachytherapy. This approach eliminates the introduction of additional uncertainties arising from image registration, scan to scan variability, and noise amplification. The triple-channel method was validated using external beam enhanced dynamic wedge fields, and restrictions to ensure accurate dosimetry were established, such as the length of time a given film calibration remains valid.

The developed film calibration and measurement methods were used in Chapter 4 to perform Gafchromic film dose measurements in a PMMA eye phantom irradiated with a 16 mm COMS plaque and a model #930 (Super9) Eye Physics plaque loaded with I-125 seeds at a reference depth of 6 mm (5 mm tumour height assuming 1 mm of sclera). The film doses were compared to Plaque Simulator treatment planning system (TPS) calculated doses obtained using Monte Carlo (MC) simulated TG-43 dose parameters that accounted for the PMMA material of the phantom. Differences on the plaque central axis (CAX) of +8% for the COMS plaques and -8% for the Super9 plaque were observed, likely caused by plaque tilt on the eye phantom and seed positioning differences within the plaque seed slots, respectively. Additional MC simulations of the experimental set-up were performed to provide reference quality comparisons for the 16 mm COMS plaque, as MC simulation results are considered the "gold standard" in radiation physics dosimetry. A high level of agreement was found between Plaque Simulator and MC simulations: within 0.06% at the tumour apex and within 1.4% at off-axis distances less than ±6 mm from the plaque CAX for the COMS plaque. However, agreement was worse at off-axis positions beyond ±10 mm from the CAX. At these locations differences of up to 13% were

observed, though this was partly (~1%) due to slightly different scattering conditions surrounding the eye phantom for the different calculation methods. Highly accurate Gafchromic film measurements are challenging for ocular brachytherapy and are extremely susceptible to set-up uncertainties such as the aforementioned reasons resulting in the film and Plaque Simulator dose differences. Controlling these sources of uncertainty could improve the accuracy of EBT3 Gafchromic film ocular brachytherapy plaque irradiations. These uncertainties as well as others also affect the accuracy with which dose is delivered for patient treatments. Therefore, understanding the uncertainties and how they impact dosimetry is vital to performing high quality treatments for patients with ocular melanomas.

The work presented in Chapter 5 addresses the physical and clinical uncertainties affecting dose delivery in order to: 1) determine the accuracy with which the prescribed dose is delivered to the prescription point (tumour apex); 2) identify the sources of uncertainty most significantly impacting the treatment and develop methods to minimize them; and 3) determine an appropriate size of margin to apply at the tumour apex in order to ensure adequate dosimetric coverage there, usually the point of minimum dose within the tumour.

To accomplish this, a comprehensive dosimetric uncertainty analysis was performed at the tumour apex for a 16 mm COMS plaque and a Super9 plaque loaded with I-125 seeds, using the Guide to the expression of Uncertainty in Measurement/National Institute of Standards and Technology approach. This included evaluating uncertainties due to seed construction/azimuthal fluence variations, source strength, plaque assembly, treatment planning calculations, tumour height measurements, plaque placement, and plaque tilt. Uncertainties associated with seed construction were determined using EBT3 Gafchromic film measurements around single seeds, plaque assembly uncertainties were determined using high resolution microCT scanning of loaded plaques to measure seed positions in the plaques, plaque placement uncertainties were determined from ophthalmologist estimated values, and all other uncertainties were determined from previously published studies. The total uncertainty, ranging from 13.1% – 18.2%, was used to infer an appropriate treatment margin to be applied at the tumour apex to ensure coverage at the prescription point with the prescribed dose, which ranged from 1.2 – 1.8 mm depending on the plaque type and prescription depth (tumour height). The sources of uncertainty contributing most substantially to the total dosimetric uncertainty were seed placement within the plaque, treatment planning calculation, tumour height measurement, and plaque tilt. Developing methods

to minimize these uncertainties can improve the accuracy of treatment delivery. Though it is common clinical practice to apply an apex margin to the tumour to account for uncertainty in the tumour height measurement in addition to applying the recommended minimum 2 mm basal margin, the size of an adequate dosimetric apex margin has not been previously determined. This work presents an uncertainty-based, rational approach to choosing an apex margin to promote adequate radiation coverage of the prescription point and therefore has immediate clinical relevancy.

To progress beyond the current TG-43 formalism used for ocular brachytherapy dosimetry and most other forms of brachytherapy treatment, new model-based dose calculation algorithms (MBDCAs) have recently become available to perform brachytherapy dose calculations. The TG-43 formalism has a number of limitations which arise due to assuming an infinite homogeneous water medium, including ignoring inter-seed attenuation, differing scattering conditions, and any heterogeneous materials present in the treatment field (both applicator and patient tissue materials). The last two in particular have a significant effect on dosimetry for ocular brachytherapy. The effects of the plaque materials on the dose distribution in water for a number of different styles of plaques have been investigated, but only very recently has a full eye model including realistic eye materials been studied. The latter results demonstrate the large effects the heterogeneous materials in the eye can have on dosimetry due to the low-energy radiation sources used for treatment.

To further explore the possibility of performing patient specific model-based dose calculations, an informal collaboration was established with a commercial TPS vendor to implement and apply collapsed-cone superposition dose calculations using I-125 sources for COMS plaque therapy. The TPS, Oncentra Brachy (OcB), incorporates the Advanced Collapsed cone Engine (ACE) algorithm that previously has only been used with Ir-192 and Co-60 high-dose-rate sources. Therefore, moving forward with this line of investigation required that both an I-125 source and the COMS plaques be introduced into the software. The work presented in Chapter 6 outlines the methods required to do this and describes the subsequent evaluation of the ACE algorithm in a number of stages of progressing complexity: for a single seed in water, for three sizes of COMS plaques in water, for a voxelized eye phantom containing various ocular structures and materials, and for a patient CT dataset having realistic variability in tissue densities throughout the entire patient model. MC simulations were performed to supply

reference dosimetry data for comparison. Overall, ACE dosimetry showed good agreement with MC within the tumour and along the plaque CAX for fully loaded COMS plaques, on average within < 2.6%. However, depending on the plaque position, doses within the optic disc or fovea could differ substantially by up to 21%. Improvements in how OcB/ACE handles the intra-voxel presence of applicator materials could mitigate this issue. Doses to tissues in the eye differed substantially from those calculated using water-based planning (Plaque Simulator) (up to 37%), which could have an impact on clinical treatment planning decisions for ocular brachytherapy. That said, the influence of choice of tissue materials needs to be further investigated, and the material library within OcB expanded.

The work presented in this thesis represents a comprehensive effort to improve clinical dosimetry for eye plaque therapy using a number of different methods and technologies to address several aspects of dosimetry. There are, however, a number of other areas that require further research if the accuracy of ocular brachytherapy dosimetry is to continue to improve.

As the clinical application of MBDCAs is still very much in a preliminary phase, particularly for ocular brachytherapy, the TG-43 formalism will continue to be used in the near future. Immediate improvements could be made by updating the low-energy TG-43 consensus datasets using more current data and validating them using experimental measurements. As demonstrated in Chapter 5, using different TG-43 datasets to perform dose calculations can have a large effect on the doses within the eye. Including seed specific correction factors for plaque materials could also improve the accuracy of dose calculations within a TG-43 based calculation scheme.

As also discussed in Chapter 5, the uncertainties present in treatment delivery vary depending on the specific scenario (dome-shaped tumour, eccentrically placed plaque, partially loaded plaque, etc.). However they can also depend on other factors such as ocular muscle involvement, mushroom shaped tumour, plaque in close proximity to the optic nerve, use of a notched plaque, as well as the style of plaque. These represent uninvestigated scenarios which could be characterized by moderately different values of uncertainty, and therefore require different margins to be applied at the tumour apex as well as around the basal edges of the tumour. The work presented in Chapter 5 provides a foundation for exploring the uncertainties in these other potentially more complex scenarios. Means to minimize some of the uncertainties identified could also be investigated to improve the accuracy of treatment delivery, such as novel

or high-resolution imaging methods to enhance tumour delineation and dimensional measurements, and elucidation of factors that affect plaque tilt and means to reduce them.

To be able to transition away from TG-43 water-based planning to fully model-based planning, a number of areas need to be further investigated. Research is required to gain sufficiently accurate knowledge of the compositions and densities of the various tissues in the eye. The dose calculation accuracy of ACE for ocular brachytherapy treatments was determined in this work, but if inappropriate tissue compositions are used these results will have diminished clinical significance. Once the tissue properties are known with greater certainty, the material library in ACE could be expanded and a cohort of patients examined to determine population variations due to differences in ocular tissue densities, tumour positions relative to other structures in the eye, and patient anatomy including eye size, tumour size, and lens thickness, all of which will affect dose throughout the eye. This assessment could also help determine the clinical relevance of the dose calculation uncertainties near the plaque penumbra and decide if improvements in OcB/ACE are required to reduce them.

By improving the accuracy of dosimetry for ocular brachytherapy, including accounting for plaque and patient heterogeneities as well as uncertainties present in the treatment process, a more accurate determination of doses to critical structures within the eye as well as the tumour can be achieved. This, in turn, will allow more accurate and meaningful comparisons between different treatment protocols to be performed, and ultimately illuminate the influence of treatment variables such as implant duration/dose-rate, prescription dose, and radionuclide selection on clinical outcomes.

Bibliography

H. Acar, S.-T. Chiu-Tsao, I. Ozbay, G. Kemikler, and S. Tuncer, "Evaluation of material heterogeneity dosimetric effects using radiochromic film for COMS eye plaques loaded with ^{125}I seeds (model I25.S16)," Med. Phys. **40**, 011708 (2013).

H. Afsharpour, G. Landry, M. D'Amours, S. Enger, B. Reniers, E.S. Poon, J.-F. Carrier, F. Verhaegen, and L. Beaulieu, "ALGEBRA: ALgorithm for the heterogeneous dosimetry based on GEANT4 for BRAchytherapy," Phys. Med. Biol. **57**, 3273–3280 (2012).

A. Ahnesjö and M.M. Aspradakis, "Dose calculations for external photon beams in radiotherapy," Phys. Med. Biol. **44**, R99–R155 (1999).

A. Ahnesjö, B. van Veelen, and A. Carlsson Tedgren, "Collapsed cone dose calculations for heterogeneous tissues in brachytherapy using primary and scatter separation source data," Comput. Methods Programs Biomed. **139**, 17–29 (2017).

T. Aland, T. Kairn, and J. Kenny, "Evaluation of a Gafchromic EBT2 film dosimetry system for radiotherapy quality assurance," Australas. Phys. Eng. Sci. Med. **34**, 251–260 (2011).

W. Alberti, B. Pothmann, P. Tabor, K. Muskalla, K.-P.P. Hermann, and D. Harder, "Dosimetry and physical treatment planning for iodine eye plaque therapy," Int. J. Radiat. Oncol. Biol. Phys. **20**, 1087–1092 (1991).

S. Aldelaijan, H. Mohammed, N. Tomic, L.-H. Liang, F. DeBlois, A. Sarfehnia, W. Abdel-Rahman, J. Seuntjens, and S. Devic, "Radiochromic film dosimetry of HDR ^{192}Ir source radiation fields," Med. Phys. **38**, 6074 (2011).

P.R. Almond, P.J. Biggs, B.M. Coursey, W.F. Hanson, M.S. Huq, R. Nath, and D.W.O. Rogers, "AAPM's TG-51 protocol for clinical reference dosimetry of high-energy photon and electron beams.," Med. Phys. **26**, 1847–1870 (1999).

A. Almony, S. Breit, H. Zhao, J. Garcia-Ramirez, D.B. Mansur, and J.W. Harbour, "Tilting of radioactive plaques after initial accurate placement for treatment of uveal melanoma," Arch. Ophthalmol. **126**, 65–70 (2008).

American Joint Committee on Cancer, "Malignant melanoma of the uvea," in *AJCC cancer staging manual*, 7th ed., edited by S.B. Edge, D.R. Byrd, C.C. Compton, A.G. Fritz, F.L. Greene and A. Trotti (Springer, New York, NY, 2010), pp. 547–559.

G. Anagnostopoulos, D. Baltas, P. Karaiskos, E. Pantelis, P. Papagiannis, and L. Sakelliou, "An analytical dosimetry model as a step towards accounting for inhomogeneities and bounded geometries in ^{192}Ir brachytherapy treatment planning," Phys. Med. Biol. **48**, 1625–1647 (2003).

C. Andrés, A. del Castillo, R. Tortosa, D. Alonso, and R. Barquero, "A comprehensive study of the Gafchromic EBT2 radiochromic film. A comparison with EBT.," Med. Phys. **37**, 6271–6278 (2010).

J.N. Aronowitz, S. V Aronowitz, and R.F. Robison, "Classics in brachytherapy: Margaret Cleaves introduces gynecologic brachytherapy," Brachytherapy **6**, 293–297 (2007).

P. Aryal, J.A. Molloy, and M.J. Rivard, "A modern Monte Carlo investigation of the TG-43 dosimetry parameters for an ^{125}I seed already having AAPM consensus data," Med. Phys. **41**, 021702 (10 pp.) (2014).

P. Aryal, J.A. Molloy, and M.J. Rivard, "Independent dosimetric assessment of the model EP917 episcleral brachytherapy plaque," Med. Phys. **41**, 092102 (11 pp.) (2014).

M.A. Astrahan, *Plaque Simulator*, (URL: http://eyephysics.com/PS/Index.html). Last accessed May 31, 2017.

M.A. Astrahan, G. Luxton, G. Jozsef, T.D. Kampp, P.E. Liggett, M.D. Sapozink, and Z. Petrovich, "An interactive treatment planning system for ophthalmic plaque radiotherapy," Int. J. Radiat. Oncol. Biol. Phys. **18**, 679–687 (1990).

M.A. Astrahan, G. Luxton, Q. Pu, and Z. Petrovich, "Conformal episcleral plaque therapy," Int. J. Radiat. Oncol. Biol. Phys. **39**, 505–519 (1997).

M.A. Astrahan, "Improved treatment planning for COMS eye plaques," Int. J. Radiat. Oncol. Biol. Phys. **61**, 1227–1242 (2005).

M.A. Astrahan, A. Szechter, and P.T. Finger, "Design and dosimetric considerations of a modified COMS plaque: the reusable 'seed-guide' insert," Med. Phys. **32**, 2706–2716 (2005).

F.H. Attix, *Introduction to Radiological Physics and Radiation Dosimetry*, 2nd Ed. (Wiley-VCH Verlag GmbH & Co. KGaA, Weinheim, 2004).

J.J. Augsburger, "Is observation really appropriate for small choroidal melanomas?," Trans. Am. Ophthalmol. Soc. **91**, 147–175 (1993).

F. Ballester, D. Granero, J. Pérez-Calatayud, C.S. Melhus, and M.J. Rivard, "Evaluation of high-energy brachytherapy source electronic disequilibrium and dose from emitted electrons," Med. Phys. **36**, 4250–4256 (2009).

F. Ballester and R. Nath, "Radionuclides in Brachytherapy: Current and Potential New Sources," in *Comprehensive Brachytherapy: Physical and clinical aspects*, edited by J.L.M. Venselaar, D. Baltas, A.S. Meigooni and P.J. Hoskin (Taylor & Francis Group, LLC, Boca Raton, FL, 2013), pp. 29–42.

F. Ballester, Å. Carlsson Tedgren, D. Granero, A. Haworth, F. Mourtada, G.P. Fonseca, K. Zourari, P. Papagiannis, M.J. Rivard, F.-A. Siebert, R.S. Sloboda, R.L. Smith, R.M. Thomson, F. Verhaegen, J. Vijande, Y. Ma, and L. Beaulieu, "A generic high-dose rate 192Ir brachytherapy source for evaluation of model-based dose calculations beyond the TG-43 formalism," Med. Phys. **42**, 3048–3062 (2015).

H. Basil, *Brachytherapy, Conquering cancer, The first 100 years* (Best Cure Foundation, Brachytherapy Research & Educational Foundation, Springfield, VA, 2014).

L.J. van Battum, H. Huizenga, R.M. Verdaasdonk, and S. Heukelom, "How flatbed scanners upset accurate film dosimetry," Phys. Med. Biol. **61**, 625–649 (2016).

L. Beaulieu, Å. Carlsson Tedgren, J.-F. Carrier, S.D. Davis, F. Mourtada, M.J. Rivard, R.M. Thomson, F. Verhaegen, T.A. Wareing, and J.F. Williamson, "Report of the Task Group 186 on model-based dose calculation methods in brachytherapy beyond the TG-43 formalism: Current status and recommendations for clinical implementation," Med. Phys. **39**, 6208–6236 (2012).

L. Beaulieu, Y. Ma, and B. van Veelen, "ACE Advanced Collapsed cone Engine," White Paper Elekta 1–16 (2014).

D.J. Bell and M.W. Wilson, "Choroidal melanoma: natural history and management options," Cancer Control **11**, 296–303 (2004).

M.J. Berger and J.H. Hubbell, "XCOM: Photon cross sections on a personal computer," in *Report NBSIR87-3597* (National Institute of Standards Technology (NIST), Gaithersburg, MD, 1987).

M.J. Berger, J.S. Coursey, M.A. Zucker, and J. Chang, *ESTAR, PSTAR, and ASTAR: Computer programs for calculating stopping-power and range tables for electrons, protons, and helium ions (version 1.2.3, online)* (National Institute of Standards and Technology, Gaithersburg, MD, 2005) (available URL: http://physics.nist.gov/Star).

L. Bergman, B. Nilsson, G. Lundell, M. Lundell, and S. Seregard, "Ruthenium Brachytherapy for Uveal Melanoma, 1979–2003: Survival and Functional Outcomes in the Swedish Population," Ophthalmology **112**, 834–840 (2005).

T. van den Bosch, E. Kilic, D. Paridaens, and A. De Klein, "Genetics of uveal melanoma and cutaneous melanoma: Two of a kind?," Dermatol. Res. Pract. **2010**, 360136 (13 pp.) (2010).

T.A.D. Brown, K.R. Hogstrom, D. Alvarez, K.L. Matthews, K. Ham, and J.P. Dugas, "Dose-response curve of EBT, EBT2, and EBT3 radiochromic films to synchrotron-produced monochromatic x-ray beams," Med. Phys. **39**, 7412–7417 (2012).

W.M. Butler, W.S. Bice, L.A. DeWerd, J.M. Hevezi, M.S. Huq, G.S. Ibbott, J.R. Palta, M.J. Rivard, J. Seuntjens, and B.R. Thomadsen, "Third-party brachytherapy source calibrations

and physicist responsibilities: report of the AAPM Low Energy Brachytherapy Source Calibration Working Group," Med. Phys. **35**, 3860–3865 (2008).

S.F. Byrne and R.L. Green, *Ultrasound of the eye and orbit* (Mosby Year Book Inc., St. Louis, MO, 1992).

Canadian Cancer Society's Advisory Committee on Cancer Statistics, *Canadian Cancer Statistics 2016* (Canadian Cancer Society, Toronto, ON, 2016).

Cancer.Net, *Eye Cancer: Statistics*, (URL: http://www.cancer.net/cancer-types/eye-cancer/statistics). Last accessed April 11, 2017.

Å.K. Carlsson and A. Ahnesjö, "Point kernels and superposition methods for scatter dose calculations in brachytherapy," Phys. Med. Biol. **45**, 357–357 (2000).

Å.K. Carlsson and A. Ahnesjö, "The collapsed cone superposition algorithm applied to scatter dose calculations in brachytherapy," Phys. Med. Biol. **27**, 2320–2332 (2000).

A. Carlsson Tedgren and G.A. Carlsson, "Specification of absorbed dose to water using model-based dose calculation algorithms for treatment planning in brachytherapy," Phys. Med. Biol. **58**, 2561–2579 (2013).

Å. Carlsson Tedgren and A. Ahnesjö, "Optimization of the computational efficiency of a 3D, collapsed cone dose calculation algorithm for brachytherapy," Med. Phys. **35**, 1611 (2008).

Å. Carlsson Tedgren, F. Verhaegen, and L. Beaulieu, "On the introduction of model-based algorithms performing nonwater heterogeneous corrections into brachytherapy treatment planning," in *Comprehensive Brachytherapy: Physical and clinical aspects*, edited by J.L.M. Venselaar, D. Baltas, A.S. Meigooni and P.J. Hoskin (Taylor & Francis Group, LLC, Boca Raton, FL, 2013).

A.K. Carlsson Tedgren and A. Ahnesjö, "Accounting for high Z shields in brachytherapy using collapsed cone superposition for scatter dose calculation.," Med. Phys. **30**, 2206–2217 (2003).

V. Casanova Borca, M. Pasquino, G. Russo, P. Grosso, D. Cante, P. Sciacero, G. Girelli, M.R. La Porta, and S. Tofani, "Dosimetric characterization and use of GAFCHROMIC EBT3 film for IMRT dose verification," J. Appl. Clin. Med. Phys. **14**, 4111 (2013).

J.-P. Caujolle, V. Paoli, E. Chamorey, C. Maschi, S. Baillif, J. Herault, P. Gastaud, and J.M. Hannoun-Levi, "Local recurrence after uveal melanoma proton beam therapy: Recurrence types and prognostic consequences," Int. J. Radiat. Oncol. Biol. Phys. **85**, 1218–1224 (2013).

B. Cawston-Grant, H. Morrison, G. Menon, and R.S. Sloboda, "Experimental verification of Advanced Collapsed-cone Engine for use with a multichannel vaginal cylinder applicator," J. Appl. Clin. Med. Phys. **18**, 16–27 (2017).

M.B. Chadwick, M. Herman, P. Obložinský, M.E. Dunn, Y. Danon, A.C. Kahler, D.L. Smith, B. Pritychenko, G. Arbanas, R. Arcilla, R. Brewer, D.A. Brown, R. Capote, A.D. Carlson, Y.S. Cho, H. Derrien, K. Guber, G.M. Hale, S. Hoblit, *et al.*, "ENDF/B-VII.1 Nuclear Data for Science and Technology: Cross Sections, Covariances, Fission Product Yields and Decay Data," Nucl. Data Sheets **112**, 2887–2996 (2011).

M.J.P. Chamberland, R.E.P. Taylor, D.W.O. Rogers, and R.M. Thomson, "egs_brachy: a versatile and fast Monte Carlo code for brachytherapy," Phys. Med. Biol. **61**, 8214–8231 (2016).

D.H. Char, J.M. Quivey, J.R. Castro, S. Kroll, and T. Phillips, "Helium ions versus iodine 125 brachytherapy in the management of uveal melanoma. A prospective, randomized, dynamically balanced trial," Ophthalmology **100**, 1547–54 (1993).

D.H. Char, S.M. Kroll, and J. Castro, "Ten-year follow-up of helium ion therapy for uveal melanoma," Am. J. Ophthalmol. **125**, 81–89 (1998).

D.H. Char, T. Miller, and J.B. Crawford, "Uveal tumour resection," Br. J. Ophthalmol. **85**, 1213–1219 (2001).

O. Chibani and J.F. Williamson, "MCPI (c): A sub-minute Monte Carlo dose calculation engine for prostate implants.," Med. Phys. **32**, 3688–3698 (2005).

S.-T. Chiu-Tsao, L.L. Anderson, K. O'Brien, L. Stabile, and J.C. Liu, "Dosimetry for ^{125}I seed (model 6711) in eye plaques," Med. Phys. **20**, 383–389 (1993).

S.-T. Chiu-Tsao, L. Boulay, I. Kanna, A. de la Zerda, and J.H. Kim, "Dose distribution in the eye for ^{103}Pd seed in COMS eye plaque," Med. Phys. **22**, 923 (1995).

S.-T. Chiu-Tsao, "Episcleral eye plaques for treatment of intraocular malignancies and benign diseases," in *Brachytherapy Physics: Joint AAPM/ABS Summer School*, 2nd Ed., edited by B.R. Thomadsen, M.J. Rivard and W.M. Butler (Medical Physics, Madison, WI, 2005), pp. 673–705.

S.-T. Chiu-Tsao, "Pterygium brachytherapy physics," in *Brachytherapy Physics: Joint AAPM/ABS Summer School*, 2nd ed., edited by B.R. Thomadsen, M.J. Rivard and W.M. Butler (Medical Physics, Madison, WI, 2005), pp. 707–717.

S.-T. Chiu-Tsao, D.C. Medich, and J. Munro, "The use of new GAFCHROMIC EBT film for ^{125}I seed dosimetry in Solid Water phantom," Med. Phys. **35**, 3787–3799 (2008).

S.-T. Chiu-Tsao, M.A. Astrahan, P.T. Finger, D.S. Followill, A.S. Meigooni, C.S. Melhus, F. Mourtada, M.E. Napolitano, R. Nath, M.J. Rivard, D.W.O. Rogers, and R.M. Thomson, "Dosimetry of ^{125}I and ^{103}Pd COMS eye plaques for intraocular tumors: Report of Task Group 129 by the AAPM and ABS," Med. Phys. **39**, 6161–6184 (2012).

S.-T. Chiu-Tsao, J.J. Napoli, S.D. Davis, J. Hanley, and M.J. Rivard, "Dosimetry for ^{131}Cs and ^{125}I seeds in solid water phantom using radiochromic EBT film," Appl. Radiat. Isot. **92**, 102–114 (2014).

D.J. Coleman, D.H. Abramson, R.L. Jack, and L.A. Franzen, "Ultrasonic diagnosis of tumors of the choroid," Arch. Ophthalmol. **91**, 344–354 (1974).

Collaborative Ocular Melanoma Study Group, "Design and methods of a clinical trial for a rare condition: the Collaborative Ocular Melanoma Study. COMS Report No. 3," Control. Clin. Trials **14**, 362–391 (1993).

Collaborative Ocular Melanoma Study Group, "COMS Manual of Procedures, Chapter 12: Radiation," in *COMS manual of procedures PB95-179693*(National Technical Information Service, Springfield, VA, 1995).

Collaborative ocular melanoma study group, "Mortality in patients with small choroidal melanoma. COMS Report No. 4," Arch. Ophthalmol. **115**, 886–893 (1997).

Collaborative Ocular Melanoma Study Group, "Factors predictive of growth and treatment of small chroidal melanomas. COMS Report No. 5," Arch. Ophthalmol. **115**, 1537–1544 (1997).

Collaborative Ocular Melanoma Study Group, "The Collaborative Ocular Melanoma Study (COMS) randomized trial of pre-enucleated radiation of large choroidal melanoma II: Initial Mortality Findings. COMS Report No .10," Am. J. Ophthalmol. **125**, 779–796 (1998).

Collaborative Ocular Melanoma Study Group, "Echography (ultrasound) procedures for the collaborative ocular melanoma study (COMS), Report No.12, Part II," J. Ophthalmic Nurs. Technol. **18**, 219–232 (1999).

Collaborative Ocular Melanoma Study Group, "The COMS Randomized Trial of Iodine 125 Brachytherapy for Choroidal Melanoma, III: initial mortality findings. COMS Report No. 18," Arch. Ophthalmol. **119**, 969–982 (2001).

Collaborative Ocular Melanoma Study Group, "Assessment of metastatic disease status at death in 435 patients with large choroidal melanoma in the Collaborative Ocular Melanoma Study (COMS): COMS report No. 15.," Arch. Ophthalmol. **119**, 670–676 (2001).

Collaborative Ocular Melanoma Study Group, "Collaborative Ocular Melanoma Study (COMS) randomized trial of I-125 brachytherapy for medium choroidal melanoma: I. visual acuity after 3 years COMS report No. 16," Ophthalmology **108**, 348–366 (2001).

Collaborative Ocular Melanoma Study Group, "The COMS Randomized Trial of Iodine 125 Brachytherapy for Choroidal Melanoma: IV. Local treatment failure and enucleation in the first 5 years after brachytherapy. COMS report no. 19," Ophthalmology **109**, 2197–2206 (2002).

Collaborative Ocular Melanoma Study Group, "The COMS Randomized Trial of Iodine 125 Brachytherapy for Choroidal Melanoma: V. Twelve-year mortality rates and prognosis factors: COMS Report No. 28," Arch. Ophthalmol. **124**, 1684–1693 (2006).

Collaborative Ocular Melanoma Study Group, "Incidence of Cataract and Outcomes after Cataract Surgery in the First 5 Years after Iodine 125 Brachytherapy in the Collaborative Ocular Melanoma Study. COMS Report No. 27," Ophthalmology **114**, 1363–1371 (2007).

B. Damato, I. Patel, I.R. Campbell, H.M. Mayles, and R.D. Errington, "Local tumor control after ^{106}Ru brachytherapy of choroidal melanoma," Int. J. Radiat. Oncol. **63**, 385–391 (2005).

J.F. Dempsey, D.A. Low, A.S. Kirov, and J.F. Williamson, "Quantitative optical densitometry with scanning-laser film digitizers.," Med. Phys. **26**, 1721–1731 (1999).

S. Devic, J. Seuntjens, G. Hegyi, E.B. Podgorsak, C.G. Soares, A.S. Kirov, I. Ali, J.F. Williamson, and A. Elizondo, "Dosimetric properties of improved GafChromic films for seven different digitizers.," Med. Phys. **31**, 2392–2401 (2004).

S. Devic, J. Seuntjens, E. Sham, E.B. Podgorsak, C.R. Schmidtlein, A.S. Kirov, and C.G. Soares, "Precise radiochromic film dosimetry using a flat-bed document scanner.," Med. Phys. **32**, 2245–2253 (2005).

S. Devic, N. Tomic, C.G. Soares, and E.B. Podgorsak, "Optimizing the dynamic range extension of a radiochromic film dosimetry system," Med. Phys. **36**, 429–437 (2009).

S. Devic, S. Aldelaijan, H. Mohammed, N. Tomic, L. Liang, F. Deblois, and J. Seuntjens, "Absorption spectra time evolution of EBT-2 model GAFCHROMIC™ film," Med. Phys. **37**, 2207–2214 (2010).

S. Devic, "Radiochromic film dosimetry: Past, present, and future," Phys. Medica **27**, 122–134 (2011).

S. Devic, N. Tomic, and D. Lewis, "Reference radiochromic film dosimetry: Review of technical aspects," Phys. Medica **32**, 541–556 (2016).

L.A. DeWerd, G.S. Ibbott, A.S. Meigooni, M.G. Mitch, M.J. Rivard, K.E. Stump, B.R. Thomadsen, and J.L.M. Venselaar, "A dosimetric uncertainty analysis for photon-emitting brachytherapy sources: report of AAPM Task Group No. 138 and GEC-ESTRO," Med. Phys. **38**, 782–801 (2011).

K. Dieckmann, J. Bogner, D. Georg, M. Zehetmayer, G. Kren, and R. Pötter, "A linac-based stereotactic irradiation technique of uveal melanoma," Radiother. Oncol. **61**, 49–56 (2001).

M. Diener-West, S.M. Reynolds, D.J. Agugliaro, R. Caldwell, K. Cumming, J.D. Earle, D.L. Green, B.S. Hawkins, J. Hayman, I. Jaiyesimi, J.M. Kirkwood, W.J. Koh, D.M. Robertson, J.M. Shaw, and J. Thoma, "Screening for metastasis from choroidal melanoma: The Collaborative Ocular Melanoma Study Group Report 23," J. Clin. Oncol. **22**, 2438–2444 (2004).

J. Dolan, Z. Lia, and J.F. Williamson, "Monte Carlo and experimental dosimetry of an ^{125}I brachytherapy seed," Med. Phys. **33**, 4675–4684 (2006).

R. Dunavoelgyi, K. Dieckmann, A. Gleiss, S. Sacu, K. Kircher, M. Georgopoulos, D. Georg, M. Zehetmayer, and R. Poetter, "Local Tumor Control, Visual Acuity, and Survival After Hypofractionated Stereotactic Photon Radiotherapy of Choroidal Melanoma in 212 Patients Treated Between 1997 and 2007," Int. J. Radiat. Oncol. **81**, 199–205 (2011).

J.D. Earle, R.W. Kline, and D.M. Robertson, "Selection of iodine 125 for the Collaborative Ocular Melanoma Study.," Arch. Ophthalmol. **105**, 763–764 (1987).

K.M. Egan, L.M. Ryan, and E.S. Gragoudas, "Survival implications of enucleation after definitive radiotherapy for choroidal melanoma," Arch. Ophthalmol. **116**, 366–370 (1998).

E. Egger, L. Zografos, A. Schalenbourg, D. Beati, T. Böhringer, L. Chamot, and G. Goitein, "Eye retention after proton beam radiotherapy for uveal melanoma," Int. J. Radiat. Oncol. Biol. Phys. **55**, 867–880 (2003).

Evaluation of measurement data—Guide to the expression of uncertainty in measurement, *International Organization for Standardization (ISO)*, Joint Committee for Guides in Metrology (JCGM 100, 2008), corrected version 2010, http://www.bipm.org/utils/common/documents/jcgm/JCGM_100_2008_E.pdf.

M.D.C. Evans, M.A. Astrahan, and R. Bate, "Tumor localization using fundus view photography for episcleral plaque therapy," Med. Phys. **20**, 769–775 (1993).

B.C. Ferreira, M.C. Lopes, and M. Capela, "Evaluation of an Epson flatbed scanner to read Gafchromic EBT films for radiation dosimetry," Phys. Med. Biol. **54**, 1073–1085 (2009).

C. Fiandra, M. Fusella, F.R. Giglioli, A.R. Filippi, C. Mantovani, U. Ricardi, and R. Ragona, "Comparison of Gafchromic EBT2 and EBT3 for patient-specific quality assurance: cranial stereotactic radiosurgery using volumetric modulated arc therapy with multiple noncoplanar arcs," Med. Phys. **40**, 082105 (2013).

P.T. Finger, "Radiation therapy for choroidal melanoma," Surv. Ophthalmol. **42**, 215–232 (1997).

P.T. Finger, J.M. Romero, R.B. Rosen, R. Iezzi, R. Emery, and A. Berson, "Three-dimensional ultrasonography of choroidal melanoma: localization of radioactive eye plaques," Arch. Ophthalmol. **116**, 305–312 (1998).

P.T. Finger, A. Berson, and A. Szechter, "Palladium-103 plaque radiotherapy for choroidal melanoma: Results of a 7-year study," Ophthalmology **106**, 606–613 (1999).

P.T. Finger, K.J. Chin, and G. Duvall, "Palladium-103 Ophthalmic Plaque Radiation Therapy for Choroidal Melanoma: 400 Treated Patients," Ophthalmology **116**, 790–796 (2009).

P.T. Finger, K.J. Chin, and G.-P. Yu, "Risk Factors for Radiation Maculopathy after Ophthalmic Plaque Radiation for Choroidal Melanoma," Am. J. Ophthalmol. **149**, 608–615 (2010).

P.T. Finger, K.J. Chin, G.-P. Yu, and N.S. Patel, "Risk factors for cataract after palladium-103 ophthalmic plaque radiation therapy," Radiat. Oncol. Biol. **80**, 800–806 (2011).

G.P. Fonseca, B. Reniers, G. Landry, S. White, M. Bellezzo, P.C.G. Antunes, C.P. de Sales, E. Welteman, H. Yoriyaz, and F. Verhaegen, "A medical image-based graphical platform-Features, applications and relevance for brachytherapy," Brachytherapy **13**, 632–639 (2014).

J. Fontanesi, D. Meyer, S. Xu, and D. Tai, "Treatment of choroidal melanoma with I-125 plaque," Int. J. Radiat. Oncol. Biol. Phys. **26**, 619–623 (1993).

N.L. Gagne, K.L. Leonard, K.E. Huber, J.E. Mignano, J.S. Duker, N. V Laver, and M.J. Rivard, "BEDVH—A method for evaluating biologically effective dose volume histograms: Application to eye plaque brachytherapy implants," Med. Phys. **39**, 976 (2012).

N.L. Gagne, K.L. Leonard, and M.J. Rivard, "Radiobiology for eye plaque brachytherapy and evaluation of implant duration and radionuclide choice using an objective function," Med. Phys. **39**, 3332 (2012).

N.L. Gagne and M.J. Rivard, "Quantifying the dosimetric influences of radiation coverage and brachytherapy implant placement uncertainty on eye plaque size selection," Brachytherapy **12**, 508–520 (2013).

D.G. Godfrey, R.G. Waldron, and A. Capone, "Transpupillary thermotherapy for small choroidal melanoma," Am. J. Ophthalmol. **128**, 88–93 (1999).

J.T. Goorley, M. James, T. Booth, F. Brown, J. Bull, J. Cox, and J. Durkee, "Initial MCNP6 Release Overview," Nucl. Technol. **180**, 298–315 (2012).

J.T. Goorley, M.R. James, T.E. Booth, F.B. Brown, J.S. Bull, L.J. Cox, J.W. Durkee, J.S. Elson, M.L. Fensin, R.A. Forster, J.S. Hendricks, H.G. Hughes, R.C. Johns, B.C. Kiedrowski, and S.G. Mashnik, *MCNP6 User's Manual, Version 1.0, LA-CP-13-00634* (Los Alamos National Laboratory, 2013).

D. Granero, J. Pérez-Calatayud, F. Ballester, E. Casal, and J.M. de Frutos, "Dosimetric study of the 15 mm ROPES eye plaque," Med. Phys. **31**, 3330–3336 (2004).

J.W. Harbour, T.G. Murray, S.F. Byrne, R. Hughes, E.K. Gendron, F.J. Ehlies, and A.M. Markoe, "Intraoperative echographic localization of iodine 125 episcleral radioactive plaques for posterior uveal melanoma," Retina **16**, 129–134 (1996).

N. Hardcastle, A. Basavatia, A. Bayliss, and W.A. Tomé, "High dose per fraction dosimetry of small fields with gafchromic EBT2 film," Med. Phys. **38**, 4081–4085 (2011).

N. Hayashi, Y. Watanabe, R. Malmin, and H. Kato, "Evaluation of triple channel correction acquisition method for radiochromic film dosimetry," J. Radiat. Res. **53**, 930–935 (2012).

J. Hofbauer, C. Kirisits, A. Resch, Y. Xu, A. Sturdza, R. Pötter, and N. Nesvacil, "Impact of heterogeneity-corrected dose calculation using a grid-based Boltzmann solver on breast and cervix cancer brachytherapy.," J. Contemp. Brachytherapy **8**, 143–9 (2016).

S.J. van Hoof, P. V Granton, G. Landry, M. Podesta, and F. Verhaegen, "Evaluation of a novel triple-channel radiochromic film analysis procedure using EBT2," Phys. Med. Biol. **57**, 4353–4368 (2012).

J.H. Hubbell, and S.M. Seltzer. (2004), *Tables of X-Ray Mass Attenuation Coefficients and Mass Energy-Absorption Coefficients* (version 1.4). National Institute of Standards and Technology, Gaithersburg, MD. (URL: http://physics.nist.gov/xaamdi). Last accessed January 24, 2017.

J.L. Hungerford, A.J.E. Foss, I. Whelahan, R.D. Errington, A. Kacperek, and J. Kongerud, "Side Effects of Photon and Proton Radiotherapy for Ocular Melanoma," Front. Radiat. Ther. Oncol. **30**, 287–293 (1997).

D.E. Hyer, A. Sheybani, G.M. Jacobson, and Y. Kim, "The dosimetric impact of heterogeneity corrections in high-dose-rate 192Ir brachytherapy for cervical cancer: Investigation of both conventional Point-A and volume-optimized plans," Brachytherapy **11**, 515–520 (2012).

ICRP, "Basic anatomical and physiological data for use in radiological protection: reference values," in *Annals of the ICRP 89* (ICRP, Washington, DC, 2002).

ICRP, "Adult reference comutational phantoms," in *ICRP Report No. 110* (ICRP, Washington, DC, 2009).

ICRU, "Photon, electron, proton and neutron interaction data for body tissues," in *ICRU Report No. 46* (ICRU Publications, Bethesda, MD, 1992).

ICRU, "Prescribing, recording, and reporting photon beam therapy," in *ICRU Report 62 (Supplement to ICRU Report 50)* (ICRU, Washington, DC, 1999).

ICRU, "Prescribing , Recording , and Reporting Brachytherapy for cancer of the cervix," in *ICRU Report No. 89* (ICRU Publications, Bethesda, MD, 2013).

D. Jacob, M. Lamberto, L. DeSiyza Lawrence, and F. Mourtada, "Clinical transition to model-based dose calculation algorithm: A retrospective analysis of high-dose-rate tandem and ring brachytherapy of the cervix," Brachytherapy **16**, 624–629 (2017).

H.E. Johns and J.R. Cunningham, *The physics of radiology*, 4th Ed. (Charles C Thomas, Springfield, IL, IL, 1983).

R. Jones, E. Gore, W. Mieler, K. Murray, M. Gillin, K. Albano, and B. Erickson, "Posttreatment visual acuity in patients treated with episcleral plaque therapy for choroidal melanoma: Dose and dose rate effects," Int. J. Radiat. Oncol. Biol. Phys. **52**, 989–995 (2002).

P. Karaiskos, P. Papagiannis, L. Sakelliou, G. Anagnostopoulos, and D. Baltas, "Monte Carlo dosimetry of the selectSeed ^{125}I interstitial brachytherapy seed," Med. Phys. **28**, 1753–1760 (2001).

A. Karvat, C. Duzenli, R. Ma, K. Paton, and T. Pickles, "The treatment of choroidal melanoma with [198]Au plaque brachytherapy," Radiother. Oncol. **59**, 153–156 (2001).

R. Kath, J. Hayungs, N. Bornfeld, W. Sauerwein, K. Hoffken, and S. Seeber, "Prognosis and treatment of disseminated uveal melanoma," Cancer **72**, 2219–2223 (1993).

F.M. Khan, *The physics of radiation therapy*, 5th ed. (Lippincott Williams & Wilkins, Philadelphia, PA, 2014).

C. Kirisits, M.J. Rivard, D. Baltas, F. Ballester, M. De Brabandere, R. Van Der Laarse, Y. Niatsetski, P. Papagiannis, T.P. Hellebust, J. Perez-Calatayud, K. Tanderup, J.L.M. Venselaar, and F.A. Siebert, "Review of clinical brachytherapy uncertainties: Analysis guidelines of GEC-ESTRO and the AAPM," Radiother. Oncol. **110**, 199–212 (2014).

M. Kleineidam, R. Guthoff, and S.M. Bentzen, "Rates of local control, metastasis, and overall survval in patients with posterior uveal melanomas treated with ruthenium-106 plaques," Radiother. Oncol. **28**, 148–156 (1993).

R.W. Kline, *Coordinate Localization*, (URL: http://rpc.mdanderson.org/rpc/credentialing/Coordinate Localization.doc).

R.W. Kline and P.D. Yeakel, "Ocular melanoma, I-125 plaques," Med. Phys. **14**, 475 (1987).

R.W. Kline and J.D. Earle, "Implications of TG-43 for dose prescription and calculations for I-125 eye plaques," Med. Phys. **23**, 1054 (1996).

T. Knöös, M. Nilsson, and L. Ahlgren, "A method for conversion of Hounsfield number to electron density and prediction of macroscopic pair production cross-sections," Radiother. Oncol. **5**, 337–345 (1986).

A.L. Krintz, W.F. Hanson, G.S. Ibbott, and D.S. Followill, "Verification of Plaque Simulator Dose Distributions Using Radiochromic Film," Med. Phys. **29**, 1220–1221 (2002).

A.L. Krintz, W.F. Hanson, G.S. Ibbott, and D.S. Followill, "A reanalysis of the Collaborative Ocular Melanoma Study Medium Tumor Trial eye plaque dosimetry," Int. J. Radiat. Oncol. Biol. Phys. **56**, 889–898 (2003).

E. Kujala, T. Mäkitie, and T. Kivelä, "Very long-term prognosis of patients with malignant uveal melanoma.," Invest. Ophthalmol. Vis. Sci. **44**, 4651–4659 (2003).

A. de la Zerda, S.-T. Chiu-Tsao, J. Lin, L.L. Boulay, I. Kanna, J.H. Kim, and H.-S. Tsao, "^{125}I eye plaque dose distribution including penumbra characteristics," Med. Phys. **23**, 407–418 (1996).

G. Landry, M.J. Rivard, J.F. Williamson, and F. Verhaegen, "Monte Carlo Methods and Applications for Brachytherapy Dosimetry and Treatment Planning," in *Monte Carlo Techniques in Radiation Therapy*, edited by J. Seco and F. Verhaegen (Taylor & Francis Group, LLC, Boca Raton, FL, 2013), pp. 125–143.

K.L. Leonard, N.L. Gagne, J.E. Mignano, J.S. Duker, E.A. Bannon, and M.J. Rivard, "A 17-year retrospective study of institutional results for eye plaque brachytherapy of uveal melanoma using 125I, 103Pd, and 131Cs and historical perspective," Brachytherapy **10**, 331–339 (2011).

M. Lesperance, M. Inglis-Whalen, and R.M. Thomson, "Model-based dose calculations for COMS eye plaque brachytherapy using an anatomically realistic eye phantom," Med. Phys. **41**, 021717 (12 pp.) (2014).

M. Lesperance, M. Martinov, and R.M. Thomson, "Monte Carlo dosimetry for ^{103}Pd, ^{125}I, and ^{131}Cs ocular brachytherapy with various plaque models using an eye phantom," Med. Phys. **41**, 031706 (2014).

D. Lewis, A. Micke, X. Yu, and M.F. Chan, "An efficient protocol for radiochromic film dosimetry," Med. Phys. **39**, 6339 (2012).

P. Lindsay, A. Rink, M. Ruschin, and D.A. Jaffray, "Investigation of energy dependence of EBT and EBT-2 gafchromic film," Med. Phys. **37**, 571–576 (2010).

P.K. Lommatzsch, "Treatment of choroidal melanomas with ^{106}Ru/^{106}Rh beta-ray applicators," Surv. Ophthalmol. **19**, 85–100 (1974).

P.K. Lommatzsch, "Results after -irradiation (^{106}Ru/^{106}Rh) of choroidal melanomas: 20 years' experience," Br. J. Ophthalmol. **70**, 844–851 (1986).

P.K. Lommatzsch, C. Werschnik, and E. Schuster, "Long-term follow-up of Ru-106/Rh-106 brachytherapy for posterior uveal melanoma," Graefe's Arch Clin Exp Ophthalmol **238**, 129–137 (2000).

G. Luxton, M.A. Astrahan, and Z. Petrovich, "Backscatter measurements from a single seed of ^{125}I for ophthalmic plaque dosimetry," Med. Phys. **15**, 397–400 (1988).

G. Luxton, M.A. Astrahan, P.E. Liggett, D.L. Neblett, D.M. Cohen, and Z. Petrovich, "Dosimetric calculations and measurements of gold plaque ophthalmic irradiators using iridium-192 and iodine-125 seeds," Int. J. Radiat. Oncol. **15**, 167–176 (1988).

G. Luxton, "Comparison of radiation dosimetry in water and in solid phantom materials for I-125 and Pd-103 brachytherapy sources: EGS4 Monte Carlo study," Med. Phys. **21**, 631–641 (1994).

B.D. Lynch, J. Kozelka, M.K. Ranade, J.G. Li, W.E. Simon, and J.F. Dempsey, "Important considerations for radiochromic film dosimetry with flatbed CCD scanners and EBT GAFCHROMIC® film," Med. Phys. **33**, 4551–4556 (2006).

C.M. Ma, C.W. Coffey, L.A. DeWerd, C. Liu, R. Nath, S.M. Seltzer, and J.P. Seuntjens, "AAPM protocol for 40-300 kV x-ray beam dosimetry in radiotherapy and radiobiology," Med. Phys. **28**, 868–893 (2001).

Y. Ma, F. Lacroix, M.-C. Lavallée, and L. Beaulieu, "Validation of the Oncentra Brachy Advanced Collapsed cone Engine for a commercial ^{192}Ir source using heterogeneous geometries," Brachytherapy **14**, 939–952 (2015).

Y. Ma, J. Vijande, F. Ballester, A. Carlsson Tedgren, D. Granero, A. Haworth, F. Mourtada, G.P. Fonseca, K. Zourari, P. Papagiannis, M.J. Rivard, F.-A. Siebert, R.S. Sloboda, R. Smith, M.J.P. Chamberland, R.M. Thomson, F. Verhaegen, and L. Beaulieu, "A generic TG-186 shielded applicator for the commissioning of model-based dose calculation algorithms for high-dose-rate 192Ir brachytherapy," Med. Phys. Accepted (2017).

A. Mahata and P.B. Ravindran, "Investigation of the use of Gafchromic EBT film for routine IMRT QA," Radiother. Oncol. **84**, S54 (2007).

J.A. Martín-Viera Cueto, V. Parra Osorio, C. Moreno Sáiz, F. Navarro Guirado, F.J. Casado Villalón, and P. Galán Montenegro, "A universal dose–response curve for radiochromic films," Med. Phys. **42**, 221–231 (2015).

C. Maschi, J. Thariat, J. Herault, and J.-P. Caujolle, "Tumour Response in Uveal Melanomas Treated with Proton Beam Therapy," Clin. Oncol. **28**, 198–203 (2014).

G. Massillon-JL, "Energy Dependence of the New Gafchromic EBT3 Film: Dose Response Curves for 50 kV, 6 and 15 MV X-Ray Beams," Int. J. Med. Physics,Clinical Eng. Radiat. Oncol. **01**, 60–65 (2012).

R.R. Mayer, F. Ma, Y. Chen, R.I. Miller, A. Belard, J. McDonough, and J.J. O'Connell, "Enhanced dosimetry procedures and assessment for EBT2 radiochromic film," Med. Phys. **39**, 2147 (2012).

S. McCauley Cutsinger, K.M. Furutani, and S. Corner, "A Method to Verify Eye Plaque Seed Coordinates Using the FARO Edge," Brachytherapy **14**, S68–S69 (2015).

T.J. McCaw, J.A. Micka, and L.A. DeWerd, "Characterizing the marker-dye correction for Gafchromic® EBT2 film: A comparison of three analysis methods," Med. Phys. **38**, 5771 (2011).

I.W. McLean, W.D. Foster, and L.E. Zimmerman, "Prognostic factors in small malignant melanomas of choroid and ciliary body," Arch. Ophthalmol. **95**, 48–58 (1977).

D.C. Medich, M.A. Tries, and J.J. Munro, "Monte Carlo characterization of an ytterbium-169 high dose rate brachytherapy source with analysis of statistical uncertainty," Med. Phys. **33**, 163–172 (2006).

A.S. Meigooni, J.L. Hayes, H. Zhang, and K. Sowards, "Experimental and theoretical determination of dosimetric characteristics of IsoAid ADVANTAGE ^{125}I brachytherapy source," Med. Phys. **29**, 2152–2158 (2002).

C.S. Melhus and M.J. Rivard, "Approaches to calculating AAPM TG-43 brachytherapy dosimetry parameters for ^{137}Cs, ^{125}I, ^{192}Ir, ^{103}Pd, and ^{169}Yb sources," Med. Phys. **33**, 1729–1737 (2006).

C.S. Melhus and M.J. Rivard, "COMS eye plaque brachytherapy dosimetry simulations for ^{103}Pd, ^{125}I, and ^{131}Cs," Med. Phys. **35**, 3364–3371 (2008).

I. Méndez, P. Peterlin, R. Hudej, A. Strojnik, and B. Casar, "On multichannel film dosimetry with channel-independent perturbations.," Med. Phys. **41**, 011705 (2014).

I. Méndez, "Model selection for radiochromic film dosimetry," Phys. Med. Biol. **60**, 4089–4104 (2015).

A. Micke, D.F. Lewis, and X. Yu, "Multichannel film dosimetry with nonuniformity correction," Med. Phys. **38**, 2523–2534 (2011).

L. Missotten, W. Dirven, A. Van der Schueren, A. Leys, G. De Meester, and E. Van Limbergen, "Results of treatment of choroidal malignant melanoma with high-dose-rate strontium-90 brachytherapy," Graefe's Arch. Clin. Exp. Ophthalmol. **236**, 164–173 (1998).

M.G. Mitch and S.M. Seltzer, "SU-EE-A2-03: Model-Specific Uncertainties in Air-Kerma Strength Measurements of Low-Energy Photon-Emitting Brachytherapy Sources," Med. Phys. **34**, 2337 (2007).

G. Modorati, E. Miserocchi, L. Galli, P. Picozzi, and P. Rama, "Gamma knife radiosurgery for uveal melanoma: 12 years of experience," Br. J. Ophthalmol. **93**, 40–44 (2009).

R.F. Moore, "Choroidal sarcoma treated by the intraocular insertion of radon seeds," Br. J. Ophthalmol. **14**, 145–156 (1930).

M.A. Morgan, R.K. Ten Haken, and T.S. Lawrence, "Essentials of Radiation Therapy," in *DeVita, Hellman, and Rosenberg's Cancer: Principles & Practice of Oncology*, 10th ed., edited by V.T. DeVita, T.S. Lawrence and S.A. Rosenberg (Lippincott Williams & Wilkins, Philadelphia, PA, 2015), pp. 136–155.

H. Morrison, M.P. Larocque, G. Menon, H.-S. Jans, E. Weis, and R.S. Sloboda, "Delivered dose uncertainty analysis for partially loaded and eccentrically placed 16 mm COMS plaques compared to fully loaded plaques for brachytherapy treatment of uveal melanoma," International Society of Ocular Oncology (ISOO) Bienniel Conference (URL: http://isoo2017.com/ISOO abstracts/Saturday sessions/Saturday 115 - 225/Saturday 115pm to 225pm_4.pdf) (2017).

T.G. Murray, "Small choroidal melanoma," Arch. Ophthalmol. **115**, 1577–1578 (1997).

S. Nag, J.M. Quivey, J.D. Earle, D. Followill, J. Fontanesi, and P.T. Finger, "The American Brachytherapy Society recommendations for brachytherapy of uveal melanomas," Int. J. Radiat. Oncol. Biol. Phys. **56**, 544–555 (2003).

R. Nath, L.L. Anderson, G. Luxton, K.A. Weaver, J.F. Williamson, and A.S. Meigooni, "Dosimetry of interstitial brachytherapy sources: recommendations of the AAPM Radiation Therapy Committee Task Group No. 43. American Association of Physicists in Medicine," Med. Phys. **22**, 209–234 (1995).

R. Nath, "Overview of brachytherapy physics," in *Brachytherapy Physics: Joint AAPM/ABS Summer School*, 2nd ed., edited by B.R. Thomadsen, M.J. Rivard and W.M. Butler (Medical Physics, Madison, WI, 2005), pp. 1–5.

R. Nath, "Sources and delivery systems I: Radionuclides," in *Brachytherapy Physics: Joint AAPM/ABS Summer School*, 2nd ed., edited by B.R. Thomadsen, M.J. Rivard and W.M. Butler (Medical Physics, Madison, WI, 2005), pp. 25–45.

H. Newman, K.J. Chin, and P.T. Finger, "Subfoveal Choroidal Melanoma: Pretreatment characteristics and response to plaque radiation therapy," Arch. Ophthalmol. **129**, 892–898 (2011).

H. Newman, P.T. Finger, K.J. Chin, and A.C. Pavlick, "Systemic bevacizumab (Avastin) for exudative retinal detachment secondary to choroidal melanoma.," Eur. J. Ophthalmol. **21**, 796–801 (2011).

A. Niroomand-Rad, C.R. Blackwell, B.M. Coursey, K.P. Gall, J.M. Galvin, W.L. McLaughlin, A.S. Meigooni, R. Nath, J.E. Rodgers, and C.G. Soares, "Radiochromic film dosimetry: Recommendations of AAPM Radiation Therapy Committee Task Group 55," Med. Phys. **25**, 2093–2115 (1998).

NUDAT 2.6, National Nuclear Data Centre, Brookhaven National Laboratory, (URL: http://www.nndc.bnl.gov/chart/decaysearchdirect.jsp?nuc=125I&unc=nds). Last accessed January 24, 2017.

S. Packer, S. Stoller, M.L. Lesser, F.S. Mandel, and P.T. Finger, "Long-term results of iodine 125 irradiation of uveal melanoma.," Ophthalmology **99**, 767–773; discussion 774 (1992).

L. Paelinck, W. De Neve, and C. De Wagter, "Precautions and strategies in using a commercial flatbed scanner for radiochromic film dosimetry.," Phys. Med. Biol. **52**, 231–242 (2007).

A.L. Palmer, D. Bradley, and A. Nisbet, "Evaluation and implementation of triple-channel radiochromic film dosimetry in brachytherapy," J. Appl. Clin. Med. Phys. **15**, 280–296 (2014).

E. Pantelis, P. Papagiannis, P. Karaiskos, A. Angelopoulos, G. Anagnostopoulos, D. Baltas, N. Zamboglou, and L. Sakelliou, "The effect of finite patient dimensions and tissue inhomogeneities on dosimetry planning of 192 Ir HDR breast brachytherapy: a Monte Carlo dose verification study," Int. J. Radiat. Oncol. Biol. Phys. **61**, 1596–1602 (2005).

E. Pantelis, V. Peppa, V. Lahanas, E. Pappas, and P. Papagiannis, "BrachyGuide: a brachytherapy-dedicated DICOM RT viewer and interface to Monte Carlo simulation software," J. Appl. Clin. Med. Phys. **16**, 5136 (2015).

P. Papagiannis, L. Beaulieu, and F. Mourtada, "Computational methods for the dosimetric characterization of brachytherapy sources," in *Comprehensive Brachytherapy: Physical and clinical aspects*, edited by J.L.M. Venselaar, D. Baltas, A.S. Meigooni and P.J. Hoskin (Taylor & Francis Group, LLC, Boca Raton, FL, 2013), pp. 85–103.

P. Papagiannis, E. Pantelis, and P. Karaiskos, "Current state of the art brachytherapy treatment planning dosimetry algorithms.," Br. J. Radiol. **87**, 20140163 (2014).

T. Pawlicki, M. Whitaker, and G. Kim, "SU-GG-T-275: On Improving the Accuracy of EBT2 Film Dosimetry Using a Flatbed Scanner," Med. Phys. **37**, 3248–3249 (2010).

J.F. Pérez Azorín, L.I. Ramos García, and J.M. Martí-Climent, "A method for multichannel dosimetry with EBT3 radiochromic films.," Med. Phys. **41**, 062101 (2014).

B.A. Perez, P. Mettu, L. Vajzovic, D. Rivera, A. Alkaissi, B.A. Steffey, J. Cai, S. Stinnett, J.J. Dutton, E.G. Buckley, E. Halperin, L.B. Marks, P. Mruthyunjaya, and D.G. Kirsch, "Uveal melanoma treated with iodine-125 episcleral plaque: An analysis of dose on disease control and visual outcomes," Int. J. Radiat. Oncol. Biol. Phys. **89**, 127–136 (2014).

E. Pilotto, S. Vujosevic, V. De Belvis, R. Parrozzani, B. Boccassini, and E. Midena, "Long-term choroidal vascular changes after iodine brachytherapy versus transpupillary thermotherapy for choroidal melanoma," Eur. J. Ophthalmol. **19**, 646–653 (2009).

J. Poder and S. Corde, "I-125 ROPES eye plaque dosimetry: Validation of a commercial 3D ophthalmic brachytherapy treatment planning system and independent dose calculation software with GafChromic® EBT3 films," Med. Phys. **40**, 121709 (11 pp.) (2013).

E.S. Poon, B. Reniers, S. Devic, T. Vuong, and F. Verhaegen, "Dosimetric characterization of a novel intracavitary mold applicator for ^{192}Ir high dose rate endorectal brachytherapy treatment," Med. Phys. **33**, 4515–4526 (2006).

E.S. Poon, Y. Le, J.F. Williamson, and F. Verhaegen, "BrachyGUI: an adjunct to an accelerated Monte Carlo photon transport code for patient-specific brachytherapy dose calculations and analysis," J. Phys. Conf. Ser. **102**, 012018 (2008).

R. Potter and E. Van Limbergen, "Uveal melanoma," in *The GEC ESTRO handbook of brachytherapy*, edited by A. Gerbaulet, R. Potter, J.J. Mazeron, H. Meertens and E. Van Limbergen (Belgium, 2002), pp. 591–610.

J.M. Quivey, D.H. Char, T.L. Phillips, K.A. Weaver, J.R. Castro, and S.M. Kroll, "High intensity 125-iodine (^{125}I) plaque treatment of uveal melanomas," Int. J. Radiat. Oncol. Biol. Phys. **26**, 613–618 (1993).

J.M. Quivey, J.J. Augsburger, L. Snelling, and L.W. Brady, "^{125}I plaque therapy for uveal melanoma. Analysis of the impact of time and dose factors on local control," Cancer **77**, 2356–62 (1996).

Radiological Society of North America, *Introduction to Cancer Therapy (Radiation Oncology)*, (URL: https://www.radiologyinfo.org/en/info.cfm?pg=intro_onco). Last accessed April 19, 2017.

J.A. Raffi, S.D. Davis, C.G. Hammer, J.A. Micka, K.A. Kunugi, J.E. Musgrove, J.W. Winston, T.J. Ricci-Ott, and L.A. DeWerd, "Determination of exit skin dose for ^{192}Ir intracavitary accelerated partial breast irradiation with thermoluminescent dosimeters," Med. Phys. **37**, 2693–2702 (2010).

L.I. Ramos Garcia and J.F. Pérez Azorin, "Improving the calibration of radiochromic films by the use of uncertainties in optical density and dose," Med. Phys. **40**, 071726 (2013).

S.K. Ray, R. Bhatnagar, W.F. Hartsell, and G.R. Desai, "Review of eye plaque dosimetry based on AAPM task group 43 recommendations," Int. J. Radiat. Oncol. Biol. Phys. **41**, 701–706 (1998).

C. Richter, J. Pawelke, L. Karsch, and J. Woithe, "Energy dependence of EBT-1 radiochromic film response for photon (10 kVp-15 MVp) and electron beams (6-18 MeV) readout by a flatbed scanner," Med. Phys. **36**, 5506–5514 (2009).

A. Rink, I.A. Vitkin, and D.A. Jaffray, "Characterization and real-time optical measurements of the ionizing radiation dose response for a new radiochromic medium," Med. Phys. **32**, 2510–2516 (2005).

A. Rink, "Point-based ionization radiation dosimetry using radiochromic materials and a fibreoptic readout system" Ph.D. Thesis, University of Toronto, Canada (2008).

M.J. Rivard, B.M. Coursey, L.A. DeWerd, W.F. Hanson, M.S. Huq, G.S. Ibbott, M.G. Mitch, R. Nath, and J.F. Williamson, "Update of AAPM Task Group No. 43 Report: A revised AAPM protocol for brachytherapy dose calculations," Med. Phys. **31**, 633–674 (2004).

M.J. Rivard, C.S. Melhus, and B.L. Kirk, "Brachytherapy dosimetry parameters calculated for a new ^{103}Pd source," Med. Phys. **31**, 2466–2470 (2004).

M.J. Rivard, W.M. Butler, L.A. DeWerd, M.S. Huq, G.S. Ibbott, A.S. Meigooni, C.S. Melhus, M.G. Mitch, R. Nath, and J.F. Williamson, "Supplement to the 2004 update of the AAPM Task Group No. 43 Report," Med. Phys. **34**, 2187–2205 (2007).

M.J. Rivard, J.L.M. Venselaar, and L. Beaulieu, "The evolution of brachytherapy treatment planning," Med. Phys. **36**, 2136–2153 (2009).

M.J. Rivard, "Monte Carlo radiation dose simulations and dosimetric comparison of the model 6711 and 9011 ^{125}I brachytherapy sources," Med. Phys. **36**, 486–491 (2009).

M.J. Rivard, S.-T. Chiu-Tsao, P.T. Finger, A.S. Meigooni, C.S. Melhus, F. Mourtada, M.E. Napolitano, D.W.O. Rogers, R.M. Thomson, and R. Nath, "Comparison of dose calculation methods for brachytherapy of intraocular tumors," Med. Phys. **38**, 306–316 (2011).

K.R. Russell and A. Ahnesjö, "Dose calculation in brachytherapy for a ^{192}Ir source using a primary and scatter dose separation technique," Phys. Med. Biol. **41**, 1007–1024 (1996).

K.R. Russell, A.K. Carlsson Tedgren, and A. Ahnesjö, "Brachytherapy source characterization for improved dose calculations using primary and scatter dose separation," Med. Phys. **32**, 2739 (2005).

R. Sambuelli, J.D. Luna, V.E. Reviglio, A. Aoki, and C.P. Juarez, "Small choroidal melanoma with massive extraocular extension : invasion through posterior scleral emissary channels," Int. Ophthalmol. **24**, 213–218 (2001).

A.M. Sarici and H. Pazarli, "Gamma-knife-based stereotactic radiosurgery for medium- and large-sized posterior uveal melanoma," Graefe's Arch. Clin. Exp. Ophthalmol. **251**, 285–294 (2013).

A.A. Schoenfeld, D. Poppinga, D. Harder, K.-J. Doerner, and B. Poppe, "The artefacts of radiochromic film dosimetry with flatbed scanners and their causation by light scattering from radiation-induced polymers.," Phys. Med. Biol. **59**, 3575–97 (2014).

S.M. Seltzer, P.J. Lamperti, M.G. Mitch, J.T. Weaver, and B.M. Coursey, "New National Air-Kerma-Strength Standards for ^{125}I and ^{103}Pd Brachytherapy Seeds," J. Res. Natl. Inst. Stand. Technol. **108**, 337–358 (2003).

S.M. Seltzer, P.J. Lamperti, R. Loevinger, M.G. Mitch, J.T. Weaver, and B.M. Coursey, "Erratum: New National Air-Kerma-Strength Standards for ^{125}I and ^{103}Pd Brachytherapy Seeds," J. Res. Natl. Inst. Stand. Technol. **109**, 301 (2004).

S. Seregard, E. Trampe, I. Lax, E. Kock, and G. Lundell, "Results following episcleral ruthenium plaque radiotherapy for posterior uveal melanoma: The Swedish experience," Acta Ophthalmol. Scand. **75**, 11–16 (1997).

R. Serway, C. Vuille, and J. Faughn, *College Physics*, 8th ed. (Brooks/Cole Cengage Learning, Belmont, CA, CA, 2009).

C.L. Shields, J.A. Shields, H. Kiratli, P. De Potter, and J.R. Cater, "Risk factors for growth and metastasis of small choroidal melanocytic lesions," Ophthalmology **102**, 1351–1361 (1995).

C.L. Shields, J.A. Shields, P. de Potter, J. Carter, D. Tardio, and J. Barrett, "Diffuse choroidal melanoma: Clinical features predictive of metastasis," Arch. Ophthalmol. **114**, 956–963 (1996).

C.L. Shields, J. Cater, J.A. Shields, A.D. Singh, M.C. Santos, and C. Carvalho, "Combination of clinical factors predictive of growth of small choroidal melanocytic tumors," Arch. Ophthalmol. **118**, 360–364 (2000).

C.L. Shields, J.A. Shields, J. Cater, K. Gunduz, C. Miyamoto, B. Micaily, and L.W. Brady, "Plaque radiotherapy for uveal melanoma: Long-term visual outcome in 1106 consecutive patients," Arch. Ophthalmol. **118**, 1219–1228 (2000).

C.L. Shields, M. Naseripour, J. Cater, J.A. Shields, H. Demirci, A. Youseff, and J. Freire, "Plaque Radiotherapy for Large Posterior Uveal Melanomas (≥8-mm thick) in 354 Consecutive Patients," Ophthalmology **109**, 1838–1849 (2002).

C.L. Shields and J.A. Shields, "Ocular melanoma: relatively rare but requiring respect," Clin. Dermatol. **27**, 122–133 (2009).

J.A. Shields and C.L. Shields, *Intraocular Tumors. A text and atlas* (WB Saunders, Philadelphia, PA, 1992).

J.A. Shields and C.L. Shields, *Intraocular tumours: an atlas and textbook*, 2nd ed. (Wolters Kluwer, Lippincott Williams & Wilkins, Philadelphia, PA, 2008).

J.A. Shields and C.L. Shields, "Management of Posterior Uveal Melanoma: Past, Present, and Future," Ophthalmology **122**, 414–428 (2015).

A.D. Singh, M.E. Turell, and A.K. Topham, "Uveal melanoma: Trends in incidence, treatment, and survival," Ophthalmology **118**, 1881–1885 (2011).

C.G. Soares, S. Trichter, and S. Devic, "Radiochromic film," in *Clinical dosimetry measurements in Radiotherapy*, edited by D.W.O. Rogers and J.E. Cygler (Medical Physics Publishing, Madison, WI, 2009), pp. 759–813.

T.D. Solberg, J.J. DeMarco, G. Hugo, and R.E. Wallace, "Dosimetric parameters of three new solid core I-125 brachytherapy sources," J. Appl. Clin. Med. Phys. **3**, 119–134 (2002).

H.B. Stallard, "Radiotherapy for malignant melanoma of the choroid," Br. J. Ophthalmol. **50**, 147–155 (1966).

J.G.H. Sutherland and D.W.O. Rogers, "Monte Carlo calculated absorbed-dose energy dependence of EBT and EBT2 film," Med. Phys. **37**, 1110–1116 (2010).

H. Tabandeh, N.A. Chaudhry, T.G. Murray, F. Ehlies, R. Hughes, I.U. Scott, and A.M. Markoe, "Intraoperative echographic localization of iodine-125 episcleral plaque for brachytherapy of choroidal melanoma," Am. J. Ophthalmol. **129**, 199–204 (2000).

B.N. Taylor and C.E. Kuyatt, "Guidelines for Evaluating and Expressing the Uncertainty of NIST Measurement Results," in *NIST Technical Note 1297* (U.S. Government Printing Office, Washington DC, 1994).

R.E.P. Taylor, G. Yegin, and D.W.O. Rogers, "Benchmarking brachydose: Voxel based EGSnrc Monte Carlo calculations of TG-43 dosimetry parameters," Med. Phys. **34**, 445–457 (2007).

R.E.P. Taylor and D.W.O. Rogers, "An EGSnrc Monte Carlo-calculated database of TG-43 parameters," Med. Phys. **35**, 4228–4241 (2008).

R.E.P. Taylor and D.W.O. Rogers, *The CLRP TG-43 Parameter Database for Brachytherapy*, (URL: http://www.physics.carleton.ca/clrp/seed_database). Last accessed March 16, 2017.

The American Brachytherapy Society - Ophthalmic Oncology Task Force, "The American Brachytherapy Society consensus guidelines for plaque brachytherapy of uveal melanoma and retinoblastoma," Brachytherapy **13**, 1–14 (2014).

R.M. Thomson, R.E.P. Taylor, and D.W.O. Rogers, "Monte Carlo dosimetry for ^{125}I and ^{103}Pd eye plaque brachytherapy," Med. Phys. **35**, 5530 (2008).

R.M. Thomson and D.W.O. Rogers, "Monte Carlo dosimetry for ^{125}I and ^{103}Pd eye plaque brachytherapy with various seed models," Med. Phys. **37**, 368–376 (2010).

R.M. Thomson, G. Yegin, R.E.P. Taylor, J. Sutherland, and D.W.O. Rogers, "Fast Monte Carlo Dose Calculations for Brachytherapy with BrachyDose," Med. Phys. **37**, 3910–3911 (2010).

R.M. Thomson, R.E.P. Taylor, and D.W.O. Rogers, *The CLRP Eye Plaque Database*, (URL: http://www.physics.carleton.ca/clrp/eye_plaque). Last accessed March 14, 2017.

J. Usher-Moga, S.M. Beach, and L.A. DeWerd, "Spectroscopic output of ^{125}I and ^{103}Pd low dose rate brachytherapy sources," Med. Phys. **36**, 270–278 (2009).

E.J. Villarreal-Barajas and R.F.H. Khan, "Energy response of EBT3 radiochromic films: Implications for dosimetry in kilovoltage range," J. Appl. Clin. Med. Phys. **15**, 331–338 (2014).

B. Walters, I. Kawrakow, and D.W.O. Rogers, *DOSXYZnrc Users Manual* (National Research Council Canada, Ottawa, Canada, 2005).

K.A. Weaver, "The dosimetry of ^{125}I seed eye plaques," Med. Phys. **13**, 78–83 (1986).

White paper entitled "Gafchromic EBT2: Self-developing film for radiotherapy dosimetry," International Specialty Products, Wayne, NJ, October 2010, http://www.filmqapro.com.

N. van Wieringen, Y.R.J. van Herten, J.B. van de Kamer, A. Erogluer, A. Bel, and J. Wiersma, "Development of a QA procedure fo IMRT plans using EBT radiochromic film," Radiother. Oncol. **84**, S206 (2007).

J.F. Williamson, H. Perera, and Z. Li, "Comparison of calculated and measured heterogeneity correction factors of ^{125}I, ^{137}Cs, and ^{192}Ir brachytherapy sources near localized heterogeneities," Med. Phys. **20**, 209–222 (1992).

J.F. Williamson and M.J. Rivard, "Quantitative dosimetry methods for brachytherapy," in *Brachytherapy Physics: Joint AAPM/ABS Summer School*, 2nd ed., edited by B.R. Thomadsen, M.J. Rivard and W.M. Butler (Medical Physics, Madison, WI, 2005), pp. 233–294.

M.W. Wilson and J.L. Hungerford, "Comparison of episcleral plaque and proton beam radiation therapy for the treatment of choroidal melanoma," Ophthalmology **106**, 1579–1587 (1999).

A. Wu, E.S. Sternick, and D.J. Muise, "Effect of gold shielding on the dosimetry of an ^{125}I seed at close range," Med. Phys. **15**, 627–628 (1988).

A. Wu and F. Krasin, "Film dosimetry analyses on the effect of gold shielding for iodine-125 eye plaque therapy for choroidal melanoma," Med. Phys. **17**, 843–846 (1990).

X-5 Monte Carlo Team, *MCNP - A general Monte Carlo N-Particle Transport Code, Version 5, Volume I: Overview and Theory, LA-UR-03-1987* (Los Alamos National Laboratory, 2008).

Y. Yu, L.L. Anderson, Z. Li, D.E. Mellenberg, R. Nath, M.C. Schell, F.M. Waterman, A. Wu, and J.C. Blasko, "Permanent prostate seed implant brachytherapy: report of the American Association of Physicists in Medicine Task Group No. 64," Med. Phys. **26**, 2054–2076 (1999).

O.A. Zeidan, S.A.L. Stephenson, S.L. Meeks, T.H. Wagner, T.R. Willoughby, P.A. Kupelian, and K.M. Langen, "Characterization and use of EBT radiochromic film for IMRT dose verification," Med. Phys. **33**, 4064–4072 (2006).

H. Zhang, F. Davidorf, and Y. Qi, "Comparison of 16 mm OSU-Nag and COMS eye plaques," J. Appl. Clin. Med. Phys. **13**, 166–178 (2012).

Y. Zhu, A.S. Kirov, V. Mishra, A.S. Meigooni, and J.F. Williamson, "Quantitative evaluation of radiochromic film response for two-dimensional dosimetry," Med. Phys. **24**, 223–231 (1997).

L.W. Zimmermann, A. Amoush, and D.A. Wilkinson, "Episcleral eye plaque dosimetry comparison for the Eye Physics EP917 using Plaque Simulator and Monte Carlo simulation," J. Appl. Clin. Med. Phys. **16**, 226–239 (2015).

K. Zourari, T. Major, A. Herein, V. Peppa, C. Polgar, and P. Papagiannis, "A retrospective dosimetric comparison of TG43 and a commercially available MBDCA for an APBI brachytherapy patient cohort," Phys. Medica **31**, 669–676 (2015).